

DISSERTATION

COMBUSTION PHENOMENA IN BIOMASS GASIFIER COOKSTOVES

Submitted by

Jessica Tryner

Department of Mechanical Engineering

In partial fulfillment of the requirements

For the Degree of Doctor of Philosophy

Colorado State University

Fort Collins, Colorado

Summer 2016

Doctoral Committee:

Advisor: Anthony J. Marchese

Bryan Willson

Azer P. Yalin

Jennifer Peel

Copyright by Jessica Tryner 2016  
All Rights Reserved

## ABSTRACT

### COMBUSTION PHENOMENA IN BIOMASS GASIFIER COOKSTOVES

Approximately 2.8 billion people ( $\sim 40\%$  of the global population) rely on solid fuels, such as wood, charcoal, agricultural residues, and coal, for cooking. Exposure to emissions resulting from incomplete combustion of solid fuels leads to many adverse health impacts. These health impacts have motivated the development of solid-fuel cookstoves that reduce user exposure to carbon monoxide (CO) and fine particulate matter (PM<sub>2.5</sub>). In recent years, rating systems and emission rate targets for solid-fuel cookstove performance have been proposed. The aspirational targets included in these systems (e.g., Tier 4 in the ISO IWA tiers) have encouraged the development of cookstoves that reduce emissions of CO and PM<sub>2.5</sub> by more than 50% and 95%, respectively, compared to a baseline three-stone fire. In a top-lit up draft (TLUD) gasifier cookstove, solid biomass fuel is gasified and the resulting gaseous fuel is mixed with secondary air above the fuel bed to produce the flame that heats the cooking surface. Household biomass cookstoves that utilize gasifier designs have attracted interest due to their demonstrated ability to emit less CO and PM<sub>2.5</sub> per unit of energy delivered to the cooking surface than other cookstove designs. Unfortunately, highly variable performance has also been observed among gasifier cookstoves, and some have been found to emit more CO and PM<sub>2.5</sub> than a three-stone fire. Accordingly, three studies were conducted to: (1) identify the sources of the observed variability; (2) characterize the manner in which stove design, fuel properties, and operating mode influenced performance; (3) gain insight into how secondary air velocity affected fuel-air mixing and the flame dynamics in the secondary combustion zone; and (4) evaluate whether or not the reductions in emission rates that are sought could be achieved with the TLUD design.

In the first study, five natural draft TLUD design configurations were tested with two fuels (corn cobs and Lodgepole pine pellets) to investigate the variability in performance that had been observed in previous studies. The results indicated that stove design, fuel

type, and operator behavior all influenced emissions. Four of the five configurations exhibited lower emissions when fueled with Lodgepole pine pellets than when fueled with corn cobs. Furthermore, large transient increases in CO emission rates were observed when stoves were refueled during operation by adding fresh biomass on top of the hot char bed that was left behind after the previous batch of fuel had gasified. An energy balance model was also developed, using temperature data collected from thermocouples mounted on each configuration, to identify the factors that contributed the most to sub-unity efficiency. The results illustrated that up to 60% of the energy input to the stove as fuel could be left over as char at the end of the test, and whether or not the energy in this char was subtracted from the energy in the fuel consumed during the test when calculating the thermal efficiency of a given configuration had a large effect on the calculated efficiency value.

The manner in which cookstove design, fuel properties, and operator behavior affected TLUD performance was investigated in more detail in a second study. Seventeen different stove geometries, 4 primary air flow rates, 4 secondary air flow rates, 5 secondary air temperatures, 4 fuel moisture contents, and 4 different fuel types were tested in a modular test bed using a procedure specifically designed to capture the low emissions observed during normal operation and the high emissions observed during refueling and char burnout. The lowest high-power emissions measured during normal operation were  $1.6 \text{ g}\cdot\text{MJ}_d^{-1}$  CO (90% confidence interval (CI) = 1.1–2.1) and  $18 \text{ mg}\cdot\text{MJ}_d^{-1}$  PM<sub>2.5</sub> (90% CI = 17–19). These values were well below the Tier 4 targets of  $8 \text{ g}\cdot\text{MJ}_d^{-1}$  CO and  $41 \text{ mg}\cdot\text{MJ}_d^{-1}$  PM<sub>2.5</sub>, but post-refueling emissions were always above the Tier 4 targets. Higher secondary air velocities resulted in lower emissions. Changes in fuel type influenced the composition of the producer gas entering the secondary combustion zone during normal operation and sometimes resulted in order of magnitude changes in PM<sub>2.5</sub> emissions. Temperature measurements taken in the fuel bed indicated that the stove operated as an inverted downdraft gasifier during normal operation and as a conventional updraft gasifier after refueling. Overall, the results suggest that efforts aimed at reducing users' exposure to CO and PM<sub>2.5</sub> emissions from solid fuel

combustion need to take fuel type and operator behavior, in addition to stove design, into consideration.

The third study was designed to investigate the effects of secondary air velocity on the fuel-air mixing process and flame dynamics in the secondary combustion zone by employing high-speed imaging techniques. Images of OH\* chemiluminescence, acetone (which served as a fuel tracer) planar laser-induced fluorescence (PLIF), and OH PLIF were collected at multi-kHz repetition rates in a burner designed to generate a two-dimensional replica of the secondary combustion zone in a gasifier cookstove. This burner featured two opposed planar jets that formed an inverse non-premixed flame in which the air and fuel were in cross flow. Images were collected for various air and fuel velocities. Regular deflecting oscillation of the jets, which has been reported previously for isothermal, non-reacting, unconfined opposed planar jets, was observed in some cases but appeared to be suppressed by convection in the vertical direction and buoyancy effects in other cases. The acetone PLIF images revealed that a high air jet velocity resulted in more extensive mixing of the air and fuel below the height of air injection. As a result, the reaction zone was located further below the top of the burner in comparison to the low air velocity case. These results suggest that higher air jet velocities may lead to lower emissions from gasifier cookstoves as a result of better fuel-air mixing and a lower reaction front location that allows more time for CO and PM to be oxidized before reactions are quenched by the cold cooking surface; however, the literature suggests that unconfined opposed axisymmetric jets do not exhibit deflecting oscillation behavior and, as a result, there are limitations associated with the use of opposed planar jets as a model for the secondary air jets in a gasifier cookstove.

## ACKNOWLEDGMENTS

First and foremost, I want to thank my advisor, Prof. Anthony Marchese, for providing me with guidance, unwavering support, regular encouragement, and a wealth of opportunities for professional development. He has been a great mentor and I hope that he knows how incredibly grateful I am. I would also like to thank my other committee members—Prof. Bryan Willson, Prof. Azer P. Yalin, and Prof. Jennifer Peel—for devoting their time and expertise.

I could not have completed the experiments described in Chapters 4 and 5 without the assistance of James Tillotson and Jeff Mohr. Thank you to James for his dedication and perpetual positive attitude. Thank you to Jeff for completing a never-ending list of tasks quickly, enthusiastically, and meticulously. Thank you to the rest of the Marchese research group for their friendship and for providing technical support on a variety of tasks, especially Marc Baumgardner, Colin Gould, Torben Grumstrup, and Tim Vaughn.

Thank you to Prof. Adam Steinberg at the University of Toronto Institute for Aerospace Studies for allowing me to utilize his laboratory and laser diagnostics equipment and for providing invaluable advice on interpretation of the CL and PLIF images. Thank you to Qiang An, who cheerfully spent many consecutive long days helping me to set up the CL/PLIF experiment and collect the images. Thank you to Rabab Haider for sharing her image processing code with me.

The work presented herein was enabled by financial support from the Multidisciplinary Approaches to Sustainable Bioenergy NSF IGERT program (award number NSF DGE 0801707), U.S. Department of Energy award number DE-EE0006086, and the Department of Mechanical Engineering PhD Teaching Fellowship. Thank you to Prof. Ken Reardon and Barb Gibson for organizing a great IGERT experience! Thank you to Prof. Courtney Jahn and John Field for supervising my laboratory rotations. Thank you to Elliott Levine, our DOE Technology Manager, and Clayton Rohman, our Project Monitor. Thank you to Prof.

Patrick Fitzhorn for awarding me the teaching fellowship and mentoring me during my first teaching experience.

Thank you to many EECL students, staff, and faculty who helped with fabrication, maintained laboratory equipment, taught me a variety of experimental techniques, assisted me with experiments, and provided exciting opportunities for collaboration, including Phil Bacon, Darryl Beemer, Kelsey Bilsback, Kirk Evans, Jason Golly, Evan Hoffmann, Mark James, Christian L'Orange, John Mizia (and his students), Jason Prapas, Prof. John Volckens, and the members of Prof. Yalin's group. It has been wonderful to work with you all!

A number of administrative staff associated with the EECL, Energy Institute, Department of Mechanical Engineering, and Engineering Business Office provided regular assistance with purchasing, travel, and graduate school forms, and helped ensure that I met the requirements for graduation. Thank you especially to Karen Mueller and Megan Kosovski. Finally, thank you to the staff at Morgan Library, especially the InterLibrary Loan staff, who helped me acquire many of the references cited in this document.

## TABLE OF CONTENTS

Abstract .....	ii
Acknowledgments.....	v
List of Tables .....	x
List of Figures .....	xii
1 Introduction .....	1
1.1 Health Impacts of Household Air Pollution and Performance Targets for Cookstoves.....	2
1.2 Why Gasifier Cookstoves?.....	7
1.3 Overview of this Dissertation .....	11
2 Background.....	13
2.1 Characterization of Biomass Fuels .....	13
2.2 Combustion of Biomass .....	20
2.3 Gasification of Biomass .....	24
2.4 Carbon Monoxide Oxidation.....	27
2.5 Particulate Matter Formation and Oxidation.....	28
3 Emissions and Efficiency of Natural Draft Gasifier Cookstoves.....	33
3.1 Introduction.....	33
3.2 Methods .....	33
3.2.1 Test Matrix .....	34
3.2.2 Test Protocol.....	37
3.2.3 Testing Equipment .....	37
3.2.4 Efficiency Calculations .....	39
3.2.5 Energy Balance Model.....	40

3.3	Results and Discussion . . . . .	49
3.3.1	Influence of Design Configuration and Fuel Type on Emissions and Efficiency . . . . .	49
3.3.2	Emissions Increases Associated with Refueling . . . . .	52
3.3.3	Further Discussion on the Experimental Results . . . . .	56
3.3.4	Energy Balance Results . . . . .	57
3.4	Conclusions . . . . .	60
4	Effects of Air Flow Rates, Secondary Air Inlet Geometry, Fuel Type, and Operating Mode on Gasifier Cookstove Performance . . . . .	63
4.1	Introduction . . . . .	63
4.2	Methods . . . . .	64
4.2.1	Modular Test Bed . . . . .	64
4.2.2	Test Matrix . . . . .	68
4.2.3	Test Procedure . . . . .	73
4.2.4	Calculations . . . . .	78
4.3	Results and Discussion . . . . .	81
4.3.1	Effects of Air Flow Rates, Fuel Moisture, and Secondary Air Delivery Parameters . . . . .	81
4.3.2	Effects of Fuel Type . . . . .	90
4.3.3	Effects of Operating Mode . . . . .	96
4.4	Conclusions . . . . .	97
5	High-Speed Imaging of Inverse Non-Premixed Cross-Flow Flames . . . . .	99
5.1	Introduction . . . . .	99
5.2	Methods . . . . .	100
5.2.1	Test Bed . . . . .	100

5.2.2	Test Matrix .....	103
5.2.3	Experimental Setup .....	103
5.2.4	Image Processing.....	106
5.3	Results and Discussion.....	108
5.3.1	OH* Chemiluminescence Images.....	108
5.3.2	PLIF Images .....	113
5.3.3	Suitability of this System as a Model for the Secondary Combustion Zone in a TLUD .....	120
5.4	Conclusions .....	123
6	Conclusions and Future Work .....	125
6.1	Conclusions .....	125
6.2	Future Work .....	131
	References.....	134
	Appendix A: Additional Information on the Methods for the Experiments Described in Chapter 3 .....	151
	Appendix B: Additional Information on the Methods and Complete Set of Results for the Experiments Described in Chapter 4 .....	155
B.1	Experimental.....	155
B.2	Results .....	162
B.2.1	Test Matrix 1 – Secondary Air Delivery Parameters .....	162
B.2.2	Test Matrix 2 – Primary Air Flow Rates, Fuel Properties, and Secondary Air Delivery Parameters .....	174
B.2.3	Gas Composition Results and Fuel Bed Temperatures .....	189

## LIST OF TABLES

1.1	Percentage of population of developing countries (as defined by the United Nations Development Programme) estimated to rely on various energy sources for cooking in 2007. <sup>3</sup> .....	2
1.2	Tiers of performance delineated in the ISO IWA. <sup>26</sup> .....	5
1.3	Emission rate targets for household solid fuel combustion recommended by the WHO. <sup>21</sup> .....	6
2.1	Properties of fuels used in the experiments described in this document. ....	19
2.2	Compositions and heating values of producer gas generated in a commercial biomass gasifier and the modular TLUD test bed described in Chapter 4 compared to natural gas. ....	25
2.3	Some important reactions associated with a gasification process. <sup>120,124–127</sup> .....	27
3.1	Dimensions of the combustion chambers in each stove configuration tested. ....	35
3.2	Table of tests conducted. ....	36
3.3	Fuel moisture and ash contents, fuel heating values, and char heating values used for calculations in this chapter. ....	36
3.4	Material properties used to calculate the energy stored in the bodies of the stove configurations (values from Incropera et al. <sup>151</sup> ).....	42
4.1	The two test matrices for which experiments were completed.....	70
4.2	Results of additional fuel moisture content tests.....	73
5.1	The five test cases. ....	103
5.2	Oscillation periods predicted for unconfined, isothermal opposed planar jets compared to those observed in the OH* CL image sequences. ....	111
6.1	Lowest high-power CO and PM <sub>2.5</sub> emissions measured during normal operation of the modular TLUD test bed.....	129

A.1	Data collected and instrumentation used in the experiments with natural draft gasifier cookstoves described in Chapter 3. . . . .	151
B.1	Thermocouples used to collect temperature data. . . . .	157
B.2	Test matrix 1 — Secondary air delivery parameters. . . . .	158
B.3	Test matrix 2 — Primary air flow rates, fuel properties, and secondary air delivery parameters. . . . .	159
B.4	Number of replicates of each data point. . . . .	160
B.5	Instrumentation used for data collection. . . . .	161

## LIST OF FIGURES

1.2	Relative risk of acute lower respiratory infection (ALRI) in children as a function of exposure to PM <sub>2.5</sub> (modified from WHO <sup>21</sup> ).....	4
1.3	Schematic of top-lit up draft (TLUD) gasifier cookstove operation.....	9
1.4	Average high-power CO and PM <sub>2.5</sub> emissions measured for different biomass cookstove types during the cold start phase of the WBT (modified from Jetter et al. <sup>75</sup> ). ....	11
2.1	A $\beta$ -D-glucopyranose molecule with the carbon atoms numbered.....	14
2.2	Examples of the pentoses (represented by $\beta$ -D-xylopyranose), hexoses (represented by $\beta$ -D-mannopyranose) and uronic acids (represented by $\alpha$ -D-glucopyranuronic acid) that make up various types of hemicellulose (adapted from Fry <sup>83</sup> ).....	15
2.3	Precursors to lignin: p-coumaryl, coniferyl, and sinapyl alcohol. ....	15
2.4	Operation of conventional updraft and stratified downdraft fixed-bed gasifiers.....	26
3.1	Renderings of the five stoves tested. ....	35
3.2	(a) The actual geometry of the region containing the refractory block, (b) the manner in which the geometry shown in (a) was modeled for Stove 1, and (c) the manner in which the geometry was modeled for Stoves 2 and 3.....	43
3.3	The resistance model used to estimate the temperature distribution within the block of refractory material.....	44
3.4	Average high-power CO emissions vs. average high-power PM <sub>10</sub> emissions compared to ISO tiers for biomass stove performance. ....	50
3.5	Average high-power CO emissions vs. average thermal efficiency compared to ISO tiers for biomass stove performance.....	51
3.6	CO emissions and fuel chamber temperatures during cold start tests completed using Stoves 1, 2, and 3 with corn cob and wood pellet fuels.....	53

3.7	CO emissions and fuel chamber temperatures during cold start tests completed using Stoves 4 and 5 with corn cob and wood pellet fuels. . . . .	55
3.8	Results of the energy balance with the energy consumption attributed to each component shown. . . . .	58
3.9	Results of the energy balance with the energy consumption attributed to each component shown as a percentage of total energy consumption. . . . .	59
4.1	A photograph of the modular TLUD test bed with key features labeled. . . . .	65
4.2	A cross-sectional view of the modular TLUD test bed with key features labeled. . .	66
4.3	Photographs of the secondary air inlets tested in this study. . . . .	67
4.4	Cross sectional renderings of the test bed with constrictions inserted before (left) and after (right) the secondary air inlet. . . . .	67
4.5	A cross-sectional rendering of the test bed configuration that allowed 10% of the secondary air to be injected earlier in the fuel chamber through six 2-mm-diameter holes spaced equally around the circumference. . . . .	68
4.6	Photographs of the fuels used in the experiments. . . . .	72
4.7	Plot of typical CO emissions ( $\text{g}\cdot\text{s}^{-1}$ ) and water temperature ( $^{\circ}\text{C}$ ) as a function of time for the three phase test procedure (normal operation, post-refueling, and char burnout). . . . .	74
4.8	A diagram illustrating the modifications that were made to the test procedure for the tests with the Lodgepole pine pellets. . . . .	75
4.9	Effects of primary air flow rate on average useful power output and dry fuel consumption rate during normal operation (Phase 1, green triangles) and post-refueling (Phase 2, gold circles). . . . .	82
4.10	Effects of primary air flow rate on average high-power CO and $\text{PM}_{2.5}$ emissions during normal operation (Phase 1, green triangles) and post-refueling (Phase 2, gold circles). . . . .	83

4.11	Effects of primary air flow rate on the average concentrations of H <sub>2</sub> , CO, CH <sub>4</sub> , O <sub>2</sub> /Ar, CO <sub>2</sub> and N <sub>2</sub> in the producer gas entering the secondary combustion zone during normal operation (Phase 1), post-refueling (Phase 2) and during char burnout (Phase 3).	84
4.12	Effects of fuel moisture content on average useful power output and dry fuel consumption rate during normal operation (Phase 1, green triangles) and post-refueling (Phase 2, gold circles).	85
4.13	Effects of fuel moisture content on average high-power CO and PM <sub>2.5</sub> emissions during normal operation (Phase 1, green triangles) and post-refueling (Phase 2, gold circles).	85
4.14	Effects of secondary to primary air flow ratio and secondary air opening size (secondary air velocity) on average high-power CO emissions during normal operation (Phase 1, green triangles) and post-refueling (Phase 2, gold circles).	86
4.15	Effects of secondary air swirl angle and constriction location on average high-power CO emissions during normal operation (Phase 1, green triangles) and post-refueling (Phase 2, gold circles).	87
4.16	Images of the secondary combustion zone during normal high-power operation (Phase 1) with varying degrees of swirl imposed at the secondary air inlet.	88
4.17	Effects of varying secondary air delivery parameters on average high-power CO and PM <sub>2.5</sub> emissions during normal operation (Phase 1, green triangles) and post-refueling (Phase 2, gold circles).	90
4.18	Effects of varying fuel type on average high-power CO and PM <sub>2.5</sub> emissions during normal operation (Phase 1, green triangles) and post-refueling (Phase 2, gold circles).	91

4.19	Effects of fuel type on the average concentrations of H <sub>2</sub> , CO, CH <sub>4</sub> , O <sub>2</sub> /Ar, CO <sub>2</sub> and N <sub>2</sub> in the producer gas entering the secondary combustion zone during normal operation (Phase 1), post-refueling (Phase 2) and during char burnout (Phase 3).....	92
4.20	Fuel bed temperatures measured with different fuel types.....	94
4.21	Effects of varying fuel type on the global equivalence ratio in the secondary combustion zone during normal operation (Phase 1, green triangles) and post-refueling (Phase 2, gold circles). ....	96
4.22	Average high-power CO and PM <sub>2.5</sub> emissions for all test cases in the second matrix with the ISO tiers for high-power emissions shown.....	98
5.1	A cross-section diagram illustrating the operational principle of the non-premixed cross-flow flame burner (left) and a photograph of the burner in operation (right).....	101
5.2	An exploded view of the two-dimensional, inverse, non-premixed cross-flow flame burner with the location of the window flush N <sub>2</sub> injection shown.....	102
5.3	A simulated producer gas mixture with the composition shown was mixed with N <sub>2</sub> in the fuel line.....	102
5.4	Diagram of the experimental setup: (a) pump laser, (b) dye laser, (c) UV mirror, (d) UV mirror, (e) UV mirror, (f) iris, (g) concave cylindrical lens ( $f = -25$ mm), (h) convex cylindrical lens ( $f = 500$ mm), (i) convex cylindrical lens ( $f = 750$ mm), (j) dichroic mirror, (k) burner, (l) filter, (m) UV lens, (n) intensifier, and (o) high-speed camera. ....	104
5.5	The positions of the laser sheet within the combustor in each of the three PLIF imaging locations: left, center, and right.....	105

5.6	Intensity of the sheet profiles recorded in the left, center, and right locations at the intensifier gain used for OH PLIF imaging (68) and acetone PLIF imaging (70) as a function of distance along the width of the sheet. ....	107
5.7	A sequence of OH* chemiluminescence images for the baseline case illustrating the oscillation of the air jets. ....	108
5.8	A sequence of OH* chemiluminescence images for the high air velocity case illustrating the oscillation of the air jets. ....	109
5.9	Average OH* chemiluminescence images for each test case. ....	112
5.10	A sequence of acetone PLIF images for the baseline case. ....	114
5.11	A sequence of acetone PLIF images for the high air velocity case. ....	114
5.12	A sequence of acetone PLIF images for the high fuel velocity case. ....	115
5.13	A sequence of acetone PLIF images for the low air velocity case. ....	115
5.14	Average acetone PLIF images for each of the five test cases. ....	116
5.15	A sequence of OH PLIF images for the baseline case. ....	117
5.16	A sequence of OH PLIF images for the high air velocity case. ....	118
5.17	A sequence of OH PLIF images for the low air velocity case. ....	118
5.18	Average OH PLIF images for each of the five test cases. ....	119
A.1	Placement of the thermocouples installed on Stoves 1, 2, and 3. ....	152
A.2	Placement of the thermocouples installed on Stove 4. ....	153
A.3	Placement of the thermocouples installed on Stove 5. ....	154
B.1	A drawing of the test bed with the locations of the thermocouples listed in Table B.1 shown. ....	156
B.2	Effects of varying secondary to primary air flow ratio and secondary air opening size (secondary air velocity) on average high-power CO emissions and useful power output during normal operation (Phase 1, green triangles) and post-refueling (Phase 2, gold circles). ....	162

B.3	Effects of varying secondary air swirl angle and downward angle on average high-power CO emissions and useful power output during normal operation (Phase 1, green triangles) and post-refueling (Phase 2, gold circles). . . . .	163
B.4	Effects of varying secondary air temperature and the pot gap on average high-power CO emissions and useful power output during normal operation (Phase 1, green triangles) and post-refueling (Phase 2, gold circles). . . . .	164
B.5	Effects of varying the constriction location on average high-power CO emissions and useful power output during normal operation (Phase 1, green triangles) and post-refueling (Phase 2, gold circles). . . . .	165
B.6	Effects of varying secondary to primary air flow ratio and secondary air opening size (secondary air velocity) average high-power dry fuel consumption rate and mass loss rate during normal operation (Phase 1, green triangles) and post-refueling (Phase 2, gold circles). . . . .	166
B.7	Effects of varying secondary air swirl angle and downward angle on average high-power dry fuel consumption rate and mass loss rate during normal operation (Phase 1, green triangles) and post-refueling (Phase 2, gold circles). . . . .	167
B.8	Effects of varying secondary air temperature and the pot gap on average high-power dry fuel consumption rate and mass loss rate during normal operation (Phase 1, green triangles) and post-refueling (Phase 2, gold circles). . . . .	168
B.9	Effects of varying the constriction location on average high-power dry fuel consumption rate and mass loss rate during normal operation (Phase 1, green triangles) and post-refueling (Phase 2, gold circles). . . . .	169
B.10	Effects of varying secondary to primary air flow ratio and secondary air opening size (secondary air velocity) on average CO emissions and mass loss rate during char burnout. . . . .	170

B.11	Effects of varying secondary air swirl angle and downward angle on average CO emissions and mass loss rate during char burnout. ....	171
B.12	Effects of varying secondary air temperature and the pot gap on average CO emissions and mass loss rate during char burnout. ....	172
B.13	Effects of varying the constriction location on average CO emissions and mass loss rate during char burnout. ....	173
B.14	Effects of varying primary air flow rate and fuel moisture content on average high-power CO and PM <sub>2.5</sub> emissions during normal operation and post-refueling. ....	174
B.15	Effects of varying fuel type and fuel bulk density on average high-power CO and PM <sub>2.5</sub> emissions during normal operation and post-refueling. ....	175
B.16	Effects of varying secondary air delivery parameters on average high-power CO and PM <sub>2.5</sub> emissions during normal operation and post-refueling. ....	176
B.17	Effects of varying primary air flow rate and fuel moisture content on average high-power useful power output and fuel consumption rate during normal operation (Phase 1, green triangles) and post-refueling (Phase 2, gold circles). ....	177
B.18	Effects of varying fuel type and fuel bulk density on average high-power useful power output and fuel consumption rate during normal operation (Phase 1, green triangles) and post-refueling (Phase 2, gold circles). ....	178
B.19	Effects of varying secondary air delivery parameters on average useful power output and fuel consumption rate during normal operation (Phase 1, green triangles) and post-refueling (Phase 2, gold circles). ....	179
B.20	Effects of varying primary air flow rate and fuel moisture content on average high-power mass loss rate and global equivalence ratio in the secondary combustion zone during normal operation (Phase 1, green triangles) and post-refueling (Phase 2, gold circles). ....	180

B.21	Effects of varying fuel type and fuel bulk density on average high-power mass loss rate and global equivalence ratio in the secondary combustion zone during normal operation (Phase 1, green triangles) and post-refueling (Phase 2, gold circles). . . . .	181
B.22	Effects of varying secondary air delivery parameters on average high-power mass loss rate and global equivalence ratio in the secondary combustion zone during normal operation (Phase 1, green triangles) and post-refueling (Phase 2, gold circles). . . . .	182
B.23	Effects of varying primary air flow rate and fuel moisture content on average CO and PM <sub>2.5</sub> emissions during char burnout. . . . .	183
B.24	Effects of varying fuel type and fuel bulk density on average CO and PM <sub>2.5</sub> emissions during char burnout. . . . .	184
B.25	Effects of varying secondary air delivery parameters on average CO and PM <sub>2.5</sub> emissions during char burnout. . . . .	185
B.26	Effects of varying primary air flow rate and fuel moisture content on the average mass loss rate during char burnout. . . . .	186
B.27	Effects of varying fuel type and fuel bulk density on the average mass loss rate during char burnout. . . . .	187
B.28	Effects of varying secondary air delivery parameters on the average mass loss rate during char burnout. . . . .	188
B.29	Effects of primary air flow rate on the average concentrations of H <sub>2</sub> , CO, CH <sub>4</sub> , O <sub>2</sub> /Ar, CO <sub>2</sub> and N <sub>2</sub> in the producer gas entering the secondary combustion zone during normal operation (Phase 1), post-refueling (Phase 2) and during char burnout (Phase 3). . . . .	189

B.30	Effects of fuel moisture content (for Douglas fir chips) on the average concentrations of H <sub>2</sub> , CO, CH <sub>4</sub> , O <sub>2</sub> /Ar, CO <sub>2</sub> and N <sub>2</sub> in the producer gas entering the secondary combustion zone during normal operation (Phase 1), post-refueling (Phase 2) and during char burnout (Phase 3). . . . .	190
B.31	Effects of fuel type on the average concentrations of H <sub>2</sub> , CO, CH <sub>4</sub> , O <sub>2</sub> /Ar, CO <sub>2</sub> and N <sub>2</sub> in the producer gas entering the secondary combustion zone during normal operation (Phase 1), post-refueling (Phase 2) and during char burnout (Phase 3). . . . .	191
B.32	Effects of fuel bulk density (for corn cobs) on the average concentrations of H <sub>2</sub> , CO, CH <sub>4</sub> , O <sub>2</sub> /Ar, CO <sub>2</sub> and N <sub>2</sub> in the producer gas entering the secondary combustion zone during normal operation (Phase 1), post-refueling (Phase 2) and during char burnout (Phase 3). . . . .	192
B.33	Effects of secondary air delivery parameters on the average concentrations of H <sub>2</sub> , CO, CH <sub>4</sub> , O <sub>2</sub> /Ar, CO <sub>2</sub> and N <sub>2</sub> in the producer gas entering the secondary combustion zone during normal operation (Phase 1), post-refueling (Phase 2) and during char burnout (Phase 3). . . . .	193
B.34	Effects of primary air flow rate on the average composition of the producer gas entering the secondary combustion zone during normal operation (Phase 1), post-refueling (Phase 2) and during char burnout (Phase 3). . . . .	194
B.35	Effects of fuel moisture content (for Douglas fir chips) on the average composition of the producer gas entering the secondary combustion zone during normal operation (Phase 1), post-refueling (Phase 2) and during char burnout (Phase 3). . . . .	195
B.36	Effects of fuel type on the average composition of the producer gas entering the secondary combustion zone during normal operation (Phase 1), post-refueling (Phase 2) and during char burnout (Phase 3). . . . .	196

B.37	Effects of fuel bulk density (for corn cobs) on the average composition of the producer gas entering the secondary combustion zone during normal operation (Phase 1), post-refueling (Phase 2) and during char burnout (Phase 3).....	197
B.38	Effects of secondary air delivery parameters on the average composition of the producer gas entering the secondary combustion zone during normal operation (Phase 1), post-refueling (Phase 2) and during char burnout (Phase 3).....	198
B.39	Fuel bed temperatures measured with different fuel types.....	199
B.40	Fuel bed temperatures measured with different primary air flow rates.....	200
B.41	Fuel bed temperatures measured with different moisture contents.....	201

# CHAPTER 1

## Introduction

The number of people worldwide estimated to rely primarily on solid fuel for cooking has remained constant at approximately 2.8 billion since 1980, even though the percentage of households relying on solid cooking fuel has declined from 62% to 41% over the same time period.<sup>1</sup> Use of solid fuel for cooking is most prevalent in Sub-Saharan Africa and Southeast Asia (see Figure 1.1), where 77% of households (646 million people) and 61% of households (1 billion people), respectively, were estimated to cook primarily with solid fuel in 2010.<sup>1</sup>

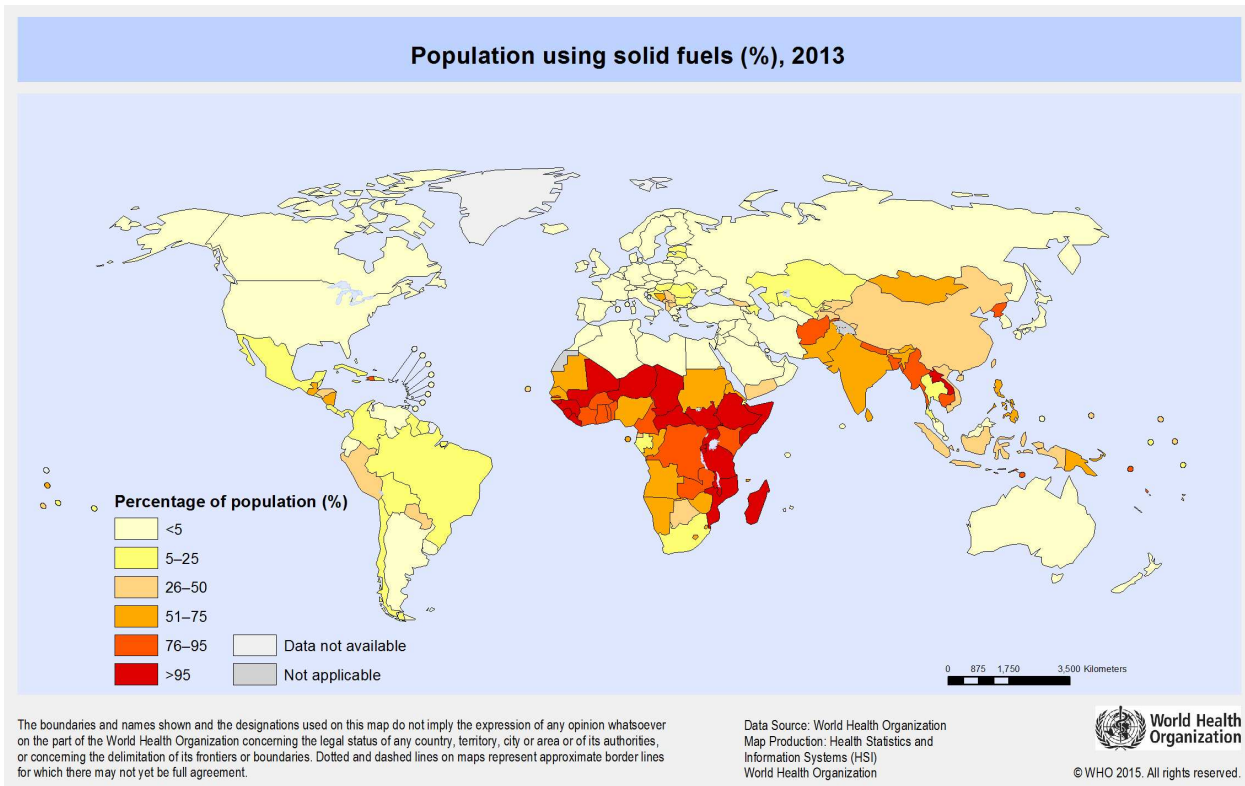


**Figure 1.1: Percentage of population in each country estimated to use solid fuels, such as wood, coal, charcoal, dung, and agricultural residues, for cooking in 2013.<sup>2</sup>**

The term “solid fuel” encompasses wood, coal, charcoal, dung, and agricultural residues.<sup>1,3</sup> According to a 2007 estimate, the majority of people who rely on solid fuels use wood, wood byproducts, or agricultural residues as their primary cooking fuel (see Table 1.1) and approximately 400 million people, primarily in China, use coal.<sup>3</sup>

**Table 1.1: Percentage of population of developing countries (as defined by the United Nations Development Programme) estimated to rely on various energy sources for cooking in 2007.<sup>3</sup>**

Solid fuels		Other energy sources	
Wood, wood byproducts, and agricultural residues	42%	Gas	33%
Coal	8%	Electricity	4%
Charcoal	3%	Kerosene	4%
Dung	3%	Other	3%

Proper air-to-fuel ratios, efficient mixing of air and fuel, as well as the temperatures and residence times required for pollutant oxidation are difficult to maintain in household solid-fuel cooking stoves. Consequently, combustion of solid fuels for cooking results in incomplete conversion of fuel carbon to carbon dioxide, emission of carbon monoxide (CO) and particulate matter less than 2.5  $\mu\text{m}$  in aerodynamic diameter (PM<sub>2.5</sub>), and exposure of users to these dangerous air pollutants.

### 1.1 Health Impacts of Household Air Pollution and Performance Targets for Cookstoves

Exposure to household air pollution (HAP) resulting from solid fuel use is associated with an increased risk of acute lower respiratory infection (ALRI) in children<sup>4</sup> and chronic obstructive pulmonary disease (COPD) in adults.<sup>5</sup> In addition, exposure to HAP from coal combustion has been associated with an increased risk of lung cancer.<sup>6</sup> Tentative links between exposure to biomass smoke and other adverse health outcomes, such as asthma, otitis media, lung cancer, nasopharyngeal/laryngeal cancer, interstitial lung disease, ischemic heart disease, low birth weight, perinatal mortality, tuberculosis, and cataracts, have also been reported.<sup>7-9</sup>

An estimated 2.9 million deaths were attributed to HAP resulting from solid fuel use in the 2013 Global Burden of Disease Study.<sup>10</sup> Indeed, more deaths were attributed to this risk than to unsafe water, unsafe sanitation, or child and maternal malnutrition. Exposure to HAP was identified as the seventh leading risk factor contributing to the global burden of disease (in terms of disability-adjusted life years) overall, the sixth leading risk factor

in developing countries, the sixth leading risk factor in Sub-Saharan Africa, and the third leading risk factor in South Asia.<sup>10</sup>

Improved cookstove interventions in which stoves with chimneys replaced stoves without chimneys have been associated with decreased risk of lung cancer,<sup>11</sup> COPD,<sup>12</sup> and pneumonia<sup>13</sup> among coal users. After installation of improved cookstoves with chimneys in homes of biomass fuel users, one study observed mean reductions in systolic blood pressure of 5.9 mmHg (95% confidence interval (CI) = 11.3–0.4 mmHg reduction) among women over 40 and 4.6 mmHg (95% CI = 10.0 mmHg reduction to 0.8 mmHg increase) among obese women.<sup>14</sup> Another study reported a 22% reduction (95% CI = 41% reduction to 6% increase) in cases of physician-diagnosed pneumonia and a 33% reduction (95% CI = 55%–2% reduction) in cases of severe physician-diagnosed pneumonia among children under 18 months.<sup>15</sup> One study on biomass fuel users observed a lower decline in forced expiratory volume in 1 second (FEV<sub>1</sub>) over one year of follow-up among users who adopted an improved chimney stove,<sup>16</sup> but another study found no improvement in lung function after a similar intervention.<sup>17</sup> Reductions in health risks may not be observed at all if “improved” stoves are of poor quality and result in neither lower emissions nor sustained use.<sup>18,19</sup>

Efforts to mitigate the health impacts of HAP are complicated by the non-linear exposure-response relationship between relative risk of ALRI and exposure to PM<sub>2.5</sub> (see Figure 1.2). Relative risk of ALRI in children increases relatively sharply at low levels of PM<sub>2.5</sub> exposure before leveling off at higher exposure levels.<sup>20,21</sup> This relationship suggests that only modest improvements in health will be obtained unless large reductions are made in exposure.<sup>20,22</sup> To date, exposure-response curves for other adverse health outcomes, such as COPD, have been largely derived from data on ambient air pollution (AAP) in western cities, environmental tobacco smoke (ETS), and active smoking.<sup>23,24</sup> Individuals who cook with solid fuels are expected to experience PM<sub>2.5</sub> doses that are intermediate between ETS and active smoking.<sup>22</sup> Concentrations of particulate matter ranging from 100’s to 1000’s of  $\mu\text{g}\cdot\text{m}^{-3}$  have been measured in kitchens of solid fuel users, but the data on how these concentrations translate

to personal exposures and adverse health outcomes is insufficient.<sup>25</sup> Additional data, particularly on the exposure-response relationship between HAP and COPD,<sup>20,21</sup> would allow the magnitude of emissions reductions required to generate improvements in user health to be determined with greater certainty.<sup>25</sup>

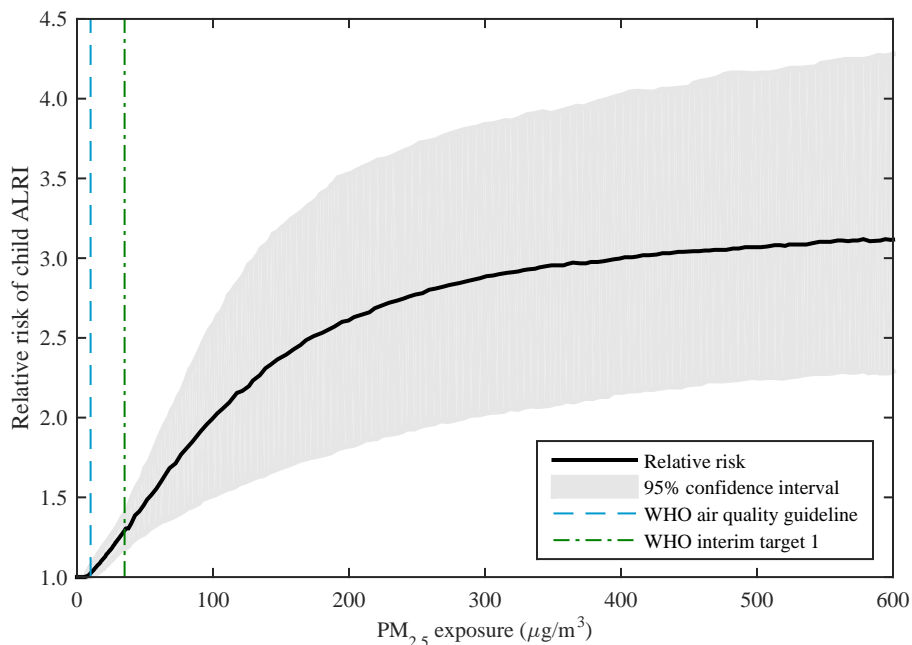


**Figure 1.2: Relative risk of acute lower respiratory infection (ALRI) in children as a function of exposure to  $PM_{2.5}$  (modified from WHO<sup>21</sup>). This integrated exposure-response curve was developed using data on ambient air pollution, secondhand smoke, and household air pollution.<sup>20</sup>**

In 2012, an ISO International Workshop Agreement (IWA) established a tiered rating system for biomass cookstove performance<sup>26</sup> that was modeled after the EPA tiers for emissions from nonroad diesel engines.<sup>27–29</sup> The agreement created a quantitative system for evaluating and comparing the performance of different cookstoves. The tiers for emissions (high-power, low-power, and indoor) and fuel efficiency (thermal efficiency and specific fuel consumption) are shown in Table 1.2. Tier 0 represents a level of performance that is similar to or worse than a three-stone fire or traditional cookstove. Tier 4 represents an aspirational level of performance that would be expected to reduce health risks to users. In accordance

with the shape of the exposure-response curve shown in Figure 1.2, there is a 95% reduction in high-power and indoor PM<sub>2.5</sub> emissions between Tier 0 and Tier 4.

**Table 1.2: Tiers of performance delineated in the ISO IWA.<sup>26</sup>**

	Tier 0	Tier 1	Tier 2	Tier 3	Tier 4
High-power emissions					
CO (g·MJ <sub>d</sub> <sup>-1</sup> )	> 16	≤ 16	≤ 11	≤ 9	≤ 8
PM <sub>2.5</sub> (mg·MJ <sub>d</sub> <sup>-1</sup> )	> 979	≤ 979	≤ 386	≤ 168	≤ 41
Low-power emissions					
CO (g·min <sup>-1</sup> ·L <sup>-1</sup> )	> 0.20	≤ 0.20	≤ 0.13	≤ 0.10	≤ 0.09
PM <sub>2.5</sub> (mg·min <sup>-1</sup> ·L <sup>-1</sup> )	> 8	≤ 8	≤ 4	≤ 2	≤ 1
Indoor emissions					
CO (g·min <sup>-1</sup> )	> 0.97	≤ 0.97	≤ 0.62	≤ 0.49	≤ 0.42
PM <sub>2.5</sub> (mg·min <sup>-1</sup> )	> 40	≤ 40	≤ 17	≤ 8	≤ 2
High-power thermal efficiency (%)	< 15	≥ 15	≥ 25	≥ 35	≥ 45
Low-power specific fuel consumption (MJ·min <sup>-1</sup> ·L <sup>-1</sup> )					
	> 0.050	≤ 0.050	≤ 0.039	≤ 0.028	≤ 0.017

The high-power emissions and thermal efficiency metrics in Table 1.2 correspond to the cold start and hot start phases of the popular Water Boiling Test (WBT) protocol for laboratory testing of biomass cookstoves. Metrics for high-power CO and PM<sub>2.5</sub> emissions are expressed as mass emitted per unit of energy delivered to the cooking surface. The low-power emissions and specific fuel consumption metrics correspond to the simmer phase of the WBT. Metrics for low-power CO and PM<sub>2.5</sub> emissions are expressed as mass emitted per unit time per volume of water simmered.<sup>26</sup> During the cold start phase, the stove body starts out at room temperature and emissions and efficiency are measured while a pot of water (typically 5 L) is brought from room temperature to boiling. The hot start phase begins immediately after the end cold start phase, while the stove body is still hot. Once again, emissions and efficiency are measured while a pot of water is brought from room temperature to boiling. The simmer phase begins immediately after the end of the hot start phase, and emissions and specific fuel consumption are measured while the temperature of the pot of water is maintained just below the boiling temperature for 45 minutes.<sup>30</sup>

In 2014, the World Health Organization (WHO) recommended emission rate targets<sup>21</sup> for biomass cookstoves that would reduce CO and PM<sub>2.5</sub> concentrations in kitchens to levels that meet WHO air quality guidelines (AQG)<sup>31,32</sup> (see Table 1.3). The intermediate emission rate target (I-ERT) would result in 60% of kitchens meeting the WHO interim target (IT-1) for annual average PM<sub>2.5</sub> concentration (35  $\mu\text{g}\cdot\text{m}^{-3}$ ) and the WHO AQG for 24-hour average CO concentration (7  $\text{mg}\cdot\text{m}^{-3}$ ). The final emission rate target (ERT) would result in 90% of kitchens meeting the WHO AQG for annual average PM<sub>2.5</sub> concentration (10  $\mu\text{g}\cdot\text{m}^{-3}$ ) and 24-hour average CO concentration (7  $\text{mg}\cdot\text{m}^{-3}$ ).<sup>21</sup> Both the AQG and IT-1 are indicated by vertical lines in Figure 1.2. Meeting the AQG would be expected to effectively eliminate the increased risk of child ALRI from HAP, and meeting IT-1 would be expected to reduce the relative risk from 3 to 1.3. Note that the intermediate ERTs for CO and PM<sub>2.5</sub> emissions from unvented cookstoves are similar to the Tier 4 targets for indoor emissions, but the final ERTs are approximately 3x and 10x lower, respectively, than the Tier 4 targets for indoor emissions. Given that the Tier 4 metrics are already ambitious, the WHO guidelines are likely to be extremely difficult to achieve using solid fuels.

**Table 1.3: Emission rate targets for household solid fuel combustion recommended by the WHO.**<sup>21</sup>

Target	Unvented emissions		Vented emissions	
	CO ( $\text{g}\cdot\text{min}^{-1}$ )	PM <sub>2.5</sub> ( $\text{mg}\cdot\text{min}^{-1}$ )	CO ( $\text{g}\cdot\text{min}^{-1}$ )	PM <sub>2.5</sub> ( $\text{mg}\cdot\text{min}^{-1}$ )
Intermediate Emission Rate Target	0.35	1.75	1.45	7.15
Emission Rate Target	0.16	0.23	0.59	0.80

Furthermore, the exclusive use of mass-based metrics for PM<sub>2.5</sub> in the ISO IWA tiers and the WHO emission rate targets may limit the risk reduction achieved by bringing emissions in line with these metrics. The health impacts of PM exposure may be a function of the number of particles inhaled, and ultra-fine particles (UFPs) (i.e., particles < 100 nm in diameter) have been hypothesized to be more detrimental to human health than larger fine particles.<sup>33,34</sup> Because particle mass is a cubic function of diameter, UFPs can contribute to a large fraction of the total number of particles while contributing to a very small fraction

of the total mass of PM.<sup>35</sup> Consequently, a large reduction in the mass of PM<sub>2.5</sub> emitted can be achieved by reducing the number of larger particles emitted by a relatively small amount while leaving the number of UFPs emitted unchanged. If UFPs do pose a greater risk to human health than larger fine particles, reducing the mass of PM<sub>2.5</sub> emitted may fail to reduce health risks if the reduction in mass is not accompanied by a reduction—or, worse yet, is accompanied by an increase—in the number of UFPs emitted.<sup>36</sup> Health impacts resulting from exposure to PM may also be influenced by the composition of the particles.<sup>37</sup>

## 1.2 Why Gasifier Cookstoves?

Emerging data on the health impacts of HAP have led to several questions. The first question is: Should efforts to transition users to cleaner cooking solutions focus on improved biomass cookstoves, cleaner fuels (such as LPG and electricity), or both? In addition to recommending the emission rate targets shown in Table 1.3, the WHO recommended that various agencies work to facilitate rapid and widespread adoption of cleaner fuels among people currently relying on solid fuels for cooking.<sup>21</sup> Others have also promoted this goal.<sup>38–41</sup> However, given that the number of people relying on solid fuels has remained constant at approximately 2.8 billion since 1980,<sup>1</sup> there is widespread acknowledgment that there are barriers associated with the transition to cleaner cooking fuels<sup>42–44</sup> and that this transition is likely to take some time.<sup>45</sup> The Global Alliance for Clean Cookstoves, which was launched in 2010, is pursuing both approaches and aims to “foster the adoption of clean cookstoves and fuels in 100 million households by 2020.”<sup>46</sup> The WHO guidelines also acknowledge that intermediate technologies between open biomass fires and clean fuels are likely to be needed.<sup>21</sup>

Development of improved biomass cookstoves is also motivated by evidence of “fuel stacking” and “stove stacking” among populations in transition to clean cooking fuels. Even when people begin to use clean fuels, such as LPG, they do not adopt clean fuels exclusively.<sup>47–50</sup> Instead, they use different stoves and fuels for different tasks just like people in the developed world use a variety of appliances (e.g., gas burners, microwave ovens, electric toaster ovens) for different cooking tasks.<sup>51</sup> Even if LPG were able to fulfill 100% of a family’s

cooking needs, continuous access to LPG may be limited by distribution issues and seasonal variations in cost.<sup>50</sup> Use of an indoor open fire for just a few minutes per day can result in very high exposures that eclipse reductions in emissions resulting from use of clean fuels.<sup>52</sup> Consequently, even if LPG is adopted, low-emitting solid-fuel stoves that meet a variety of cooking needs are likely to be instrumental in achieving the desired reductions in exposure to CO and PM<sub>2.5</sub>.<sup>47</sup> As stated by Ruiz-Mercado and Masera<sup>50</sup>:

It has also been documented that ICS interventions targeting mixed users (i.e., those households who already have access to clean fuels but still rely on traditional fires) have been most effective in terms of health and fuel/energy savings. . . Therefore, promoting access to both clean modern fuels and clean stoves for traditional fuels in the same households should not be seen as competing but rather complementary objectives of cookstove programs. (p. 54)

Efforts to develop low-emitting, affordable biomass cookstoves that meet a variety of user needs are ongoing,<sup>53</sup> and there has been much speculation regarding whether use of gasifier cookstoves<sup>1</sup> can result in large reductions in user exposure to CO and PM<sub>2.5</sub>.<sup>54-56</sup> More specifically, can gasifier cookstoves meet the Tier 4 performance targets outlined in the ISO IWA tiers? Can they operate reliably enough to achieve low emissions in the laboratory *and* in the field? Can they fulfill user needs so that they will displace open fires and traditional stoves? These questions are addressed, in part, in this dissertation.

In a gasifier cookstove, solid biomass is converted to a gaseous fuel via partial oxidation. This gaseous fuel is then transported away from the solid fuel bed, mixed with additional air, and combusted to heat the cooking surface. Top-lit up draft (TLUD) gasifier cookstoves were designed to minimize emissions by minimizing tar production and improving fuel-air mixing.<sup>57</sup> The former is accomplished by using an inverted downdraft gasifier design in which pyrolysis gases pass through a flaming pyrolysis zone<sup>58</sup> and the latter is accomplished via spatial separation of the gas-phase combustion of the volatiles from the devolatilization of the solid biomass.<sup>57,59</sup> A TLUD gasifier operates as a conventional stratified downdraft gasifier<sup>58</sup> that has been turned upside down (see Figure 1.3). The fuel chamber is batch-

---

<sup>1</sup>sometimes also called “semi-gasifier” or “micro-gasifier” cookstoves

loaded with a bed of solid biomass and the fuel bed is ignited on the top. Primary air flows up through the base of the fuel chamber and provides the oxidizer needed to gasify the biomass. The oxidation zone (also called the primary combustion or flaming pyrolysis zone) progresses downward through the fuel bed. The pyrolysis gases that are released from the solid biomass are partially oxidized in the flaming pyrolysis zone and then pass up through the hot char bed where they may react further. The heat released during the partial oxidation of the pyrolysis gases drives the continued pyrolysis of the biomass. The producer gas leaving the hot char bed mixes with secondary air near the top of the stove and the flame that heats the cooking surface is formed.<sup>57</sup> The flame in the secondary combustion zone is an inverse non-premixed flame in which oxidizer is injected into the upward-flowing fuel. In a “natural draft” stove, both the primary and secondary air flows are driven entirely by natural convection. In a “forced-air” stove, air flow is externally driven by a fan or blower, for example, and is also assisted by buoyancy.

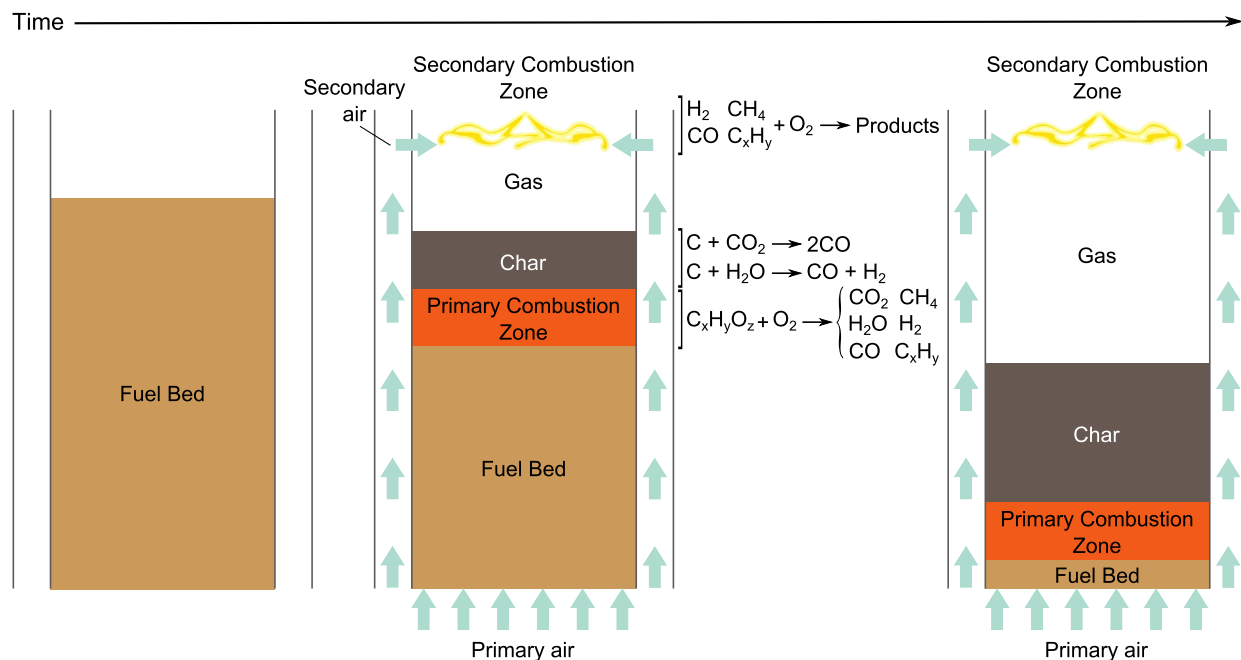


**Figure 1.3: Schematic of top-lit up draft (TLUD) gasifier cookstove operation.**

Gasifier cookstoves have been marketed and studied extensively in India<sup>55,60–66</sup> and China.<sup>67,68</sup> In Indian households, gasifier stoves have been found to be used in combina-

tion with LPG and kerosene stoves.<sup>63</sup> There are also reports of gasifier cookstoves being marketed elsewhere in Asia<sup>59,69–71</sup> as well as in Africa,<sup>59,70</sup> Central America,<sup>70</sup> and South America.<sup>59</sup> Gasifier cookstoves have been promoted as being capable of operating on a variety of fuels including woody stems, leaves, and stalks;<sup>59</sup> wood chips;<sup>57,72</sup> wood sticks standing vertically;<sup>57,70</sup> wood pellets;<sup>59,72</sup> peanut shell pellets;<sup>72</sup> pellets made from other agricultural residues;<sup>60,70</sup> briquettes;<sup>59,70</sup> rice hulls;<sup>69</sup> coconut shell;<sup>70,72</sup> palm nut shell;<sup>72</sup> mango prunings;<sup>70</sup> corn cobs;<sup>70</sup> and other agricultural residues.<sup>70</sup> The potential to serve as a versatile clean cooking solution for users who are dependent upon a variety of locally-available fuels adds to the appeal of gasifier cookstoves.

Gasifier cookstoves have been demonstrated to emit less CO and PM<sub>2.5</sub> than other biomass cookstove designs in several studies in which many cookstoves were tested in the laboratory using the WBT.<sup>73–75</sup> High-power CO and PM<sub>2.5</sub> emissions measured during the cold start phase of the WBT in an oft-cited study conducted by Jetter et al.<sup>75</sup> have been re-plotted in Figure 1.4 to illustrate how emissions from gasifier cookstoves compared to emissions from other cookstove types and to the ISO IWA tiers. Although none of the stoves exhibited Tier 4 high-power PM<sub>2.5</sub> emissions, the three stoves that exhibited Tier 3 high-power emissions were all gasifiers. However, a wide range of performance was observed among the different gasifier designs and the highest-emitting stove in the study was also a gasifier. Four other gasifier stoves had emissions in the Tier 0 to Tier 1 range. Several studies on emissions from household biomass cookstoves in the field reported lower emissions from gasifier cookstoves, especially forced-air gasifier cookstoves, compared to traditional and rocket elbow cookstoves.<sup>64–66</sup> Taken as a whole, these results suggest that gasifier cookstoves have a higher potential to meet the Tier 4 performance targets than other cookstove designs, but that achieving this goal will require a better understanding of the factors that contribute to the range of performance observed in Figure 1.4.

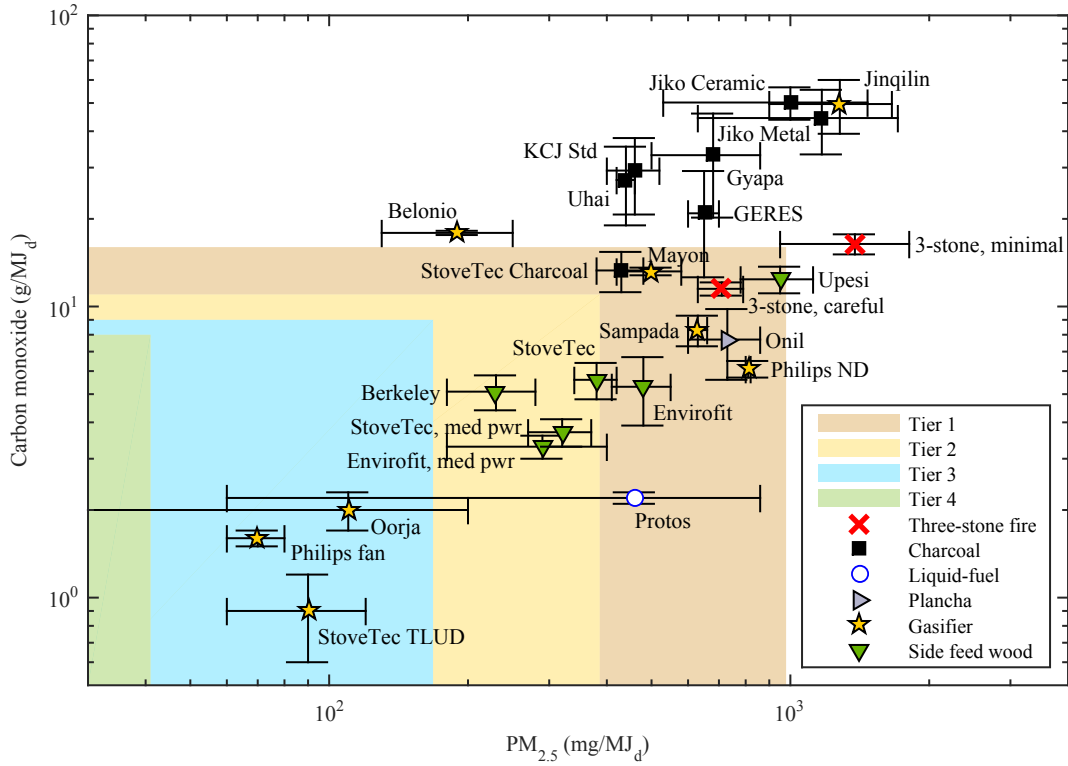


**Figure 1.4: Average high-power CO and PM<sub>2.5</sub> emissions measured for different biomass cookstove types during the cold start phase of the WBT (modified from Jetter et al.<sup>75</sup>). Error bars represent one standard deviation.**

### 1.3 Overview of this Dissertation

The objectives of the studies presented in this dissertation were to: (1) identify the causes of the variability in performance among different gasifier cookstoves seen in Figure 1.4; (2) characterize the manner in which stove design, fuel properties, and operating mode influenced performance; (3) gain insight into how secondary air velocity affected fuel-air mixing and the flame dynamics in the secondary combustion zone; and (4) evaluate whether or not the reductions in emission rates that are sought (i.e., Tier 4 performance) could be achieved using the TLUD gasifier design. Three separate studies were conducted in pursuit of these objectives.

In the first study, sources of variability in TLUD performance were investigated by testing five natural draft TLUD design configurations in the laboratory using two different biomass fuels. All five design configurations were derived from commercially-available stoves. An

energy balance model was also developed, using temperature data collected during the experiments, to determine the greatest sources of efficiency loss in each configuration. Emissions were found to be influenced by cookstove design, fuel type, and operator behavior, and refueling was found to result in large transient increases in CO emission rates. These results are presented in Chapter 3.

In the second study, the effects of stove design parameters, fuel type, and operating mode on TLUD performance were investigated in more detail. A modular test bed was constructed to allow design parameters to be varied easily and to facilitate the collection of detailed performance data. A new laboratory test procedure was also developed to capture three different operating modes that were found, through the first study, to be characteristic of the TLUD design and representative of both best- and worst-case scenario performance. More than one hundred tests were conducted in which design parameters and fuel properties (fuel type, moisture content, and bulk density) were varied and the resulting emissions were measured. Emissions were found to decrease with increasing secondary air velocity, but changes in fuel type and operating mode sometimes resulted in order of magnitude changes in PM<sub>2.5</sub> emissions. These results are presented in Chapter 4.

In the third study, the impact of secondary air jet velocity on fuel-air mixing and flame dynamics in the secondary combustion zone was investigated using high-speed imaging techniques. A burner was designed to generate a two-dimensional inverse non-premixed cross-flow flame as a replica of the secondary combustion zone in a TLUD and to provide optical access for planar laser-induced fluorescence (PLIF) imaging. The burner was fueled with an acetone-seeded simulated producer gas mixture that flowed up from the base of the burner through a bed of glass beads. Air was injected above the fuel bed through two opposing slots. Five test cases involving low, medium, and high fuel and air velocities were investigated. Images of OH\* chemiluminescence were collected at 3 kHz and images of OH and acetone PLIF were collected at 10 kHz. The results are presented in Chapter 5.

## CHAPTER 2

### Background

This chapter contains a brief introduction to characterization of biomass fuels, combustion of biomass, gasification of biomass, carbon monoxide oxidation, and particulate matter formation and oxidation. This information is included to aid in understanding of the experimental methods and interpretation of the experimental results presented in Chapters 3, 4, and 5.

#### 2.1 Characterization of Biomass Fuels

Lignocellulosic biomass fuels can be characterized in terms of their biochemical components, by the results of proximate and ultimate analyses, and in terms of intensive physical properties. All biomass fuels contain some mass fraction of moisture and inorganic material. When fuels are characterized in terms of biochemical components, the remainder of the mass is typically divided between cellulose, hemicelluloses, lignin, and extractives. In a proximate analysis, the remainder of the mass is divided between volatile matter and fixed carbon. In an ultimate analysis, the remainder of the mass is divided between carbon, hydrogen, nitrogen, oxygen, and sulfur. Intensive properties of interest include heating value, density, bulk density, specific heat, thermal conductivity, porosity, and permeability.<sup>76-78</sup>

The key biochemical components are the cellulose, hemicelluloses, and lignin that comprise the plant cell wall.<sup>76</sup> Cellulose and hemicelluloses are often collectively referred to as “hollocellulose”.<sup>77</sup> Cellulose serves as the primary structural component of the cell wall,<sup>79</sup> and hemicelluloses hold the cellulose fibrils together.<sup>80</sup> Lignin provides structural rigidity, plays an important role in water transport, and protects against degradation.<sup>80</sup>

Cellulose is a linear homopolymer composed entirely of  $\beta$ -D-glucopyranose (see Figure 2.1).<sup>79</sup> Two  $\beta$ -D-glucopyranose molecules are linked by a 1,4 glycosidic bond to form a disaccharide called cellobiose.<sup>79,80</sup> The glucose molecules in the disaccharide are oriented such that, if the first is considered to be “right-side up,” the second is “upside-down”.<sup>80-82</sup>

As a result of this configuration, two hydrogen bonds form between the two glucopyranose molecules: one between the  $\text{-OH}$  group attached to the C-2 atom on the first molecule and the  $\text{-OH}$  group attached to the C-6 atom on the second molecule, and one between the oxygen inside the pyranose ring on the first molecule and the  $\text{-OH}$  group attached to the C-3 atom on the second molecule.<sup>79,81</sup> Cellobiose disaccharides, the repeating units of cellulose, are linked together, also via  $\beta$ -(1,4) glycosidic bonds, into long chains of indeterminate length, and many parallel chains cluster together into microfibrils.<sup>79,80,83</sup> Cellulose is characterized by extensive hydrogen bonding between the individual glucose molecules in a single chain and between adjacent chains in a microfibril.<sup>79-81,83</sup> This structure may be the reason that cellulose is more difficult to break down than hemicellulose.<sup>84</sup>

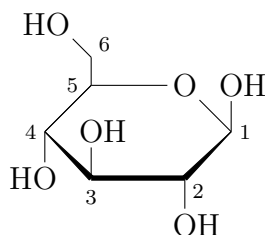


**Figure 2.1: A  $\beta$ -D-glucopyranose molecule with the carbon atoms numbered.**

Hemicelluloses are branched heteropolymers composed of pentoses (e.g., xylose, arabinose, and rhamnose), hexoses (e.g., glucose, mannose, and galactose), and uronic acids (e.g., 4-O-methylglucuronic acid, D-glucuronic acid, and D-galacturonic acid) (see Figure 2.2).<sup>76,85</sup> Several types of hemicellulose exist,<sup>80</sup> and each typically features two to four of these base units.<sup>76</sup> Hemicelluloses consist of long homo- or hetero-polymer backbone chains connected to short branches of other base units.<sup>85</sup> In xylans, a family of hemicelluloses common in hardwoods and agricultural residues,<sup>76,85,86</sup> the backbone is comprised of  $\beta$ (1-4)-linked D-xylopyranose units.<sup>87</sup> In glucomannans, a family of hemicelluloses common in softwoods,<sup>76,85</sup> the backbone is comprised of  $\beta$ (1-4)-linked D-glucopyranose and D-mannopyranose units.<sup>87</sup> The heterogeneous, branched nature of hemicelluloses limits hydrogen bonding between hemicellulose chains and prevents the formation of crystalline structures.<sup>76</sup> Hemicellulose does, however, form hydrogen bonds with cellulose.<sup>83</sup>

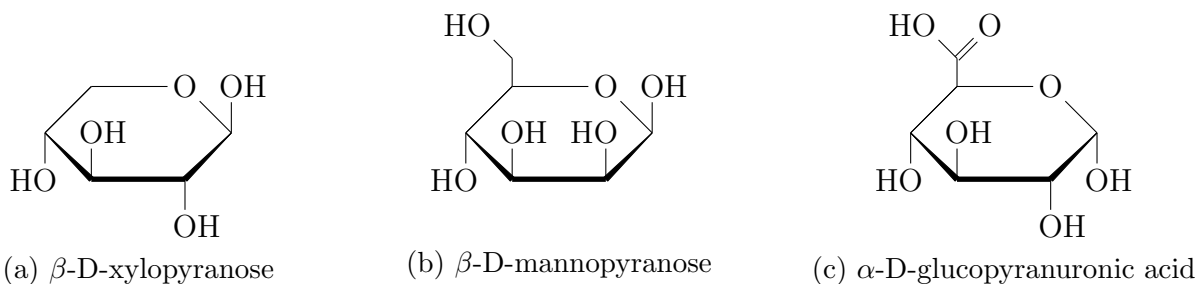


**Figure 2.2:** Examples of the pentoses (represented by  $\beta$ -D-xylopyranose), hexoses (represented by  $\beta$ -D-mannopyranose) and uronic acids (represented by  $\alpha$ -D-glucopyranuronic acid) that make up various types of hemicellulose (adapted from Fry<sup>83</sup>).

Lignin is a highly-branched, three-dimensional polymer comprised of three phenylpropanoid alcohols: p-coumaryl alcohol, coniferyl alcohol, and sinapyl alcohol (see Figure 2.3).<sup>76,77,80</sup> These precursors are bound, through a variety of linkages, such that only single aromatic rings exist in the polymer.<sup>76</sup>

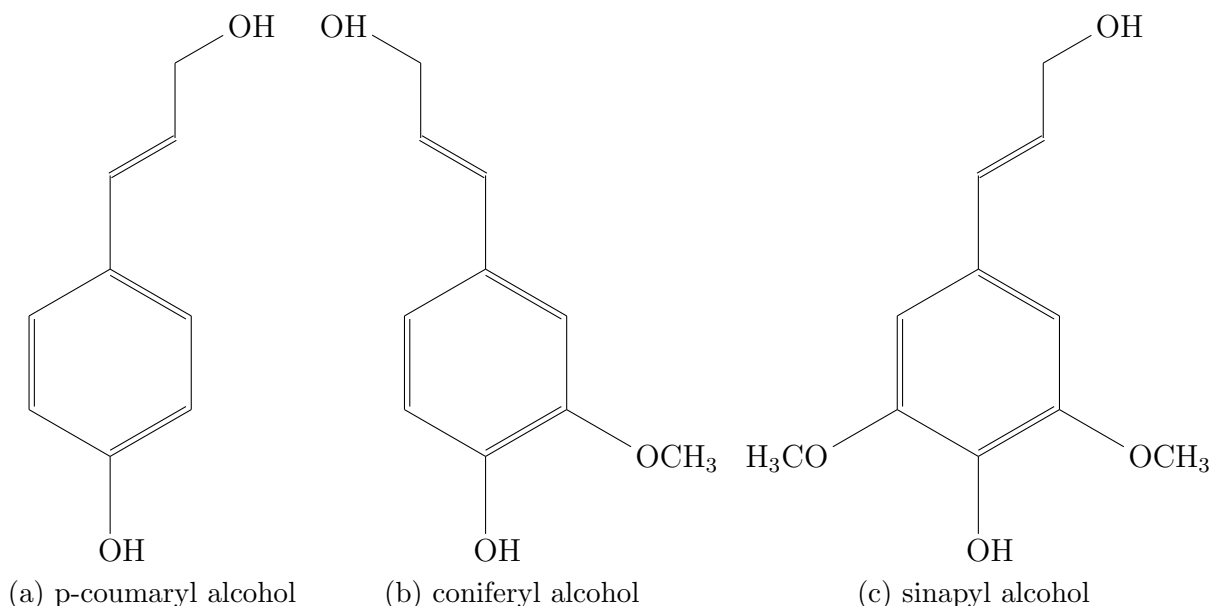


**Figure 2.3:** Precursors to lignin: p-coumaryl, coniferyl, and sinapyl alcohol.

A proximate analysis is used to characterize biomass fuel in terms of the mass fractions of moisture, volatile matter, fixed carbon, and ash.<sup>76</sup> The volatile matter is the fraction of mass, not including the moisture, that is released in the vapor phase when the fuel is pyrolyzed. The volatile matter content is determined by measuring the amount of mass lost from a

sample that has been heated in a tube furnace at 950 °C for 7 minutes.<sup>88</sup> The ash content is the inorganic material left over after the fuel has completely oxidized.<sup>89</sup> Fixed carbon, which is calculated as the difference between the total mass and the masses of moisture, volatiles, and ash,<sup>90</sup> is the fraction of combustible material that remains in the solid phase after the fuel has pyrolyzed.

The heating value of a fuel is a measure of the heat released, per unit mass, when the fuel undergoes complete combustion.<sup>91</sup> Complete combustion occurs when all of the carbon in the fuel is converted to CO<sub>2</sub> and all of the hydrogen in the fuel is converted to H<sub>2</sub>O. The heating value is equal to the difference in enthalpy between the reactants and the products at 25 °C.<sup>92</sup> The higher heating value (HHV) is equal to the enthalpy difference when all of the water in the products is in the liquid phase, and the lower heating value (LHV) is equal to the enthalpy difference when all of the water in the products is in the gas phase.<sup>92</sup> Although the water in the products ends up in the liquid phase when heating value is measured in a bomb calorimeter, water in the exhaust from real-world combustion devices is typically in the gas phase. Therefore, the heating value of a fuel is typically defined in terms of the LHV. The LHV can be calculated from the heating value measured in a bomb calorimeter as described in ASTM D5865.<sup>93</sup>

Porosity is the ratio of pore volume to total volume. Porosity may be considered in terms of either the voids space present within a single particle or the voids between the many particles in a fuel bed. Particle porosity and bed porosity are related to particle density (i.e., the density of a single piece of fuel) and bulk density, respectively, as shown in Equations 2.1 and 2.2:<sup>76</sup>

$$\rho_{particle,dry} = \rho_{cell\ wall} (1 - \epsilon_{particle}) \quad (2.1)$$

where  $\rho_{particle,dry}$  is the density of a single dry piece of fuel in kg·m<sup>-3</sup>,  $\rho_{cell\ wall}$  is the density of the solid cell wall (1500 kg·m<sup>-3</sup>),<sup>76,77</sup> and  $\epsilon_{particle}$  is the particle porosity.

$$\rho_{bulk} = \rho_{particle,ad} (1 - \epsilon_{bed}) \quad (2.2)$$

where  $\rho_{bulk}$  is the bulk density of the fuel bed in  $\text{kg}\cdot\text{m}^{-3}$ ,  $\rho_{particle,ad}$  is the density of a single piece of fuel on an as-determined basis in  $\text{kg}\cdot\text{m}^{-3}$ , and  $\epsilon_{bed}$  is the bed porosity.

Dry particle density can be calculated from as-determined particle density as shown in Equation 2.3:<sup>76</sup>

$$\rho_{particle,dry} = (1 - M_{ad}) \rho_{particle,ad} \quad (2.3)$$

Permeability is “a measure of the ease with which fluids are transported through a porous solid under the influence of a pressure gradient”.<sup>94</sup> Permeability is governed by the porosity of a material and by the extent to which the pores are connected.<sup>94</sup> The permeability of a biomass fuel may affect the distribution of pyrolysis products by affecting the residence time of the pyrolysis products in the high-temperature pyrolysis zone.<sup>76</sup> Note that natural (i.e., non-densified) biomass fuels are anisotropic and that the permeability is thus dependent upon the direction in which the fluid is being transported.<sup>94</sup> Hardwoods tend to have higher permeabilities than softwoods and Rocky Mountain Douglas fir (one of the fuels tested in the study described in Chapter 4) has one of the lowest permeabilities among natural woods.<sup>94</sup> Pelletized wood fuels have lower permeabilities than natural wood fuels and can be considered isotropic.<sup>76</sup>

Thermal conductivity is a measure of the rate at which heat is transferred through a material by conduction for a given temperature gradient.<sup>77</sup> Similar to the permeability, the thermal conductivity is dependent upon the direction in which heat is being conducted in anisotropic materials.<sup>76</sup> The specific heat of a material is the amount of energy required to raise the temperature of a unit mass of the material by one degree.<sup>77</sup> Together, the thermal conductivity and specific heat determine the rate at which the temperature of a biomass fuel is raised to the reaction temperature.<sup>77</sup>

Properties of the biomass fuels used in the experiments described in Chapters 3 and 4 are shown in Table 2.1. These fuels include softwoods (Lodgepole pine and Douglas fir), a hardwood (Eucalyptus), and an agricultural residue (corn cobs). Compared to wood,

agricultural residues are typically characterized by lower lignin content and higher ash content.<sup>77,95</sup> The lower lignin content (15%), higher hemicellulose content (32%), and higher ash content (2.14%) of the corn cobs in comparison to the wood fuels ( $\approx 28\%$  lignin,  $\approx 24\%$  hemicellulose, and  $< 0.7\%$  ash) can be seen in Table 2.1. The fractions of cellulose, hemicellulose, and lignin reported in Table 2.1 were taken from the literature and converted to 100% on a dry, ash- and extractives-free basis. An ultimate analysis was performed on each fuel by Hazen Research, Inc. in Golden, CO, USA. The moisture and ash content values shown in Table 2.1 are the values reported by Hazen. Volatile contents were measured at Colorado State University in accordance with ASTM standard 872-82 (2013) for particulate wood fuels. Higher heating values were measured using an IKA C200 calorimeter. Lower heating values were calculated in accordance with ASTM standard D5865-13 (2013) using the measured higher heating values and the hydrogen contents obtained from the ultimate analyses.

**Table 2.1: Properties of fuels used in the experiments described in this document.**

	Lodgepole pine	Douglas fir	Eucalyptus	Corn cobs
Species	<i>Pinus contorta</i>	<i>Pseudotsuga menziesii</i>	unknown	<i>Zea mays</i>
Form	pellets	chips	chips	chips
Moisture (weight %, wet basis)	6.84	7.38	7.18	6.38
Ash (weight %, dry basis)	0.68	0.19	0.69	2.14
Biochemical analysis <sup>96,97</sup> (dry, ash- and extractives-free basis)				
Cellulose	48	48	50	53
Hemicellulose	24	23	24	32
Lignin	28	29	27	15
Proximate analysis (weight %, dry basis)				
Volatile matter	85.42	87.48	78.82	82.88
Fixed carbon	13.91	12.32	20.49	14.99
Ultimate analysis (weight %, dry basis)				
C	51.99	52.17	52.39	48.39
H	6.09	6.11	5.83	5.89
N	0.10	0.09	0.20	0.40
S	0.00	0.00	0.03	0.04
O	41.16	41.44	40.85	43.15
Physical properties				
HHV <sub>ad</sub> (J·g <sup>-1</sup> )	19,980	19,120	17,600	17,090
LHV <sub>d</sub> (J·g <sup>-1</sup> )	20,120	19,320	17,700	16,980
Density (wet basis)	1,100	580	660	250
± 95% CI (kg·m <sup>-3</sup> )	± 70	± 40	± 20	± 20
Bulk density (wet basis)	636	160	230	174
± 95% CI (kg·m <sup>-3</sup> )	± 4	± 1	± 2	± 2
Particle porosity	0.32	0.64	0.59	0.84
Bed porosity	0.42	0.72	0.65	0.31

## 2.2 Combustion of Biomass

Lignocellulosic biomass does not react directly with the oxidizer in a combustion process; instead, the biomass decomposes into light gases, tars, and char upon heating, and these products of pyrolysis react with the oxidizer.<sup>98</sup> A piece of solid biomass fuel undergoes four sequential steps during a combustion process: drying, heating, pyrolysis (devolatilization), and char oxidation.<sup>77</sup> When a large fuel particle is heated, a temperature gradient exists within the particle and, as a result, drying, heating and pyrolysis occur simultaneously at different locations.<sup>99</sup> In a conventional biomass combustion process, such as a stick of wood burning in an open fire, the volatiles (light gases and tars) released during pyrolysis react with the air surrounding the solid fuel in a non-premixed flame. The heat released from this flame drives the continued drying, heating, and pyrolysis of the biomass. Because volatiles are flowing out of the solid surface, and because the oxygen in the surrounding air is being consumed in the flame, the oxygen in the air cannot reach the solid surface until devolatilization is complete. Once the devolatilization process is complete, the solid char is oxidized via heterogeneous reaction with  $O_2$ ,  $CO_2$ , and  $H_2O$ . Descriptions of the entire biomass combustion process can be found in Edwards<sup>100</sup>, Tillman<sup>77</sup>, and Ragland and Bryden<sup>91</sup>. The pyrolysis and char oxidation steps, which occur in both conventional combustion and gasification processes, are discussed in more detail below.

The term “pyrolysis” refers to thermal decomposition of fuel in the absence of oxygen.<sup>100</sup> During pyrolysis, the volatile portion of the biomass is converted into light gases and tars and driven out of the solid particle through the pore structure.<sup>77</sup> The relative yields and chemical composition of the light gases, tar, and char produced during pyrolysis can be influenced by: (1) the conditions under which pyrolysis occurs, (2) the biochemical composition of the biomass, and (3) the physical properties of the biomass. At temperatures below 225 °C, reactions that lead to the release of light gases and the formation of char are favored. At temperature between 225 and 525 °C, depolymerization reactions that release volatile tars

are favored. At temperatures above 525 °C, decomposition reactions that release light gases and tar, and lead to the formation of char, are favored.<sup>101</sup>

The term “tar” typically refers to condensable organic compounds that are heavier than benzene.<sup>102</sup> Pyrolysis products can be classified as primary, secondary, and tertiary products: Primary products are formed directly from decomposition of the solid biomass, whereas secondary and tertiary products are produced when primary products undergo additional reactions in the gas phase.<sup>103</sup> Evans and Milne<sup>103</sup> provide an extensive list of the primary, secondary, and tertiary pyrolysis products that have been observed experimentally. Primary tars are characterized by monomers of the building blocks of cellulose, hemicellulose, and lignin as well as fragments of these monomers; secondary tars are characterized by phenols and alkenes; and tertiary tars are characterized by methyl derivatives of aromatics and polycyclic aromatic hydrocarbons (PAHs).<sup>103–105</sup>

Hemicellulose pyrolyzes first when biomass is heated, followed by cellulose.<sup>106,107</sup> Yang et al.<sup>106</sup> reported that most of the weight loss from hemicellulose and cellulose occurred between 220–315 °C and 315–400 °C, respectively. Lignin, on the other hand, pyrolyzes more slowly over a wide temperature range.<sup>106,107</sup> Yang et al.<sup>106</sup> reported that lignin heated at a rate of 10 °C·min<sup>-1</sup> experienced steady weight loss over a temperature range of 160–900 °C. Liu et al.<sup>107</sup> reported that lignin heated at a rate of 60 °C·min<sup>-1</sup> experienced more pronounced weight loss over a temperature range of 200–550 °C.

Several studies have reported the yields of light gases, tar, and char from pyrolysis of isolated samples of cellulose, hemicellulose, and lignin.<sup>108–110</sup> Worasuwannarak et al.<sup>108</sup> reported that, for samples heated to 600 °C at a rate of 10 °C·min<sup>-1</sup>, hemicellulose (xylan) yielded the largest fraction of light gases and water vapor, cellulose yielded the largest fraction of tar, and lignin yielded the largest fraction of char. The char yields were 7%, 28%, and 63% for cellulose, hemicellulose (xylan), and lignin, respectively.<sup>108</sup> Hosoya et al.<sup>109</sup> reported similar results for samples heated to 800 °C: hemicellulose yielded the largest fraction of water vapor (15.3% for glucomannan and 11.5% for xylan), cellulose yielded the largest

fraction of tar (72.0%), and lignin yielded the largest fraction of char (40.6%) on a mass basis. In terms of the light gas fraction, Yang et al.<sup>106</sup> reported that cellulose yielded more CO, hemicellulose yielded more CO<sub>2</sub>, and lignin yielded more H<sub>2</sub> and CH<sub>4</sub> on a molar basis.

Ranzi and coworkers<sup>101,111</sup> have developed the most detailed chemical kinetic model for biomass pyrolysis, which consists of three independent submodels that utilize lumped chemistry to model the multistep devolatilization of cellulose, hemicellulose (modeled as a regular polymer of xylose), and lignin. At low temperatures, cellulose decomposes into char and water vapor. At higher temperatures, cellulose proceeds through an active intermediate before either depolymerizing to form levoglucosan, or decomposing into other products, including hydroxyacetaldehyde, glyoxal, acetaldehyde, propanal, 5-hydroxymethylfurfural, CO<sub>2</sub>, CO, CH<sub>4</sub>, H<sub>2</sub>O, and char, through a series of radical and  $\beta$ -scission reactions. Decomposition via radical and  $\beta$ -scission reactions becomes important at temperatures above 450–500 °C. Levoglucosan is the major tar product at low temperatures and hydroxyacetaldehyde is the major tar product at temperatures above 450–500 °C. Pyrolysis of hemicellulose is modeled by depolymerization into two solid-phase intermediates: HCE1 and HCE2. The first intermediate, HCE1, either vaporizes (thus contributing to the tar fraction) or decomposes into char and light gases. The second intermediate, HCE2, decomposes into char and light gases. Lignin is modeled as decomposing into p-Coumaryl alcohol, phenol, CH<sub>3</sub>CHO, CH<sub>3</sub>OH, C<sub>2</sub>H<sub>4</sub>, C<sub>2</sub>H<sub>2</sub>, CH<sub>2</sub>O, CH<sub>4</sub>, CO, H<sub>2</sub>, CO<sub>2</sub>, H<sub>2</sub>O, and char, among other products, in a multi-step process that involves several intermediates.<sup>101,111</sup>

Although the mechanism described above models the pyrolysis of cellulose, hemicellulose, and lignin independently, its developers acknowledge<sup>111</sup> that several experimental studies have demonstrated interactions among these three components<sup>107–109,112</sup> and between these components and inorganic constituents.<sup>110</sup> Worasuwanarak et al.<sup>108</sup> reported that cellulose-xylan and cellulose-lignin interactions resulted in decreased tar yields, with the cellulose-lignin interaction resulting in a greater decrease. Hosoya et al.<sup>112</sup> also reported that the cellulose-hemicellulose interaction was weaker than the cellulose-lignin interaction;

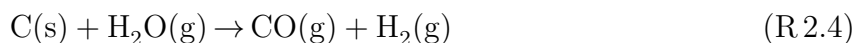
however, they found that the cellulose-lignin interaction *increased* the tar yield and decreased the char yield. Liu et al.<sup>107</sup> reported that cellulose-hemicellulose interactions decreased the yield of levoglucosan and increased the yield of hydroxyacetaldehyde. They also reported a strong interaction between hemicellulose and lignin.<sup>107</sup> Jensen and Dam-Johansen<sup>110</sup> reported that washing wheat straw to remove the mineral components resulted in lower gas yields, higher tar yields, and lower char yields. Furthermore, adding KCl to samples of cellulose, hemicellulose, and washed straw resulted in higher gas yields, lower tar yields, and higher char yields.<sup>110</sup> The presence of minerals was hypothesized to affect interactions between the cellulose, hemicellulose, and lignin in the biomass.<sup>110</sup>

Physical properties of the biomass fuel can also affect the yields of light gases, tar, and char from a pyrolysis process. For fuel particles that are pyrolyzing in a thermally-thick regime, properties that lead to longer residence times inside the solid particle and/or the fuel bed, such as a larger particle size, are expected to increase the residence time for reactions that convert tars to light gases and thus result in higher gas yields.<sup>99</sup> Properties that lead to higher devolatilization rates, such as higher thermal conductivity or lower specific heat, decrease the residence time for secondary reactions that convert tars to light gases and result in lower gas yields.<sup>113</sup> Properties that lead to lower temperatures in the fuel bed, such as a higher moisture content, decrease the rates of reactions that convert tars to light gases and result in lower gas yields.<sup>99,114</sup>

Overall, kinetic models of cellulose, hemicellulose, and lignin pyrolysis reflect a trend in which long residence times (i.e., slow heating rates) and low final temperatures result in high yields of char and light gases. Short residence times (i.e., fast heating rates) and moderate final temperatures result in high yields of tar. Long residence times and high final temperatures result in high yields of light gases.<sup>101</sup> These trends are supported by experimental data.<sup>114</sup>

Solid char is oxidized via heterogeneous surface reactions between the solid carbon and gas-phase O<sub>2</sub>, CO<sub>2</sub>, and H<sub>2</sub>O.<sup>115</sup> In general, heterogeneous surface reactions involve the

following steps: (1) dissociative adsorption of the oxidizer to the solid surface, (2) reaction between the adsorbed oxidizer and the solid, and (3) desorption of the products from the solid surface.<sup>116,117</sup> The overall reactions between char and O<sub>2</sub>, CO<sub>2</sub>, and H<sub>2</sub>O are shown below.<sup>77,92,118</sup> Tilghman and Mitchell<sup>117</sup> present a more detailed chemical kinetic model for combustion and gasification of char.



The rates of the exothermic char-O<sub>2</sub> reactions (R 2.1 and R 2.2) are much faster than the rates of the endothermic gasification reactions (R 2.3 and R 2.4),<sup>117</sup> but the latter two reactions can become important if oxygen is not present at the surface of the char<sup>91</sup> (e.g., if the CO is burning in a non-premixed flame surrounding the particle<sup>115</sup>). Furthermore, CO is the main product of the heterogeneous oxidation of char by O<sub>2</sub> (i.e., Reaction R 2.1 dominates over Reaction R 2.2) at temperatures above 1200 °C.<sup>117,119</sup>

### 2.3 Gasification of Biomass

Gasification is the conversion of a solid fuel to a gaseous fuel.<sup>58</sup> Often, including in the context of the research presented in this dissertation, gasification refers to the production of a gaseous fuel from a solid, carbonaceous fuel via partial oxidation.<sup>120</sup> When solid biomass is gasified using air as the oxidizer, a low-energy fuel gas, often termed “producer gas,” that contains CO and H<sub>2</sub> as the major fuel components is generated.<sup>121</sup> The producer gas also contains small fractions of CH<sub>4</sub> and other low molecular weight hydrocarbons as well as larger fractions of CO<sub>2</sub>, H<sub>2</sub>O, and N<sub>2</sub>.<sup>120</sup> Producer gases generated in a commercial biomass

gasifier and in the modular TLUD test bed described in Chapter 4 are compared to natural gas in Table 2.2.

**Table 2.2: Compositions and heating values of producer gas generated in a commercial biomass gasifier and the modular TLUD test bed described in Chapter 4 compared to natural gas.**

Gasifier type	Air-blown downdraft	Top-lit updraft	Top-lit updraft	Pipeline- quality natural gas <sup>123</sup>
Fuel	Poplar chips <sup>122</sup>	Lodgepole pine pellets	Douglas fir chips	
Biomass moisture content (weight %, wet basis)	13	7	7	-
Gas composition (mole %)				
H <sub>2</sub>	17.5	9.3	4.6	-
CO	19.7	14.3	13.6	-
CH <sub>4</sub>	3.5	2.7	2.1	94.9
C <sub>2</sub> H <sub>x</sub>	1.9	1.3	1.0	2.5
C <sub>3</sub> H <sub>y</sub>	0.2	0.2	0.2	0.2
O <sub>2</sub> /Ar	1.9	3.5	4.1	-
CO <sub>2</sub>	12.7	12.8	11.6	0.7
N <sub>2</sub>	42.7	55.8	62.8	1.6
Lower heating value (MJ·kg <sup>-1</sup> )	6.16	3.89	2.93	47.6
(MJ·m <sup>-3</sup> ) @ 15.6 °C, 101.3 kPa	6.56	4.51	3.54	33.9

The following four processes take place in all gasifiers: oxidation, reduction, pyrolysis, and drying.<sup>124</sup> The spatial sequence in which these processes take place is dependent upon the gasifier design. Many different designs exist,<sup>58,120</sup> but the two that are most relevant to this work are the fixed-bed updraft and stratified downdraft designs shown in Figure 2.4.

In a conventional updraft gasifier, primary air reacts with char in the oxidation zone at the bottom of the fuel bed. The oxidation zone is where the exothermic combustion reactions listed in Table 2.3 take place. The heat required for the endothermic Boudouard and steam gasification reactions, and for the pyrolysis process, is released in these reactions. Once the oxygen in the primary air has been consumed, the products of the oxidation reactions are reduced as they pass through the remainder of the char layer. The reduction zone is where the char gasification reactions listed in Table 2.3 take place. The hot gases leaving

the char layer then pyrolyze and dry the unreacted solid fuel as they flow up through the fuel bed.<sup>58,120,124</sup> Because the gases and tars released during pyrolysis only pass through low-temperature sections of the fuel bed where no oxidizer is present, there is a high concentration of primary tars in the producer gas at the exit.<sup>105</sup> Updraft gasifiers may also be referred to as counterflow gasifiers because air flows up through the fuel bed and unreacted fuel flows downward.<sup>121</sup>

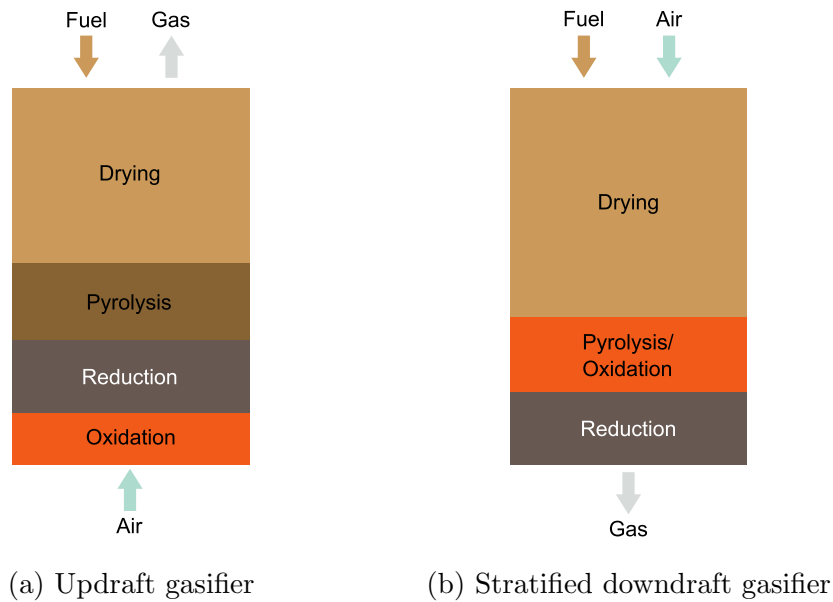


**Figure 2.4: Operation of conventional updraft and stratified downdraft fixed-bed gasifiers.**

In a stratified downdraft gasifier, primary air passes through unreacted solid biomass before oxidizing the volatiles released from the biomass in the flaming pyrolysis zone. The heat released by the oxidation reactions drives the pyrolysis and drying of the upstream biomass. The products leaving the flaming pyrolysis zone are reduced when they pass through the downstream char layer.<sup>58</sup> As a result of the presence of oxidizer and high-temperatures in the flaming pyrolysis zone, most of the tars released during pyrolysis are consumed and there is only a low concentration of tertiary tars in the producer gas at the exit.<sup>105</sup> Downdraft gasifiers may also be referred to as coflow gasifiers because air and fuel both flow downward.<sup>121</sup> A TLUD cookstove is designed to operate as an inverted downdraft gasifier.<sup>57</sup>

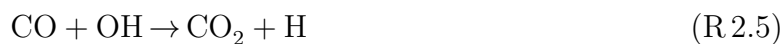
**Table 2.3: Some important reactions associated with a gasification process.**<sup>120,124–127</sup>

Name	Reaction	$\Delta H$ (kJ·mol <sup>-1</sup> )
Combustion reactions		
	$C(s) + O_2(g) \rightarrow CO_2(g)$	-394
	$2 C(s) + O_2(g) \rightarrow 2 CO(g)$	-221
	$2 CO(g) + O_2(g) \rightarrow 2 CO_2(g)$	-566
	$2 H_2(g) + O_2(g) \rightarrow 2 H_2O(g)$	-484
Char gasification reactions		
Boudouard	$C(s) + CO_2(g) \rightarrow 2 CO(g)$	+172
Steam gasification	$C(s) + H_2O(g) \rightarrow CO(g) + H_2(g)$	+131
Hydrogasification	$C(s) + 2 H_2(g) \rightarrow CH_4(g)$	-75
Other		
Water-gas shift	$CO(g) + H_2O(g) \rightleftharpoons CO_2(g) + H_2(g)$	-41

The fuel-to-air equivalence ratio ( $\phi$ ) for a gasification process is typically between 5 and 2.5, and the ideal equivalence ratio is 4. At  $\phi = 4$ , if the product composition were to reach equilibrium, all of the char would be converted to gas (e.g., CO), and the fraction of energy in the solid fuel that was converted to gaseous fuel would reach a maximum.<sup>124</sup> At higher equivalence ratios, not all of the solid char would be gasified and some energy would remain in the solid phase. At lower equivalence ratios, more of the CO and H<sub>2</sub> in the gas would be converted to CO<sub>2</sub> and H<sub>2</sub>O, and the heating value of the gas would decrease.<sup>58</sup>

## 2.4 Carbon Monoxide Oxidation

Carbon monoxide (CO) is the primary fuel component in producer gas.<sup>58</sup> Carbon monoxide is also a poisonous gas<sup>32</sup> and a pollutant for which emissions targets have been set in the ISO IWA<sup>26</sup> and WHO guidelines<sup>21</sup> for biomass cookstoves. Consequently, oxidation of CO is of key importance. The primary oxidizer of CO is the OH radical:



The H atom produced in Reaction R 2.5 can go on to produce more OH radicals via Reaction R 2.6:



Together, Reactions R 2.5 and R 2.6 are the most important reactions in combustion.<sup>118</sup> More than 95% of CO is thought to be consumed via Reaction R 2.5 at atmospheric pressure.<sup>128</sup>

Complete conversion of CO to CO<sub>2</sub> requires that OH radicals be available and that temperatures remain above 1100 K so that Reaction R 2.5 will proceed quickly. The presence of hydrocarbon species inhibits CO oxidation because Reaction R 2.5 competes with reactions between OH radical and hydrocarbons, and Reaction R 2.6 competes with reactions between H atom and hydrocarbons. The rates of Reactions R 2.5 and R 2.6 are lower than the rates of reaction of OH radical and H atom with many hydrocarbons, so conversion of CO to CO<sub>2</sub> is typically delayed until after the hydrocarbons have been converted to CO.<sup>115</sup>

## 2.5 Particulate Matter Formation and Oxidation

Reductions in particulate matter emissions from biomass cookstoves can be achieved through combined efforts to reduce particulate formation and promote particulate oxidation. Consequently, the processes through which particulates are formed and oxidized are reviewed briefly below.

Several types of aerosols can form from gas-phase precursors during a combustion process, including inorganic (ash) particles, soot, condensible organic particles, and sulfuric acid droplets. Submicron particles composed of inorganic material, condensible organics, and sulfuric acid form via condensation—the former at high temperatures and the latter two at exhaust temperatures. Soot, on the other hand, forms through a series of chemical reactions.<sup>129</sup> Particles do not always fit exclusively into one of these four categories. Condensible organic vapors in the exhaust can condense onto the surfaces of existing particles or can

nucleate to form new particles; however, condensation onto existing soot particles, inorganic ash particles, or sulfuric acid droplets is more probable than direct nucleation.<sup>129,130</sup>

The term “soot” is typically used to refer to carbonaceous particles produced via chemical reaction during a combustion process.<sup>118,129,131,132</sup> Soot typically consists of chain-like aggregates composed of many primary particles,<sup>133</sup> and these primary particles have an ordered nanostructure characterized by graphitic segments.<sup>134</sup> Soot formation in non-premixed flames occurs in high-temperature zones on the fuel side of the flame.<sup>133</sup> The soot formation process consists of several steps: (1) formation of the polycyclic aromatic hydrocarbons (PAHs) that are precursors to soot; (2) inception of primary particles; (3) growth of primary particles via coalescence, coagulation, surface reactions, and condensation of vapors; and (4) aggregation of primary particles.<sup>135</sup>

Although many different fuel-dependent pathways to PAH formation may exist,<sup>135</sup> the mechanism that is most commonly used to describe growth of PAHs during hydrocarbon combustion is that of hydrogen abstraction followed by acetylene ( $C_2H_2$ ) addition (abbreviated HACA). In this mechanism, which is described by Frenklach<sup>136</sup>, Wang<sup>135</sup>, and Law<sup>118</sup>, a hydrogen radical extracts another hydrogen atom from an aromatic ring, creating a radical site on the ring. Acetylene is then added to the radical site and, as a result, an ethynyl ( $-C_2H$ ) group bonds to the aromatic ring and an H atom is released. Next, another hydrogen atom is extracted from an adjacent carbon on the ring. Acetylene subsequently bonds to the new radical site, and the two branches form an additional aromatic ring. If the new ring features a radical site, PAH growth will continue via  $C_2H_2$  addition. If the new ring is not a radical, hydrogen abstraction will need to occur before  $C_2H_2$  addition can continue.<sup>118,135,136</sup> Formation of PAH precursors during biomass combustion has been proposed to proceed through two pathways. In the first pathway, light hydrocarbons produced during pyrolysis form PAHs via the HACA mechanism described above. In the second pathway, one- and two-ring aromatics are produced during decomposition of lignin, with cyclopentadiene serving as an important intermediate.<sup>137</sup>

The particle inception step, in which gas-phase PAHs form particles, is currently not well understood, and Wang<sup>135</sup> discusses several theories that could explain this process. Newly-formed particles, sometimes called “nuclei,” are less than 2 nm in diameter, but the primary particles found in aggregates are typically 10-30 nm in diameter.<sup>133</sup> As noted previously, coalescence, coagulation, surface reactions, and condensation of vapors can all contribute to primary particle growth. These processes are described in reviews by Lighty et al.<sup>129</sup>, Frenklach<sup>136</sup>, and Wang<sup>135</sup>. Growth by coagulation occurs when multiple soot nuclei collide and stick together, and subsequent surface growth around the aggregate restores the spherical shape of the particle. Growth via surface reactions occurs when gas-phase molecules, such as C<sub>2</sub>H<sub>2</sub>, react with the solid surface of the particle. Chain-like aggregates are thought to form when primary particles collide and stick together, but surface growth does not restore the spherical shape of the particle because the rate of surface growth has become too slow and/or the colliding particles have become too large.<sup>136</sup>

As an example of the types of particles that can be formed during biomass combustion, particles emitted from open biomass burning (more specifically, savanna burning in southern Africa) have been classified as inorganic particles, organic particles, “tar balls,” and soot.<sup>138,139</sup> However, inorganic and organic particles were not mutually exclusive categories. For example, inorganic particles coated in organic matter<sup>138</sup> and “organic particles with inorganic inclusions”<sup>139</sup> were observed. Spherical particles composed entirely of carbonaceous material that were not aggregated with other particles and lacked the ordered nanostructure that is characteristic of soot were dubbed “tar balls.”<sup>139,140</sup> These particles were hypothesized to form via nucleation of gas-phase organic species.<sup>139</sup> Particulate emissions from flaming fires contained more soot and fewer organic particles compared to emissions from smoldering fires.<sup>139</sup> Similarly, particles emitted from combustion of wood chips in a laboratory reactor with primary and secondary air supply were classified as ash, particulate organic matter, and soot.<sup>141</sup> Again, these were not mutually exclusive categories and parti-

cles composed of multiple constituents, such as ash coated in organic matter, were observed in addition to particles composed of individual constituents.<sup>141</sup>

In systems that favor soot formation, emission of soot from the combustion process results from incomplete oxidation of soot in the flame zone.<sup>115</sup> Potential oxidizers of soot include OH, O, O<sub>2</sub>, CO<sub>2</sub>, and H<sub>2</sub>O. The OH radical is the primary soot oxidizer under the conditions encountered in flames and oxidation by O<sub>2</sub> is of secondary importance.<sup>142,143</sup> Because rapid soot oxidation requires the presence of the OH radical, similar to CO oxidation, high temperatures are required.<sup>115</sup>

As noted in Section 1.2, the flame in the secondary combustion zone of a gasifier cookstove is an inverse non-premixed flame, and there are several differences between the more commonly studied normal non-premixed flame and an inverse non-premixed flame in terms of the soot formation and oxidation processes. The mass of soot produced in a typical co-flow non-premixed flame is governed by the residence time in high-temperature fuel rich zones that promote soot particle growth, with longer residence times leading to more growth.<sup>144</sup> In a normal non-premixed flame, formation of PAHs and soot occur inside of the flame envelope, whereas these processes occur outside of the flame envelope in inverse flames. In both cases, soot is observed adjacent to the flame front on the fuel-rich side, where temperatures are high. Because soot formation occurs outside the high-temperature flame envelope in an inverse flame, reduced soot growth may be expected, and slightly lower soot concentrations have been observed experimentally in inverse non-premixed flames when compared to normal flames.<sup>145</sup> In a typical co-flow normal non-premixed flame, the soot formed in the fuel-rich zone is convected through the reaction zone at the top of the flame, where it has a chance to be oxidized. In an inverse non-premixed flame, on the the other hand, the soot is transported away from the reaction zone by both thermophoresis and convection, and, as a result, oxidation is inhibited.<sup>146</sup> In the inverse non-premixed flames found in the secondary combustion zone of a gasifier cookstove, the fuel flow is in the vertical direction and the air flow is in the horizontal direction. Since these flames involve air and fuel in cross flow, there

are likely to be both similarities and differences between the soot formation and oxidation processes in these inverse flames and those in the co-flow inverse flames described previously in the literature.

## CHAPTER 3

### Emissions and Efficiency of Natural Draft Gasifier Cookstoves<sup>2</sup>

#### 3.1 Introduction

The objective of the study presented in this chapter was to identify some of the underlying causes behind the variability that has been observed in gasifier cookstove performance. To accomplish this objective, five configurations of natural draft TLUD gasifier household cookstoves were tested using two different fuels to determine how changes in stove design, fuel type, and operator behavior affected performance in terms of efficiency, carbon monoxide (CO) emissions, and particulate matter (PM<sub>10</sub>) emissions. It was hypothesized that, although all of the configurations tested were natural draft TLUD gasifier cookstoves, differences in design between the five configurations would affect performance. It was also hypothesized that, although gasifier cookstoves have been promoted as being capable of utilizing a wide variety of fuels,<sup>59</sup> stove performance would also vary with fuel type (e.g., agricultural residue versus prepared pellet fuel, as discussed by Mukunda et al.<sup>62</sup>).

#### 3.2 Methods

The matrix of cookstoves and fuel types tested; the protocol used to complete the tests; the methods used to measure CO and PM<sub>10</sub> emissions, fuel use, and stove temperatures; as well as the equations used to calculate efficiency, are described below. An energy balance model, which was developed using the temperature data to determine the sources of energy loss that contribute to sub-unity efficiency, is also presented below.

---

<sup>2</sup>This chapter is based on material published in *Energy for Sustainable Development*: Tryner, J; Willson, B. D.; Marchese, A. J. The effects of fuel type and stove design on emissions and efficiency of natural-draft semi-gasifier biomass cookstoves. *Energy Sustainable Dev.* **2014**, *23*, 99-109, DOI: 10.1016/j.esd.2014.07.009. My contributions included performing the experiments, analyzing the data, creating the figures, and writing the manuscript. The text has been edited to avoid repeating information presented Chapters 1 and 2. Most notably, the Introduction section has been shortened substantially. Material that appeared in the Supplemental Information accompanying the article has been incorporated into the Methods section. The figures in the Results and Discussion section have been reformatted, but the values plotted in the figures are unchanged.

### 3.2.1 Test Matrix

Five configurations of natural draft TLUD gasifier cookstoves were tested (see Figure 3.1). Three configurations were based on a stove manufactured by the Shanxi Jinqilin Energy Technology Co. Ltd. (Shanxi, China). The first configuration was the stove in its original form as received from the manufacturer (“Stove 1”). The stove was large and equipped with a chimney. The stove body was 64 cm tall, weighed 37 kg, and was constructed primarily from steel sheet metal of various thicknesses. A refractory material lined the inside of the combustion chamber and the area under the pot. The second configuration (“Stove 2”) was a modified version of Stove 1 in which a cylindrical sheet metal duct was added above the secondary combustion zone to direct the flow of hot gases closer to the bottom of the pot. The third configuration (“Stove 3”) was a modified version of Stove 2 in which a pot skirt was added and the chimney inlet was moved from the area under the pot to the side of the pot skirt to force the hot gases to flow around the sides of the pot. These two modified configurations were created to further investigate stove performance for the purposes of the study. The fourth stove was the Philips HD4008. The Philips stove was smaller and had no chimney. This stove was 30 cm tall, weighed 3.6 kg, and was constructed of various steel alloys. The fifth stove was of the open-source Peko Pe design.<sup>147</sup> The Peko Pe stove was also a small stove without a chimney. This stove was approximately 25 cm tall, weighed 2.7 kg, and was constructed using 23 gauge stainless steel sheet metal. For simplicity, the design configurations will be referred to as Stoves 1, 2, 3, 4, and 5.

The combustion chamber in each stove was cylindrical with openings at the base where primary air entered the fuel bed and openings at the top where secondary air mixed with the gases leaving the fuel bed. The fuel bed filled the combustion chamber up to the height of the secondary air inlet and the flame that heated the cooking pot was formed at the top. In most of the configurations, the secondary air entered through a ring of small holes around the circumference of the top of the combustion chamber. More information on combustion chamber geometry is shown in Table 3.1.

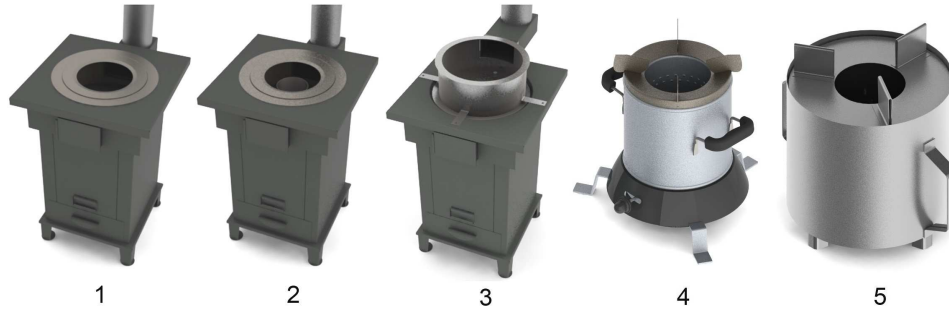


**Figure 3.1: Renderings of the five stoves tested.** Stove 1 (Jinqilin natural draft) was 64 cm tall, weighed 37 kg and was equipped with a chimney. Stoves 2 and 3 were modified versions of Stove 1. Stove 4 (Philips HD4008) was 30 cm in height and weighed 3.6 kg. Stove 5 (Peko Pe) was 25 cm in height and weighed 2.7 kg. Stoves 4 and 5 were not equipped with chimneys.

**Table 3.1: Dimensions of the combustion chambers in each stove configuration tested.**

Geometric parameter	Stoves 1, 2, & 3	Stove 4	Stove 5
Fuel chamber diameter (cm)	19	12	20
Fuel chamber height (cm)	18	13	19
Primary air inlet geometry	grate	grate	holes
Total primary air inlet area (cm <sup>2</sup> )	81	variable up to 30	1.7
Secondary air inlet geometry	holes	holes	gap
Number of secondary air holes	26	52	-
Diameter of secondary air holes (cm)	0.7	0.35	-
Total secondary air inlet area (cm <sup>2</sup> )	10	5.0	63

The stoves were tested with two different fuels: corn (*Zea mays*) cobs obtained from a farm in Windsor, CO and wood pellets made from Lodgepole pine (*Pinus contorta*) by the Rocky Mountain Pellet Company (Walden, CO, USA). Corn cobs were the manufacturer-specified fuel for Stove 1 and the Lodgepole pine pellets were a pelletized fuel that was readily available in Fort Collins, CO. Table 3.2 contains a list of all the design configuration/fuel type combinations tested. The number of replicates completed for each test is also shown.

**Table 3.2: Table of tests conducted.**

Configuration	Fuel type	No. of replicates
Stove 1 (Jinqilin natural draft)	corn cobs	4
Stove 1 (Jinqilin natural draft)	wood pellets	3
Stove 2	corn cobs	2
Stove 2	wood pellets	3
Stove 3	corn cobs	3
Stove 3	wood pellets	3
Stove 4 (Philips HD4008)	corn cobs	3
Stove 4 (Philips HD4008)	wood pellets	3
Stove 5 (Peko Pe)	corn cobs	3
Stove 5 (Peko Pe)	wood pellets	3

Corn cobs were collected manually off of the field after the corn had been harvested with a combine. The corn cobs were brought back to the laboratory and left to air dry for one week. Wood pellets were purchased from a local retailer in Fort Collins, CO that sells supplies for pellet stoves. The wood pellets were packaged in plastic bags and each bag of pellets weighed 18 kg. Properties of these fuels are shown in Table 2.1. The moisture contents, ash contents, and heating values used in the calculations in this chapter are shown in Table 3.3. The higher heating values (HHV) of each type of fuel and char were measured using an IKA C200 calorimeter (IKA, Staufen, Germany). The lower heating values (LHV) of the fuels were then calculated using estimates of the chemical composition for each fuel that were obtained from the literature. The HHV of the char produced by each fuel type was also measured. The HHV of the char was used in place of the LHV of the char in all calculations because the chemical composition of the char was unknown.

**Table 3.3: Fuel moisture and ash contents, fuel heating values, and char heating values used for calculations in this chapter.**

Fuel	Stove no.	Moisture (%) <sup>a</sup>	Ash (%) <sup>a</sup>	LHV <sub>daf</sub> (J·g <sup>-1</sup> )	HHV <sub>d, char</sub> (J·g <sup>-1</sup> )
Corn cobs	1-4	8.1 ± 0.1	1.0	18,120	28,700
	5			18,100	31,240
Wood pellets	1-4	5.5 ± 0.6	0.4	19,560	27,040
	5				25,960

<sup>a</sup>These percentages represent mass fractions and are expressed on a wet basis.

### 3.2.2 Test Protocol

The Emissions and Performance Test Protocol (EPTP), which is a modified version of the water boiling test (WBT), was used in all experiments.<sup>148</sup> The WBT<sup>30</sup> is the most common test used to evaluate cookstove performance in the laboratory<sup>149</sup> and has been used in many studies on cookstove performance.<sup>67,73-75</sup> The EPTP was created to reduce variability between test replicates without altering the general results of the WBT.<sup>150</sup> In the present study, only the cold start phase of the EPTP, in which 5 L of water are brought from 15 °C to 90 °C with the stove body starting out at room temperature, was employed. All tests were conducted in Fort Collins, CO, at an elevation of 1519 m, where water boils at 95 °C.

The corn cobs had a low bulk energy density compared to the wood pellets. This difference necessitated changes in operating procedure between tests. When the wood pellets were used, the fuel chamber of the cookstove was filled with enough pellets to complete the cold start test. When the corn cob fuel was used, the fuel chamber was filled completely with corn cobs. If the entire fuel bed was consumed prior to the completion of the cold start test, the stove was refueled by adding a new bed of corn cobs on top of the hot char bed while the stove was in operation. The operating procedure was varied between tests in this manner because a real-world user would be expected to refuel the stove to complete the cooking task that had been started. Indeed, Stove 1 had been designed by the manufacturer with a mechanism to enable refueling without removal of the pot.

### 3.2.3 Testing Equipment

Tests were conducted in a fume hood with a 1.2 m x 1.2 m cross-section and a height of 4.3 m. The air flow rate through the hood was 0.1 m<sup>3</sup>·s<sup>-1</sup>. The cross sectional area of the hood and the air flow rate were designed such that they do not affect the airflow through the stove<sup>150</sup>. High efficiency particle air (HEPA) filters installed on the air inlet locations at the base of the hood prevented particulate matter in the ambient air from entering the

hood. Exhaust gases were transported from the top of the hood to emissions analyzers by a 12.7-cm-diameter pipe.

Total mass emissions of particulate matter with an aerodynamic diameter of less than 10  $\mu\text{m}$  ( $\text{PM}_{10}$ ) were measured gravimetrically as described by L'Orange et al.<sup>150</sup>. Together, the coarse ( $\text{PM}_{10} - \text{PM}_{2.5}$ ) and fine ( $< \text{PM}_{2.5}$ ) PM fractions were collected on Teflon filters that were pre- and post-weighed on a microbalance with 1  $\mu\text{g}$  readability (MX5, Mettler-Toledo, LLC, Columbus, OH, USA). The limit of detection (LOD) and limit of quantification (LOQ) for these measurements were 16  $\mu\text{g}$  and 55  $\mu\text{g}$ . All  $\text{PM}_{10}$  mass emissions measurements were found to be above the LOQ with the exception of one measurement of 53  $\mu\text{g}$ .

CO emissions were measured at 1 Hz with Testo 335 and Testo 350 flue gas analyzers (Testo, Sparta, NJ, USA). These analyzers used electrochemical sensors to measure the mole fraction of CO in the fume hood exhaust gas. This real-time measurement of emissions allowed the effects of changes in operating procedure on emissions to be observed. Multiple steps were taken to ensure that the Testo 335 and Testo 350 flue gas analyzers were measuring CO emissions accurately. The Testo 335 and Testo 350 were spanned to measure mole fractions of CO up to 500 ppm and 10,000 ppm, respectively, using calibration gases. The Testo 335 was used when the maximum mole fraction of CO in the exhaust gas was anticipated to be below 500 ppm to provide higher resolution at lower concentrations. The Testo 350 was used when the maximum mole fraction was anticipated to be above 500 ppm to provide more accurate readings at higher concentrations. After the Testo 350 was spanned to read a mole fraction of 0.01, the analyzer was connected to a bottle of calibration gas with a CO mole fraction of 101 ppm to assess how accurately it would read lower concentrations. The analyzer read the mole fraction of CO in the calibration gas with an accuracy of  $\pm 5$  ppm. To further verify the accuracy of the CO analyzers, emissions were measured simultaneously using the Testo 335 and a non-dispersive infrared spectrometer (Ultramat 6, Siemens, Munich Germany) during one test. The difference between the two measurements was less than 3%.

Real-time temperature data were acquired at 1 Hz from 17 to 24 type K thermocouples (Omega Engineering, Stamford, CT, USA) installed on each stove. Gas temperature measurements included inlet air temperature, preheated secondary air temperature, and exhaust gas temperature. Temperatures were also recorded at various locations in the fuel chamber and on the outside of the stove body. An additional type K thermocouple submerged in the pot of water measured the water temperature at 0.6875 Hz. All temperature data, with the exception of the water temperature data, were acquired by a National Instruments cRIO-9072 chassis, which contained one NI 9213 thermocouple input card and two NI 9211 thermocouple input cards, and logged by a program that was created in LabVIEW™. The water temperature data were logged by a second program, also created in LabVIEW™, that also controlled the airflow rate through the fume hood and recorded the starting and ending time for each test. More information on the instrumentation used for data collection, and the placement of the thermocouples on each stove, can be found in Appendix A.

### 3.2.4 Efficiency Calculations

In addition to the emissions and temperature measurements described above, fuel consumption measurements were made for each of the configuration/fuel type combinations in Table 3.2. The equations that were used to calculate efficiency based on these measurements are described below.

The *thermal efficiency* of each stove is defined as the ratio of the energy transferred to the water to the difference between the energy available in the fuel and the energy contained in the char remaining at the end of the test. Thermal efficiency was calculated using Equation 3.1<sup>148</sup>:

$$\eta = \frac{c_{p,H_2O}m_{H_2O}\Delta T_{H_2O} + h_{v,H_2O}m_{H_2O}^{evap}}{m_f(1 - MC_f)LHV_{f,dry} - m_fMC_f(c_{p,H_2O}\Delta T_{H_2O,f} + h_{v,H_2O}) - m_cLHV_c} \quad (3.1)$$

where  $c_{p,H_2O}$  was the specific heat of water in  $J \cdot g^{-1} \cdot K^{-1}$ ,  $m_{H_2O}$  was the mass of water boiled in g,  $\Delta T_{H_2O}$  was the change in the water temperature between the beginning and

end of the test in K,  $h_{v,H_2O}$  was the heat of vaporization of water in  $J \cdot g^{-1}$ ,  $m_{H_2O_{evap}}$  was the mass of water evaporated out of the pot during the test in g,  $m_f$  was the mass of wet fuel consumed in g,  $MC_f$  was the moisture content of the fuel (as a mass fraction on a wet basis),  $LHV_{f,dry}$  was the lower heating value of the fuel on a dry basis in  $J \cdot g^{-1}$ ,  $\Delta T_{H_2O,f}$  was the temperature change that the water in the fuel had to undergo before it was evaporated (assumed to be 75 K),  $m_c$  was the mass of the ash and charcoal remaining at the end of the test in g, and  $LHV_c$  was the lower heating value of the charcoal produced from the fuel in  $J \cdot g^{-1}$ .

The *overall efficiency* of each stove was defined herein as the ratio of the energy transferred to the water to the energy available in the dry mass of fuel consumed (Equation 3.2).

$$\eta_{OA} = \frac{c_{p,H_2O}m_{H_2O}\Delta T_{H_2O} + h_{v,H_2O}m_{H_2O_{evap}}}{m_f(1 - MC_f)LHV_{f,dry} - m_fMC_f(c_{p,H_2O}\Delta T_{H_2O,f} + h_{v,H_2O})} \quad (3.2)$$

In this formulation, the energy remaining in the charcoal left at the end of the test represented an energy loss. Although the chemical energy contained in this char is still available for subsequent use, it should not be assumed that it will be converted into thermal energy.<sup>64</sup> It should be noted, however, that most studies on stove performance do account for the energy remaining in the char and report the thermal efficiency shown in Equation 3.1.<sup>73–75</sup>

### 3.2.5 Energy Balance Model

To determine the major sources of efficiency loss and to inform future design efforts, all of the energy sources, sinks, and components of energy transfer present during stove operation were accounted for in a thermodynamic energy balance model. The sources of energy include the energy in the fuel and the energy in the inlet air. The energy contained in the char remaining at the end of the test was counted as an energy sink. The energy transfer components included the energy transferred to the water, the energy transferred to (and stored in) the stove body, the energy lost through convection and radiation heat

transfer from the outside of the stove body to the surroundings, and the energy lost through the exhaust gases.

The portion of the energy contained in the fuel that could have been used to heat the cooking surface was calculated using Equation 3.3:

$$E_f = m_f(1 - MC_f)LHV_{f,dry} - m_fMC_f(c_{p,H_2O}\Delta T_{H_2O,f} + h_{v,H_2O}) \quad (3.3)$$

where  $m_f$  was the mass of fuel consumed in g,  $MC_f$  was the moisture content of the fuel (as a mass fraction on a wet basis),  $LHV_{f,dry}$  was the lower heating value of the dry fuel in  $J \cdot g^{-1}$ ,  $\Delta T_{H_2O,f}$  was the temperature change that the water in the fuel had to undergo before it was evaporated (assumed to be 75 K), and  $h_{v,H_2O}$  was the heat of vaporization of water  $J \cdot g^{-1}$ . The second term on the right hand side of Equation 3.3 represented energy contained in the fuel that had to be used to evaporate the water stored in the fuel.

The energy transferred to the water was calculated using Equation 3.4:

$$E_{H_2O} = m_{H_2O}c_{p,H_2O}(T_f - T_i) + h_{v,H_2O}m_{H_2Oevap} \quad (3.4)$$

where  $E_{H_2O}$  was the energy transferred to the water in J,  $m_{H_2O}$  was the mass of water in kg,  $c_{p,H_2O}$  was the specific heat of the water in  $J \cdot kg^{-1} \cdot K^{-1}$ ,  $T_f$  was the final temperature of the water (90 °C),  $T_i$  was the initial temperature of the water (13 °C to 17 °C),  $h_{v,H_2O}$  was the heat of vaporization of water (2260  $J \cdot g^{-1}$ ), and  $m_{H_2Oevap}$  was the mass of water evaporated out of the pot during the test in g.

The energy contained in the char remaining at the end of the test was calculated using Equation 3.5:

$$E_c = m_cHHV_c \quad (3.5)$$

where  $E_c$  was the energy contained in the char in J,  $m_c$  was the mass of char in g, and  $HHV_c$  was the higher heating value of the char in  $J \cdot g^{-1}$ .

For Stoves 4 and 5, the energy added to the stove body was calculated by multiplying the mass of the stove by the specific heat of the metallic stove body and the change in temperature of the stove body between the beginning and end of the test (Equation 3.6).

$$E_{stove} = m_{stove}C(T_f - T_i) \quad (3.6)$$

where  $E_{stove}$  was the energy stored in the stove body in J,  $m_{stove}$  was the mass of the stove in kg,  $C$  was the specific heat of the material the stove is constructed from in  $\text{J}\cdot\text{kg}^{-1}\cdot\text{K}^{-1}$ ,  $T_f$  was the final temperature of the stove body in K, and  $T_i$  was the initial temperature of the stove body in K. The specific alloys from which Stoves 4 and 5 were constructed was unknown and properties of plain carbon steel and AISI 304 stainless steel were assumed for these calculations (see Table 3.4).

**Table 3.4: Material properties used to calculate the energy stored in the bodies of the stove configurations (values from Incropera et al.<sup>151</sup>).**

Property	Plain carbon steel	AISI 304 SS	Cement mortar
Density ( $\text{kg}\cdot\text{m}^{-3}$ )	7854	7900	1860
Specific heat ( $\text{J}\cdot\text{kg}^{-1}\cdot\text{K}^{-1}$ )	434	477	780
Thermal conductivity ( $\text{W}\cdot\text{m}^{-1}\cdot\text{K}^{-1}$ )	60.5	14.9	0.72

Calculating the quantity of the energy stored in the bodies of Stoves 1, 2, and 3 was more complicated because, although these stoves were constructed primarily of steel, the stove bodies also contained a large mass of dense refractory material. The refractory material was expected to be at a higher temperature than the steel frame because the refractory material was directly exposed to the hot gases that passed under the pot. The large mass and low thermal conductivity of the refractory material (in comparison to the steel) required the development of an additional heat transfer model to determine the quantity of thermal energy stored in the refractory material.

The block of refractory material was situated above the secondary combustion zone and below the pot. The area below the pot consisted of a cylindrical cavity with a diameter of 31 cm and a height of 11 cm. The block of refractory material filled the area between this

cavity and the steel frame of the stove and had a total volume of  $6,270 \text{ cm}^3$ . The steel frame was estimated to weigh 25 kg and the block of refractory material was estimated to weigh 12 kg. The properties of the steel frame were taken to be the properties of plain carbon steel and the properties of the refractory material were taken to be the properties of cement mortar (see Table 3.4).

A top view of the actual geometry of the region containing the refractory material is shown in Figure 3.2a. The refractory material is shaded gray. The block of refractory material was modeled as a cylindrical ring with the same inner radius and the same volume as the actual geometry. The modeled geometry for Stove 1 is shown in Figure 3.2b. The difference between  $r_2$  and  $r_3$  in the model geometry was equal to the actual thickness of the steel walls of the stove. For Stoves 2 and 3, the geometry was modeled as shown in Figure 3.2c.

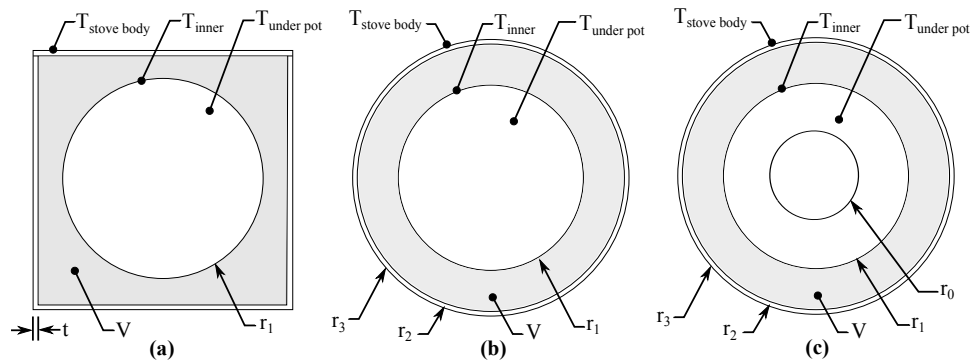


**Figure 3.2:** (a) The actual geometry of the region containing the refractory block, (b) the manner in which the geometry shown in (a) was modeled for Stove 1, and (c) the manner in which the geometry was modeled for Stoves 2 and 3.

Although the overall heat transfer process was transient, the heat transfer through the block of refractory material was assumed to be steady over the course of each 1-second time step and a resistance model was employed to estimate the temperature profile within the block (see Figure 3.3). The temperature of the air under the pot and the temperature of the outside of the stove body were measured. The air under the pot was at the highest temperature and the stove body was at the lowest temperature. The thermal resistance elements included convection between the hot gases under the pot and the inside walls of

the block of refractory material, conduction through the block of refractory material, and conduction through the steel wall of the stove.

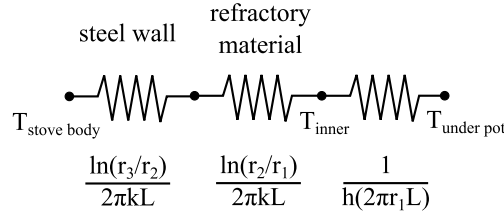


**Figure 3.3: The resistance model used to estimate the temperature distribution within the block of refractory material.**

Temperature data were recorded at 1 Hz intervals and each of the following values was calculated at every time step: (1) Rayleigh number, (2) Nusselt number, (3) the convection coefficient, (4) the total thermal resistance between the hot gases under the pot and the outside of the stove body, (5) the heat transfer through the refractory block at that instant, and (6) the temperature of the inner wall of the refractory block.

For all of the calculations, the properties of the air in the region under the pot were based on the average under pot temperature over the course of the entire test. The air was modeled as an ideal gas.

The Rayleigh number was calculated using Equation 3.7:<sup>151</sup>

$$Ra_L = \frac{g\beta(T_\infty - T_s)L^3}{\nu\alpha} \quad (3.7)$$

where  $Ra_L$  was the Rayleigh number,  $g$  was the acceleration due to gravity ( $9.81 \text{ m} \cdot \text{s}^{-2}$ ),  $\beta$  was the volumetric thermal expansion coefficient of the fluid in  $\text{K}^{-1}$ ,  $T_\infty$  was the temperature of the fluid in K,  $T_s$  was the temperature of the surface in K,  $L$  was the length over which convection takes place in m,  $\nu$  was the kinematic viscosity in  $\text{m}^2 \cdot \text{s}^{-1}$ , and  $\alpha$  was the thermal diffusivity in  $\text{m}^2 \cdot \text{s}^{-1}$ .

For an ideal gas:

$$\beta = \frac{1}{T_{film}} \quad (3.8)$$

where  $T_{film}$  was the film temperature in K.<sup>151</sup>

Consequently, the Rayleigh number was calculated as:

$$Ra_L = \frac{g(T_{under\ pot} - T_{inner})L^3}{\left(\frac{T_{under\ pot} + T_{inner}}{2}\right)\nu\alpha} \quad (3.9)$$

At the first time step, the temperature of the inner wall was assumed to be equal to the initial temperature of the outside walls of the stove. At each time step, a new inner wall temperature was calculated. The new inner wall temperature was then used to calculate the Rayleigh number in the next time step. The temperature of the inner wall was assumed to be uniform over the entire surface.

The correlation chosen to calculate the Nusselt number depended on which configuration was used during the test (Stove 1, 2, or 3). When Stove 1 was used, the inner wall was modeled as an isothermal flat plate due to the large diameter of the cavity. The Nusselt number correlation developed by Churchill and Chu<sup>152</sup> for use at low Rayleigh numbers was used:

$$\overline{Nu}_L = 0.68 + \frac{0.670Ra_L^{1/4}}{[1 + (0.492/Pr)^{9/16}]^{4/9}}, \quad Ra_L \leq 10^9 \quad (3.10)$$

where  $\overline{Nu}_L$  was the average Nusselt number over the length of the plate,  $Ra_L$  was the Rayleigh number, and  $Pr$  was the Prandtl number (0.7 for air).

For Stoves 2 and 3, a Nusselt number correlation developed by Nagendra et al.<sup>153</sup> for free convection between two vertical cylinders, when the inner cylinder is at a high temperature and the outer cylinder is at a low temperature, was used:

$$\overline{Nu}_L = \frac{0.48Ra_L}{6830\left(\frac{L}{d_1}\right)^4\frac{d_0}{L} + Ra_L^{3/4}}, \quad \frac{L}{d_0}Ra_L^{-1/4} \leq 0.1 \quad (3.11)$$

where  $\overline{Nu}_L$  was the average Nusselt number,  $Ra_L$  was the Rayleigh number,  $L$  was the length over which the convection takes place in m,  $d_1$  was the diameter of the outer cylinder in m, and  $d_0$  was the diameter of inner cylinder in m. The outer cylinder was the inner wall of the block of refractory material. The inner cylinder was the outer wall of the cylindrical duct.

The convection coefficient was calculated from the Nusselt number as shown in Equation 3.12:<sup>151</sup>

$$\bar{h}_L = \frac{\overline{Nu}_L k}{L} \quad (3.12)$$

where  $k$  was the thermal conductivity of the air in  $\text{W}\cdot\text{m}^{-1}\cdot\text{K}^{-1}$ .

Thermal resistance is defined as:<sup>151</sup>

$$\Sigma R = \frac{\Delta T}{Q} \quad (3.13)$$

where  $\Sigma R$  is the total thermal resistance between the two nodes in  $\text{K}\cdot\text{W}^{-1}$ ,  $\Delta T$  is the temperature difference between the two nodes in  $\text{K}$ , and  $Q$  is the heat transfer in  $\text{W}$ .

When the total resistance and temperature difference between the two nodes is known, Equation 3.13 can be rearranged to calculate the heat transfer between the two nodes. The total heat transfer through the refractory block was calculated at each time step as:

$$Q = \frac{T_{\text{under pot}} - T_{\text{stove body}}}{\frac{\ln(r_3/r_2)}{2\pi k_{\text{steel}}L} + \frac{\ln(r_2/r_1)}{2\pi k_{\text{cement}}L} + \frac{1}{\bar{h}_L(2\pi r_1 L)}} \quad (3.14)$$

The inner wall temperature was then calculated at each time step as:

$$T_{\text{inner}} = T_{\text{under pot}} - \frac{Q}{\bar{h}_L(2\pi r_1 L)} \quad (3.15)$$

The energy stored in the block of refractory material was calculated using the initial temperature of the block and temperature profile within the block calculated at the final time step:

$$E_{\text{block}} = \rho C(2\pi L) \int_{r_1}^{r_2} [T_f(r) - T_i] r dr \quad (3.16)$$

$$T_f(r) = T_{\text{inner},f} - Q_f \frac{\ln(r/r_1)}{2\pi k L} \quad (3.17)$$

where  $E_{\text{block}}$  was the energy stored in the block of refractory material in  $\text{J}$ ,  $\rho$  was the density of the block ( $1860 \text{ kg}\cdot\text{m}^{-3}$ ),  $C$  was the specific heat of the block ( $780 \text{ J}\cdot\text{kg}^{-1}\cdot\text{K}^{-1}$ ),  $L$  was the height of the block in  $\text{m}$ ,  $T_f(r)$  was the final temperature of the block as a function

of radius in K,  $T_i$  was the initial temperature of the entire stove body in K,  $T_{inner,f}$  was the final temperature of the inside wall of the block in K,  $Q_f$  was the heat transfer through the block at the final time step in W,  $r$  was the radius in m,  $r_1$  was the radius of the inner wall of the refractory block in m,  $r_2$  was the outer radius of the refractory block in m, and  $k$  was the thermal conductivity of the refractory block ( $0.72 \text{ W}\cdot\text{m}^{-1}\cdot\text{K}^{-1}$ ).

A program was written in MATLAB<sup>®</sup> to solve Equation 3.16. The inputs to the program were the initial temperature of the stove body ( $T_i$ ), the final inner wall temperature ( $T_{inner,f}$ ), and the final heat transfer ( $Q_f$ ).

The energy stored in the steel frame was calculated by multiplying the mass of the frame by the specific heat of the frame and the change in temperature between the beginning and end of the test:

$$E_{frame} = m_{steel}C_{steel}(T_f - T_i) \quad (3.18)$$

where  $E_{frame}$  was the energy stored in the steel frame in J,  $m_{steel}$  was the mass of the steel frame (25 kg),  $C_{steel}$  was the specific heat of the specific heat of plain carbon steel ( $434 \text{ J}\cdot\text{kg}^{-1}\cdot\text{K}^{-1}$ ),<sup>151</sup>  $T_f$  was the temperature of the steel frame at the end of the test in K, and  $T_i$  was the temperature of the steel frame at the beginning of the test in K. At each time step the entire steel frame was assumed to be at the average temperature measured by the four thermocouples installed on the outside walls of the stove.

For Stoves 1, 2, and 3, the total energy stored in the stove body was calculated by adding the amount of energy stored in the steel frame to the amount of energy stored in the block of refractory material:

$$E_{stove\ body} = E_{frame} + E_{block} \quad (3.19)$$

The heat lost through convection from the stove body was calculated using Equation 3.20:

$$E_{conv} = \int_0^{t_f} h(t)A [T(t) - T_\infty] dt \quad (3.20)$$

where  $E_{conv}$  was the energy lost through convection in J,  $h$  was the convection coefficient in  $W \cdot m^{-2} \cdot K^{-1}$ ,  $A$  was the surface area of the sides of the stove in  $m^2$ ,  $T$  was the temperature of the stove body in K,  $T_{\infty}$  was the temperature of the surroundings in K, and  $t_f$  was the length of the test in s.

Equation 3.20 was integrated numerically using the outside stove body temperature that was recorded every second during the test as  $T(t)$ . The Rayleigh number, Nusselt number, and the convection coefficient were recalculated at every time step. The average of the primary and secondary air inlet temperatures at time 0 were taken as the ambient air temperature.

The outer surfaces of Stoves 1, 2, and 3 were modeled as 4 vertical plates. The outer surfaces of Stoves 4 and 5 were modeled as single vertical plates with surface areas equal to the surface areas of the cylindrical outer walls. The outside walls were assumed to be isothermal at each time step. The convection coefficient was calculated using the Nusselt number correlation for natural convection over a vertical flat plate shown in Equation 3.10.

The radiation heat loss from the stove body was calculated using Equation 3.21:

$$E_{rad} = \int_0^{t_f} \epsilon \sigma A [T(t)^4 - T_{\infty}^4] dt \quad (3.21)$$

where  $E_{rad}$  was the energy lost through radiation in J,  $\epsilon$  was the emissivity of the stove,  $\sigma$  was the Stefan-Boltzmann constant ( $W \cdot m^{-2} \cdot K^{-4}$ ),  $A$  was the surface area of the stove in  $m^2$ ,  $T(t)$  was the temperature of the stove body in K, and  $T_{\infty}$  was the temperature of the surroundings in K. Equation 3.21 was integrated numerically using the same temperatures used in Equation 3.20.

The amount of energy transferred to the water, contained in the char at the end of the test, stored in the stove body, and lost through radiation and convection from the outside walls of the stove was subtracted from the total energy contained in the fuel input at the beginning of the test. The difference was taken to be the amount of energy lost through the exhaust from the stove.

### 3.3 Results and Discussion

The high power carbon monoxide emissions, high power particulate matter emissions, and thermal efficiencies measured during the experiments, as well as the results of the energy balance calculations, are presented below. First, the differences between the results for each design configuration/fuel type combination are discussed. The high-power emissions and efficiency for each combination are also compared to the tier ratings for biomass cookstove performance established at the ISO International Workshop on Clean and Efficient Cookstoves.<sup>26</sup> Second, the real-time carbon monoxide emissions measurements are used to identify large, transient increases in emissions associated with refueling of gasifier cookstoves. Third, some further discussion on the emissions results is provided. Fourth, the results of the energy balance model are presented.

#### 3.3.1 Influence of Design Configuration and Fuel Type on Emissions and Efficiency

As shown in Figure 3.4, the high-power CO and PM<sub>10</sub> emissions from all five configurations were affected by changes in fuel type. For four out of five configurations, the measured emissions were lower when wood pellets were used as fuel instead of corn cobs. For example, when Stove 1 was fueled with wood pellets instead of corn cobs, CO emissions decreased by a factor of 47 and PM<sub>10</sub> emissions decreased by a factor of 6. Similarly, when Stove 4 stove was fueled with wood pellets instead of corn cobs, CO emissions decreased by a factor of 2. When Stove 5 was fueled with wood pellets instead of corn cobs, CO emissions decreased by a factor of 11 and PM<sub>10</sub> emissions decreased by a factor of 3.

Although the design changes made to Stove 1 resulted in reduced emissions, Stoves 1, 2, and 3 produced higher emissions than Stoves 4 and 5. Stove 5 exhibited the lowest CO and PM<sub>10</sub> emissions overall. The range of performance observed in Figure 3.4 is similar to the range of performance observed for different gasifier cookstoves in Figure 1.4. The average high-power CO emissions measured for Stoves 1, 2, and 3 fueled with corn cobs and Stove 3 fueled with wood pellets were higher than the average high-power CO emissions reported

for carefully- and minimally-tended three stone fires.<sup>75</sup> On the other hand, the average high-power  $PM_{10}$  emissions measured for Stoves 1, 2, 4, and 5 fueled with wood pellets were lower than the average high-power  $PM_{2.5}$  emissions reported for side feed wood stoves.<sup>75</sup>

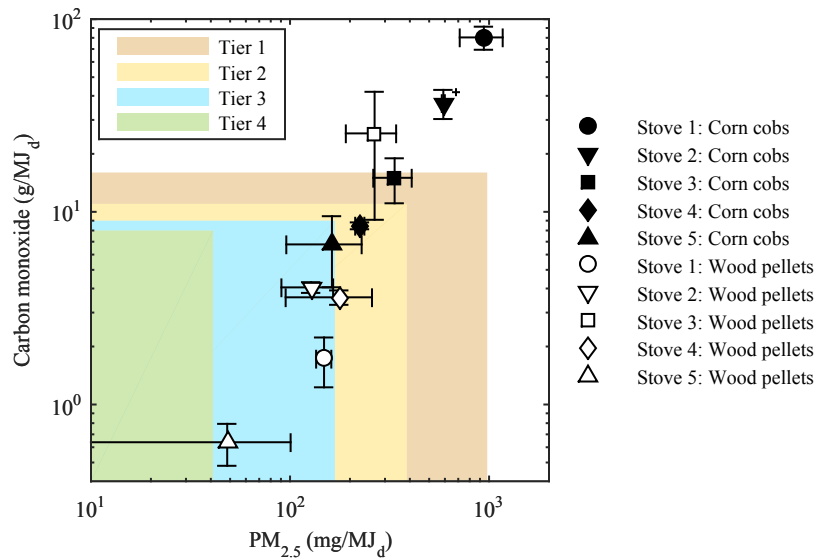


**Figure 3.4: Average high-power CO emissions vs. average high-power  $PM_{10}$  emissions compared to ISO tiers for biomass stove performance. Error bars represent one standard deviation with the exception of the error bars on the data point for Stove 2 fueled with corn cobs. This data point (marked with a ‘+’) is based on only two test replicates and the error bars represent the total range of the two results.**

Stoves 4 and 5 were more efficient than Stoves 1, 2, and 3 (see Figure 3.5). Unlike emissions, thermal efficiency was not affected by fuel type (Figure 3.5). The average thermal efficiencies for Stove 1 fueled with corn cobs and Stove 1 fueled with wood pellets were 8.3% and 9.0%, respectively. The average thermal efficiencies for Stove 2 fueled with corn cobs and Stove 2 fueled with wood pellets were 12.3% and 12.2%. Similarly, the average thermal efficiencies for Stove 3 fueled with corn cobs and Stove 3 fueled with wood pellets were 20.1% and 19.9%. The thermal efficiency of a given design configuration is expected to depend primarily upon stove geometry.

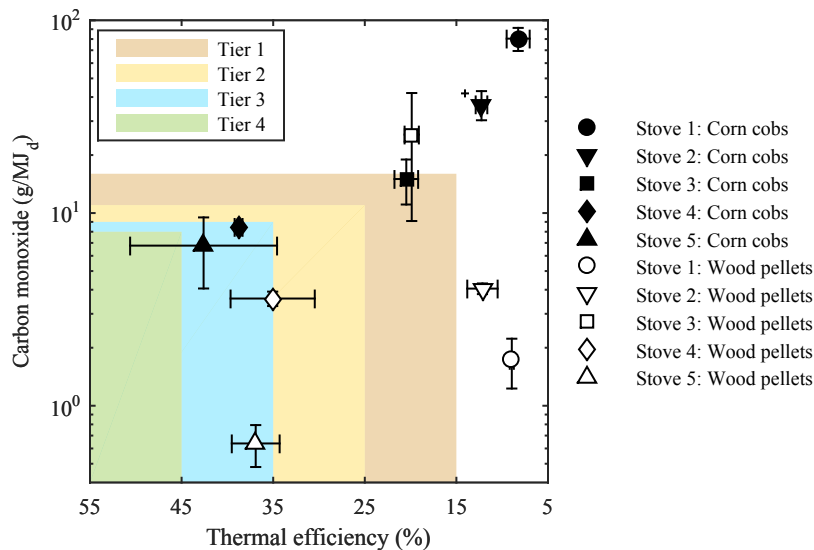


**Figure 3.5: Average high-power CO emissions vs. average thermal efficiency compared to ISO tiers for biomass stove performance. Error bars represent one standard deviation with the exception of the error bars on the data point for Stove 2 fueled with corn cobs. This data point (marked with a ‘+’) is based on only two test replicates and the error bars represent the total range of the two results.**

In terms of the ISO tier ratings, Stoves 1, 2, and 3 had the most variable performance, which ranged from Tier 0 to Tier 3 depending on the fuel type and design configuration implemented. The performance of Stove 4 was the least variable; emissions remained within Tier 2 for both fuel types. Emissions from Stove 5 were on the border between Tier 2 and Tier 3 when the stove was fueled with corn cobs and on the border between Tier 3 and Tier 4 when the stove was fueled with wood pellets (Figure 3.4). Although several of the configuration/fuel type combinations met the Tier 4 high-power CO rating, only Stove 5 operating on wood pellets came close to meeting the Tier 4 high-power PM rating. The emissions results for Stove 5 are noteworthy since previous studies indicated that natural draft gasifier cookstoves did not perform as well as forced-air gasifier cookstoves,<sup>64,74</sup> and suggested that such low PM emissions were only achievable with forced-air gasifier cookstoves.<sup>75</sup> These results suggest that natural draft TLUDs have the potential to meet both of the high-power Tier 4 emissions ratings.

### 3.3.2 Emissions Increases Associated with Refueling

The two design changes made to Stove 1 to create Stoves 2 and 3 were motivated by the low efficiencies measured with Stove 1. The efficiency increased when the cylindrical duct and pot skirt were added above the secondary combustion zone (see Figure 3.5). The effect of these design changes on CO and PM<sub>10</sub> emissions varied depending on the fuel type. Specifically, when corn cobs were used as a fuel, emissions from Stoves 2 and 3 were lower than those from Stove 1. When wood pellets were used as a fuel, emissions from Stoves 2 and 3 were higher than those from Stove 1 (see Figure 3.4).

The high CO emissions observed when Stove 1 was operated using corn cob fuel resulted from the need to refuel the stove prior to completion of the cold start test due to the low bulk energy content in the corn cobs and high thermal mass of the stove. This determination was made by comparing real-time CO measurements with real-time temperature measurements taken inside the fuel chamber. Fuel bed temperature measurements allowed tracking of the primary combustion zone during stove operation. Data from a representative cold start performed with Stove 1 and corn cob fuel are shown in Figure 3.6. CO emission levels were lowest at the beginning of the test, just after ignition, when gasification had not yet started. CO emissions became noticeably higher once gasification started. Emissions increased once again when the entire fuel bed had gasified and the char began to burn. After the char was burnt, fuel had to be added to continue the test. Subsequent batches of fuel were consumed quickly and CO emissions became higher than at any other point during the test. During these times the stove was no longer operating purely as a TLUD. Refueling may have also resulted in sharp increases in PM emissions, but real-time PM emissions were not measured in this study.

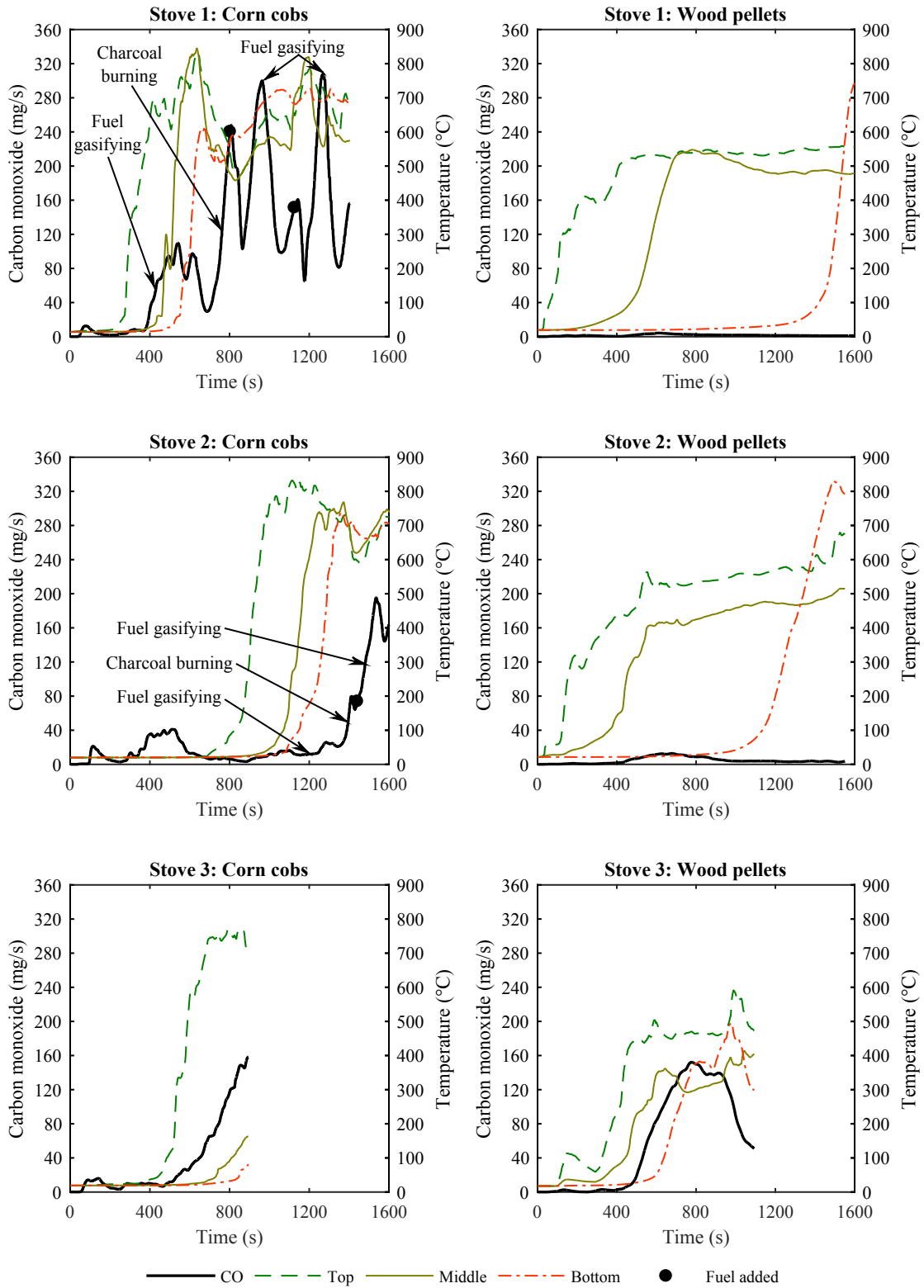
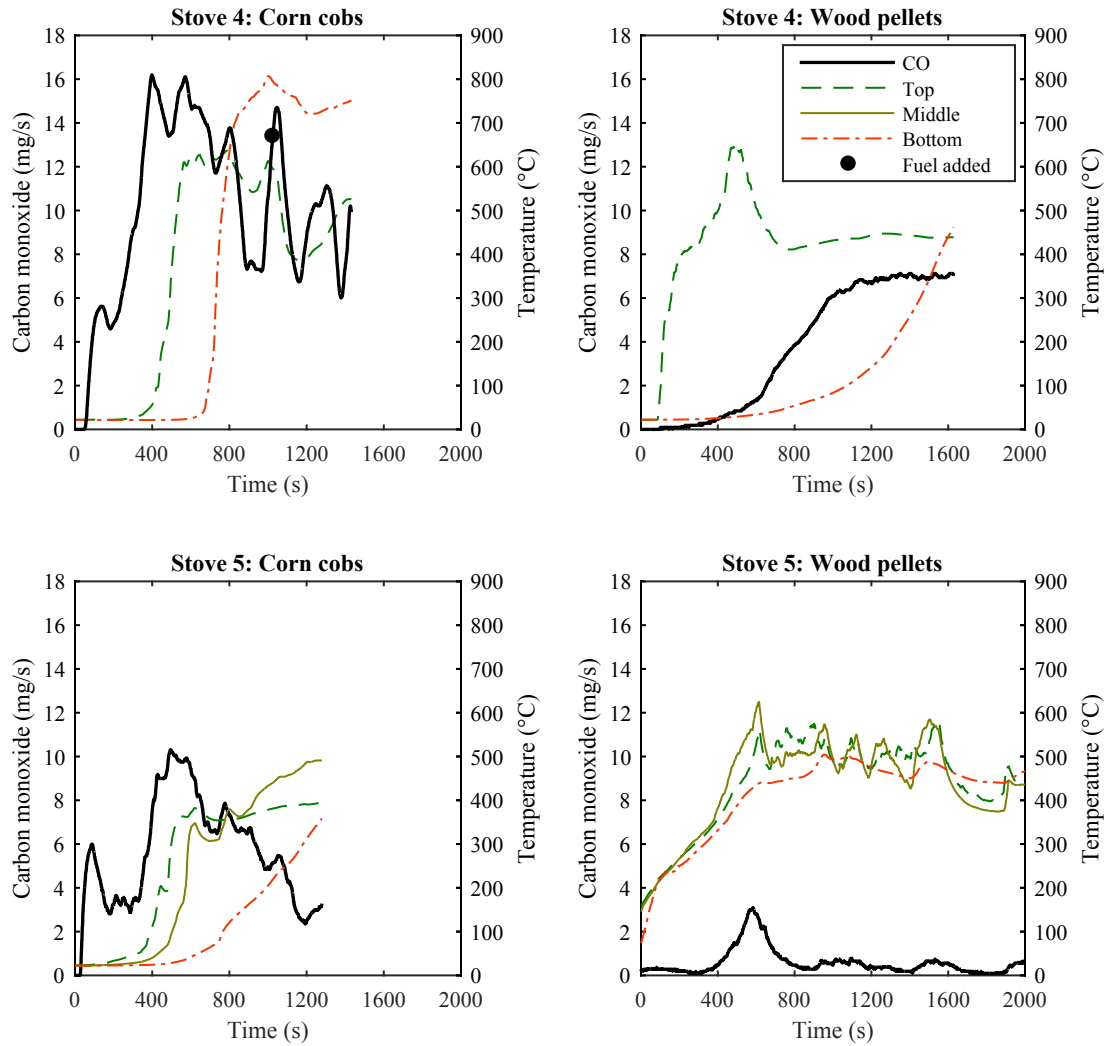


Figure 3.6: CO emissions and fuel chamber temperatures during cold start tests completed using Stoves 1, 2, and 3 with corn cob and wood pellet fuels.

Similar CO emissions trends were observed when Stoves 2 and 3 were operated using corn cob fuel. Because Stoves 2 and 3 exhibited improved the heat transfer to the pot, the stoves were refueled fewer times. The lower overall emissions for the tests were the result of reducing the number of transient increases in emissions associated with refueling events. For Stove 2, consumption of the original batch of corn cob fuel proceeded more slowly than in Stove 1 and the stove only had to be refueled once during the test (see Figure 3.6). For Stove 3, the approximate time to boil was reduced from 25 minutes (for Stove 1) to 15 minutes and the stove did not have to be refueled during the test.

The real-time carbon monoxide emission rate remained below  $5 \text{ mg}\cdot\text{s}^{-1}$  for the entire duration of the cold start when Stove 1 was fueled with wood pellets (see Figure 3.6). In this case, Stove 1 did not require refueling prior to completion of the test. The real-time CO emission rate remained below  $15 \text{ mg}\cdot\text{s}^{-1}$  for the entire duration of the cold start when Stove 2 was fueled with wood pellets. For Stove 3 fueled with wood pellets, on the other hand, the peak real-time CO emissions rate was more than  $150 \text{ mg}\cdot\text{s}^{-1}$ . In this configuration, the modifications may have affected the airflow through the stove and enhanced heat transfer from the hot gases to the pot may have actually limited the oxidation of pollutants by reducing the gas temperature.

As noted above, the average high-power emissions from Stove 4 fell within Tier 2 for both fuel types. The maximum CO emission rate was  $16 \text{ mg}\cdot\text{s}^{-1}$  when the stove was fueled with corn cobs and  $7 \text{ mg}\cdot\text{s}^{-1}$  when the stove was fueled with wood pellets. Stove 4 had to be refueled once during the cold start when corn cobs were used. However, a large increase in the CO emission rate was not observed upon refueling. Stove 5 did not require refueling during the cold start when either fuel was used (see Figure 3.7).



**Figure 3.7: CO emissions and fuel chamber temperatures during cold start tests completed using Stoves 4 and 5 with corn cob and wood pellet fuels.**

These results illustrate the impact of the bulk energy density of the fuel on CO emissions. It is understood that the choice of fuel type used in the field is dictated by cost and availability. However, the results underscore the need to incorporate the fuel type that the consumer is known to be most likely to use into the stove design for TLUD gasifier cookstoves.

These results also illustrate how changes in operator behavior can affect stove performance. This point has been illustrated with other types of cookstoves in previous studies. Jetter et al.<sup>75</sup> tested a three stone fire and two rocket elbow stoves under different operating conditions and observed a substantial variation in emissions performance. If the natural

draft TLUD gasifier cookstoves tested in this study were to be tested by different operators, either in the laboratory or under real-world conditions, the technique used by different operators to refuel the stove, and the frequency at which different operators refueled, would most likely lead to substantial variability in the results. Since refueling has been demonstrated to result in large, transient emission rate increases, gasifier cookstove dissemination projects should be accompanied by training to educate users on the issues associated with adding fuel onto the hot char bed.

### **3.3.3 Further Discussion on the Experimental Results**

Because only the cold start phase of the EPTP was completed, the results do not provide a complete picture of the performance of each stove. The results of the hot start phase are also typically considered when evaluating high-power performance, and ISO IWA tiers were also established for low-power emissions and fuel consumption.<sup>26</sup> However, the purpose of this study was not to provide a comprehensive review of stove performance. Rather, the purpose was to illustrate how performance could vary between five different stove configurations that operate under the same natural draft TLUD operating principle.

Another limitation associated with the experimental results is the small sample sizes used and the high variance associated with the CO and PM<sub>10</sub> measurements. This variance is illustrated by the error bars, which depict one standard deviation, in Figures 3.4 and 3.5. The use of larger sample sizes would have improved the level of confidence in the overall magnitudes of the emissions measurements. However, the experimental results illustrate the range of performance that is possible with natural draft TLUDs cookstoves, and the real-time CO emissions measurements illustrate how performance can be affected by fuel type, operating conditions, and user behavior. Efficiency measurements, on the other hand, were less variable and the coefficient of variance for all efficiency measurements was below 20%.

Three of the design configurations tested (Stoves 1, 2, and 3) included chimneys. In addition to the tiers for overall high-power emissions, ISO IWA tiers for indoor emissions have been established<sup>26</sup> to help evaluate the potential for improving user health by using

a chimney to direct emissions away from the user and out of the home. Indoor emissions, which represent the difference between the total emissions from the stove and the portion of those emissions that would be directed out of the home through the chimney, were not measured in this study. Consequently, the total emissions from the chimney stoves may not necessarily be comparable to the total emissions from the non-chimney stoves from the perspective of health impacts. However, field studies involving chimney stoves have shown that not all of the emissions produced by a chimney stove are directed out of the home and that high concentrations of CO and PM may still be measured inside homes with chimney stoves.<sup>154–156</sup> Because a portion of the emissions produced by a chimney stove are expected to remain in the home, lower overall emissions from chimney stoves are expected to correlate with lower indoor emissions.

It should also be noted that all five stoves exhibited increases in CO emission rates during shut-down. These increases in emission rates are not shown in Figures 3.6 and 3.7, however, because emissions from the shut-down process are not included in the EPTP or any other water boiling test. However, the existence of shut-down emissions, as well as mitigation methods, should be considered since users will be exposed to these emissions during real-world use of gasifier cookstoves.

### **3.3.4 Energy Balance Results**

The results of the energy balance model are shown in Figures 3.8 and 3.9. The calculated quantities of energy transferred to the water and stove body; remaining in the char; and transferred out of the stove via the exhaust gases, convection and radiation are shown. For each configuration/fuel type combination, the results are reported in terms of total energy required to complete the cold start test (Figure 3.8) and as a fraction of the total energy contained in the fuel input into the stove during the test (Figure 3.9).

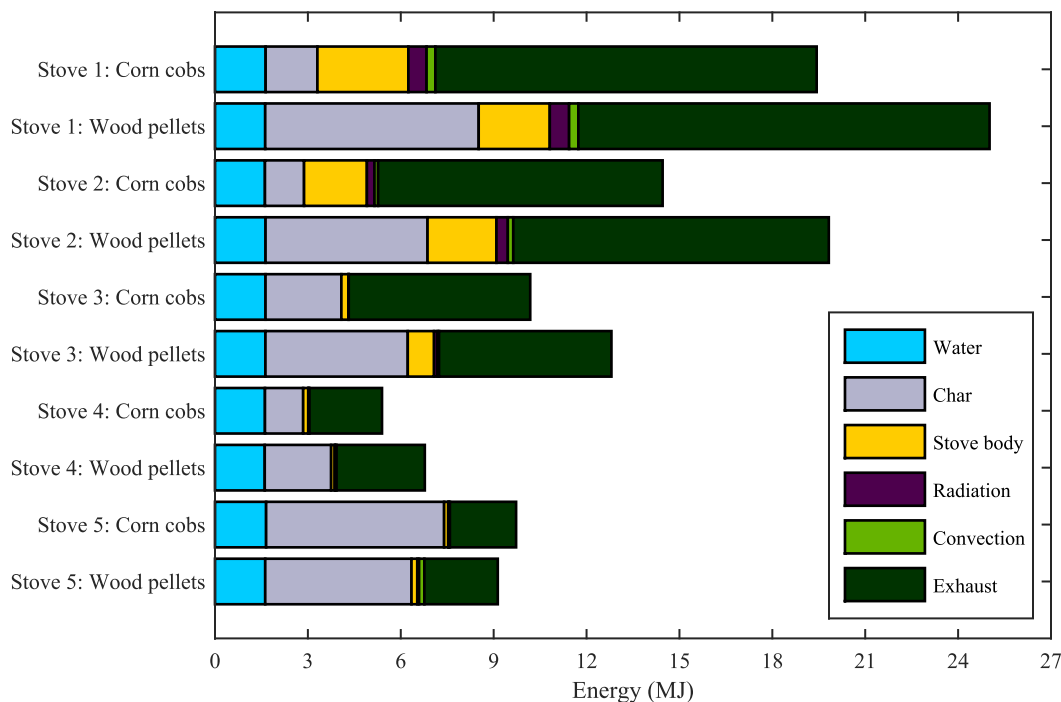


**Figure 3.8: Results of the energy balance with the energy consumption attributed to each component shown. The overall length of the bar for each test case represents the total energy input into the stove, in the form of fuel, to bring 5 L of water from 15 to 90 °C.**

Stove 1 used the greatest amount of energy to complete the test (Figure 3.8). Compared to Stoves 4 and 5, Stoves 1, 2 and 3 had more heat addition to the stove body and energy transferred out of the stove via the exhaust gases. These larger losses were the result of the high thermal mass of Stoves 1, 2, and 3 as well as the presence of the chimney.<sup>74</sup> The thermal efficiency of a cookstove is primarily dependent upon the ability to transfer heat to the cooking surface through radiation from the flame and convection from the hot gases. The amount of heat transferred to the cooking surface by convection is proportional to the area over which the hot gases flow. Stoves 1 and 2 only allowed heat to be transferred to the pot by radiation and by hot gases impinging on the bottom of the pot. The surface area for convection was limited to the area of the bottom of the pot. Consequently, thermal efficiencies were low. Stove 3, which included a pot skirt, had a larger area over which convective heat transfer to the pot could occur because the hot gases were forced to flow

around the sides of the pot. It should be noted that, for Stove 3, a faster time to boil also resulted in reduced energy losses due to stove body heating, despite the high thermal mass of the stove, as evidenced by the results for Stoves 2 and 3 operating with corn cobs. These results suggest that the stove body never reached a steady state temperature.

For Stoves 4 and 5, which had lower thermal masses due to their smaller sizes and lack of refractory lining, energy losses due to stove body heating, convection, and radiation were all very low (Figure 3.8). Although the thermal efficiencies of Stoves 4 and 5 were comparable (Figure 4), Stove 5 used more energy to complete the test than Stove 4 (Figure 3.8). This difference was due to the fact that more of the energy input to Stove 5 was left over as char at the end of the test (Figure 3.9).

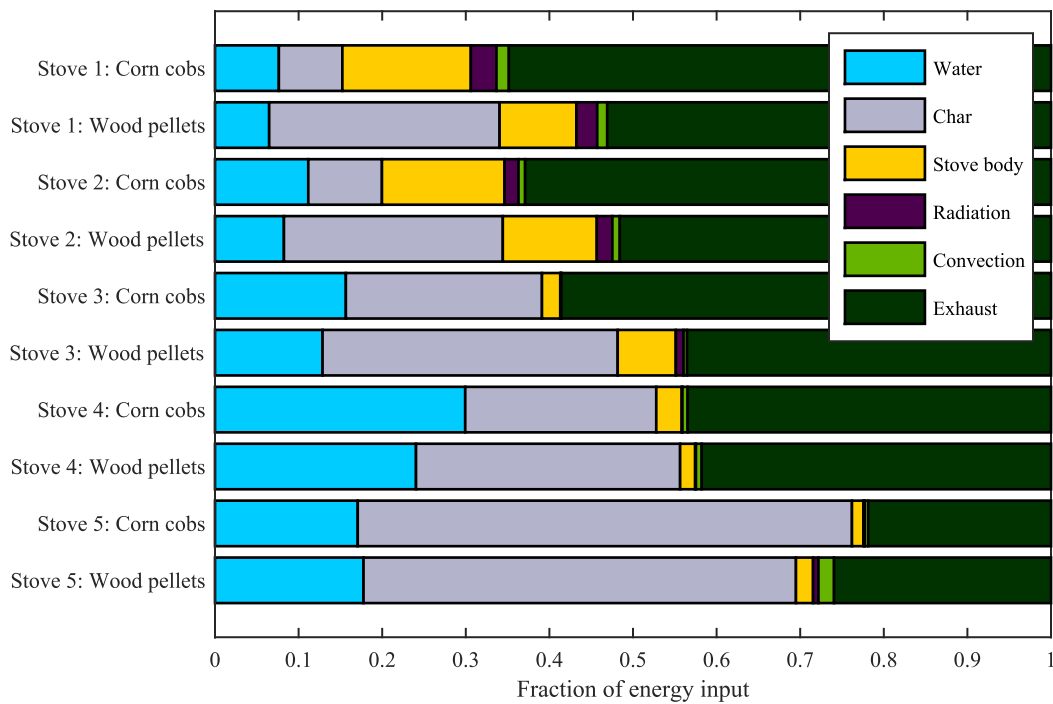


**Figure 3.9: Results of the energy balance with the energy consumption attributed to each component shown as a percentage of total energy consumption.**

The average fraction of the energy input to the stove in the form of fuel that was left over as char at the end of the test was 52% for Stove 5 fueled with corn cobs and 59% for Stove 5 fueled with wood pellets. This value was 28% for Stove 1 fueled with wood pellets, 26%

for Stove 2 fueled with wood pellets, 23% for Stove 3 fueled with corn cobs, 35% for Stove 3 fueled with wood pellets, 23% for Stove 4 fueled with corn cobs, and 32% for Stove 4 fueled with wood pellets. These results illustrate why it is important to consider the difference between the thermal efficiency and overall efficiency when evaluating a gasifier cookstove—especially if the cookstove has been designed to produce charcoal or biochar. Although the average thermal efficiency of Stove 5 was approximately 42%, the average overall efficiency was only 17% (Figure 3.9).

If the char that is left over after the fuel is gasified is put to some use (for example, as a fuel in a charcoal-burning stove or as a soil amendment), the low overall efficiency may not be a disadvantage to the stove user. For example, some combination TLUD/charcoal cookstoves have been designed in which the fuel chamber can be removed to transform a TLUD into a charcoal stove once the gasification process is complete.<sup>70</sup> However, it is recommended that testing protocols include a calculation of efficiency, similar to the “overall efficiency” calculation used in this study and shown in Equation 3.2, in which the energy remaining in the char at the end of the test is *not* subtracted from the energy input into the stove in the form of fuel. The thermal efficiency calculation typically used in the WBT and EPTP test protocols<sup>30,148</sup> is primarily a measure of how efficiently heat is transferred to the pot and does not always reflect how efficiently a given stove uses fuel overall.

### 3.4 Conclusions

The results of this study illustrate that differences in stove design among natural draft TLUD gasifier cookstoves can lead to high-power emissions that span Tiers 0 to 3 in the ISO IWA rating system. In addition, the results illustrate that changes in fuel type and operator behavior can result in order of magnitude changes in CO emissions for the same natural draft TLUD gasifier cookstove. The results also suggest that natural draft TLUDs have the potential to achieve Tier 3 high-power emissions when operated under controlled conditions (specified fuel type and operating procedure). Although additional work is needed to develop

a natural draft TLUD that achieves Tier 4 performance, Tier 4 high-power emissions and thermal efficiency may be within reach using this relatively simple design.

The instantaneous CO and temperature measurements strongly suggest that refueling TLUDs results in a sharp increase in CO emissions. In the field, there is no guarantee that users will refrain from refueling the stove during operation and thereby be exposed to high emissions. Improving the thermal efficiency of a stove can reduce the incidence of these transient increases in CO emissions by increasing the amount of useful energy that can be delivered to the cooking surface without refueling. However, eliminating these transient increases altogether by developing a stove design that can respond to transient conditions may be necessary to ensure low CO emissions in the field. Overall, it is important to consider real-world operating conditions when designing a gasifier cookstove and efforts should not focus only on designing a stove that performs well during laboratory tests and achieves high ratings according to the ISO IWA tiers. Specifically, the effects that all modes of stove operation, including refueling, transition to char combustion, and shut-down, have on emissions should be considered even if these operational modes do not necessarily occur during the course of a WBT.

Stoves should be tested in the laboratory using as many fuels that may be used in the field as possible. Existing TLUD gasifier cookstove designs should not be promoted as capable of utilizing any biomass as fuel. Although the stove will function using a wide variety of fuels, emissions performance will vary. This study clearly shows that TLUD gasifier cookstoves that exhibit Tier 3 emissions with one fuel type may exhibit Tier 0 emissions with another fuel type. Accordingly, further research and development efforts must be aimed at developing cookstove designs whose emissions and performance are more robust and not as strongly affected by the solid biomass fuel type and/or stove operating conditions.

Furthermore, the results of the energy balance modeling illustrate that, for some designs, up to 60% of the energy contained in the fuel that is consumed by TLUD gasifier cookstoves is left over in the form of char after the fuel bed is gasified. This result illustrates the

importance of considering the difference between the fraction of the energy *released* from the fuel that is transferred to the cooking pot and the fraction of the energy contained in the total mass of fuel consumed that is transferred to the cooking pot. It is also important to consider whether or not the char that is produced will be useful to the target consumer.

## CHAPTER 4

### Effects of Air Flow Rates, Secondary Air Inlet Geometry, Fuel Type, and Operating Mode on Gasifier Cookstove Performance<sup>3</sup>

#### 4.1 Introduction

In Chapter 3, emissions from natural draft TLUDs were found to be affected by both fuel type and operator behavior. In some cases, the total emissions were dominated by large, transient increases in emission rates.<sup>157</sup> Increases in emission rates have been observed when stoves transitioned from gasifying volatile biomass to burning the char left behind by the gasification process<sup>62,157-161</sup> and when batch-fed stoves were refueled by adding volatile fuel on top of a hot char bed.<sup>157,162</sup> Emissions associated with refueling are important because real-world users have been found to refuel TLUDs in this manner.<sup>71</sup>

Given the promising yet variable nature of TLUD performance, questions remain as to what must be done, in terms of cookstove design and dissemination, to achieve the consistently low emissions required<sup>52</sup> to meet targets for household air pollution reduction.<sup>21,26</sup> Accordingly, the objectives of the study presented in this chapter were to characterize how stove design parameters and fuel properties, as well as refueling and transition to char burnout, affect TLUD operation and performance.

This study expands upon previous work in which the effects of fuel type,<sup>62,157,159</sup> fuel moisture content,<sup>68,163</sup> fuel particle size,<sup>159,163-165</sup> primary air flow rate,<sup>72,158,160,161</sup> ratio of secondary to primary air flow,<sup>62,72,160</sup> secondary air inlet area,<sup>62,166</sup> chimney sections,<sup>165</sup> and operating mode<sup>67,159</sup> on gasifier cookstove performance were investigated experimentally. A comprehensive evaluation of performance, including measurements of CO and PM<sub>2.5</sub> emis-

---

<sup>3</sup>This chapter is based on material that has been submitted as a journal article: Tryner, J; Tillotson, J. W.; Baumgardner, M. E.; Mohr, J. T.; DeFoort, M. W.; Marchese, A. J. The effects of air flow rates, secondary air inlet geometry, fuel type, and operating mode on the performance of semi-gasifier cookstoves. My contributions to this publication included performing the experiments (in conjunction with James Tillotson), analyzing the data (also in conjunction with James Tillotson), creating the figures, and writing the manuscript. The text has been edited to avoid repeating information that has already been presented Chapters 1 and 2 of this dissertation. Most notably, the Introduction section has been shortened substantially. The Methods and Results and Discussion sections have been expanded to incorporate material that appeared in the Supporting Information accompanying the journal article into the main text.

sions, useful power output, producer gas composition, and fuel bed temperatures, was completed. As noted in previous studies, existing test protocols such as the Water Boiling Test<sup>30</sup> (WBT) are not well suited for batch-fed cookstove designs<sup>167</sup> and may fail to capture the range of operating modes and emission rates observed in the field.<sup>67,71</sup> Consequently, a new test procedure was developed to evaluate the range of performance that can be observed with batch-fed TLUDs in various modes of operation including refueling and transition to char burnout.

## 4.2 Methods

A description of the test bed used to vary cookstove design parameters is provided below, followed by descriptions of the test matrices, the test procedure used to evaluate performance, and the equations used to calculate emissions, useful power output, fuel consumption rate, fuel gas production rate, and global equivalence ratio in the secondary combustion zone.

### 4.2.1 Modular Test Bed

The modular TLUD test bed, shown in Figures 4.1 and 4.2, is similar to those used in previous studies.<sup>72,158,159</sup> The baseline geometry was designed to be similar to the Philips HD4012 stove (a high-performing<sup>75</sup> commercially-available gasifier cookstove) and to accommodate the modifications necessary for data collection. The test bed was constructed from Schedule 10 stainless steel pipe and 11 Ga. and 16 Ga. stainless steel sheet metal. Primary and secondary air flows were driven by compressed air, which was regulated to 276 kPa, and flow rates were controlled using rotameters. Secondary air was preheated by two electric heaters connected to PID controllers to mimic the preheating that typically occurs as air flows up along the outer walls of the combustion chamber to reach the secondary combustion zone (see Figure 1.3). These features allowed the primary air flow rate, secondary air flow rate, and secondary air temperature to be set to known values so that: (1) the influence of these parameters on performance could be investigated and (2) the influence of other design parameters could be investigated independently of the air flow rates.

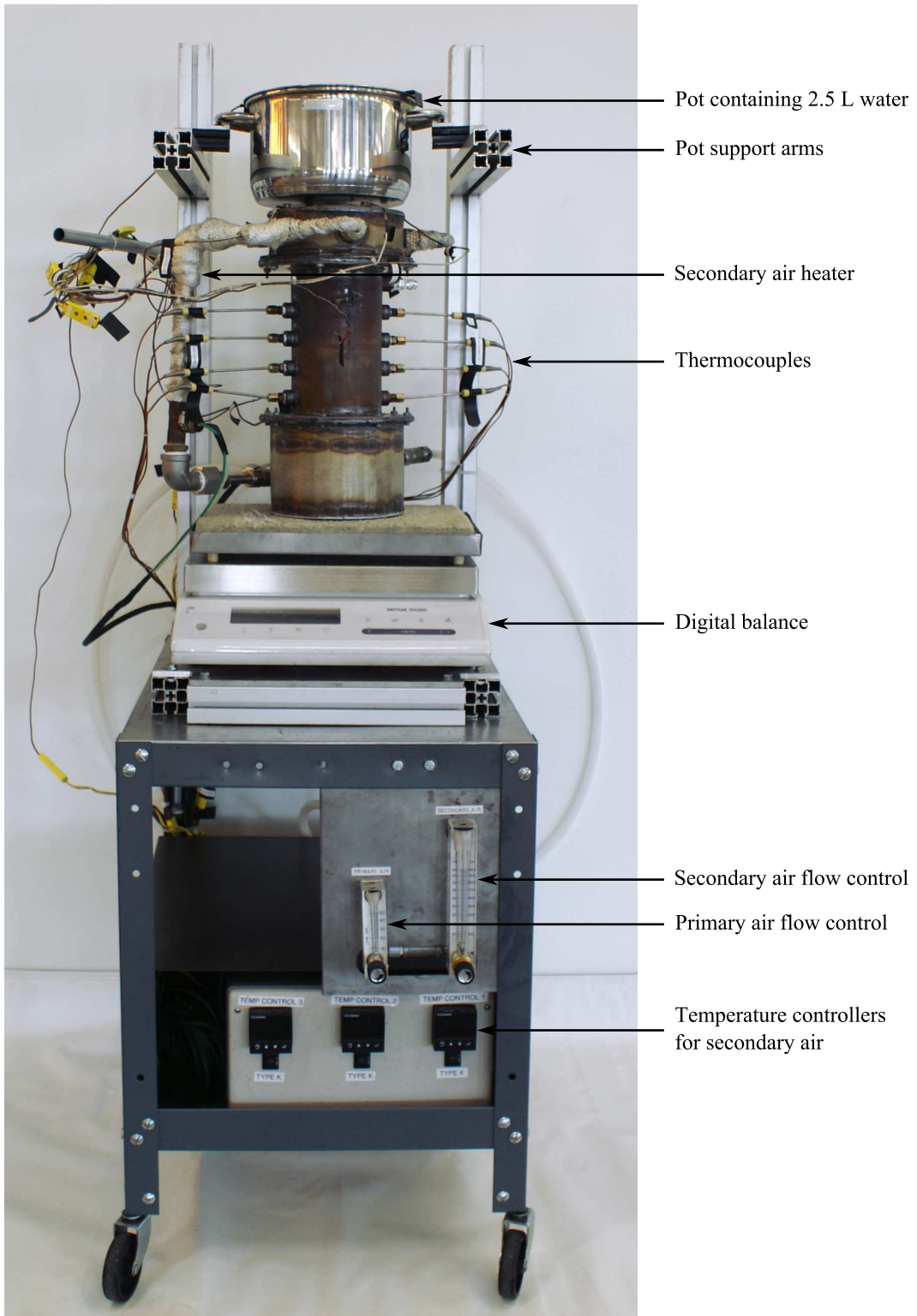
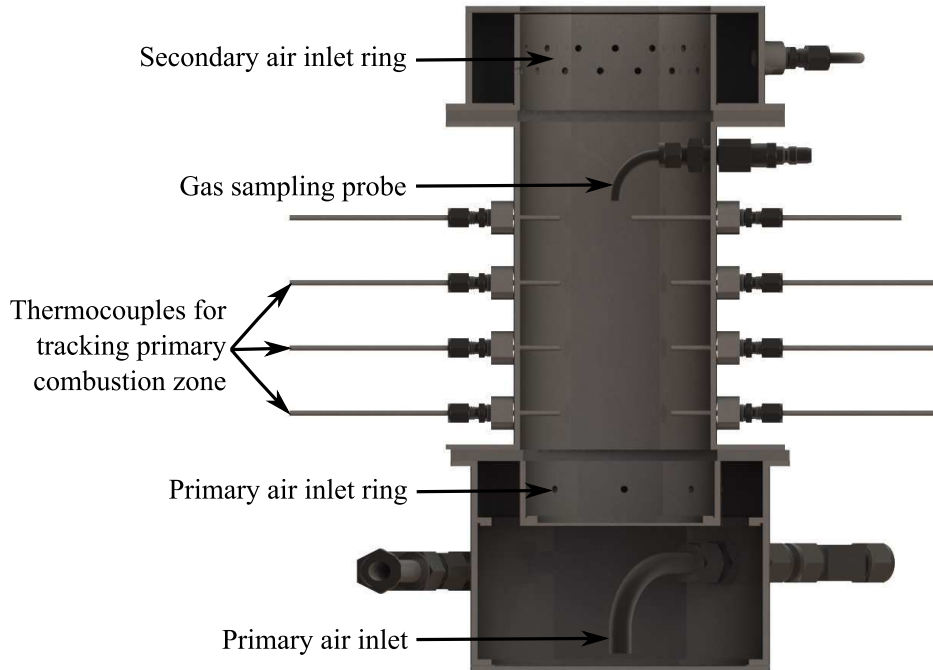


Figure 4.1: A photograph of the modular TLUD test bed with key features labeled.



**Figure 4.2: A cross-sectional view of the modular TLUD test bed with key features labeled.**

The ring through which secondary air entered the combustion chamber was designed to be removable to facilitate variation of the inlet geometry. Secondary air inlets that featured 32 holes ranging from 2 to 10 mm in diameter were tested (see Figure 4.3). Inlets that featured 4-mm-diameter holes positioned at various angles to induce swirl in the horizontal plane or direct the secondary air down towards the fuel bed were also tested (see Figure 4.3). During relevant experiments, the arms that supported the pot were adjusted to change the distance between the top of the test bed and the pot, constrictions intended to recirculate gases inside the stove were inserted before and after the secondary air inlet (see Figure 4.4), and an insulated chimney with a diameter of 108 mm and a height of 100 mm<sup>168</sup> was installed downstream of the secondary air inlet. Another assembly allowed 10% of the secondary air to be injected earlier in the fuel chamber through six 2-mm-diameter holes spaced equally around the circumference (see Figure 4.5).



Figure 4.3: Photographs of the secondary air inlets tested in this study.

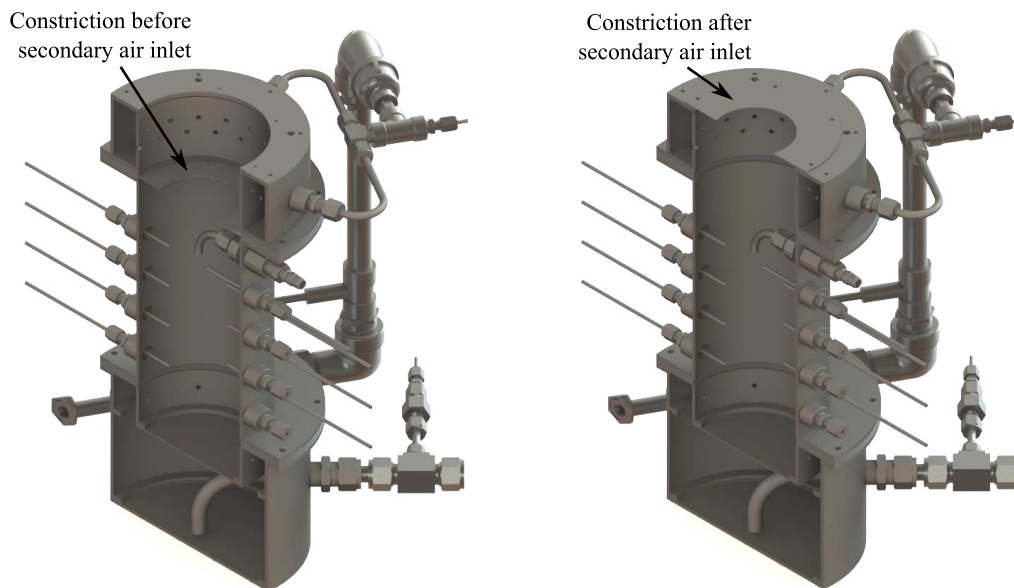
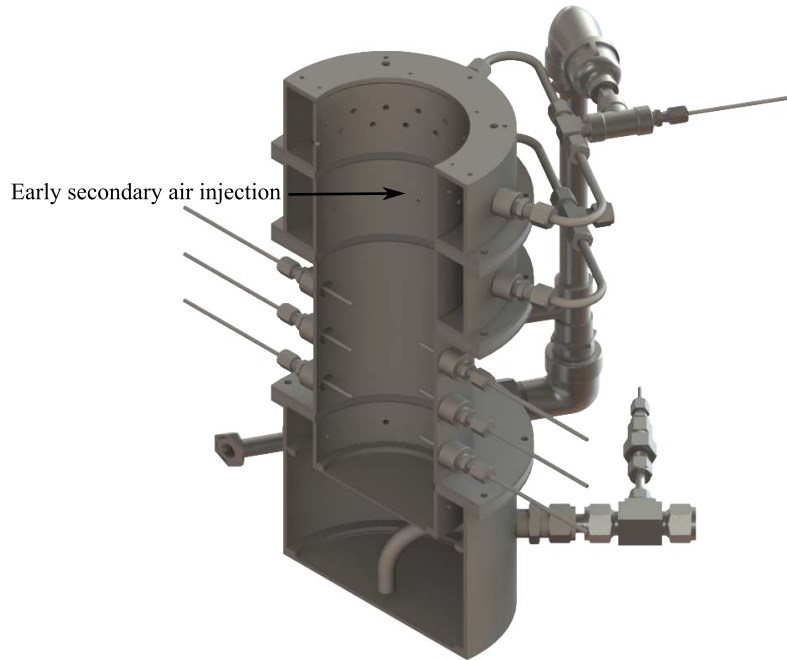


Figure 4.4: Cross sectional renderings of the test bed with constrictions inserted before (left) and after (right) the secondary air inlet.



**Figure 4.5:** A cross-sectional rendering of the test bed configuration that allowed 10% of the secondary air to be injected earlier in the fuel chamber through six 2-mm-diameter holes spaced equally around the circumference.

The test bed was mounted on a digital balance that recorded the mass of the system at a rate of 1 Hz. Thermocouples installed along the height of the fuel chamber tracked the progression of the primary combustion zone. Gas entering the secondary combustion zone was sampled for compositional analysis via a probe installed between the fuel bed and the secondary air inlet. Several additional thermocouples were installed throughout the test bed, and temperature data from all thermocouples were logged at 1 Hz. For information on the thermocouples used and their locations see Table B.1 and Figure B.1 in Appendix B.

#### 4.2.2 Test Matrix

Experiments were conducted using the two test matrices shown in Table 4.1. For each test, one parameter was varied and all others were held constant at the default values shown in bold. Together, the parameters shown in bold represent the “baseline” test case. The default secondary air hole diameter of 4 mm was selected because it was similar to the diameter of the secondary air holes on the Philips HD4012<sup>70,75,169</sup> and Philips HD4008<sup>75,157,169</sup> stoves.

The total secondary air inlet area for the baseline case was approximately 400 mm<sup>2</sup>. Several commercially-available fan-powered gasifier stoves, including the Philips HD4010,<sup>73</sup> Philips HD4012, and BioLite CampStove,<sup>70,169,170</sup> have similar secondary air inlet areas. Default secondary air swirl and downward angles of 0° were selected for simplicity. The default case did not include any constrictions or other features for the same reason. A default pot gap of 15 mm was selected because pot gaps of less than 20 mm are often used on rocket-elbow cookstoves and smaller gaps are expected to improve heat transfer to the pot. Larger pot gaps (30 and 45 mm) were also tested because several commercially-available gasifier cookstoves have pot gaps in this range.

Douglas fir (*Pseudotsuga menziesii*) wood chips were used as the default fuel because they resulted in shorter test times and higher emissions than the wood pellet fuel. As a result of the shorter test time, the number of test cases that could be evaluated increased. As a result of the higher emissions, variations in emissions between test cases were easier to identify. The default fuel moisture content (7% by mass on a wet basis) was the moisture content of the fuels stored in the open-air in the laboratory.

The default primary air flow rate of 25 g·min<sup>-1</sup> was selected to consume a fuel bed filled with Lodgepole pine pellets in 60 minutes assuming an equivalence ratio of 4 for the gasification process.<sup>124</sup> The 60 minute time to consume the fuel bed was identical to the time selected by Mukunda et al.<sup>62</sup> during the design of the Oorja-Plus gasifier cookstove. A default secondary to primary air flow ratio of three was selected because this ratio makes the overall combustion process stoichiometric when an equivalence ratio of 4 is assumed for the gasification process. A secondary to primary air flow ratio of three was also used by Mukunda et al.<sup>62</sup> and Reed et al.<sup>72</sup>. A default secondary air temperature of 200 °C was deemed reasonable based on temperature measurements of preheated secondary air flows made in commercially-available gasifier cookstoves.<sup>157,166</sup>

**Table 4.1: The two test matrices for which experiments were completed. Baseline configuration data are indicated in bold.**

Matrix 1 — Secondary air delivery parameters			
Parameter	Values tested	Parameter	Values tested
Secondary to primary air flow ratio	2 <b>3</b> 4 5	Secondary air opening	<b>4-mm-dia. holes</b> 6-mm-dia. holes 8-mm-dia. holes 10-mm-dia. holes
Secondary air swirl angle	<b>0°</b> 15° 30° 45°	Secondary air downward angle	<b>0°</b> 10° 20° 30°
Pot gap	<b>15 mm</b> 30 mm 45 mm	Constriction location	<b>None</b> Before secondary air inlet, 2.50:4.25 ratio After secondary air inlet, 2.50:4.25 ratio
Secondary air temperature	100 °C 150 °C <b>200 °C</b> 250 °C 300 °C		
Matrix 2 Primary air flow rates, fuel properties, and secondary air delivery parameters			
Parameter	Values tested	Parameter	Values tested
Primary air flow rate (g·min <sup>-1</sup> )	15 20 <b>25</b> 30	Fuel moisture content (weight % on wet basis)	0 <b>7</b> 15 25
Fuel type	<i>Corn cob chips</i> Eucalyptus chips <b>Douglas fir chips</b> Lodgepole pine pellets	Fuel bulk density (corn cobs) (kg·m <sup>-3</sup> )	<i>174</i> 137 126
Secondary air delivery parameters	<b>4-mm-dia. holes</b> 2-mm-dia. holes Insulated chimney Early secondary air injection		

For the first test matrix, CO emissions, useful power output, fuel consumption rate, and mass loss rate were measured while secondary air delivery parameters were varied. Douglas fir (*Pseudotsuga menziesii*) wood chips with a moisture content of 7% on a wet basis and a

bulk density of  $156 \text{ kg}\cdot\text{m}^{-3}$  (95% CI = 155–157) were used as the fuel and the primary air flow rate was set to  $25 \text{ g}\cdot\text{min}^{-1}$ .

For the second test matrix, CO and PM<sub>2.5</sub> emissions, useful power output, producer gas composition, fuel consumption rate, and mass loss rate were measured while primary air flow rate, fuel properties, and secondary air delivery parameters were varied. The secondary air delivery parameters tested were informed by the results from the first test matrix. The Douglas fir chips used as the default fuel had a bulk density of  $160 \text{ kg}\cdot\text{m}^{-3}$  (95% CI = 159–161) and were more uniform in size and shape than the chips used in the first matrix (see Figure 4.6). The “corn cob chips” and “ $174 \text{ kg}\cdot\text{m}^{-3}$  bulk density” cases shown in italics in Table 4.1 were identical. Primary air flow rates ranging from 15 to  $30 \text{ g}\cdot\text{min}^{-1}$  were tested. These air flow rates covered the range of the  $18 \text{ g}\cdot\text{min}^{-1}$  primary air flow rate for which the Oorja stove was designed<sup>62</sup> and the primary air flow rates ranging from 15 to  $25 \text{ g}\cdot\text{min}^{-1}$  that were tested in other studies utilizing a TLUD with metered air flow.<sup>158,159</sup>

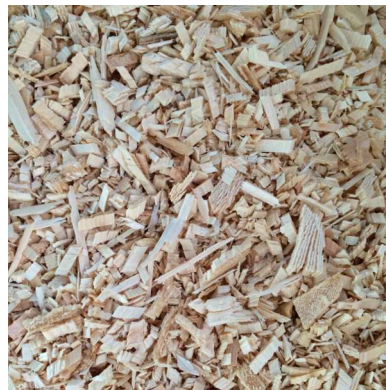
A list of the tests completed, and the value that each parameter was set to during each test, can be found in Tables B.2 and B.3 in Appendix B. Detailed fuel properties, including the results of proximate and ultimate analyses, biochemical compositions, heating values, densities, porosities, and moisture contents, are shown in Table 2.1. Bulk density was measured by placing the fuel in a cylindrical vessel with the same inner diameter as the test bed fuel chamber. The bulk density of the chipped corn cobs ( $174 \text{ kg}\cdot\text{m}^{-3}$ ) is shown in Table 2.1. The bulk densities of the whole and cut corn cobs were  $126 \text{ kg}\cdot\text{m}^{-3}$  and  $137 \text{ kg}\cdot\text{m}^{-3}$ , respectively.

The moisture contents shown in Table 2.1 were used in all calculations, except for in test cases in which the fuel moisture content was purposefully adjusted to a different value. Additional moisture content measurements were made in accordance with ASTM standard E871-82 (2013) for particulate wood fuels and are shown in Table 4.2. The standards for particulate wood fuels were selected because three of the four fuels (Douglas fir chips, Euca-

lyptus chips, and Lodgepole pine pellets) were particulate wood fuels. The same procedure was used to measure the moisture content of the corn cobs for consistency.



(a) Douglas fir chips used for Test Matrix 1



(b) Douglas fir chips used for Test Matrix 2



(c) Eucalyptus chips



(d) Lodgepole pine pellets



(e) Corn cobs - whole



(f) Corn cobs - cut



(g) Corn cobs - chips

**Figure 4.6: Photographs of the fuels used in the experiments.**

**Table 4.2: Results of additional fuel moisture content tests.**

Fuel	Moisture content (weight %, wet basis)				Number of replicates
	Nominal	Average	Minimum	Maximum	
Lodgepole pine pellets	7	7.15	6.89	7.74	4
Douglas fir chips	0	0.43	0.30	0.56	2
Douglas fir chips	7	8.25	8.24	8.26	2
Douglas fir chips	15	15.55	15.02	16.07	2
Douglas fir chips	25	25.09			1
Eucalyptus chips	7	7.30			1
Corn cob chips	7	6.80	6.67	6.93	2
All fuels stored in open air in laboratory	7	7.30	6.67	8.26	10

### 4.2.3 Test Procedure

The test procedure that was developed to capture three characteristic operating modes (normal, post-refueling, and char burnout) is represented graphically in Figure 4.7. During the first phase (normal operation), the test bed started at room temperature and the fuel chamber was filled with 1.5 L of biomass. To ignite the fuel bed, 50 mL of biomass was wetted with 2 mL of kerosene, placed on top of the fuel bed, and lit with a match. A stainless steel pot containing 2.5 L of water at  $15 \pm 2$  °C was placed on the pot support, and emissions were measured while the water in the pot was heated to 90 °C. This volume of water (2.5 L) was selected to ensure that a pot of water could be boiled using the lower bulk density fuels. This phase was similar to the cold start phase of the WBT<sup>30</sup> and Emissions and Performance Test Protocol.<sup>148,150</sup> As shown in previous studies<sup>71,157</sup> and the results below, the emissions measured during this phase represented the best-case scenario for high-power performance.

When the water temperature reached 90 °C and the first phase ended, the pot of water was removed and the test bed was allowed to operate normally until the secondary flame extinguished. The latter event signaled that the first batch of fuel had been consumed. For the second phase (refueling), 1.0 L of biomass fuel was added to the fuel chamber on top of the hot char bed left behind by the first batch of fuel. The test bed was re-lit using 50 mL of

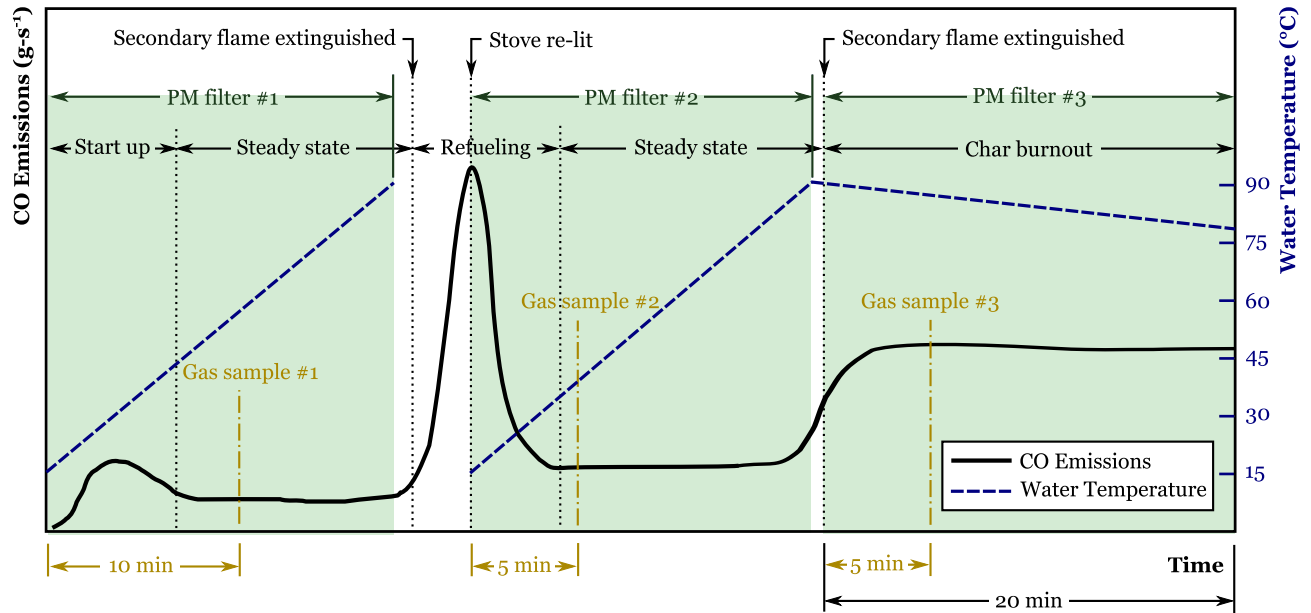


**Figure 4.7: Plot of typical CO emissions ( $\text{g}\cdot\text{s}^{-1}$ ) and water temperature ( $^{\circ}\text{C}$ ) as a function of time for the three phase test procedure (normal operation, post-refueling, and char burnout).**

biomass wetted with 2 mL of kerosene. Emissions and power-output measurements resumed when a pot containing 2.5 L of water at  $15 \pm 2$   $^{\circ}\text{C}$  was placed on the pot support and continued until the water temperature reached 90  $^{\circ}\text{C}$  or the secondary flame extinguished. As shown in previous studies<sup>71,157</sup> and the results below, emissions measured during this phase typically represented the worst-case scenario for high-power performance.

The third phase started when the secondary flame extinguished. During this phase, the pot of water was left on the pot support and the remaining char from the two fuel batches was allowed to burn while emissions were measured for 20 minutes. The producer gas entering the secondary combustion zone was sampled for approximately 30-60 seconds starting at ten minutes after the start of Phase 1, five minutes after the start of Phase 2, and five minutes after the start of Phase 3.

During the tests with Lodgepole pine pellet fuel, two modifications were made to Phases 1 and 2 of the procedure: (1) 2.5 L of water was boiled twice (i.e., a total of 5 L of water was boiled using two identical pots) and (2) the producer gas was sampled 30 minutes after

the start of Phase 1 and 15 minutes after the start of Phase 2. A diagram that illustrates these modifications is shown in Figure 4.8. The modifications were necessary to capture the same steady-state operation that was captured in the tests with the lower bulk density fuels using the higher bulk density pellet fuel.

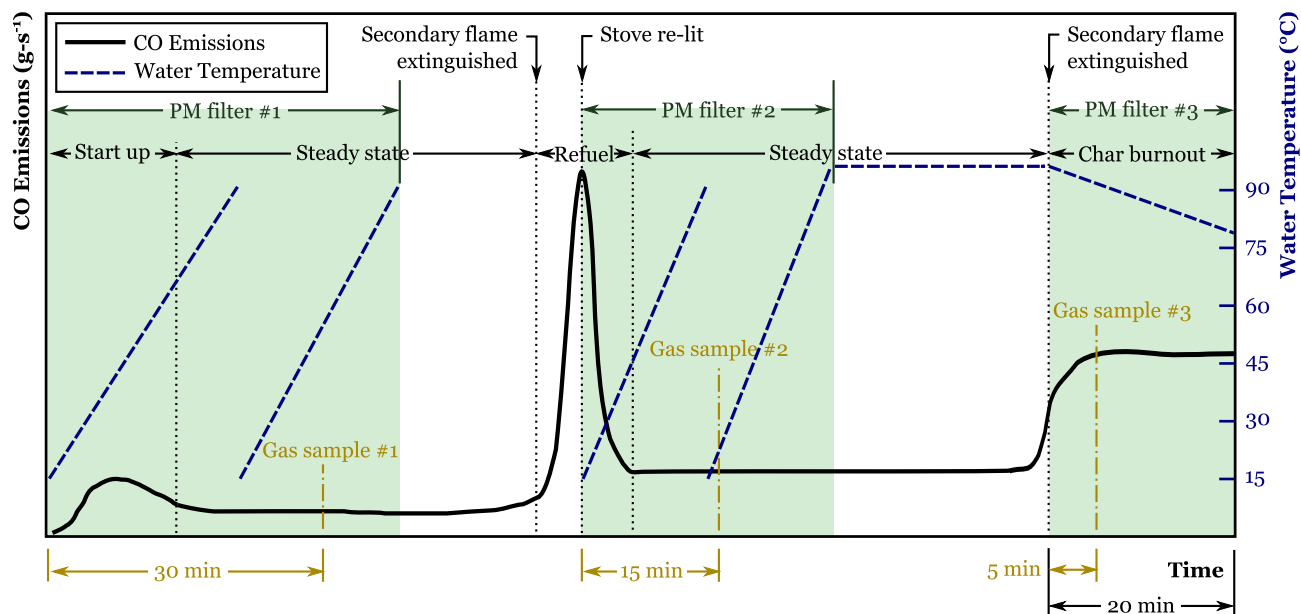


**Figure 4.8:** A diagram illustrating the modifications that were made to the test procedure for the tests with the Lodgepole pine pellets.

The longer burn time associated with a fuel bed of Lodgepole pine pellets (60 minutes) in comparison to the lower bulk density fuels (20 minutes) allowed for 5 L of water to be boiled in accordance with a typical WBT<sup>30</sup> or EPTP.<sup>148</sup> Five liters of water were boiled by boiling 2.5 L of water twice so that the same pot was used for all of the tests. The first pot was removed once the water temperature reached 90 °C and a second, identical pot containing 2.5 L of water at  $15 \pm 2$  °C was immediately placed on the stove. Because the start-up time was longer with the Lodgepole pine wood pellets, boiling 2.5 L of water twice and sampling emissions for a longer period of time allowed a larger fraction of Phase 1 to represent steady-state operation.

The total burn time of a bed of Douglas fir chips, as well as the other low bulk density fuels, was approximately 20 minutes and the producer gas sample was collected 10 minutes

after the stove was lit. The total burn time of a bed of Lodgepole pine wood pellets was 60 minutes, so the producer gas sample was collected 30 minutes after the stove was lit for consistency. During Phase 2 of the tests with the lower bulk density fuel, the producer gas sample was collected 5 minutes after the stove was re-lit and this represented half of the delay between the start of Phase 1 and the Phase 1 producer gas sampling time. During Phase 2 of the tests with the Lodgepole pine wood pellets, the producer gas sample was collected 15 minutes after the stove was re-lit and this also represented half of the delay between the start of Phase 1 and the Phase 1 producer gas sampling time.

The ending temperature of the water for the two high-power phases and the fire starting fuel were derived from the Emissions and Performance Test Protocol (EPTP)<sup>148</sup> developed at Colorado State University. The EPTP is a modified version of the Water Boiling Test (WBT) and was designed to improve repeatability between test replicates.<sup>150</sup> In the EPTP, the cold- and hot-start phases both end when the water temperature has reached 90 °C.<sup>148</sup> A lighting technique was desired that would: (1) be consistent with existing laboratory test procedures and (2) would result in the stove starting quickly and reliably to minimize variability between replicates. Kerosene is specified as the fire starting fuel for charcoal cookstoves in the EPTP.<sup>148</sup> For consistency, kerosene was also chosen as the fire starting fuel for these tests with batch-fed gasifier cookstoves.

Experiments were conducted in a fume hood with a 1.2 m × 1.2 m footprint and a height of 4.3 m. The walls of the fume hood extended to the floor. The flow rate through the hood was constant at 0.1 m<sup>3</sup>·s<sup>-1</sup>. Carbon monoxide concentrations and PM<sub>2.5</sub> were sampled from a 12.7-cm-diameter exhaust pipe at the top of the hood. Concentrations of CO and CO<sub>2</sub> in the fume hood exhaust were measured at 1 Hz using non-dispersive infrared gas analyzers (ULTRAMAT 6, Siemens AG). The instruments used to collect data during each test, the rates at which real-time data were logged, and the data logging software used to record real-time data are listed in Table B.5 in Appendix B.

The flow through the hood and sampling duct was maintained by a Roots blower and the flow rate was verified using a carbon mass balance. The calibration was performed by subliming a known mass of dry ice inside of the hood and recording the concentration of CO<sub>2</sub> in the exhaust vs. time at 1 Hz using the NDIR analyzer. The CO<sub>2</sub> concentration vs. time was corrected for background and converted to a mass flow rate of CO<sub>2</sub> using the assumed volumetric flow rate (0.1 m<sup>3</sup>·s<sup>-1</sup>) along with the temperature and pressure measured in the exhaust line. The mass flow rate of CO<sub>2</sub> was integrated over time to obtain the total mass of CO<sub>2</sub> that passed through the exhaust, and this mass was checked against the initial mass of dry ice.

Particulate matter emissions were measured gravimetrically. Exhaust gas was sampled isokinetically and passed through a 2.5 μm cyclone (URG-2000-30EHS, URG Corporation). Flow through the sampling system was driven by two diaphragm pumps (DOA-P707-FB, Gast Manufacturing, Inc.) and metered by a mass flow controller (MCPH-50SLPM-D-30PSIA, Alicat Scientific Inc.). The volumetric flow rate was verified using a soap bubble flow meter. Particulate matter was collected on 47-mm-diameter PTFE filters (7592-104, Whatman) and filters were pre- and post-weighed on a balance with 1 μg readability (MX5, Mettler-Toledo Inc.). The limit of detection (LOD) and limit of quantification (LOQ) for these measurements were 10 μg and 29 μg, respectively. The LOD and LOQ were calculated based on the change in mass of 56 filter blanks. All but three samples (one 27 μg sample and two 28 μg samples) were above the LOQ.

Producer gas samples passed through an ice bath, desiccant column, and 2-μm filter to remove tars, moisture, and particulates. Samples were collected in 1-liter sample bags (FlexFoil®PLUS, SKC Inc.) for approximately 30-60 seconds until the sample bag was full. Samples were analyzed at Empact Analytical Systems Inc. in Brighton, CO, USA, using a gas chromatograph with a thermal conductivity detector, in accordance with ASTM D1945. Concentrations of He, H<sub>2</sub>, O<sub>2</sub>/Ar, N<sub>2</sub>, CO, CO<sub>2</sub>, CH<sub>4</sub>, as well as C<sub>2</sub>, C<sub>3</sub>, C<sub>4</sub>, C<sub>5</sub>, and C<sub>6</sub>+ hydrocarbons were reported.

The number of replicates collected for each data point is listed in Table B.4. A recent study suggests that 10 or more replicate tests may be necessary for the width of the confidence intervals on PM<sub>2.5</sub> emissions measurements to asymptote to a constant value.<sup>171</sup> In this study, 3-4 replicates were collected for most data points to allow a large number of cases to be screened and 90% confidence intervals were calculated for the results.

#### 4.2.4 Calculations

The mass of carbon monoxide emitted per megajoule of energy delivered to the cooking surface during high-power operation (Phases 1 and 2) was calculated using Equation 4.1:

$$CO_{high} = \frac{\int_0^t X_{CO} (M_{CO}/M_{air}) \dot{V} \rho_{air} dt}{m_{H_2O,i} C_{H_2O} (T_f - T_i) + h_{fg,H_2O} (m_{H_2O,f} - m_{H_2O,i})} \quad (4.1)$$

where  $X_{CO}$  was the mole fraction of CO in the fume hood exhaust,  $M_{CO}$  was the molecular weight of CO (28.01 kg·kmol<sup>-1</sup>),  $M_{air}$  was the molecular weight of air (28.97 kg·kmol<sup>-1</sup>),  $\dot{V}$  was the volumetric flow rate through the fume hood in m<sup>3</sup>·s<sup>-1</sup>,  $\rho_{air}$  was the density of air in kg·m<sup>-3</sup>,  $m_{H_2O,i}$  and  $m_{H_2O,f}$  were the masses of the water in the pot at the start and end of the test phase, respectively, in kg,  $C_{H_2O}$  was the specific heat of water (4179 J·kg<sup>-1</sup>·K<sup>-1</sup>),  $T_f$  was the temperature of the water in the pot at the end of the test phase in °C,  $T_i$  was the temperature of the water at the start of the phase in °C, and  $h_{fg,H_2O}$  was the heat of vaporization of water (2257 J·kg<sup>-1</sup>).

The mass of particulate matter emitted per megajoule delivered to the cooking surface during high-power operation (Phases 1 and 2) was calculated using Equation 4.2:

$$PM_{2.5,high} = \frac{m_{filter} (A_{probe}/A_{duct})}{m_{H_2O,i} C_{H_2O} (T_f - T_i) + h_{fg,H_2O} (m_{H_2O,f} - m_{H_2O,i})} \quad (4.2)$$

where  $m_{filter}$  was the mass of PM<sub>2.5</sub> accumulated on the filter in mg, and  $A_{probe}$  and  $A_{duct}$  were the cross-sectional areas of the sampling probe and fume hood exhaust duct, respectively, in m<sup>2</sup>.

Phase 3 carbon monoxide emissions were calculated using Equation 4.3:

$$CO_{P3} = \frac{\int_0^{t_3} X_{CO} (M_{CO}/M_{air}) \dot{V} \rho_{air} dt}{t_3} \quad (4.3)$$

where  $t_3$  was the duration of the third phase.

Phase 3 particulate matter emissions were calculated using Equation 4.4:

$$PM_{2.5,P3} = \frac{m_{filter} (A_{probe}/A_{duct})}{t_3} \quad (4.4)$$

Note that Equations 4.2 and 4.4 assume isokinetic sampling. As discussed in Section 4.2.3, the volumetric flow rate through the PM sampling probe was maintained using a mass flow controller and verified using a soap bubble flow meter.

The average useful power outputs and dry fuel consumption rates for Phases 1 and 2 were calculated using equations similar to those used by Huangfu et al.<sup>68</sup>. Average useful power output was calculated using Equation 4.5:

$$P_{useful} = \frac{m_{H_2O,i} c_{H_2O} (T_f - T_i) + h_{fg,H_2O} (m_{H_2O,i} - m_{H_2O,f})}{t_f - t_i} \quad (4.5)$$

where  $m_{H_2O,i}$  and  $m_{H_2O,f}$  were the masses of the water in the pot at the start and end of the phase, respectively, in g,  $c_{H_2O}$  was the specific heat of water in  $J \cdot g^{-1} \cdot K^{-1}$ ,  $T_f$  was the temperature of the water in the pot at the end of the phase in  $^{\circ}C$ ,  $T_i$  was the temperature of the water at the start of the phase in  $^{\circ}C$ ,  $h_{fg,H_2O}$  was the heat of vaporization of water in  $J \cdot g^{-1}$ ,  $t_f$  was the time at which the water in the pot reached  $T_f$ , in s, and  $t_i$  was the time at which the pot of water was placed on the stove in s.

The average rate of dry solid biomass fuel consumption was calculated using Equation 4.6:

$$\dot{m}_{dry\ solid\ fuel} = \frac{m_{solid\ fuel} (1 - MC_{fuel})}{t_e - t_i} \quad (4.6)$$

where  $m_{solid\ fuel}$  was the mass of fuel added to the stove at the start of the phase in g,  $MC_{fuel}$  was the moisture content of the fuel as weight % on a wet basis,  $t_i$  was the time at which the stove was lit in s, and  $t_e$  was the time at which the secondary flame extinguished

at the end of the phase in s. The solid fuel consumption rate was calculated as shown in Equation 4.6, and not simply set equal to the mass loss rate recorded by the digital balance ( $\frac{dm}{dt}$ ), because some mass of solid char was left behind after the biomass had devolatilized. In this manner, the remaining char was treated as a product of the gasification process.

The mass flow rate of producer gas entering the secondary combustion zone was calculated by applying the conservation of mass to a control volume drawn around the fuel/char bed:

$$\frac{dm}{dt} = \dot{m}_{primary\ air} - \dot{m}_{fuel\ gas} \quad (4.7)$$

where  $\frac{dm}{dt}$  was the rate of change of the mass of the fuel/char bed recorded by the digital balance in  $\text{g}\cdot\text{min}^{-1}$ ,  $\dot{m}_{primary\ air}$  was the primary air flow rate in  $\text{g}\cdot\text{min}^{-1}$ , and  $\dot{m}_{fuel\ gas}$  was the mass flow rate of gas leaving the fuel bed and entering the secondary combustion zone in  $\text{g}\cdot\text{min}^{-1}$ .

The stoichiometric air-to-fuel ratio in the secondary combustion zone was calculated from the gas composition and fuel gas flow rate using Equation 4.8:

$$(\dot{m}_{air}/\dot{m}_{fuel})_{stoic} = \frac{M_{air}}{M_{gas}} \times 4.76 \times \left( \frac{1}{2}x_{CO} + \frac{1}{2}x_{H_2} + 2x_{CH_4} + \frac{7}{2}x_{C_2} + 5x_{C_3} \right) \quad (4.8)$$

where  $M_{air}$  and  $M_{gas}$  were the molecular weights of air and the fuel gas, respectively, in  $\text{g}\cdot\text{mol}^{-1}$ , and  $x$  was the mole fraction of each component in the fuel gas. Mole fractions of hydrocarbons larger than  $C_3$  were negligible. The small concentration of  $O_2$  in the gas samples was neglected.

Global equivalence ratios in the fuel bed and secondary combustion zone were calculated using Equation 4.9:

$$\phi = \frac{(\dot{m}_{air}/\dot{m}_{fuel})_{stoic}}{(\dot{m}_{air}/\dot{m}_{fuel})} \quad (4.9)$$

where  $\dot{m}_{air}$  was the mass flow rate of primary or secondary air in  $\text{g}\cdot\text{min}^{-1}$  and  $\dot{m}_{fuel}$  was the fuel consumption rate calculated using Equation 4.6 or the fuel gas flow rate calculated using Equation 4.7 in  $\text{g}\cdot\text{min}^{-1}$ .

### 4.3 Results and Discussion

A complete set of experimental results is provided in Appendix B. The variability in the CO emissions, useful power output, fuel consumption rate, and mass loss rate measurements (as measured by the coefficient of variation,  $\hat{C}_v$ , for each data point for which  $N \geq 3$ ) was lower for the second test matrix. The reduced variability was attributed to the use of more uniform wood chips that allowed for more reliable operation of the test bed. The producer gas entering the secondary combustion zone consisted primarily of H<sub>2</sub>, CO, CH<sub>4</sub>, CO<sub>2</sub>, and N<sub>2</sub>, and the mole fraction of hydrocarbons larger than CH<sub>4</sub> was less than 2% in all samples.

#### 4.3.1 Effects of Air Flow Rates, Fuel Moisture, and Secondary Air Delivery Parameters

Useful power output and average dry fuel consumption rate increased linearly ( $r^2 \geq 0.99$ ) with primary air flow for the range of flow rates tested (see Figure 4.9). The global equivalence ratio in the fuel bed remained between 3 and 5 when the primary air flow rate was varied, and the fuel consumption rate increased linearly with primary air flow rate (see Figure 4.9). For Matrix 2 tests conducted with the default primary air flow, the average global equivalence ratio in the fuel bed remained between 3 and 4 for 58% of Phase 1 data points and 75% of Phase 2 data points (see Figures B.17–B.19). The producer gas composition during Phase 1 was not affected by primary air flow rate (see Figure 4.11).

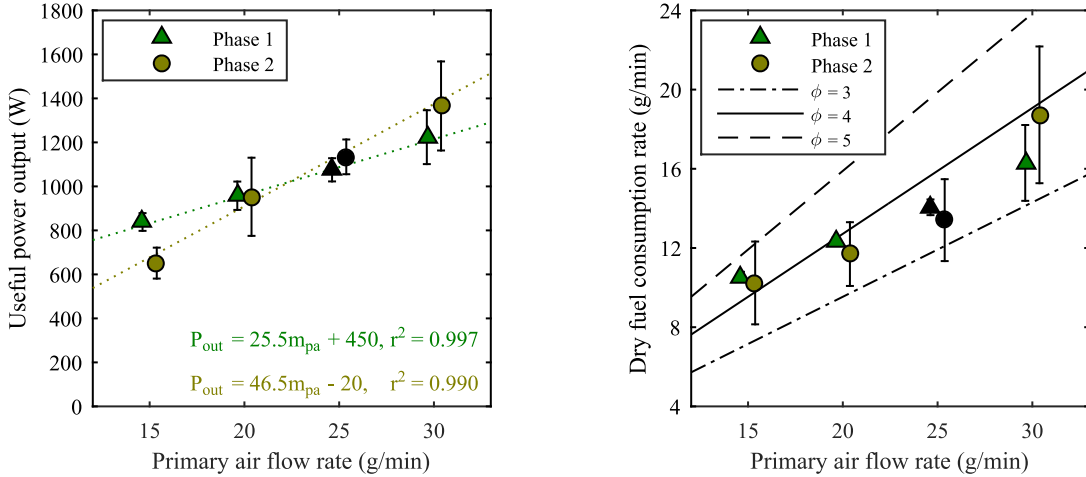


**Figure 4.9: Effects of primary air flow rate on average useful power output and dry fuel consumption rate during normal operation (Phase 1, green triangles) and post-refueling (Phase 2, gold circles). Black symbols refer to the baseline configuration (Douglas fir chip fuel, 7% moisture content, 25 g·min<sup>-1</sup> primary air, 75 g·min<sup>-1</sup> secondary air, 200 °C secondary air temperature, 4-mm-dia. secondary air holes, no swirl, no downward angle, 15 mm pot gap, no flow constriction, no other features). Error bars represent 90% confidence intervals. Data points have been offset slightly on either side of the values listed in Table 4.1 to improve the readability of the plot.**

The average high-power PM<sub>2.5</sub> emissions measured during normal operation remained between 21 mg·MJ<sub>d</sub><sup>-1</sup> and 42 mg·MJ<sub>d</sub><sup>-1</sup> when the primary air flow rate was varied (see Figure 4.10). The secondary flame was difficult to re-light after refueling when the primary air flow rate was low and, as a result, the variability in Phase 2 PM<sub>2.5</sub> emissions was high for the test cases with primary air flow rates of 15 g·min<sup>-1</sup> and 20 g·min<sup>-1</sup>. Higher primary air flow rates may have made the test bed easier to re-light after refueling by causing fuel gas production to resume more quickly. The concentration of CO in the producer gas samples taken during Phase 2 increased with primary air flow rate (see Figure 4.11). Phase 3 PM<sub>2.5</sub> emissions decreased with increasing primary air flow rate (see Figure B.23).

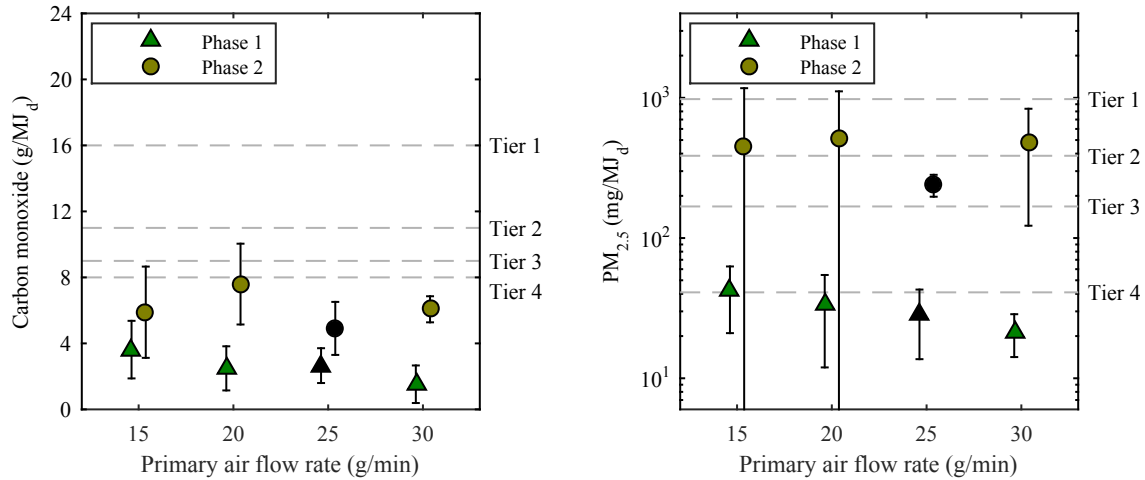


**Figure 4.10: Effects of primary air flow rate on average high-power CO and PM<sub>2.5</sub> emissions during normal operation (Phase 1, green triangles) and post-refueling (Phase 2, gold circles). Black symbols refer to the baseline configuration (Douglas fir chip fuel, 7% moisture content, 25 g·min<sup>-1</sup> primary air, 75 g·min<sup>-1</sup> secondary air, 200 °C secondary air temperature, 4-mm-dia. secondary air holes, no swirl, no downward angle, 15 mm pot gap, no flow constriction, no other features). Error bars represent 90% confidence intervals. Data points have been offset slightly on either side of the values listed in Table 4.1 to improve the readability of the plot.**

Useful power output and average dry fuel consumption rate decreased linearly ( $r^2 \geq 0.94$ ) with increasing fuel moisture content (see Figure 4.12). Comparison of the fuel consumption rate, useful power output, and emissions results suggests that fuel moisture content did not affect the combustion or heat transfer efficiencies of the stove. Huangfu et al.<sup>68</sup> observed similar results for pellet fuels with moisture contents in this range. Fuel moisture content did not affect CO or PM<sub>2.5</sub> emissions during normal operation (Phase 1), but Phase 2 (post-refueling) emissions increased with increasing moisture content (see Figure 4.13). In general, Phase 3 PM<sub>2.5</sub> emissions decreased with increasing fuel moisture content (see Figure B.23). Similar to the test cases with low primary air flow rates, the secondary combustion zone was difficult to re-light after refueling for higher moisture contents (15% and 25%), and relighting difficulties likely contributed to the higher Phase 2 emissions that were measured for the higher moisture content fuels. Higher moisture contents may have made the test bed difficult to re-light after refueling by preventing fuel gas production from resuming quickly.

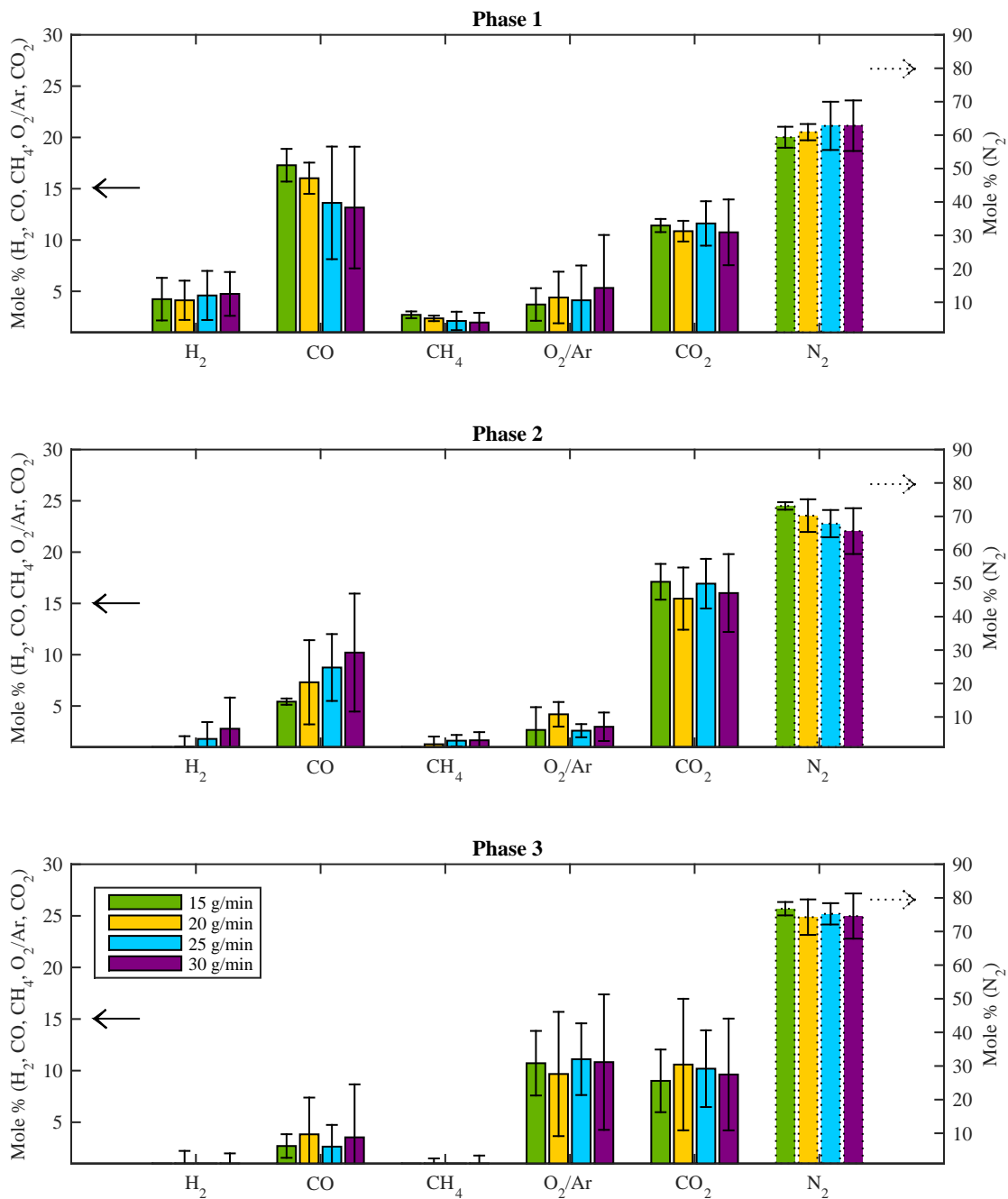
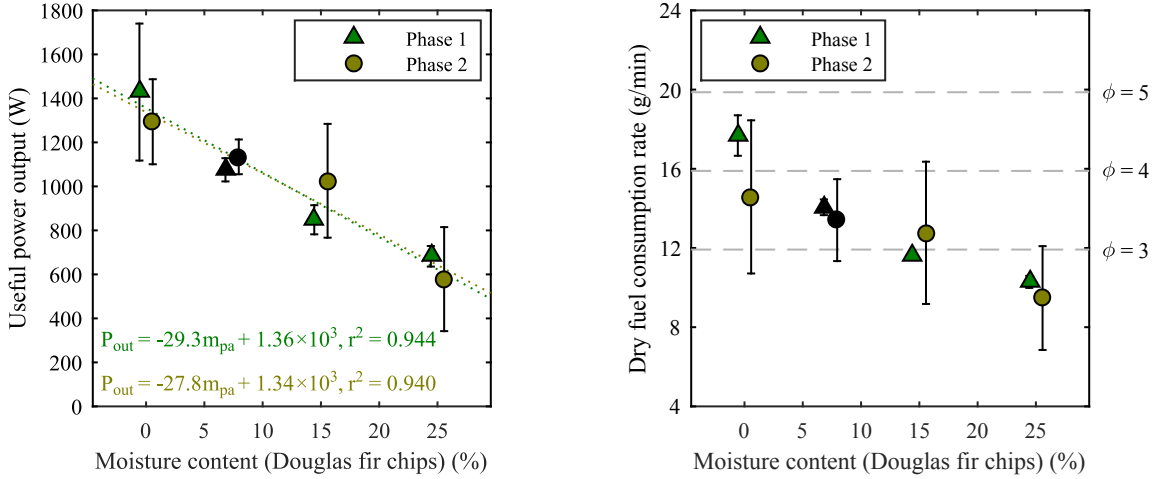
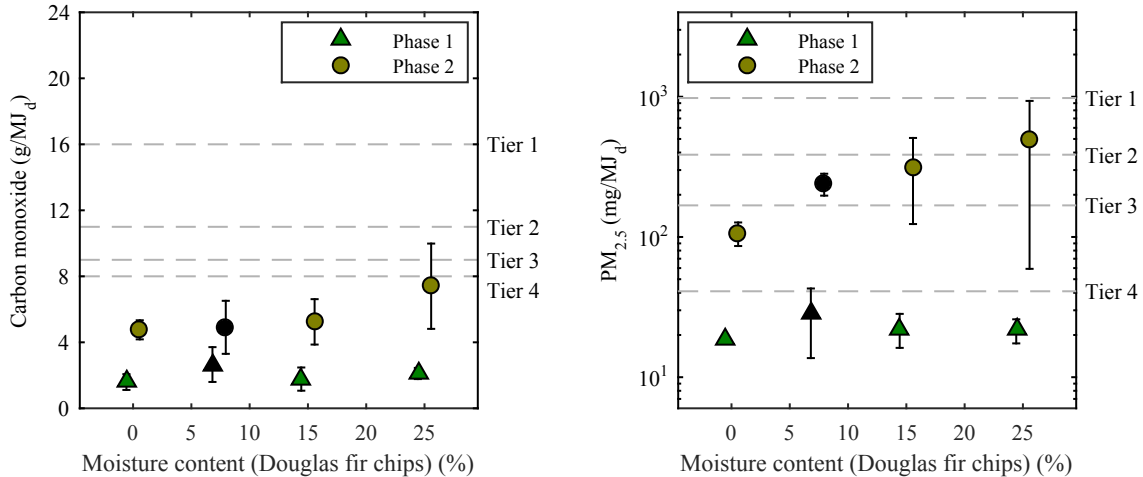


Figure 4.11: Effects of primary air flow rate on the average concentrations of H<sub>2</sub>, CO, CH<sub>4</sub>, O<sub>2</sub>/Ar, CO<sub>2</sub> and N<sub>2</sub> in the producer gas entering the secondary combustion zone during normal operation (Phase 1), post-refueling (Phase 2) and during char burnout (Phase 3). Error bars represent 90% confidence intervals.



**Figure 4.12: Effects of fuel moisture content on average useful power output and dry fuel consumption rate during normal operation (Phase 1, green triangles) and post-refueling (Phase 2, gold circles). Black symbols refer to the baseline configuration (Douglas fir chip fuel, 7% moisture content, 25 g·min<sup>-1</sup> primary air, 75 g·min<sup>-1</sup> secondary air, 200 °C secondary air temperature, 4-mm-dia. secondary air holes, no swirl, no downward angle, 15 mm pot gap, no flow constriction, no other features). Error bars represent 90% confidence intervals. Data points have been offset slightly on either side of the values listed in Table 4.1 to improve the readability of the plot.**



**Figure 4.13: Effects of fuel moisture content on average high-power CO and PM<sub>2.5</sub> emissions during normal operation (Phase 1, green triangles) and post-refueling (Phase 2, gold circles). Black symbols refer to the baseline configuration (Douglas fir chip fuel, 7% moisture content, 25 g·min<sup>-1</sup> primary air, 75 g·min<sup>-1</sup> secondary air, 200 °C secondary air temperature, 4-mm-dia. secondary air holes, no swirl, no downward angle, 15 mm pot gap, no flow constriction, no other features). Error bars represent 90% confidence intervals. Data points have been offset slightly on either side of the values listed in Table 4.1 to improve the readability of the plot.**

A minimum in high-power (Phase 1 and 2) CO emissions was observed for secondary to primary air flow ratios of 3:1 and 4:1 (see Figure 4.14). This result is in agreement with previous studies<sup>62,72</sup> that recommended a secondary to primary air flow ratio of approximately 3:1 for high-power operation. Higher secondary air velocities resulted in lower CO emissions (see Figure 4.14). These higher velocities most likely led to better mixing between the secondary air and the fuel gas. This result stands in contrast to previous work<sup>62</sup> in which CO emissions decreased with increasing secondary air inlet area; however, the total secondary air flow rate was not decoupled from the inlet area in that study.<sup>166</sup>

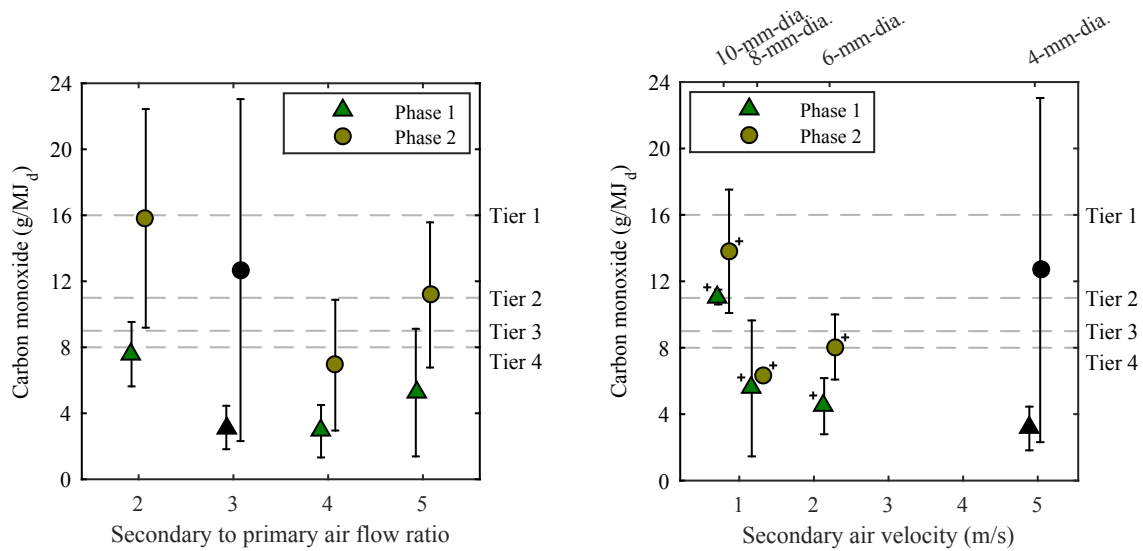


**Figure 4.14: Effects of secondary to primary air flow ratio and secondary air opening size (secondary air velocity) on average high-power CO emissions during normal operation (Phase 1, green triangles) and post-refueling (Phase 2, gold circles). Black symbols refer to the baseline configuration (Douglas fir chip fuel, 7% moisture content, 25 g·min<sup>-1</sup> primary air, 75 g·min<sup>-1</sup> secondary air, 200 °C secondary air temperature, 4-mm-dia. secondary air holes, no swirl, no downward angle, 15 mm pot gap, no flow constriction, no other features). Average values that were calculated from only two replicates are marked with a ‘+’. Error bars represent 90% confidence intervals for markers with no ‘+’ and the total range of the measurements for markers with a ‘+’. Data points have been offset slightly on either side of the values listed in Table 4.1 to improve the readability of the plot.**

Varying the other secondary air delivery parameters investigated in Matrix 1 did not improve performance compared to the baseline configuration. The 15° swirl angle had a negligible effect on emissions, and the 30° and 45° swirl angles resulted in higher Phase 1

CO emissions relative to the baseline case (see Figure 4.15). Photographs of the secondary combustion zone for the 15°, 30°, and 45° swirl test cases are shown in Figure 4.16. In the photograph of the 15° case, the secondary flames are attached to the air inlets and have a bluish color. In contrast, the flames are not attached, are much more luminous, and rise further out of the top of the stove in the 30° and 45° degree cases. The higher luminosity suggests that PM<sub>2.5</sub> emissions were also higher in these two cases. The larger swirl angles may have promoted soot formation by increasing the residence time in the fuel-rich zone. In addition, impingement of the flame on the cold cooking surface in the 30° and 45° swirl cases would be expected to quench the reactions that oxidize CO and PM.

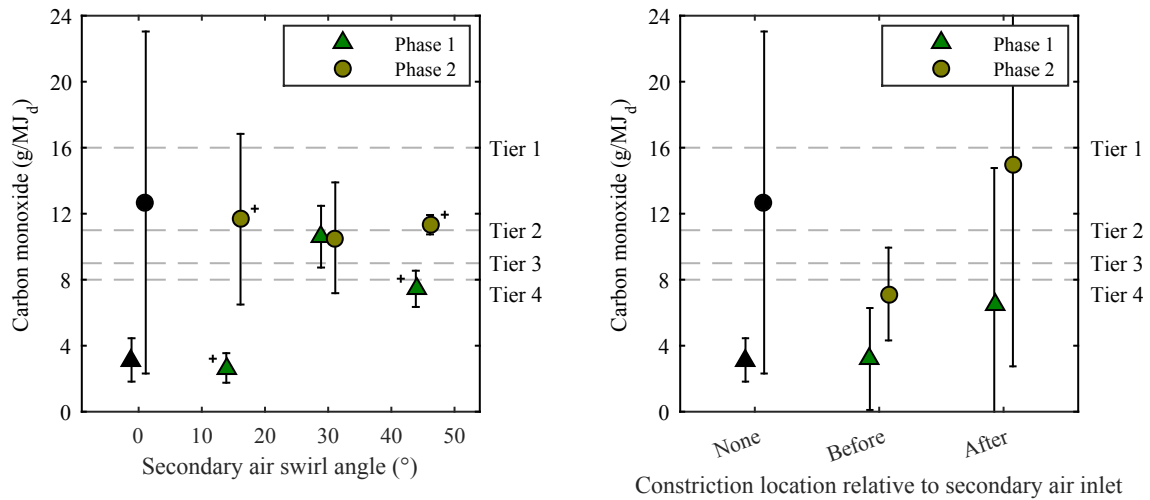


**Figure 4.15: Effects of secondary air swirl angle and constriction location on average high-power CO emissions during normal operation (Phase 1, green triangles) and post-refueling (Phase 2, gold circles). Black symbols refer to the baseline configuration (Douglas fir chip fuel, 7% moisture content, 25 g·min<sup>-1</sup> primary air, 75 g·min<sup>-1</sup> secondary air, 200 °C secondary air temperature, 4-mm-dia. secondary air holes, no swirl, no downward angle, 15 mm pot gap, no flow constriction, no other features). Average values that were calculated from only two replicates are marked with a '+'. Error bars represent 90% confidence intervals for markers with no '+' and the total range of the measurements for markers with a '+'. Data points have been offset slightly on either side of the values listed in Table 4.1 to improve the readability of the plot.**



(a) 15° swirl angle



(b) 30° swirl angle



(c) 45° swirl angle

**Figure 4.16:** Images of the secondary combustion zone during normal high-power operation (Phase 1) with varying degrees of swirl imposed at the secondary air inlet.

Both flow constriction locations (before and after the secondary air inlet) resulted in higher CO emissions and lower useful power outputs during Phase 1 (see Figure 4.15 and B.5). Instead of reducing emissions by encouraging recirculation and increasing turbulence, the constrictions appeared to function as heat sinks. Birzer et al.<sup>165</sup> reported similar results for a natural draft TLUD. The feasibility of eliminating this issue using thermally isolated heat sinks was not investigated.

Neither secondary air temperature, secondary air downward angle, nor pot gap appeared to affect high-power CO emissions or useful power output (see Figures B.3 and B.4). None of the design variations tested in the first matrix resulted in reduced CO emissions during Phase 3 compared to the baseline case (see Figures B.10–B.13). Furthermore, the parameters investigated in the first matrix did not affect the average dry fuel consumption rate nor the mass loss rate from the fuel bed (see Figures B.6–B.9). These results were expected because the Matrix 1 parameters were related to the design of the secondary combustion zone.

Average high-power CO emissions during normal operation and post-refueling fell within Tier 4 for all of the secondary air delivery strategies tested in the second matrix (see Figure 4.17). Average high-power PM<sub>2.5</sub> emissions were between 20 mg·MJ<sub>d</sub><sup>-1</sup> and 57 mg·MJ<sub>d</sub><sup>-1</sup> during normal operation and between 167 mg·MJ<sub>d</sub><sup>-1</sup> and 336 mg·MJ<sub>d</sub><sup>-1</sup> post-refueling for these same test cases. The 2-mm-diameter secondary air inlet holes resulted in average Phase 1 high-power CO and PM<sub>2.5</sub> emissions that were only 0.9 g·MJ<sub>d</sub><sup>-1</sup> and 8 mg·MJ<sub>d</sub><sup>-1</sup> lower, respectively, than those for the test case with 4-mm-diameter holes. This result may indicate diminishing returns associated with further increases in secondary air velocity. Results may be different for a natural draft or fan-powered stove. Primary and secondary air flow rates were fixed in the modular test bed. In a natural draft or fan-powered TLUD, the secondary air inlet area and/or the presence of a chimney section would be expected to affect the secondary air flow rate.

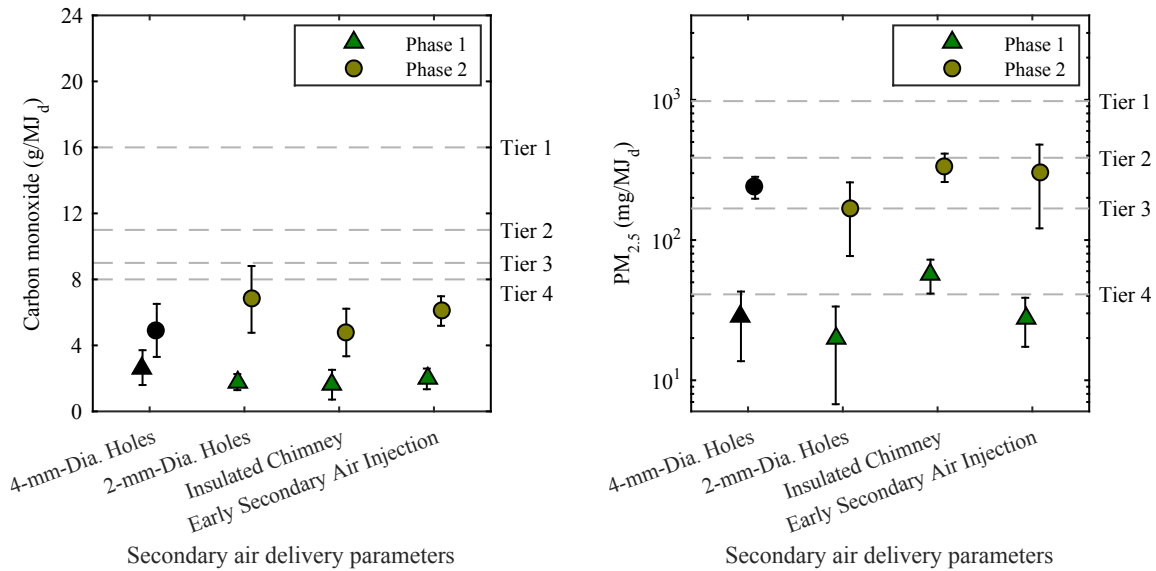


**Figure 4.17: Effects of varying secondary air delivery parameters on average high-power CO and PM<sub>2.5</sub> emissions during normal operation (Phase 1, green triangles) and post-refueling (Phase 2, gold circles). Black symbols refer to the baseline configuration (Douglas fir chip fuel, 7% moisture content, 25 g·min<sup>-1</sup> primary air, 75 g·min<sup>-1</sup> secondary air, 200 °C secondary air temperature, 4-mm-dia. secondary air holes, no swirl, no downward angle, 15 mm pot gap, no flow constriction, no other features). Error bars represent 90% confidence intervals. Data points have been offset slightly to improve the readability of the plot.**

### 4.3.2 Effects of Fuel Type

Changes in fuel type resulted in order of magnitude changes in the average high-power PM<sub>2.5</sub> emissions measured during normal operation (see Figure 4.18). The test bed exhibited the highest emissions when fueled with corn cobs and the lowest emissions when fueled with Lodgepole pine pellets during Phases 1 and 2 (see Figure 4.18). The Lodgepole pine pellets also resulted in lower Phase 3 emissions compared to the other fuels (see Figure B.24). The lower average useful power output measured during Phase 1 with Lodgepole pine pellet fuel (see Figure B.18) was attributed to the longer delay between the time when the stove was lit and the time when the secondary flame established compared to the other, lower particle- and bulk-density fuels.

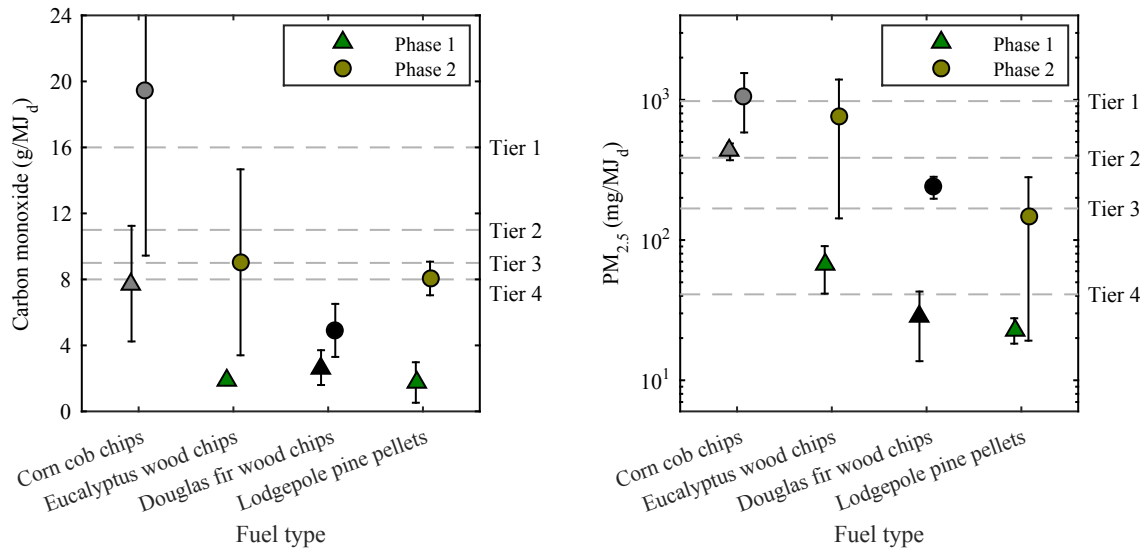


**Figure 4.18: Effects of varying fuel type on average high-power CO and PM<sub>2.5</sub> emissions during normal operation (Phase 1, green triangles) and post-refueling (Phase 2, gold circles). Black symbols refer to the baseline configuration (Douglas fir chip fuel, 7% moisture content, 25 g·min<sup>-1</sup> primary air, 75 g·min<sup>-1</sup> secondary air, 200 °C secondary air temperature, 4-mm-dia. secondary air holes, no swirl, no downward angle, 15 mm pot gap, no flow constriction, no other features). Gray symbols correspond to the test case with the highest bulk density corn cobs (174 kg·m<sup>-3</sup>). Error bars represent 90% confidence intervals. Data points have been offset slightly on either side of the true values listed in Table 4.1 to improve the readability of the plot.**

The producer gas composition during normal operation (Phase 1) was also affected by fuel type (see Figure 4.19). Differences in producer gas composition were not attributed to differences in elemental composition between the fuels. Ultimate analysis revealed that C:H:N:O ratios for the fuels were almost identical, and proximate analysis revealed that volatile and fixed carbon contents were also similar (see Table 2.1). The differences in producer gas composition and emissions may have resulted from differences in particle size, density, biochemical composition, and inorganic constituents affecting yields of light gases and tar from the gasification process.<sup>99,106,108,110,163</sup>

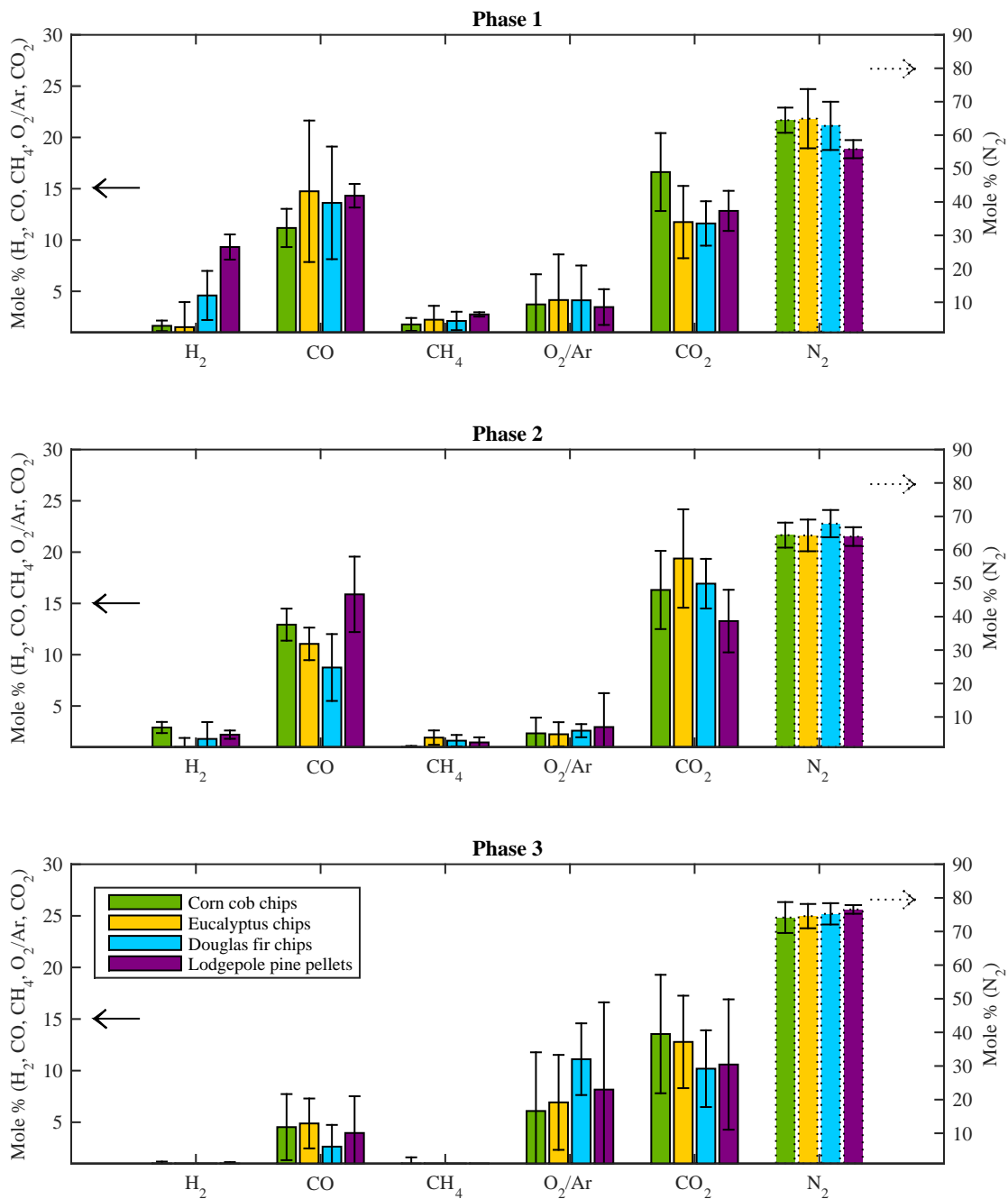


**Figure 4.19:** Effects of fuel type on the average concentrations of H<sub>2</sub>, CO, CH<sub>4</sub>, O<sub>2</sub>/Ar, CO<sub>2</sub> and N<sub>2</sub> in the producer gas entering the secondary combustion zone during normal operation (Phase 1), post-refueling (Phase 2) and during char burnout (Phase 3). Error bars represent 90% confidence intervals.

When the Lodgepole pine pellet fuel was used, average H<sub>2</sub> concentrations in the producer gas were 103% and 23% higher during Phase 1 and Phase 2, respectively, compared to the baseline (Douglas fir wood chips). Varunkumar et al.<sup>159</sup> also reported that pellet fuel resulted in higher H<sub>2</sub> concentrations in the producer gas compared to wood chip fuel. The maximum fuel bed temperatures observed upon the arrival of the flaming pyrolysis zone were highest when the Lodgepole pine pellet fuel was used (see Figure 4.20), and higher temperatures would be expected to result in increased conversion of tars to light gases.<sup>101,114,163</sup> In addition, the Lodgepole pine pellets were 6.4 mm in diameter, whereas pieces of the chipped fuels were ≤ 3-mm-thick on average. The larger particle thickness may have resulted in a longer residence time for primary pyrolysis products to undergo secondary reactions inside the particle and, as a result, increased conversion of tars to light gases.<sup>99</sup>

When the chipped corn cob fuel was used, the average H<sub>2</sub> and CO<sub>2</sub> concentrations were 64% lower and 43% higher, respectively, during Phase 1 compared to the baseline. The maximum fuel bed temperatures observed upon the arrival of the flaming pyrolysis zone were lowest when the corn cob fuel was used (see Figure 4.20), and lower temperatures would be expected to result in reduced conversion of tars to light gases.<sup>101,114,163</sup> The corn cobs had a lower lignin content and higher hemicellulose content compared to the wood fuels. Hemicellulose pyrolyzes more rapidly and over a narrower temperature range compared to lignin.<sup>106,107</sup> Yang et al.<sup>106</sup> observed a higher concentration of H<sub>2</sub> in the gaseous products of lignin pyrolysis and a higher concentration of CO<sub>2</sub> in the gaseous products of hemicellulose pyrolysis. Worasuwanarak et al.<sup>108</sup> observed higher tar yields from pyrolysis of corn cobs than from pyrolysis of rice husk and rice straw. They also reported that tar yields from pyrolysis of cellulose were reduced substantially in the presence of lignin but less substantially in the presence of hemicellulose.

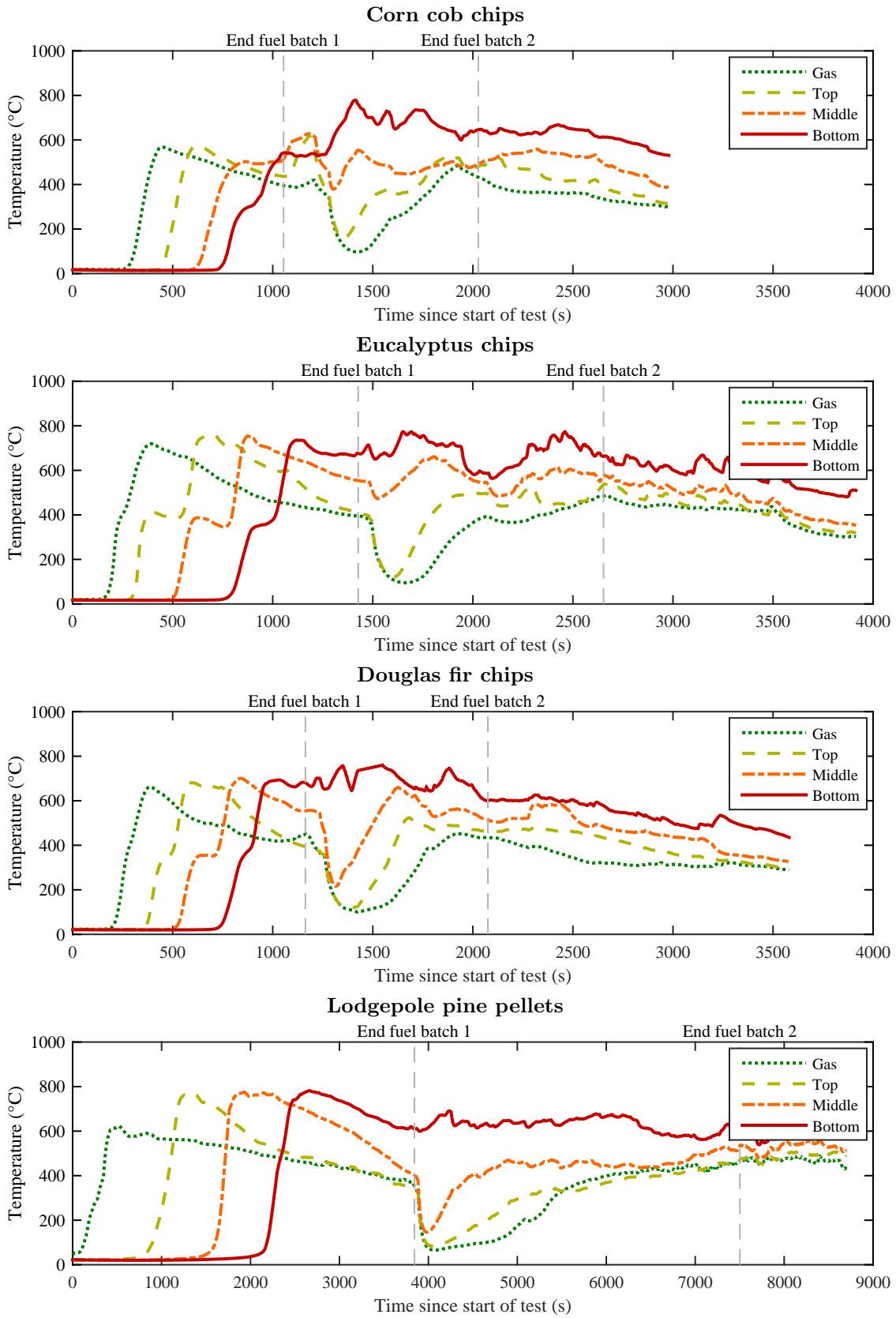
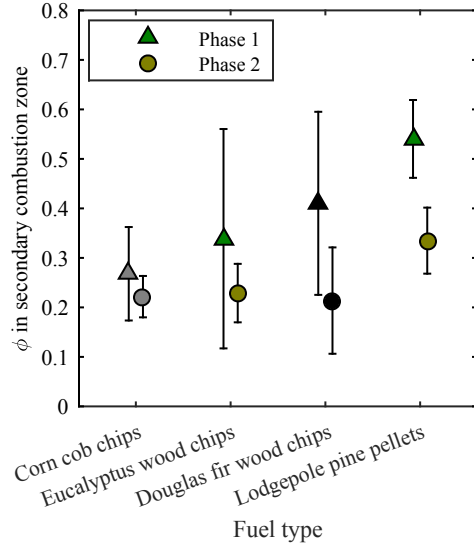


Figure 4.20: Fuel bed temperatures measured with different fuel types.

Higher tar yields would be expected to contribute to higher PM<sub>2.5</sub> emissions. Primary and secondary tars released during pyrolysis of the fuel can undergo further reaction in high-temperature zones to form PAHs,<sup>104</sup> which are precursors to soot, and condensible organics in the exhaust can condense onto existing particles or nucleate to form new particles.<sup>172,173</sup> Tar yields were not quantified in these experiments. The manner in which fuel properties affect tar yields, producer gas composition, and overall emissions from the stove are worthy of further investigation.

The global equivalence ratio calculated for the secondary combustion zone was higher during Phase 1 than during Phase 2. The equivalence ratio ranged from 0.3 and 0.7 during Phase 1 and from 0.1 to 0.4 during Phase 2 for the different test cases (see Figure 4.21 below and Figures B.20–B.22 in Appendix B). However, the values for the second phase may be biased because the presence of condensible hydrocarbons (“tars”) in the producer gas was not accounted for when calculating the equivalence ratio.

The effects that corn cob fuels with different bulk densities had on performance were difficult to identify because the corn cobs proved to be a poor fuel at all of the bulk densities tested (see Figure B.15). As a result, the emissions for the bulk density test cases were highly variable. Similar to the emissions results, the producer gas composition observed with the different-sized corn cobs was highly variable and differences between the test cases were not readily discernible (see Figure B.32). Although these results were inconclusive, the differences between Matrix 1 and Matrix 2, in terms of both the baseline test case results and the degree of variability observed across all test cases (see, for example, Figures 4.14 and 4.17), suggest that fuel bulk density, particle size, and particle uniformity play a role in ensuring reliable operation.



**Figure 4.21: Effects of varying fuel type on the global equivalence ratio in the secondary combustion zone during normal operation (Phase 1, green triangles) and post-refueling (Phase 2, gold circles). Black symbols refer to the baseline configuration (Douglas fir chip fuel, 7% moisture content,  $25 \text{ g}\cdot\text{min}^{-1}$  primary air,  $75 \text{ g}\cdot\text{min}^{-1}$  secondary air,  $200 \text{ }^\circ\text{C}$  secondary air temperature, 4-mm-dia. secondary air holes, no swirl, no downward angle, 15 mm pot gap, no flow constriction, no other features). Gray symbols correspond to the test case with the highest bulk density corn cobs ( $174 \text{ kg}\cdot\text{m}^{-3}$ ). Error bars represent 90% confidence intervals. Data points have been offset slightly to improve the readability of the plot.**

### 4.3.3 Effects of Operating Mode

Phase 2 emissions were higher than Phase 1 emissions for all test cases. The concentrations of  $\text{H}_2$ ,  $\text{CO}$ , and  $\text{CH}_4$  in the producer gas were highest during Phase 1 (normal operation) (see Figure 4.19). For the baseline case (Douglas fir chips), the average  $\text{H}_2$ ,  $\text{CO}$ , and  $\text{CH}_4$  concentrations were 61%, 36%, and 23% lower, respectively, during Phase 2 (post-refueling) and 93%, 81%, and 81% lower, respectively, during Phase 3 (char burnout). The concentration of  $\text{O}_2/\text{Ar}$  in the producer gas was low during Phases 1 and 2, but was 3.3x the average of the Phase 1 and Phase 2 values during Phase 3. The concentrations of  $\text{H}_2$ ,  $\text{CO}$ , and  $\text{CO}_2$  observed during normal operation (Phase 1) and char burnout (Phase 3) were similar to those reported by Varunkumar et al.<sup>159</sup>.

The temperatures measured in the fuel chamber revealed that gasification proceeded from the top of the biomass fuel bed to the bottom during Phase 1 and from the bottom

to the top during Phase 2 (see Figure 4.20). During Phase 1, the temperatures in the top of the fuel bed increased first, followed by the temperatures in the middle and bottom. This progression indicates that the stove operated as an inverted downdraft gasifier (i.e., as a TLUD) during Phase 1. After the first batch of fuel had completely gasified, the temperature of the bottom thermocouples remained high. After the second batch of fuel was added on top of the remaining hot char, the temperatures in the middle of the fuel bed increased first, followed by the temperatures in the top and at the gas sampling height. This progression indicates that the stove operated as a conventional updraft gasifier during Phase 2.

Together, the emissions, producer gas composition, and fuel bed temperature measurements reveal that TLUDs only really operate as TLUDs, and exhibit the associated low emissions, while the initial batch of biomass fuel is gasifying. Conventional updraft gasifier operation would be expected to result in high tar concentrations in the producer gas,<sup>105</sup> and this may be one reason for the higher PM<sub>2.5</sub> emissions observed during Phase 2. The proportion of the mass collected on the Phase 2 filter samples that is attributable to the transient emissions observed immediately after re-lighting vs. steady state post-refueling operation is unknown. The degree to which conventional updraft gasification influences steady state PM<sub>2.5</sub> emissions can be investigated by collecting separate filter samples for transient and steady state post-refueling operation in future experiments.

#### 4.4 Conclusions

The high-power CO and PM<sub>2.5</sub> emissions measured during Phases 1 and 2 for every test case in Matrix 2 are shown in Figure 4.22. Tier 4 high-power emissions were readily achievable when the baseline stove design was fueled with Douglas fir chips or Lodgepole pine pellets and operating normally (during Phase 1). However, the same stove exhibited Tier 0–3 emissions during normal operation with a low-quality fuel (corn cobs) and after refueling (during Phase 2).

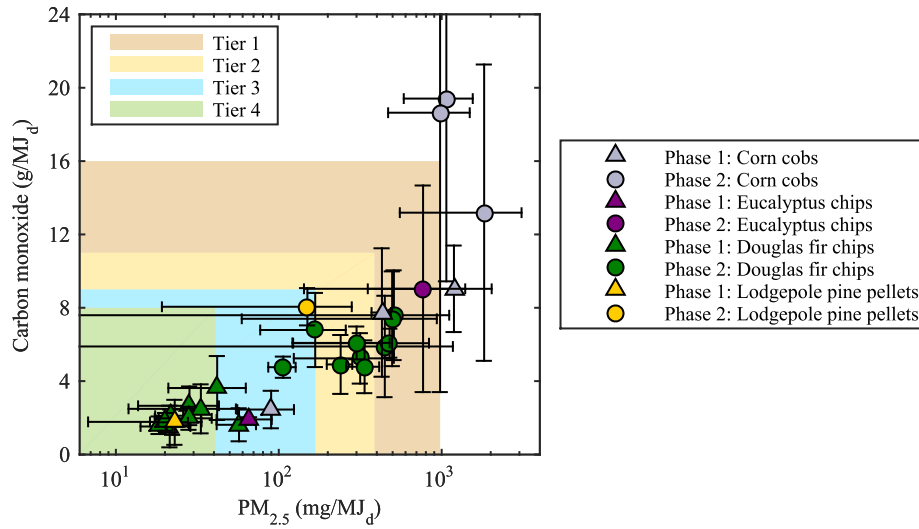


**Figure 4.22: Average high-power CO and PM<sub>2.5</sub> emissions for all test cases in the second matrix with the ISO tiers for high-power emissions shown. Error bars represent 90% confidence intervals.**

These results suggest that the effects of fuel type and operator behavior on emissions from biomass cookstoves should be considered, in addition to cookstove design, as part of efforts to reduce exposure to household air pollution resulting from solid fuel combustion. Locally available fuels and user behavior will influence performance in the field, and improving user access to high-quality prepared biomass fuels may be necessary to achieve Tier 4 emissions reliably.

## CHAPTER 5

### High-Speed Imaging of Inverse Non-Premixed Cross-Flow Flames

#### 5.1 Introduction

In recent years, Q-switched, diode-pumped, solid-state (DPSS) lasers and complementary metal-oxide semiconductor (CMOS) cameras have enabled collection of planar laser-induced fluorescence (PLIF) images at multi-kHz rates, and this so called “high-speed” PLIF imaging allows transient events in turbulent combustion systems to be resolved.<sup>174</sup> High-speed PLIF imaging has become an important tool for studying complex turbulent combustion processes in gas turbine model combustors and other research burners.<sup>175–181</sup> For example, high-speed OH PLIF applied at imaging rates of 10 kHz can be used to resolve extinction and re-ignition events both spatially and temporally.<sup>177,178</sup>

The goal of this study was to employ high-speed imaging techniques to gain a better understanding of the combustion process that occurs in the secondary combustion zone of a gasifier cookstove. The secondary combustion zone represents an unusual flame configuration that is not encountered frequently in practical combustion devices: an inverse non-premixed flame in which the air and fuel are in cross flow (see Figure 1.3). Accordingly, OH\* chemiluminescence (CL), OH PLIF, and acetone PLIF images were collected at multi-kHz repetition rates from a two-dimensional, inverse, non-premixed cross-flow flame burner that was designed to model the secondary combustion zone in a gasifier cookstove.

Chemiluminescence of electronically excited OH (OH\*) serves as a marker of heat release<sup>66,182</sup> and can be imaged to characterize the position and bulk dynamics of flame.<sup>176,183</sup> The formation of OH\* in hydrocarbon flames is attributed to Reaction R 5.1:<sup>184,185</sup>



Chemiluminescence may then occur as the electronically excited OH transitions to the ground state as shown in Reaction R 5.2:



Together, high-speed OH and acetone PLIF can be used to study processes that affect fuel-air mixing.<sup>180</sup> The gradient in OH concentration marks the high-temperature flame front, and regions of high OH concentration denote burned gases.<sup>186</sup> Acetone can be used as a fuel tracer in gaseous flows because it has a relatively high vapor pressure, strong fluorescence intensity per unit of incident radiation, and low toxicity. Furthermore, its broad absorption and emission bands (225–320 nm and 350–550 nm, respectively) allow for flexibility in terms of the excitation and detection scheme.<sup>187</sup>

Images were collected for various fuel and air velocities to investigate the influence of these velocities on fuel-air mixing and flame dynamics. The influence of these velocities was investigated because the results of the experiments with the modular top-lit up draft (TLUD) gasifier test bed (see Chapter 4) indicated that CO emissions decreased with increasing secondary air jet velocity (see Figure 4.14).

## 5.2 Methods

A description of the burner used to collect the PLIF images is provided below, followed by descriptions of the system used to fuel the burner with acetone-seeded simulated producer gas, the five cases tested, the experimental setup used to collect CL and PLIF images, and the method used to post-process the images.

### 5.2.1 Test Bed

The operational principle of the two-dimensional, inverse, non-premixed cross-flow flame burner is illustrated in Figure 5.1. Fuel gas flowed up from the base of the burner through a bed of 4-mm-diameter glass beads to simulate producer gas flowing upward from of a bed of gasifying biomass chips or pellets. Above the bed of glass beads, air was injected horizontally from two 1.6-mm-wide slots on the left and right sides of the burner that were spaced 102 mm apart. Optical access was provided by two 102-mm square quartz windows on the front and back of the burner. On either side of both air nozzles, nozzles with identical profiles

injected nitrogen at the same velocity as the air to flush the windows (see Figure 5.2). The top of the burner was open.

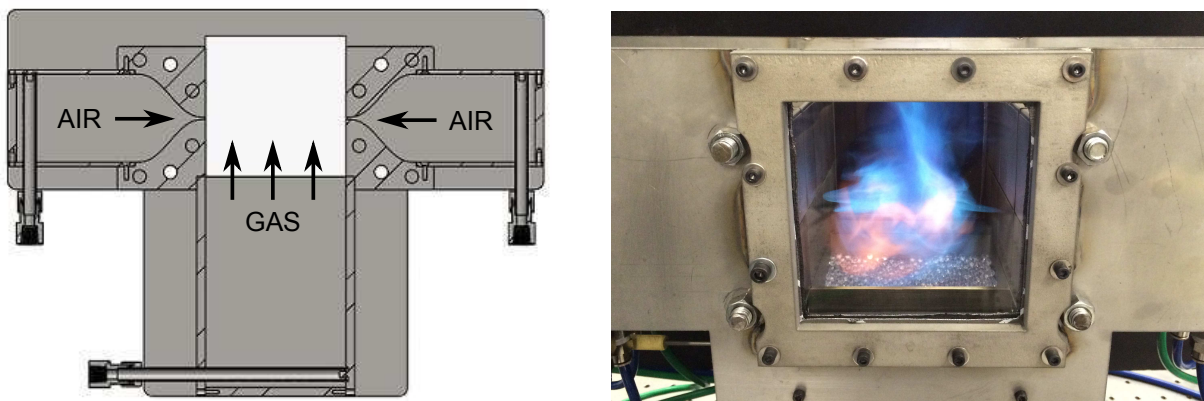


**Figure 5.1:** A cross-section diagram illustrating the operational principle of the non-premixed cross-flow flame burner (left) and a photograph of the burner in operation (right).

The burner was fueled with simulated producer gas comprised of 33% CO, 33% CO<sub>2</sub>, 22% H<sub>2</sub>, 7% CH<sub>4</sub>, and 5% C<sub>2</sub>H<sub>4</sub>. The simulated producer gas was mixed with N<sub>2</sub> in the fuel line to the burner (see Table 5.1). The composition of this fuel gas mixture was based on the composition of the producer gas sampled from the modular test bed operating on wood pellets (see Table 2.2). The producer gas/N<sub>2</sub> mixture was seeded with 5% acetone by volume by passing a fraction of the N<sub>2</sub> through a two-column acetone seeder that was maintained at 30 °C. The acetone-seeded fuel mixture then passed through a section of tubing heated to 40 °C to prevent condensation of the acetone en route to the burner (see Figure 5.3).

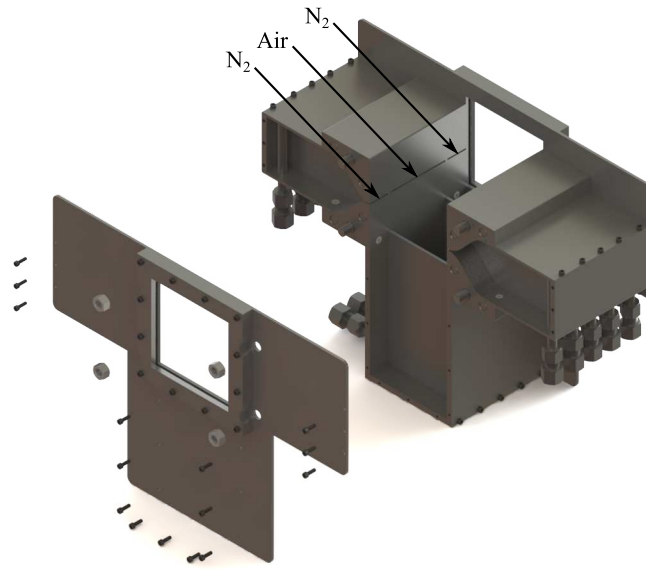


Figure 5.2: An exploded view of the two-dimensional, inverse, non-premixed cross-flow flame burner with the location of the window flush  $N_2$  injection shown.

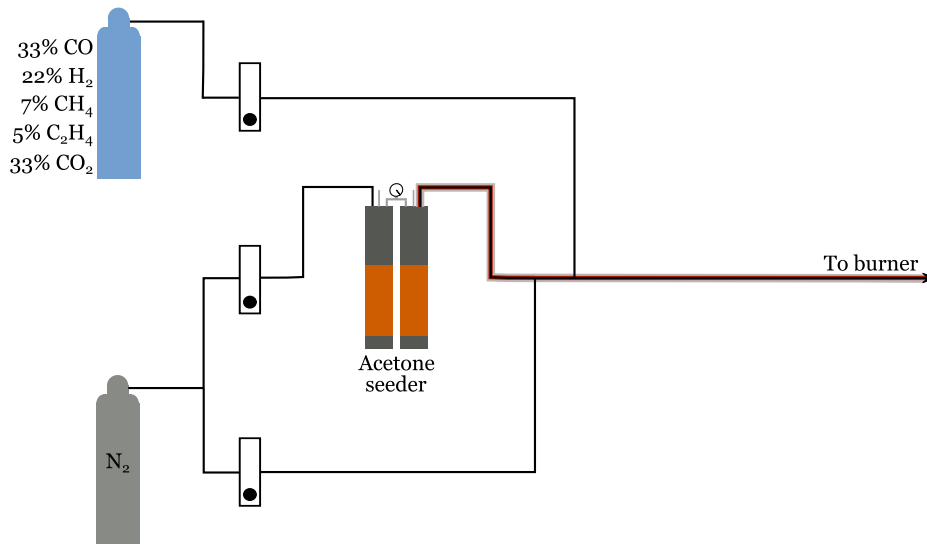


Figure 5.3: A simulated producer gas mixture with the composition shown was mixed with  $N_2$  in the fuel line. A portion of the  $N_2$  was passed through an acetone seeder so that the final producer gas/ $N_2$  mixture would be seeded with 5% acetone by volume. The fuel line after the acetone seeder was heated to 40 °C to prevent the acetone from condensing out of the fuel mixture.

### 5.2.2 Test Matrix

The five different cases that were tested are shown in Table 5.1. These test cases consisted of a baseline, a case in which the velocity of the fuel flow was lower than in the baseline, a case in which the velocity of the fuel flow was higher than in the baseline, a case in which the air velocity was lower than in the baseline, and a case in which the air velocity was higher than in the baseline. The air velocity was held constant while the fuel velocity was varied and the fuel velocity was held constant while the air velocity was varied. The fuel velocity and global equivalence ratio were manipulated by adjusting the amount of N<sub>2</sub> that the simulated producer gas was diluted with. All flows were metered using rotameters. The accuracy of the rotameters was  $\pm 1 \times 10^{-4} \text{ kg}\cdot\text{s}^{-1}$  for the air and window flush N<sub>2</sub> flows,  $\pm 3 \times 10^{-5} \text{ kg}\cdot\text{s}^{-1}$  for the fuel flow,  $\pm 1 \times 10^{-5} \text{ kg}\cdot\text{s}^{-1}$  for the N<sub>2</sub> flow into the acetone seeder, and the  $\pm 5 \times 10^{-5} \text{ kg}\cdot\text{s}^{-1}$  for the fuel dilution N<sub>2</sub>.

**Table 5.1: The five test cases.**

Test case	Velocities ( $\text{m}\cdot\text{s}^{-1}$ )		Mass flow rates ( $\text{kg}\cdot\text{s}^{-1}$ )					$\phi$	Re
	Air	Fuel	Air	Window flush N <sub>2</sub>	Fuel	Acetone seeder N <sub>2</sub>	Fuel N <sub>2</sub>		
Baseline	5.0	0.075	$1.4 \times 10^{-3}$	$8.8 \times 10^{-4}$	$2.8 \times 10^{-4}$	$7.1 \times 10^{-5}$	$2.1 \times 10^{-4}$	1.0	520
Fuel-low	5.0	0.053	$1.4 \times 10^{-3}$	$8.8 \times 10^{-4}$	$3.4 \times 10^{-4}$	$5.0 \times 10^{-5}$	0	0.6	520
Fuel-high	5.0	0.10	$1.4 \times 10^{-3}$	$8.8 \times 10^{-4}$	$2.1 \times 10^{-4}$	$9.5 \times 10^{-5}$	$4.5 \times 10^{-4}$	1.0	520
Air-low	3.2	0.075	$8.7 \times 10^{-4}$	$5.6 \times 10^{-4}$	$1.0 \times 10^{-4}$	$7.1 \times 10^{-5}$	$3.9 \times 10^{-4}$	1.0	330
Air-high	8.8	0.075	$2.4 \times 10^{-3}$	$1.6 \times 10^{-3}$	$2.9 \times 10^{-4}$	$7.1 \times 10^{-5}$	$2.0 \times 10^{-4}$	0.6	920

### 5.2.3 Experimental Setup

A dye laser (Sirah Credo) was pumped at 10 kHz with a 532-nm beam from a diode-pumped solid-state Nd:YAG laser (Edgewave Innoslab IS16II-E) with an output power of 80 W. The laser dye was Rhodamine 590 chloride dissolved in ethanol at a concentration of  $0.135 \text{ g}\cdot\text{L}^{-1}$  in the resonator and  $0.090 \text{ g}\cdot\text{L}^{-1}$  in the amplifier. The dye laser generated UV light at 283.2 nm with an average pulse energy of  $0.35 \text{ mJ}\cdot\text{pulse}^{-1}$ . This laser beam was formed into a 32-mm-wide, 0.9-mm-thick laser sheet that was directed vertically down into the top of the burner (as shown in Figure 5.4) along the  $z = 0$  plane to excite the Q<sub>1</sub>(7)

line of the A-X (1,0) transition of OH. The same laser sheet was used to excite the acetone PLIF.

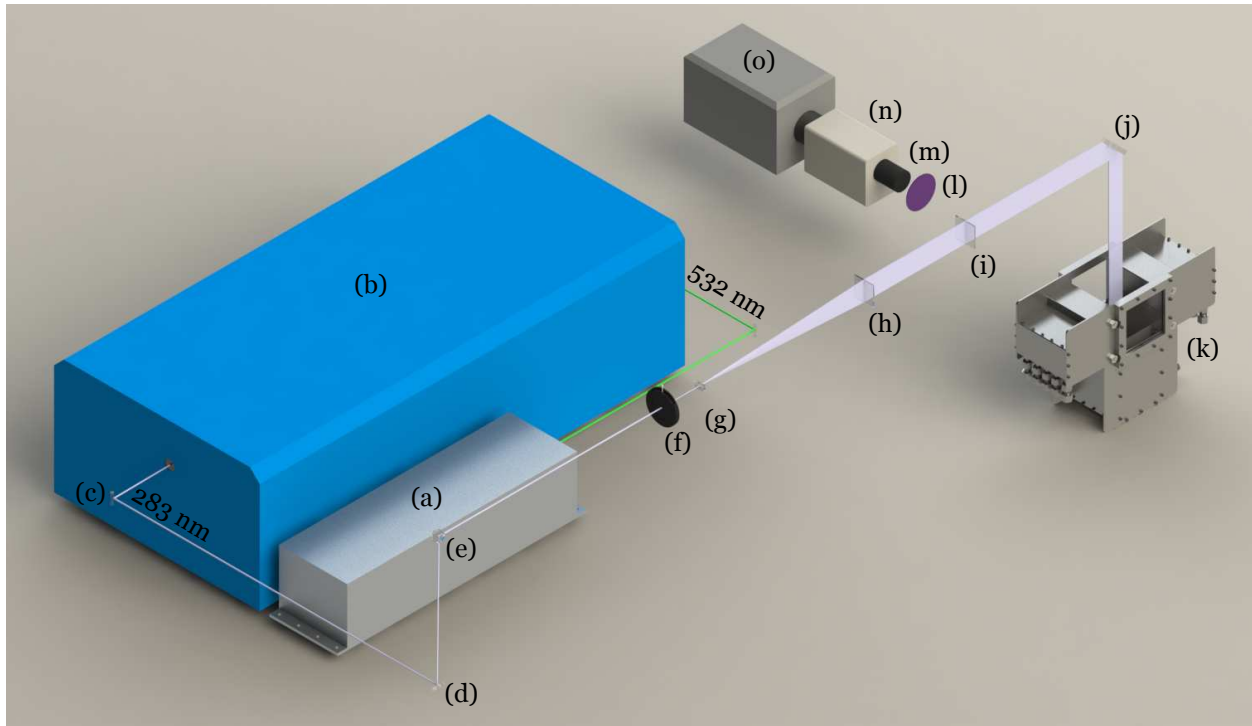


**Figure 5.4: Diagram of the experimental setup:** (a) pump laser, (b) dye laser, (c) UV mirror, (d) UV mirror, (e) UV mirror, (f) iris, (g) concave cylindrical lens ( $f = -25$  mm), (h) convex cylindrical lens ( $f = 500$  mm), (i) convex cylindrical lens ( $f = 750$  mm), (j) dichroic mirror, (k) burner, (l) filter, (m) UV lens, (n) intensifier, and (o) high-speed camera.

The laser sheet and camera field of view spanned the entire height of the window area. The burner was traversed in the x-direction to collect PLIF images at three different locations: left, center and right (see Figure 5.5). When the laser sheet was in the “left” position, the left edge of the laser sheet was adjacent to the left air nozzle. When the laser sheet was in the “right” position, the right edge of the laser sheet was adjacent to the right air nozzle. In the “center” position the laser sheet was centered in the combustor. In all three positions the laser sheet was positioned 64 mm from the inside edge of the front wall such that it was centered in the combustor in the z-direction.

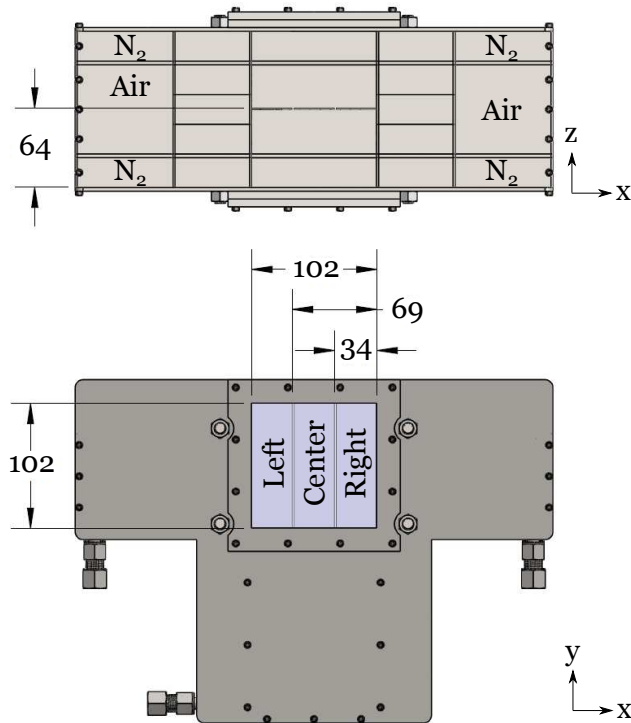


**Figure 5.5:** The positions of the laser sheet within the combustor in each of the three PLIF imaging locations: left, center, and right. The width and height of the window, the distance from the right air nozzle to the right edge of the laser sheet in the “center” and “left” positions, and the distance from the inside edge of the front wall to the center of the laser sheet are shown. The locations of window flush N<sub>2</sub> injection relative to the air injection are also illustrated.

PLIF images were collected using a high-speed camera (Photron SA5) fitted with an external intensifier (Invisible Vision 1850B100) and UV lens (Sodern Cerco,  $f = 45$  mm, F/1.8). OH PLIF images were collected at 10 kHz using a  $310 \text{ nm} \pm 5 \text{ nm}$  bandpass filter (Omega Optical) over a 200-ns gate width. Acetone PLIF images were collected at 10 kHz using a 315–710 nm bandpass filter over a 100-ns gate width. A total of 14,000 OH PLIF images and 14,000 acetone PLIF were collected at each of the three imaging locations. Additionally, OH\* CL images were collected at 3 kHz using the same imaging configuration as the OH PLIF, but without the laser sheet and using a  $60\text{-}\mu\text{s}$  gate width. A total of 10,000 CL images were collected for each test case.

#### 5.2.4 Image Processing

PLIF and CL images were corrected for the intensifier whitefield response in post-processing. Intensifier whitefield images were collected by placing a light panel with uniform illumination in front of the intensifier and setting the intensifier gain and camera sensor resolution to the same values used during the respective imaging processes. Approximately 150–300 whitefield images were averaged in post-processing. The average image was divided by the average pixel intensity so that the final whitefield correction had an average intensity of 1.

PLIF images were also corrected for the laser sheet mean intensity profile. Laser sheet profile images were collected in each of the three locations (left, center, and right) at both of the intensifier gains used for imaging. Laser sheet profile images were collected by placing a piece of cardstock on top of the burner that featured a cutout large enough for the laser sheet to pass through. The imaging area was then flooded with acetone by flowing only acetone-seeded nitrogen up through the fuel bed. Approximately 200–300 images of acetone fluorescence were collected, using the 315–710 nm bandpass filter, and averaged in post-processing. Each column of pixels in the average image was averaged along the length of the column to eliminate the effects of attenuation of the laser sheet by the acetone/nitrogen mixture. The average pixel intensity in each column was then extruded along the entire height of the image. Similar to the whitefield correction, the final image was divided by the average pixel intensity so that the final laser sheet profile correction had an average intensity of 1. Despite the asymmetry in the fuel flow discussed below, the sheet profiles recorded at the three locations were very similar (see Figure 5.6).

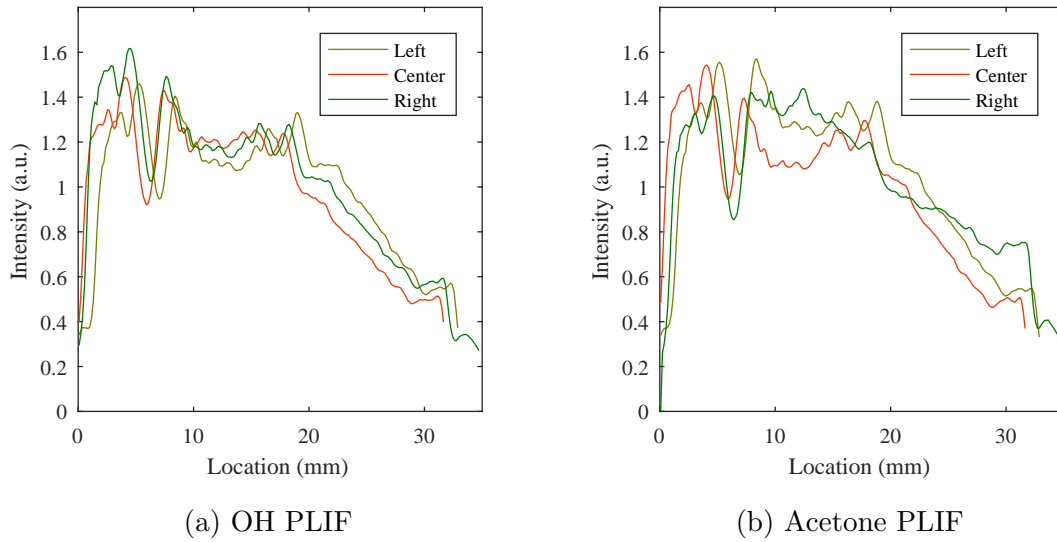


**Figure 5.6: Intensity of the sheet profiles recorded in the left, center, and right locations at the intensifier gain used for OH PLIF imaging (68) and acetone PLIF imaging (70) as a function of distance along the width of the sheet.**

Chemiluminescence images were post-processed by dividing each image by the intensifier whitefield. Pixels in locations where the intensity of the whitefield correction image was less than 0.2 were set to zero. Pixels in locations where the intensity of the CL image was less than 40 (out of an average maximum intensity of 450–1100 depending on the image set) were also set to zero to eliminate noise. The chemiluminescence images for each test case were averaged and the average images were smoothed using a median filter.

PLIF images were post-processed by dividing each image by the intensifier whitefield and the laser sheet profile. It was necessary to apply the intensifier whitefield correction separately from the laser sheet profile correction because each column of pixels in the average laser sheet image had been averaged along the length of the column and then extruded over the entire height of the image. Pixels in locations where the intensity of the whitefield or laser sheet profile correction images was less than 0.1 were set to zero. Pixels in locations where the intensity of the PLIF image was less than 15 were also set to zero to eliminate noise.

## 5.3 Results and Discussion

### 5.3.1 OH\* Chemiluminescence Images

The OH\* chemiluminescence images of the baseline and high air velocity cases revealed regular oscillation of the air jets (see Figures 5.7 and 5.8). The jets started out parallel and opposed, but were then pushed apart in the vertical direction so that one jet moved on top of the other. Once the jets moved a certain distance apart, they swung back toward, and eventually past, each other, so that the jet that was on the top became the jet that was on the bottom and that jet that was on the bottom became the jet that was on the top.<sup>188,189</sup>

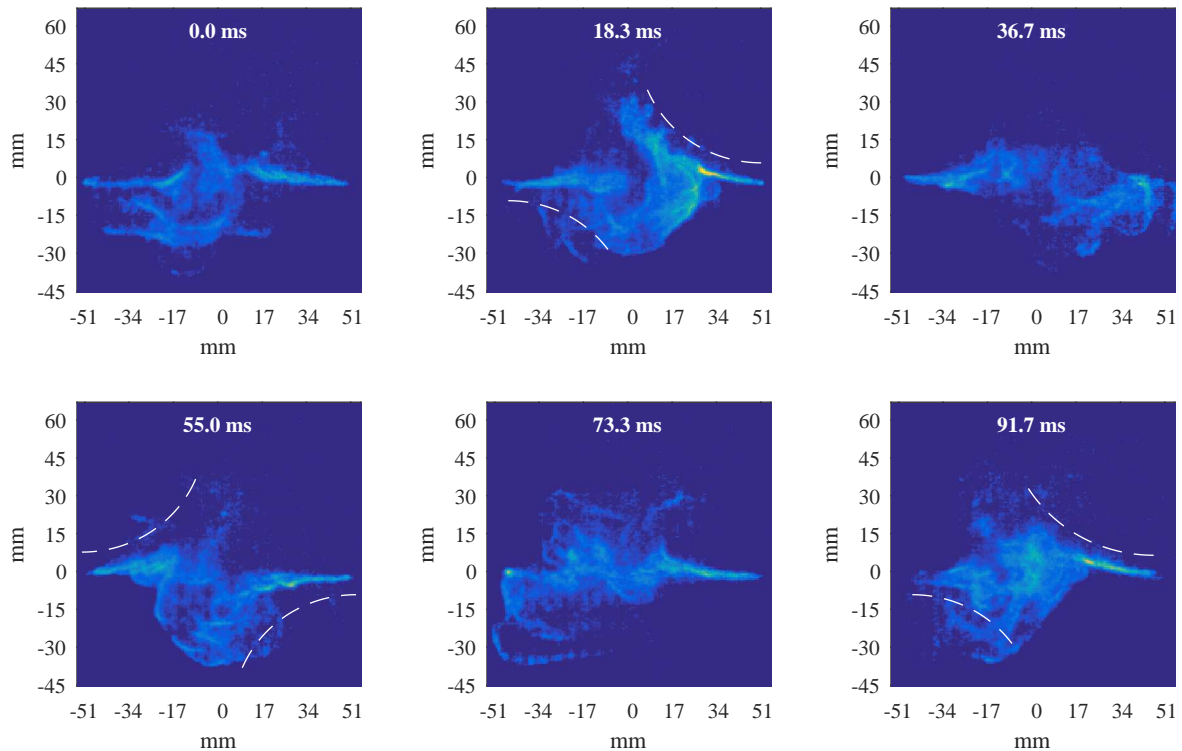


**Figure 5.7:** A sequence of OH\* chemiluminescence images for the baseline case illustrating the oscillation of the air jets.

The oscillation is illustrated in Figure 5.7 using a sequence of images from the baseline case. In the first image (0.0 ms), the two jets lie in approximately the same plane. The jets then move apart from each other in the vertical direction and at 18.3 ms the end of the left jet is pointed down towards the fuel bed and the end of the right jet is pointed up towards the top of the burner. The jets then move back towards each other and at 36.7 ms they

once again lie in the same plane; however, they do not remain in this position. Instead, the jets continue to move past each other until the end of the left jet is pointed up towards the top of the burner and the end of the right jet is pointed down towards the fuel bed (55 ms). The jets once again move back towards, and eventually past, each other so that they are in approximately the same position at 91.7 ms as they were at 18.3 ms.

The oscillation is illustrated in Figure 5.8 using a sequence of images from the high air velocity case. The sequence of events is identical to that shown in Figure 5.7; however, the oscillation is taking place at a higher frequency—as demonstrated by the shorter time step between the images. It is also more apparent that the motion of the air jets resulted in mixing of the fuel and air, and subsequent heat release, below the height of the air injection.

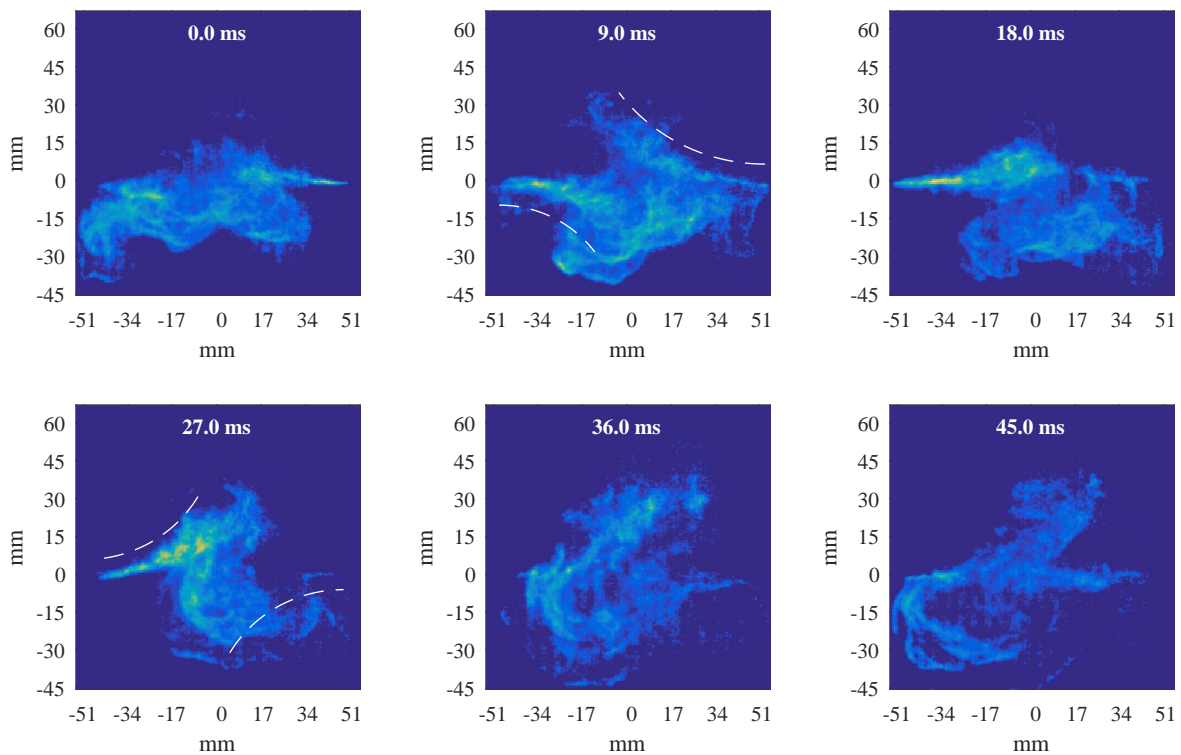


**Figure 5.8: A sequence of OH\* chemiluminescence images for the high air velocity case illustrating the oscillation of the air jets.**

This oscillation is a hydrodynamic instability that has been observed previously in isothermal, non-reacting, unconfined opposed planar jets.<sup>188–192</sup> This behavior was reported first for opposed planar jets of water<sup>188,189</sup> and later for opposed planar jets of air.<sup>190–192</sup>

The parameters that govern the onset and frequency of oscillation are the Reynolds number of the jets and the aspect ratio of the system.<sup>189,193</sup> The jet Reynolds number is calculated using the thickness of the slots from which the jets issue as the characteristic length. The aspect ratio of the system is defined as shown in Equation 5.1:

$$\alpha = \frac{d}{L} \quad (5.1)$$

where  $\alpha$  is the aspect ratio,  $d$  the thickness of the slot from which the jet issues (1.6 mm in this experiment), and  $L$  the distance between the two jets (102 mm in this experiment). The aspect ratio in the present burner is equal to 0.016.

Denshchikov et al.<sup>189</sup> reported that the oscillation period for isothermal, non-reacting, unconfined opposed planar jets was related to the jet Reynolds number and the aspect ratio as shown in Equation 5.2:

$$\frac{T}{(\rho L^2 / \mu)} = \frac{0.34}{Re} \alpha^{0.45} \quad (5.2)$$

where  $T$  was the oscillation period in s,  $\rho$  was the density of the fluid in  $\text{kg}\cdot\text{m}^{-3}$ ,  $L$  was the distance between the two opposed jets (0.102 m),  $\mu$  was the viscosity of the fluid in  $\text{kg}\cdot\text{m}^{-1}\text{s}^{-1}$ ,  $Re$  was the Reynolds number of the jets, and  $\alpha$  was the aspect ratio from Equation 5.1. Similar relationships were reported by Li et al.<sup>191</sup> and Tu et al.<sup>192</sup>; however, the relationship shown in Equation 5.2 was the first to be reported and showed the best agreement with the experimental results presented here.

The oscillation periods and frequencies predicted by Equation 5.2 for the test cases listed in Table 5.1 are shown in Table 5.2. The density and viscosity of air were evaluated at room temperature (21 °C) and atmospheric pressure (101.3 kPa). For the baseline and high air velocity cases, the predicted periods of 69 ms and 36 ms agree reasonably well with the periods of approximately 73 ms and 36 ms that were observed in Figures 5.7 and 5.8. This result suggests that the air jets behave as isothermal, non-reacting, unconfined opposed planar jets in these cases; however, additional image processing needs to be undertaken to determine whether or not this agreement is incidental. The air jets did not oscillate as

regularly in the low fuel velocity case, but the oscillation frequency appeared similar to that observed for the baseline case. Evidence of oscillation was observed even less frequently in the high fuel velocity and low air velocity cases.

**Table 5.2: Oscillation periods predicted for unconfined, isothermal opposed planar jets compared to those observed in the OH\* CL image sequences.**

Description	Velocities (m·s <sup>-1</sup> )		Re	Predicted oscillation period (ms)	Predicted oscillation frequency (Hz)
	Air	Fuel			
Baseline	5.0	0.075	520	69	15
Fuel–low	5.0	0.053	520	69	15
Fuel–high	5.0	0.10	520	69	15
Air–low	3.2	0.075	330	110	9.3
Air–high	8.8	0.075	920	39	26

Pawłowski et al.<sup>193</sup> performed a numerical simulation of opposed planar jets and observed oscillation at practically all jet Reynolds numbers for aspect ratios less than approximately 0.1. Given the small aspect ratio in the present burner, one might expect regular oscillation of the jets under all of the conditions tested in this study. However, there were several differences between a system comprised of two isothermal, non-reacting, unconfined opposed planar jets and the present burner. Specifically, in the present burner: (1) the aspect ratio ( $\alpha = 0.016$ ) was smaller than the minimum aspect ratio considered in previous studies<sup>192</sup> ( $\alpha = 0.025$ ), (2) the fuel bed situated below the plane of jet injection prevented outflow in the downward direction, (3) the air jets were subjected to a cross flow of fuel in the upward direction, and (4) the flow was subject to buoyancy effects resulting from the exothermic reaction between the air and fuel. The cross flow of the fuel (more specifically, the ratio of the jet velocity to the fuel velocity) and buoyancy, in particular, may have been highly influential. Besbes et al.<sup>190</sup> investigated planar opposed jets that were angled upwards, in addition to jets that were horizontal, and did not observe oscillatory behavior in the angled jets.

Average chemiluminescence images for each of the five test cases are shown in Figure 5.9. Compared to the baseline case, heat release was observed further below the air jets (i.e., closer to the surface of the fuel bed) in the high air velocity case. The narrower heat release

profile and lower intensities observed in the high fuel velocity case were attributed to the higher upward velocity and the larger fraction of  $N_2$  present in the fuel flow. Conversely, the broader heat release profile and higher intensities observed in the low fuel velocity case were attributed to the lower upward velocity and smaller fraction of  $N_2$  present in the fuel flow.

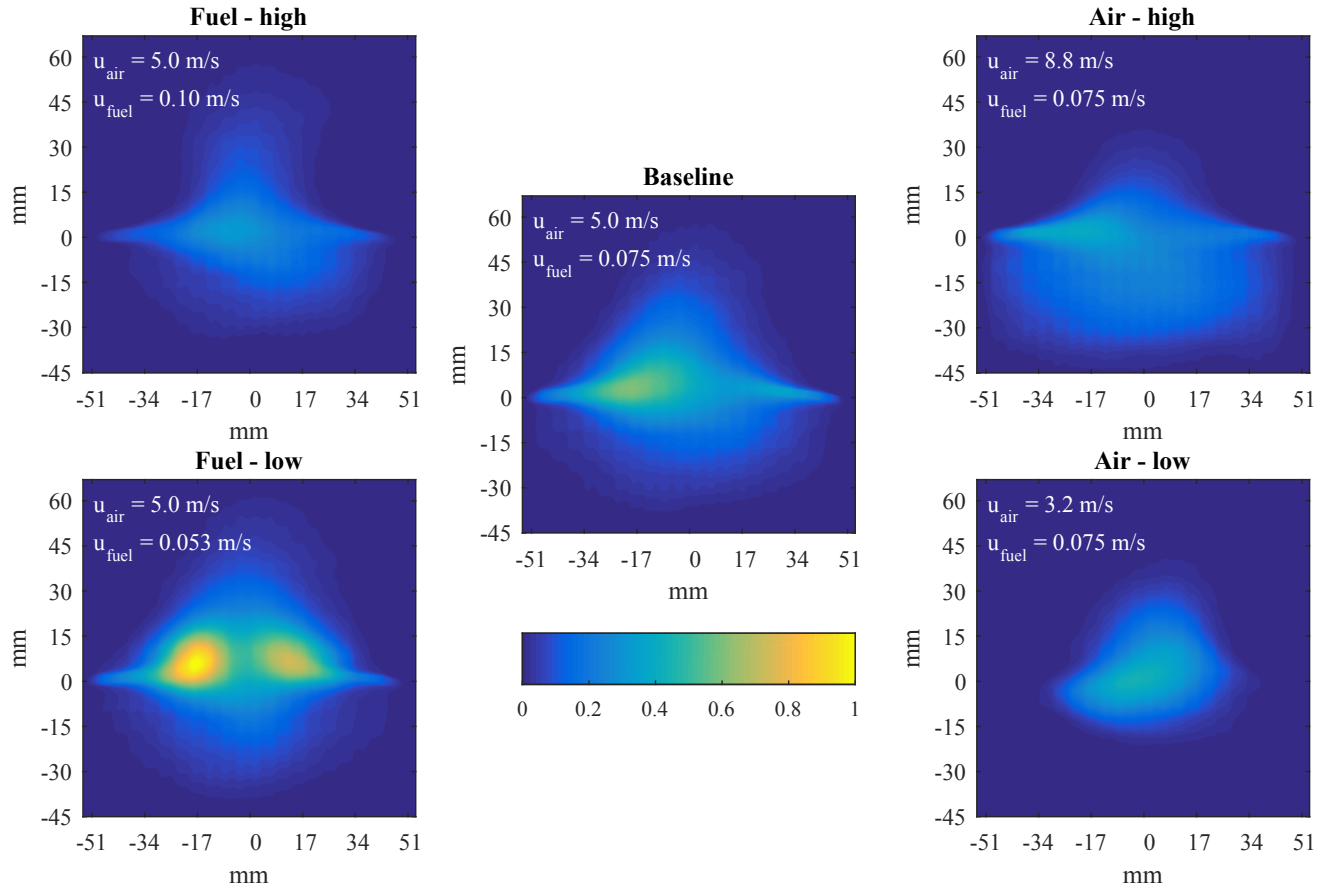


**Figure 5.9:** Average  $OH^*$  chemiluminescence images for each test case. The velocities of the air and fuel flows are indicated in the upper left corner of each image.

The only case in which no heat release was observed below the height of the air jets in the average  $OH^*$  CL images is the low air velocity case. This result may be related to the fact that this was the test case in which oscillatory behavior was least apparent. This is also the only test case in which heat release did not extend to the air nozzles on either side of the window area. Instead, all of the heat release was concentrated in the center of the image. It is possible that the mixing and heat release that was observed below the height of the air

jets, and next to the burner walls, in the other test cases allowed heat release to extend to the air nozzles by preheating the reactants.

### 5.3.2 PLIF Images

The acetone PLIF images illustrated mixing of the air and fuel below the plane of air injection. The three panels in each image correspond to the left, center, and right laser sheet positions shown in Figure 5.5. The images in each panel were recorded under the same operating conditions, but at different times. A sequence of images recorded for the baseline case is shown in Figure 5.10. A vortex that is mixing the fuel and air is seen in the left panel at 0.0 ms, 18.3 ms, and 36.6 ms. The image sequence shown in Figure 5.11, which was recorded for the high air velocity case, revealed more vigorous mixing of fuel and air than was observed in the other cases. The acetone signal was less prevalent than in the images shown in Figure 5.10.

Although oscillatory motion was observed less frequently in the high fuel velocity case, the acetone PLIF images recorded for this case also revealed fuel-air mixing below the plane of air injection. In the image sequence shown in Figure 5.12, dashed lines draw attention to circular pockets in the left and right panels where acetone is absent. Numerical simulations of opposed planar jets predict recirculation in this area even in the absence of oscillation;<sup>193</sup> however, this behavior was not observed in the images collected for the low air velocity case. In contrast, a much more steady and uniform acetone profile was observed below the height of the air jets in the low air velocity case, suggesting that less recirculation was occurring (see Figure 5.13).

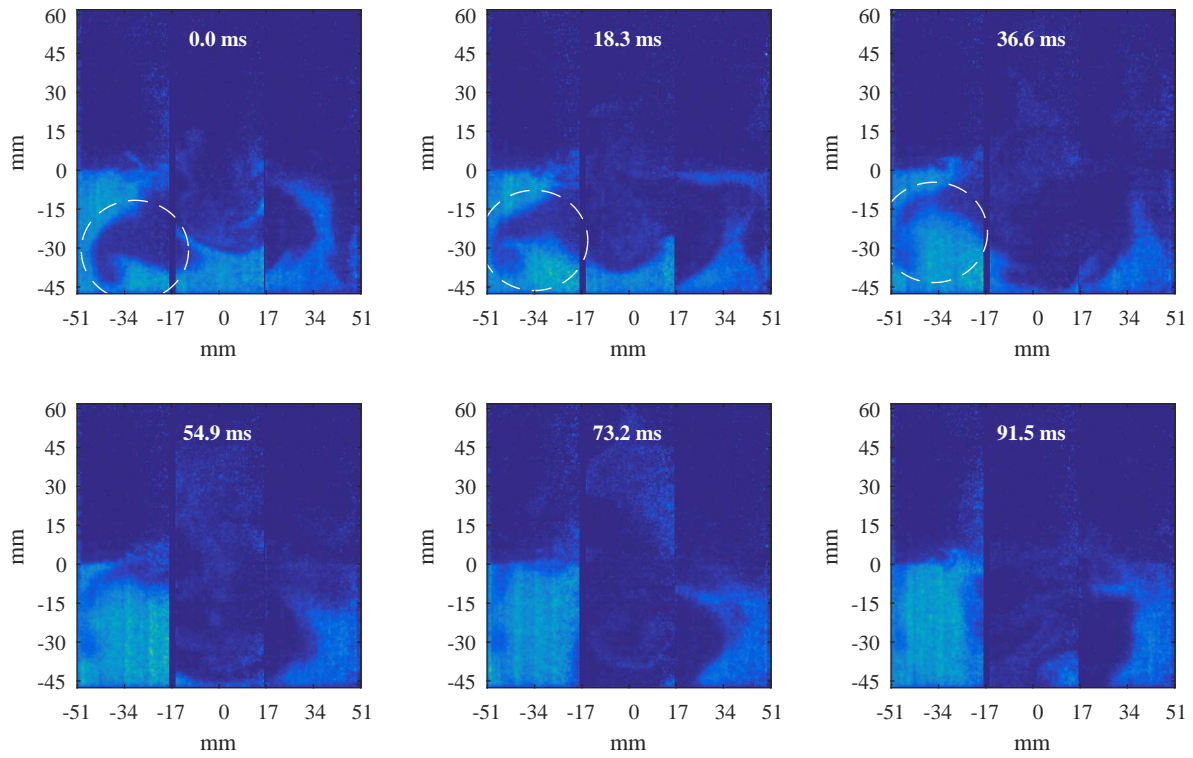


**Figure 5.10:** A sequence of acetone PLIF images for the baseline case. A vortex that appears to be mixing the fuel and air is circled.

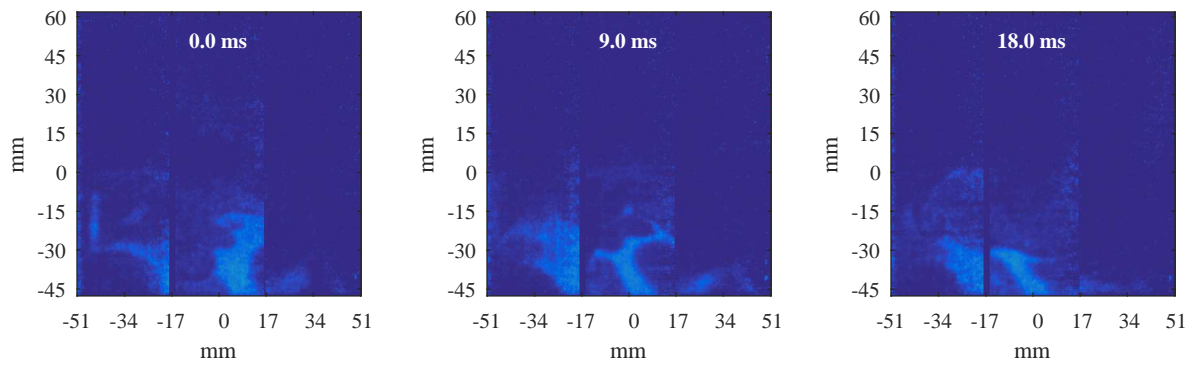


**Figure 5.11:** A sequence of acetone PLIF images for the high air velocity case.

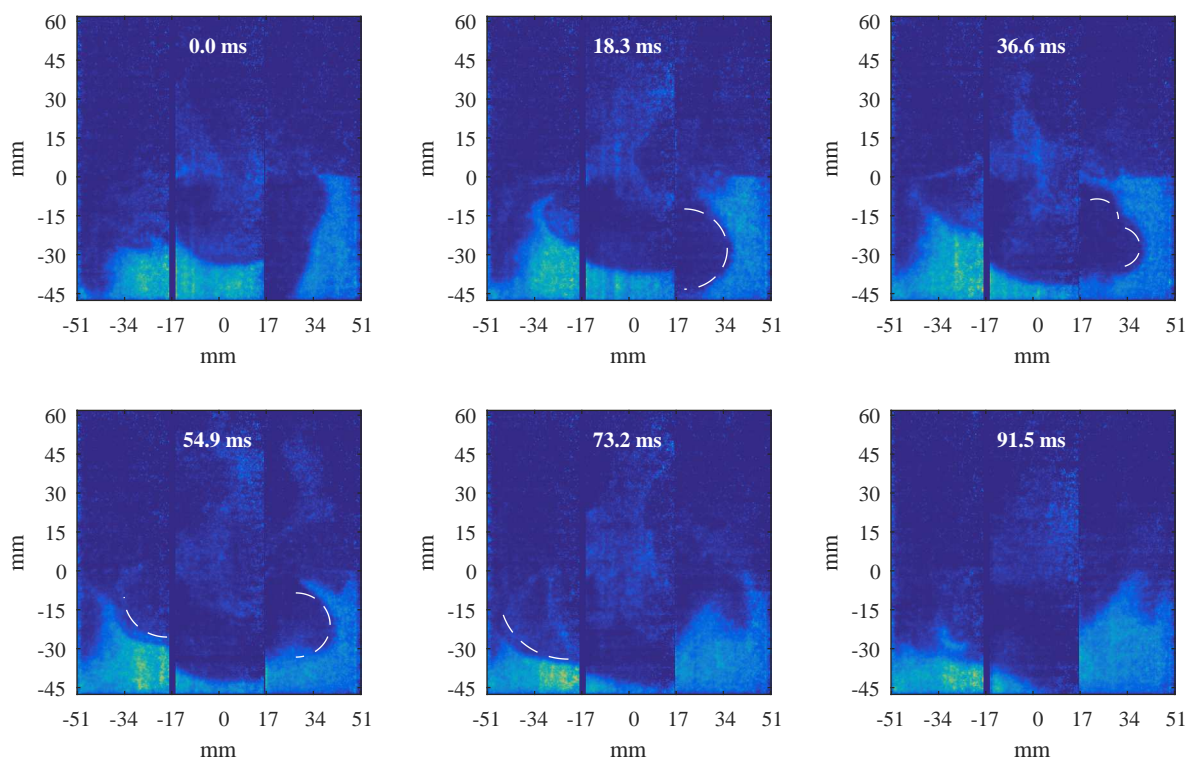


**Figure 5.12:** A sequence of acetone PLIF images for the high fuel velocity case.

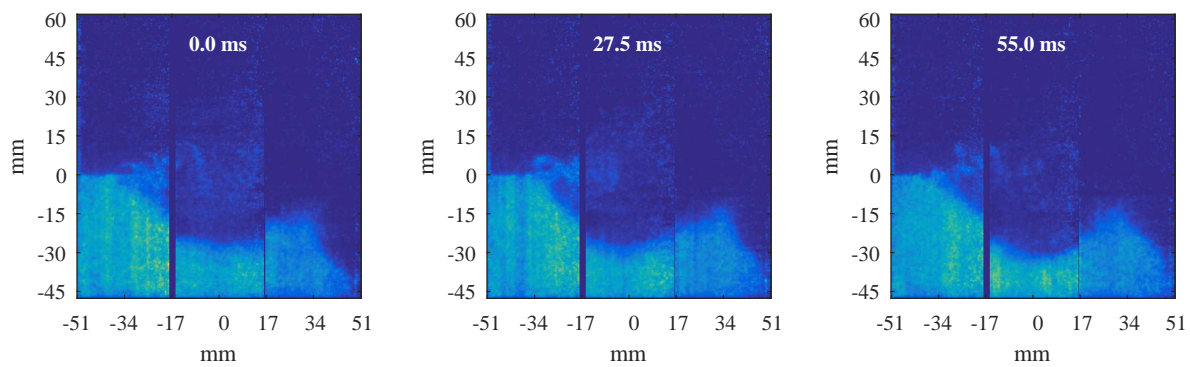


**Figure 5.13:** A sequence of acetone PLIF images for the low air velocity case.

Unfortunately, an asymmetry in the fuel flow was identified using the acetone PLIF images. As shown in Figure 5.14, the average acetone PLIF signal is stronger on the left side of the window area than on the right side, indicating that more fuel was present on the left than on the right. It is unclear whether the asymmetry was this severe throughout the entire depth of the burner, or just in the plane in which PLIF images were collected, since the OH\* CL images appear more symmetric.

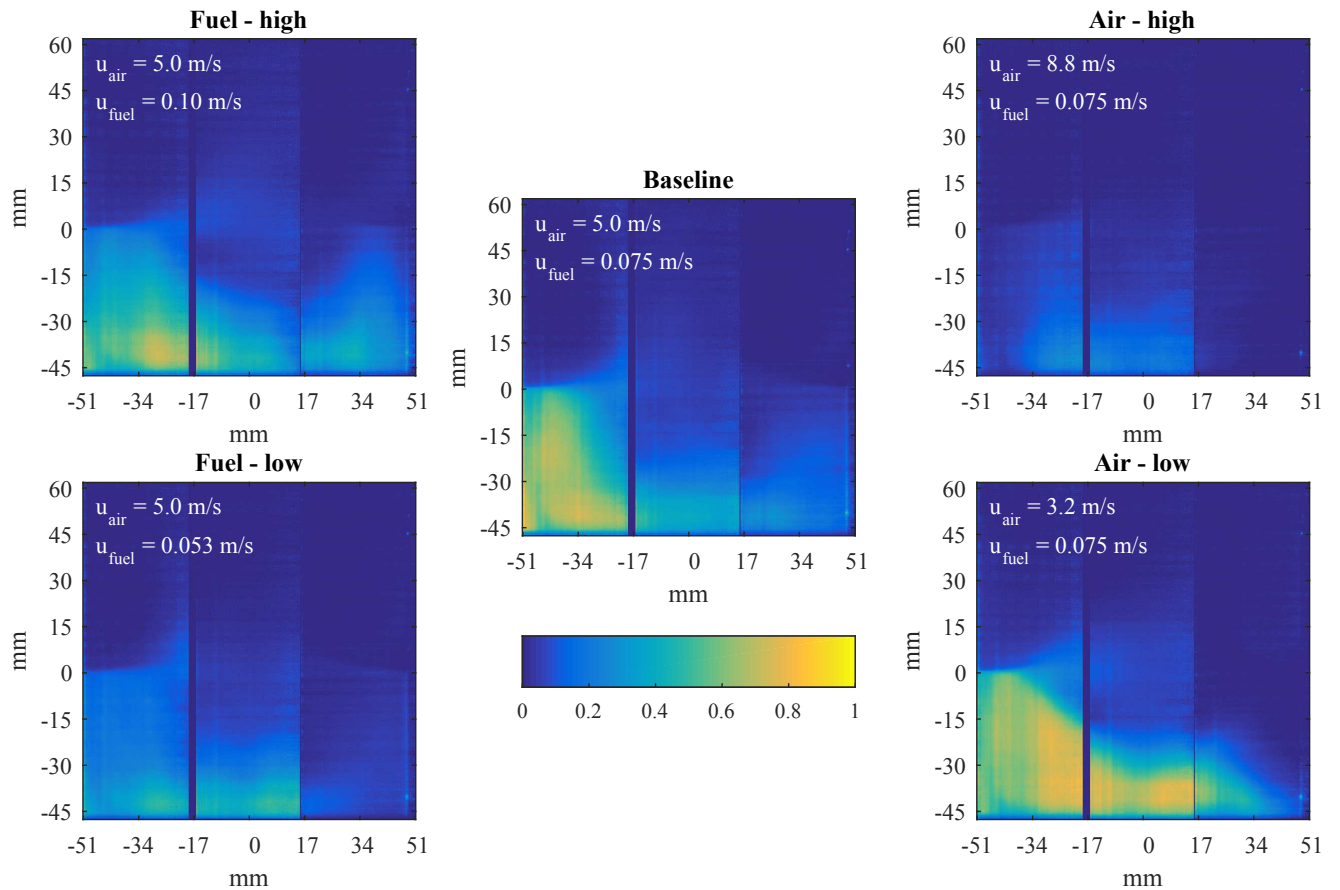


**Figure 5.14: Average acetone PLIF images for each of the five test cases. These images illustrate the asymmetry in the fuel flow.**

The OH PLIF images suggest that the air-fuel mixing illustrated in the acetone PLIF images influences the mean location and dynamics of the flame front. Sequences of OH PLIF images recorded for the baseline, low air velocity, and high air velocity cases are shown in Figures 5.15, 5.16, and 5.17 respectively. Similar to the acetone PLIF images, these images consist of three panels that include images recorded in the three laser sheet positions under

the same conditions but at different times. The PLIF signal is weaker in the images collected on the left and right sides. The images in the center were collected first, and the weak signal observed in the other images may have resulted from the wavelength of the light output from the dye laser shifting off of the transition wavelength over the course of the day.

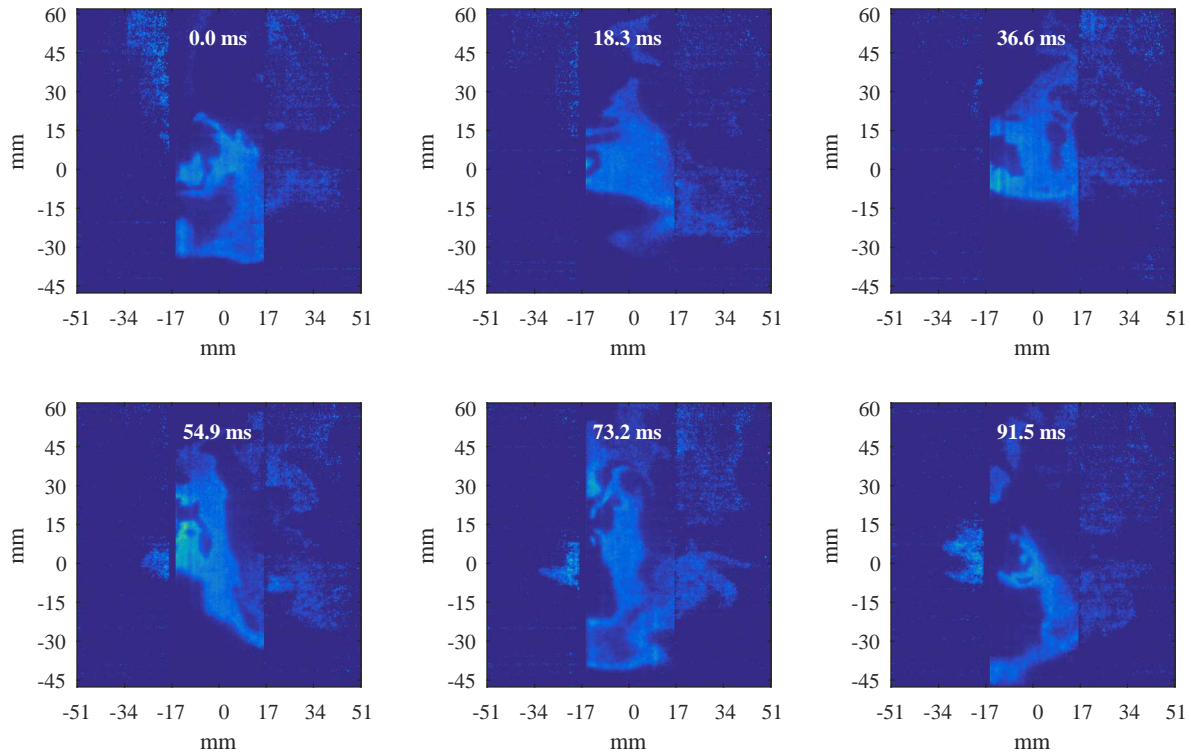


**Figure 5.15: A sequence of OH PLIF images for the baseline case.**

The OH PLIF signal frequently appeared below the height of the air jets in the baseline, low fuel velocity, high fuel velocity, and high air velocity cases (see, for example, Figures 5.15 and 5.16). In accordance with the more intense mixing observed below the air jets, the OH PLIF signal was observed near the bottom of the imaging area more frequently in the high air velocity case compared to the baseline and low air velocity cases (see Figure 5.16). The OH PLIF signal was also more dynamic in the high air velocity case in comparison to the other test cases, and vortex shedding is apparent downstream of the air jets' impingement plane. In the low air velocity case, on the other hand, the OH signal was primarily observed at and above the height of the air jets (see Figure 5.17).

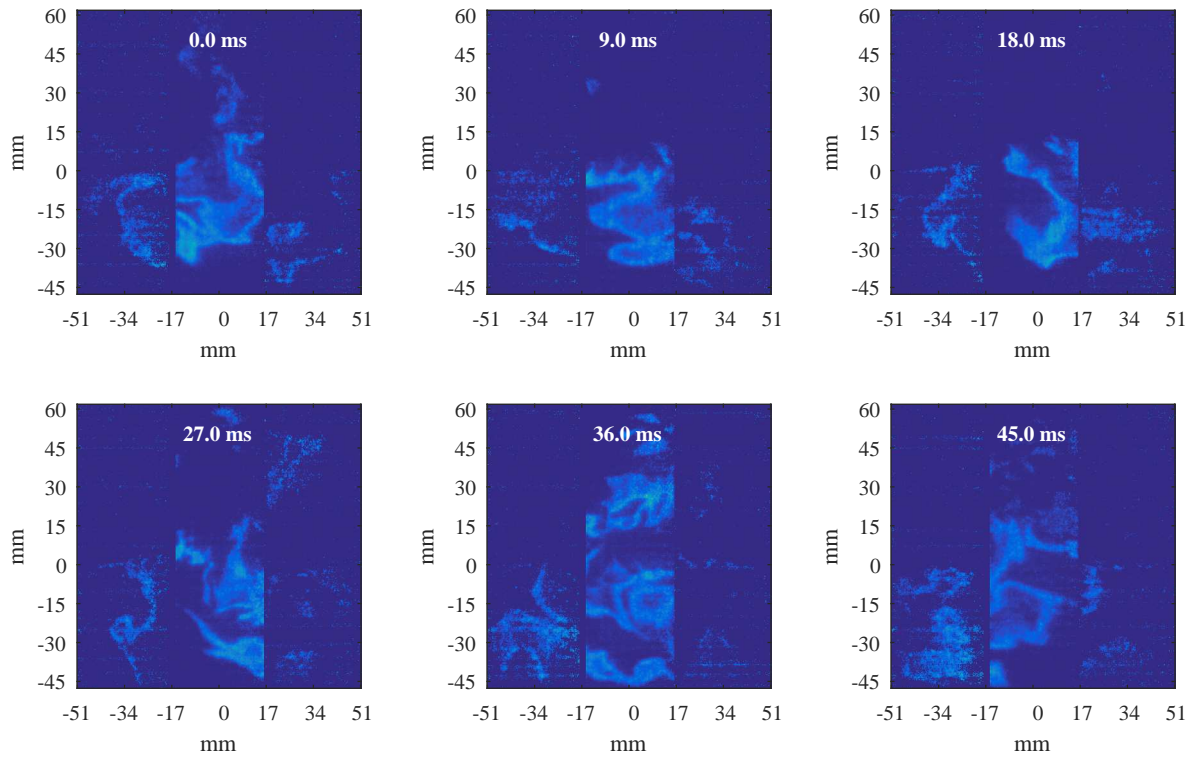


Figure 5.16: A sequence of OH PLIF images for the high air velocity case.

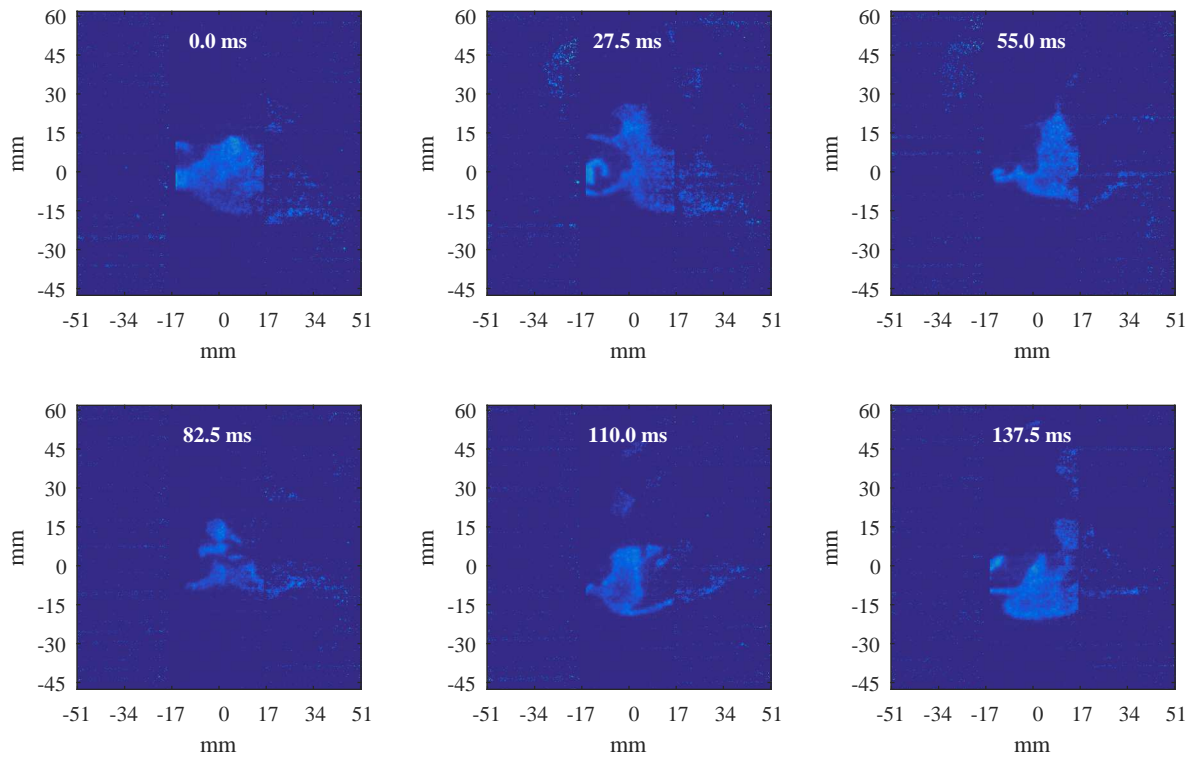
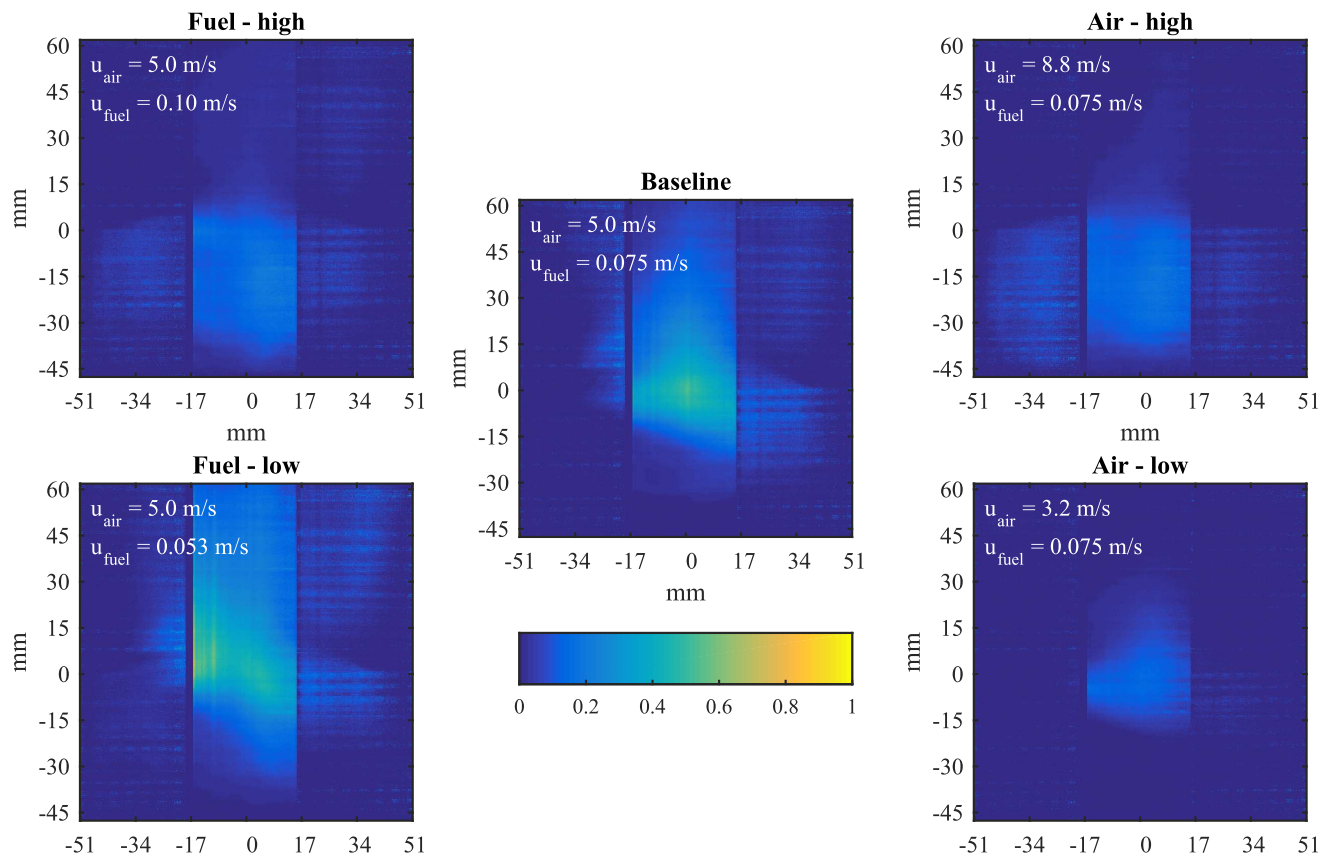


Figure 5.17: A sequence of OH PLIF images for the low air velocity case.

Average OH PLIF images for each of the five test cases are shown in Figures 5.18. Similar to the average OH\* CL signal, the average OH PLIF signal for the high air velocity case appears further below the air jets compared to the baseline and low air velocity cases. The average OH PLIF signal also appears further below the jets in the high fuel velocity case, and this result is attributed to the decreased influence of buoyancy due to the higher concentration of  $N_2$  in the fuel flow. Conversely, the average OH PLIF signal appears closer to the top of the window area in the low fuel velocity case, and this result is attributed to the increased influence of buoyancy due to the lower concentration of  $N_2$  in the fuel flow.



**Figure 5.18: Average OH PLIF images for each of the five test cases.**

Overall, the PLIF images suggest that a higher air jet velocities resulted in better mixing of air and fuel below the height of air injection and reduced the influence of buoyancy on the fluid dynamics. These changes appeared to result in a reaction zone that is situated further below the top of the burner. In a gasifier cookstove, a reaction zone that is situated

further below the top of the stove would be expected to allow oxidation of CO and PM to take place before these reactions are quenched by impingement of the flame on the relatively cold cooking surface.

### 5.3.3 Suitability of this System as a Model for the Secondary Combustion Zone in a TLUD

The burner used in this study is similar to the secondary combustion zone in a TLUD in that it features an inverse non-premixed flame in which the air and fuel are in cross flow. However, the burner featured two opposed planar jets of air whereas the secondary combustion zone in biomass gasifier cookstoves most often features opposed axisymmetric jets that may or may not impinge directly. Consequently, the limitations associated with using a system that consists of two opposed planar jets as a model for the secondary combustion zone must be assessed.

The simplest opposed jet configuration involves two isothermal, non-reacting opposed planar or axisymmetric jets configured such that outflow of the fluid in the direction perpendicular to a planar jet is unobstructed on both sides. Several researchers have investigated such planar<sup>188–193</sup> and axisymmetric<sup>191,193–196</sup> opposed jets both numerically<sup>190,193,195</sup> and experimentally.<sup>188–192,195,196</sup> These investigations have involved both liquid<sup>188,189</sup> and gaseous<sup>190–192,194,195</sup> fluids. Planar jets with  $1 \leq Re \leq 6288$  and  $0.025 \leq \alpha \leq 1$  and axisymmetric jets with  $1 \leq Re \leq 6600$  and  $0.025 \leq \alpha \leq 1$  have been considered.<sup>191–194</sup> In some studies, the jets issued from walls that surrounded the flow on two sides.<sup>192,193,195</sup> In others, the jets issued from stand-alone nozzles.<sup>188–192,194,196</sup> For simplicity, only configurations in which the velocities of the two opposed jets were equal will be considered here. The flow regimes reported for planar opposed jets include:

1. A steady, symmetric regime in which the stagnation plane is situated half way between the two jets. This regime has been identified using numerical simulation<sup>193</sup> and observed experimentally<sup>192</sup> for larger values of  $\alpha$  and small  $Re$  ( $\alpha \gtrsim 0.1 - 0.3$  and  $Re \lesssim 50$ ).

2. A steady, asymmetric regime in which the stagnation plane is shifted closer to one of the jets. This regime has been identified using numerical simulation<sup>193</sup> for  $\alpha \gtrsim 0.10$  and higher  $Re$ .
3. An unsteady regime involving periodic deflecting oscillation of the jets, as observed in the present study. This regime has been identified using numerical simulation<sup>193</sup> and observed experimentally.<sup>188–192</sup> This behavior occurs at practically all  $Re$  for  $\alpha \lesssim 0.10$ .<sup>192,193</sup>
4. An unsteady regime involving deflecting oscillation accompanied by vortex shedding. This regime was identified using numerical simulation<sup>193</sup> and was associated with larger  $Re$  than Regime 3. In fact, this behavior was predicted at all aspect ratios if  $Re$  became large enough.
5. An unsteady regime in which both jets remained on the plane of air injection, but the stagnation plane oscillated back and forth between the two nozzles. This regime has been observed experimentally<sup>191,192</sup> and was associated with larger values of  $\alpha$  and  $Re$  ( $\alpha \gtrsim 0.5$  and  $Re \gtrsim 800$ ). This is the only behavior that has been observed experimentally but has not been identified by numerical simulation. Li et al.<sup>191</sup> attributed this regime to external disturbances that exist in real-world systems.

Many of the flow regimes described for planar opposed jets have also been described for axisymmetric opposed jets with the exception of the deflecting oscillation regimes (3 and 4 above). In numerical simulations of axisymmetric jets with  $1 \leq Re \leq 2100$  and  $0.05 \leq \alpha \leq 1.5$ , Pawlowski et al.<sup>193</sup> identified solutions that corresponded to the symmetric (1) and axisymmetric (2) regimes, but did not identify any solutions that corresponded to the deflecting oscillation regimes (3 or 4). They hypothesized that the oscillatory flow regime was suppressed in the axisymmetric jet case because the axisymmetric jets diverged, and consequently decelerated, as they approached the center plane. Behavior that corresponds to the symmetric (1), asymmetric (2) and horizontal oscillation (5) regimes has been observed

experimentally.<sup>191,194,196</sup> The symmetric case has been associated with low Reynolds numbers and the asymmetric case has been associated with higher Reynolds numbers.<sup>193,195</sup>

One of the differences between the isothermal, non-reacting, unconfined opposed planar jets described above and the burner used in this study is that the fuel bed situated below the plane of jet injection prevents outflow in the downward direction. Opposed jets that are injected into a chamber in which outflow is permitted only on one end are the subject of studies on confined impinging jet (CIJ) mixers.<sup>197–202</sup> Cases in which two planar jets impinge upon each other inside of a chamber with a square cross section,<sup>197</sup> as well as cases in which two axisymmetric jets impinge upon each other inside of a chamber with a circular cross section,<sup>198–202</sup> have been investigated.

Li et al.<sup>201</sup> reported that a sort of deflecting oscillation did occur in a system consisting of two axisymmetric jets in a CIJ mixer for  $150 \leq Re \leq 300$ , and attributed this behavior to interaction of the recirculation zones that formed around the impinging jets with the jets and the walls of the mixing chamber. Behavior similar to that reported by Li et al.<sup>201</sup> appears in the images of two confined axisymmetric opposed jets presented by Fonte et al.<sup>202</sup> and is described by others for similar values of  $Re$ .<sup>199,200</sup> Unlike the deflecting oscillation reported for unconfined opposed planar jets, Li et al.<sup>201</sup> reported that the deflecting oscillation in the CIJ mixer became weaker with decreasing values of  $\alpha$  and ceased at higher Reynolds numbers.

There are also several differences between the geometry of the CIJ mixers described in these studies and the burner used in the present study: (1) the aspect ratio in the burner ( $\alpha = 0.016$ ) is smaller than the minimum aspect ratio considered in the CIJ mixers ( $\alpha = 0.083$ ),<sup>201</sup> (2) the distance between the air jets and the fuel bed in the burner ( $\approx 90\%$  of the distance between the jets) is larger than the distance between the jets and the closed end of the CIJ mixing chambers (typically half of the distance between the jets<sup>198,201,202</sup>), and (3) the walls that confine the flow in the burner do not extend as far downstream of the jets as the walls of the CIJ mixers.

Overall, the air jets in the burner used in the present study appear to behave similarly to unconfined opposed planar jets. It is unclear whether or not the deflecting oscillation observed in the chemiluminescence images for the baseline and high air velocity cases would occur in a similar system featuring opposed axisymmetric jets. However, it is also unclear whether or not the absence of oscillation would influence the trends observed in the acetone and OH PLIF images.

#### 5.4 Conclusions

The OH\* chemiluminescence images indicated that the deflecting oscillation that has been reported previously for isothermal, non-reacting, unconfined opposed planar jets also occurred in this system, comprised of reacting opposed planar jets that were subject to cross-flow, when the ratio of the jet velocity to the velocity of the cross flow was high and when the fuel was diluted with additional N<sub>2</sub> beyond that required for acetone seeding. Convection in the vertical direction and buoyancy effects appeared to suppress the oscillation in cases involving low jet velocities, high cross flow velocities, and low cross flow velocities (i.e., low N<sub>2</sub> dilution).

The PLIF images suggest that higher air jet velocities resulted in better mixing of the air and fuel below the height of air injection and resulted in a flame front location that was further below the top of the burner. These results suggest that the lower emissions that were observed with higher secondary air velocities in the TLUD test bed (see Chapter 4) may be attributable to better mixing of the air and fuel below the height of secondary air injection and a reaction zone that is located further below the top of the stove. The former would be expected to reduce the prevalence of fuel-rich zones that promote soot formation, and the latter would be expected to allow more time for oxidation of CO and PM before the gases in the secondary combustion zone impinge on the cold cooking surface.

The literature indicates that the regular deflecting oscillation that was observed in this experiment does not occur in systems involving unconfined, opposed axisymmetric jets. As a result, there may be limitations associated with the use of the burner described herein

as a model for the secondary combustion zone in a gasifier cookstove. The limitations that the observed asymmetry in the fuel flow imposes on the results also need to be considered. Future efforts should focus on investigation of a system consisting of opposed axisymmetric air jets reacting with a cross flow of fuel to ensure that the results are applicable to gasifier cookstoves.

## CHAPTER 6

### Conclusions and Future Work

The conclusions drawn from the studies presented in Chapters 3, 4, and 5 are summarized below in terms of each one of the objectives described in Section 1.3. As is typical, the knowledge gained through these studies has led to as many, if not more, new questions as conclusions. Several additional experiments are proposed involving: (1) laboratory testing of commercially available and/or prototype biomass cookstoves, (2) laboratory testing of an experimental facility similar to the modular TLUD test bed used in the study described in Chapter 4, and (3) application of laser diagnostics to a modified version of the burner used in the study described in Chapter 5.

#### 6.1 Conclusions

The first objective of the studies described herein was to identify the causes of variability in performance among different gasifier cookstove designs. To that end, five natural draft top-lit up draft gasifier cookstove design configurations were tested in the laboratory with two fuel types (corn cobs and Lodgepole pine pellets). Carbon monoxide emissions, particulate matter emissions ( $PM_{10}$ ), and efficiency were measured while 5 L of water was heated from 15 to 90 °C using a stove that started out at room temperature. One of the major conclusions drawn from this set of experiments was that cookstove design is not the only source of variability in performance—fuel type and operator behavior also influence emissions. Four of the five design configurations emitted more CO and  $PM_{10}$  during a cold start when fueled with corn cobs than when fueled with Lodgepole pine pellets. Emissions were similar with both fuels in the other configuration. Operator behavior influenced performance because large transient increases in carbon monoxide emission rates were observed when top-lit up draft gasifier cookstoves were refueled during operation by adding fresh biomass fuel on top of the hot char bed that was left behind after previous batches of fuel had gasified. Refueling emissions are important because one of the commercially-available cookstoves from which

three of the design configurations were derived was specifically designed to enable this type of refueling. Furthermore, researchers studying improved cookstove use in the field have found that users sometimes refuel gasifier stoves in this manner instead of removing the hot char and relighting the stove after each batch of fuel has been consumed.<sup>71</sup>

The second objective was to characterize the manner in which stove design, fuel properties, and operating mode influenced gasifier cookstove performance in more detail. A modular test bed that allowed design parameters, such as primary air flow rate, secondary air flow rate, and secondary air inlet design, to be controlled and varied was constructed. Carbon monoxide emissions, PM<sub>2.5</sub> emissions, useful power output, fuel consumption rate, the mass loss rate from the fuel bed, temperatures within the fuel bed, and the composition of the producer gas entering the secondary combustion zone were measured during a test in which the stove progressed through three operating modes: normal operation, post-refueling, and char burnout. More than 130 tests were conducted using 17 different stove geometries, 4 primary air flow rates, 4 secondary air flow rates, 5 secondary air temperatures, 4 fuel moisture contents, and 4 different fuel types. Higher secondary air jet velocities resulted in lower high-power CO emissions. For many cases in which the test bed was fueled with Douglas fir chips or Lodgepole pine pellets, the average high-power emissions fell within Tier 4 during normal operation, but fell within Tiers 1–3 post-refueling. In some cases, parameters that made the stove easier to re-light after refueling, such as higher primary air flow rates and lower fuel moisture contents, helped reduce the overall emissions and/or the variability in the emissions measurements associated with refueling.

In some cases, changes in fuel type resulted in order of magnitude changes in the high-power PM<sub>2.5</sub> emissions measured during normal operation. When operating normally, average high-power PM<sub>2.5</sub> emissions from the test bed fell within Tier 4 when the fuel was Lodgepole pine pellets or Douglas fir chips, Tier 3 when the fuel was Eucalyptus chips, and Tier 1 when the fuel was chipped corn cobs. Post-refueling, average high-power PM<sub>2.5</sub> emissions from the test bed fell within Tier 3 when the fuel was Lodgepole pine pellets, Tier 2

when the fuel was Douglas fir chips, Tier 1 when the fuel was Eucalyptus chips, and Tier 0 when the fuel was chipped corn cobs. Changes in fuel type also affected the composition of the producer gas entering the secondary combustion zone.

The temperature measurements taken at various heights in the fuel bed revealed that the increase in fuel bed temperature, which signaled the arrival of the pyrolysis zone, proceeded from the top of the fuel bed to the bottom during normal operation and from the bottom of the fuel bed to the top post-refueling. This difference means that the test bed operated as a TLUD, or inverted downdraft gasifier, during normal operation but as a conventional updraft gasifier post-refueling. This difference in operating mode could have important implications for emissions, as the concentration of tars in the producer gas exiting a gasifier is typically higher for updraft gasifiers than for downdraft gasifiers, and tar in the producer gas could eventually contribute to the overall particulate matter emissions from the stove. For the baseline case, the average concentrations of  $H_2$ ,  $CO$ , and  $CH_4$  in the producer gas entering the secondary combustion zone post-refueling were 61%, 36%, and 23% lower, respectively, than during normal operation.

The third objective was to gain insight into how secondary air velocity affected fuel-air mixing and the flame dynamics in the secondary combustion zone. A burner that produced a two-dimensional a model of the secondary combustion zone in a gasifier cookstove and provided optical access for planar laser-induced fluorescence (PLIF) imaging was constructed. Simulated producer gas fuel with a composition similar to that sampled from the modular test bed fueled with Lodgepole pine pellets was seeded with acetone and flowed up through a bed of glass beads before mixing with two horizontal opposed planar jets of air. The result was an inverse, non-premixed flame in which the air and fuel were in cross flow. Images of  $OH^*$  chemiluminescence were collected at 3 kHz to investigate the bulk dynamics of the flame. Images of  $OH$  PLIF and acetone PLIF were collected at 10 kHz to identify the location of the flame front and investigate the fuel-air mixing process. Images were collected at three different air jet velocities and three different fuel velocities. The PLIF images revealed that

higher air jet velocities resulted in more extensive mixing of the air and fuel below the height of the air jets and a flame front that was positioned further below the top of the burner. The results of the PLIF imaging supported the results obtained by varying the secondary air jet diameter in the modular test bed: that higher air jet velocities resulted in lower emissions, probably as a result of increased turbulence in the secondary combustion zone leading to better fuel-air mixing.

The chemiluminescence images revealed regular deflecting oscillation of the air jets in the baseline and high air velocity test cases. In other cases, the oscillation appeared to be suppressed by buoyancy effects and/or the upward convection of the fuel. This deflecting oscillation behavior has been reported previously in isothermal, non-reacting, unconfined opposed planar jets. A review of the literature suggested that this deflecting oscillation might not be observed in a similar burner featuring two opposed axisymmetric jets and, consequently, there may be limitations associated with the use of two opposed planar jets in a model for the secondary combustion zone in a gasifier cookstove. In most gasifier cookstoves, the secondary combustion zone features a ring of axisymmetric air jets which may or may not impinge directly.

The fourth objective was evaluate whether or not the reductions in emission rates that are sought (i.e., Tier 4 performance) could be achieved using the top-lit up draft gasifier design. The results presented in Chapter 4 illustrate that Tier 4 high-power CO and PM<sub>2.5</sub> emissions ( $\leq 8 \text{ g}\cdot\text{MJ}_d^{-1}$  and  $\leq 41 \text{ mg}\cdot\text{MJ}_d^{-1}$ ) were readily achieved when the modular TLUD test bed was operating normally and fueled with Lodgepole pine pellets or Douglas fir chips. The high-power emissions measured for the best-performing test cases from Chapter 4 are summarized in Table 6.1. One limitation associated with the experiments presented herein is that performance was primarily evaluated during high-power operation. Efforts to develop prototype TLUD biomass gasifier cookstoves using the knowledge gained from these experiments will also need to consider low-power performance.

**Table 6.1: Lowest high-power CO and PM<sub>2.5</sub> emissions measured during normal operation of the modular TLUD test bed.**

Test case	Phase 1 high-power emissions	
	CO (g·MJ <sub>d</sub> <sup>-1</sup> )	PM <sub>2.5</sub> (mg·MJ <sub>d</sub> <sup>-1</sup> )
	$\bar{x} \pm 90\% \text{ CI}$	$\bar{x} \pm 90\% \text{ CI}$
Baseline (Douglas fir chips, 7% moisture, 25 g·min <sup>-1</sup> primary air, 4-mm-diameter holes)	2.7 ± 1.1	28 ± 15
Early air injection	2.0 ± 0.63	28 ± 11
Lodgepole pine pellets	1.8 ± 1.2	23 ± 4.7
30 g·min <sup>-1</sup> primary air	1.5 ± 1.1	21 ± 7.2
2-mm-diameter holes	1.8 ± 0.49	20 ± 13
0% moisture content (Douglas fir chips)	1.6 ± 0.48	18 ± 1.0

A prototype forced-air top-lit up draft gasifier cookstove (shown in Figure 6.1) has been developed using the knowledge gained from the study presented in Chapter 4. At the time of writing, preliminary testing of the prototype in accordance with the Emissions and Performance Test Protocol<sup>148,150</sup> indicated that it achieved Tier 4 performance according to all of the ISO IWA emissions and efficiency metrics listed in Table 1.2 when operated normally (i.e., without refueling). In the prototype, both the primary and secondary air flows are assisted by a single fan. More information on the development and performance of the prototype can be found in a thesis by Tillotson<sup>203</sup>.



**Figure 6.1: A photograph of the prototype TLUD gasifier cookstove that was developed as a result of this work.**

Despite the low emissions shown in Table 6.1, the results presented herein suggest that efforts to evaluate the potential of improved biomass cookstoves to reduce CO and PM emissions should consider the fuels and operator behaviors that are likely to accompany stove use in the field in addition to cookstove design. It is the opinion of this author that promoting biomass cookstoves as achieving large reductions in CO and PM<sub>2.5</sub> emissions on the basis of results from controlled laboratory testing in accordance with water boiling test procedures is misleading. A real user's choice of fuel is likely to be dictated by availability and cost. Similarly, the manner in which the user operates the stove is likely to be dictated by convenience and the cooking task at hand. The results presented in Chapters 3 and 4 suggest that large differences between laboratory and real-world performance might arise as a result of differences in fuel type and operating procedure, at least in the case of gasifier cookstoves. Such differences are especially problematic if laboratory testing results in a gross underestimate of in-field emissions. Previous studies have demonstrated that laboratory tests may under- or over-estimate field emissions depending on the stove type and cooking task, with underestimation being more common.<sup>204-206</sup> Current controlled laboratory test procedures are useful for evaluating performance during the design process and comparing different cookstove models, but field testing that provides insight into the fuels that will actually be used and the manner in which the stove will be operated to complete real cooking tasks appears to be a prerequisite to drawing conclusions regarding the reduction in exposure to household air pollution that a given stove is likely to produce. One way to address this problem is to gather information on real-world use via field testing and then conduct laboratory tests that utilize representative fuels and replicate real operator behavior (as suggested by Johnson et al.<sup>207</sup> and Chen et al.<sup>208</sup>) to generate a more realistic quantification of the emissions reductions that a stove is likely to achieve. Efforts are being made to address many of the current issues with evaluation of cookstove performance through the development of new guidelines for testing as part of the forthcoming ISO standards for cookstoves and clean cooking solutions.

## 6.2 Future Work

The conventional updraft gasifier operation that was observed post-refueling in Chapter 4 was hypothesized to lead to higher concentrations of condensible organics (“tars”) in the producer gas entering the secondary combustion zone and, as a result, contribute to the higher PM<sub>2.5</sub> emissions observed post-refueling. However, the filter samples collected in those experiments contained transient PM<sub>2.5</sub> emissions observed immediately after refueling and re-lighting as well as the steady state post-refueling emissions. To investigate this hypothesis further, additional experiments should be completed in which the transient emissions associated with refueling and the steady state post-refueling emissions are collected on separate filters. For example, a “transient” filter sample could be started when the secondary flame extinguishes (i.e., after the first batch of fuel has completely gasified) and stopped 1–2 minutes after the secondary combustion zone has been re-lit. A second “steady state” filter sample could be started immediately after the first and continue until the second batch of fuel has been completely gasified and the secondary flame extinguishes once again. These experiments could be conducted using the modular TLUD test bed or a commercially-available gasifier cookstove. Particulate matter emissions could also be collected on quartz filters and analyzed for elemental and organic carbon content to provide insight into how much condensible organics contribute to the total PM<sub>2.5</sub> emissions.

In accordance with the above hypothesis, the concentrations of H<sub>2</sub> and CO in the producer gas samples collected post-refueling may have been lower because more of the carbon and hydrogen in the fuel were converted to higher molecular weight tars. Because the concentrations of H<sub>2</sub> and CO in the producer gas were lower post-refueling than during normal operation, the heating values of the producer gas samples were lower. The mass loss rates from the fuel bed were similar before and after refueling (see Figures B.20–B.22), suggesting that the mass flow rates of gas into the secondary combustion zone were similar during both phases. Despite the reduced heating values and similar mass flow rates of the producer gas, the useful power outputs measured post-refueling were similar to those measured during nor-

mal operation (see Figures B.17–B.19). Since it is unlikely that the efficiency of heat transfer to the pot changed between the two phases, the similar power outputs lend credence to the hypothesis that higher molecular weight organic molecules were present in the producer gas and contributed to heat release in the secondary combustion zone. This hypothesis can be investigated further by performing a formal energy balance using the gas composition, mass loss rate, and useful power output data.

The variation in concentrations of H<sub>2</sub> and CO in the producer gas, as well as the variation in the overall emissions from the stove, observed with different fuel types in Chapter 4 was also hypothesized to result from different fuel types leading to varying concentrations of tar in the producer gas. In that set of experiments, tars were removed from the gas samples collected between the fuel bed and the secondary combustion zone. Prior to future experiments with the modular test bed, the producer gas sampling system should be redesigned so that the tars in the gas sample can be collected to determine how tar production rates and tar composition vary with fuel type and operating mode. Guidelines for sampling tars from a gasifier are provided in Simell et al.<sup>102</sup> and an experimental system is described by Rubiano<sup>209</sup>.

More work is needed to understand why and how different fuel types result in low (i.e., Tier 4) or high (i.e., Tier 0–1) emissions. Testing one TLUD gasifier and one rocket elbow cookstove in the laboratory with as many different fuels as possible and measuring the resulting emissions could help answer the following questions: (1) What are the similarities and differences between the fuels that result in low versus high emissions? (2) Is one of the two cookstove designs more sensitive to changes in fuel type?

Additional testing should be performed to determine the degree to which the biochemical composition of the fuel, as opposed to physical properties, influences emissions. One gasifier cookstove could be tested with several varieties of pelletized fuels that have similar sizes, densities, and moisture contents, but were made from different biomass feedstocks, to separate the influence of biochemical composition from physical properties.

Some studies have reported that more efficient cookstoves, such as gasifiers, emit more ultrafine particles than an open fire.<sup>36,210</sup> As discussed in Section 1.1, ultrafine particles may be especially harmful to human health,<sup>33,34</sup> and concern has been expressed that the health benefits sought through improved cookstoves programs may not be achieved if improved stoves emit less PM<sub>2.5</sub> on a mass basis but more ultrafine particles than traditional stoves.<sup>36</sup> To investigate these concerns further, real-time PM measurements should be collected from the modular test bed and/or commercially available gasifier cookstoves using a fast mobility particle sizer (FPMS) to characterize the size distribution of PM emitted from a gasifier cookstove and the manner in which that size distribution changes with operating mode.

Two additional experiments involving the application of laser combustion diagnostics to a burner similar to that described in Chapter 5 are also proposed. First, the fuel delivery system used in the burner should be redesigned to rectify the uneven distribution of fuel that was observed in the acetone PLIF images shown in Chapter 5. Another burner that features two opposed axisymmetric jets subjected to a cross flow of fuel and optical access for laser diagnostics should also be developed. Images of OH PLIF, PAH PLIF, and soot LII could be collected from an improved burner, using an experimental setup similar to that used by Shaddix et al.<sup>145</sup>, to investigate the locations of soot precursor and soot formation relative to the flame front. Although these images would most likely need to be collected at 10 Hz and would only provide information about the average location of PAHs, soot, and OH, the images would allow the similarities and differences between the soot formation and oxidation process in a gasifier cookstove to be compared and contrasted with the soot formation and oxidation processes in normal and inverse non-premixed flames. Note that the composition of the fuel gas may have to be adjusted for these experiments to produce sootier flames. Images of OH and acetone PLIF should be collected at 10 kHz from a burner that features opposed axisymmetric jets to determine: (1) whether deflecting oscillation occurs in this system and (2) how the mixing process compares to that observed in the burner with opposed planar jets.

## REFERENCES

- [1] Bonjour, S.; Adair-Rohani, H.; Wolf, J.; Bruce, N. G.; Mehta, S.; Prüss-Ustün, A.; Lahiff, M.; Rehfuess, E. A.; Mishra, V.; Smith, K. R. Solid Fuel Use for Household Cooking: Country and Regional Estimates for 1980–2010. *Environ. Health Perspect.* **2013**, *121*, 784–790, DOI: 10.1289/ehp.1205987.
- [2] World Health Organization (WHO), Population using solid fuels (%), 2013. 2015; [http://gamapserv.who.int/mapLibrary/Files/Maps/Global\\_iap\\_exposure\\_2013.png](http://gamapserv.who.int/mapLibrary/Files/Maps/Global_iap_exposure_2013.png) (accessed Mar 4, 2016).
- [3] Legros, G.; Havet, I.; Bruce, N.; Bonjour, S. *The Energy Access Situation in Developing Countries: A Review Focusing on the Least Developed Countries and Sub-Saharan Africa*; United Nations Development Program and World Health Organization: New York, 2009.
- [4] Smith, K. R.; Samet, J. M.; Romieu, I.; Bruce, N. Indoor air pollution in developing countries and acute lower respiratory infections in children. *Thorax* **2000**, *55*, 518–532, DOI: 10.1136/thorax.55.6.518.
- [5] Kurmi, O. P.; Semple, S.; Simkhada, P.; Smith, W. C. S.; Ayres, J. G. COPD and chronic bronchitis risk of indoor air pollution from solid fuel: a systematic review and meta-analysis. *Thorax* **2010**, *65*, 221–228, DOI: 10.1136/thx.2009.124644.
- [6] Zhao, Y.; Wang, S.; Aunan, K.; Seip, H. M.; Hao, J. Air pollution and lung cancer risks in China—a meta-analysis. *Sci. Total Environ.* **2006**, *366*, 500–513, DOI: 10.1016/j.scitotenv.2005.10.010.
- [7] Bruce, N.; Perez-Padilla, R.; Albalak, R. Indoor air pollution in developing countries: a major environmental and public health challenge. *Bull. W. H. O.* **2000**, *78*, 1078–1092.
- [8] Boy, E.; Bruce, N.; Delgado, H. Birth Weight and Exposure to Kitchen Wood Smoke During Pregnancy in Rural Guatemala. *Environ. Health Perspect.* **2002**, *110*, 109–114.
- [9] Smith, K. R.; Mehta, S.; Maeusezahl-Feuz, M. Indoor air pollution from household use of solid fuels. In *Comparative Quantification of Health Risks: Global and Regional Burden of Disease Attributable to Selected Major Risk Factors*; Ez-zati, M., Lopez, A. D., Rodgers, A., Murray, C. J. L., Eds.; World Health Organization: Geneva, Switzerland, 2004; Vol. 2; Chapter 18, pp 1435–1494, [http://www.who.int/healthinfo/global\\_burden\\_disease/cra/en/](http://www.who.int/healthinfo/global_burden_disease/cra/en/) (accessed Mar 9, 2016).
- [10] Forouzanfar, M. H.; Alexander, L.; Anderson, H. R.; Bachman, V. F.; Biryukov, S.; Brauer, M.; Burnett, R.; Casey, D.; Coates, M. M.; Cohen, A. et al. Global, regional, and national comparative risk assessment of 79 behavioural, environmental and occupational, and metabolic risks or clusters of risks in 188 countries, 1990–2013: a systematic analysis for the Global Burden of Disease Study 2013. *Lancet* **2015**, *386*, 2287–2323, DOI: 10.1016/S0140-6736(15)00128-2.

- [11] Lan, Q.; Chapman, R. S.; Schreinemachers, D. M.; Tian, L.; He, X. Household Stove Improvement and Risk of Lung Cancer in Xuanwei, China. *J. Natl. Cancer Inst.* **2002**, *94*, 826–835, DOI: 10.1093/jnci/94.11.826.
- [12] Chapman, R. S.; He, X.; Blair, A. E.; Lan, Q. Improvement in household stoves and risk of chronic obstructive pulmonary disease in Xuanwei, China: retrospective cohort study. *BMJ* **2005**, *331*, 1050, DOI: 10.1136/bmj.38628.676088.55.
- [13] Shen, M.; Chapman, R. S.; Vermeulen, R.; Tian, L.; Zheng, T.; Chen, B. E.; Engels, E. A.; He, X.; Blair, A.; Lan, Q. Coal Use, Stove Improvement, and Adult Pneumonia Mortality in Xuanwei, China: A Retrospective Cohort Study. *Environ. Health Perspect.* **2010**, *117*, 261–266, DOI: 10.1289/ehp.11521.
- [14] Clark, M. L.; Bachand, A. M.; Heiderscheidt, J. M.; Yoder, S. A.; Luna, B.; Volckens, J.; Koehler, K. A.; Conway, S.; Reynolds, S. J.; Peel, J. L. Impact of a cleaner-burning cookstove intervention on blood pressure of Nicaraguan women. *Indoor Air* **2013**, *23*, 105–114, DOI: 10.1111/ina.12003.
- [15] Smith, K. R.; McCracken, J. P.; Weber, M. W.; Hubbard, A.; Jenny, A.; Thompson, L. M.; Balmes, J.; Diaz, A.; Arana, B.; Bruce, N. Effect of reduction in household air pollution on childhood pneumonia in Guatemala (RESPIRE): a randomised controlled trial. *Lancet* **2011**, *378*, 1717–1726, DOI: 10.1016/j.esd.2011.05.001.
- [16] Romieu, I.; Riojas-Rodríguez,; Marrón-Mares, A. T.; Schilman, A.; Perez-Padilla, R.; Maser, O. Improved Biomass Stove Intervention in Rural Mexico. *Am. J. Respir. Crit. Care Med.* **2009**, *180*, 649–656, DOI: 10.1164/rccm.200810-1556OC.
- [17] Clark, M. L.; Peel, J. L.; Burch, J. B.; Nelson, T. L.; Robinson, M. M.; Conway, S.; Bachand, A. M.; Reynolds, S. J. Impact of improved cookstoves on indoor air pollution and adverse health effects among Honduran women. *Int. J. Environ. Health Res.* **2009**, *19*, 357–368, DOI: 10.1080/09603120902842705.
- [18] Hanna, R.; Duflo, E.; Greenstone, M. *Up in Smoke: The Influence of Household Behavior on the Long-Run Impact of Improved Cooking Stoves*; Working Paper 18033; National Bureau of Economic Research: Cambridge, MA, 2012; <http://www.nber.org/papers/w18033> (accessed Mar 24, 2016).
- [19] J-PAL Policy Briefcase, *Up in Smoke*; Abdul Latif Jameel Poverty Action Lab: Cambridge, MA, 2012.
- [20] Bruce, N.; Smith, K. R.; Balmes, J.; Pope, D.; Dherani, M.; Zhang, J.; Duan, X.; Bates, M.; Lin, W.; Adair-Rohani, H. et al. *WHO Indoor Air Quality Guidelines: Household Fuel Combustion – Review 4: Health effects of household air pollution (HAP) exposure*; World Health Organization: Geneva, Switzerland, 2014; [http://www.who.int/indoorair/guidelines/hhfc/Review\\_4.pdf](http://www.who.int/indoorair/guidelines/hhfc/Review_4.pdf) (accessed Mar 9, 2016).
- [21] World Health Organization, *WHO guidelines for indoor air quality: household fuel combustion*; WHO Document Production Services: Geneva, Switzerland,

- 2014; <http://www.who.int/indoorair/publications/household-fuel-combustion/en> (accessed Jan 6, 2016).
- [22] Smith, K. R.; Peel, J. L. Mind the Gap. *Environ. Health Perspect.* **2010**, *118*, 1643–1645, DOI: 10.1289/ehp.1002517.
- [23] Pope III, C. A.; Burnett, R. T.; Krewski, D.; Jerrett, M.; Shi, Y.; Calle, E. E.; Thun, M. J. Cardiovascular Mortality and Exposure to Airborne Fine Particulate Matter and Cigarette Smoke: Shape of the Exposure-Response Relationship. *Circulation* **2009**, *120*, 941–948, DOI: 10.1161/CIRCULATIONAHA.109.857888.
- [24] Pope III, C. A.; Burnett, R. T.; Turner, M. C.; Cohen, A.; Krewski, D.; Jerrett, M.; Gapstur, S. M.; Thun, M. J. Lung Cancer and Cardiovascular Disease Mortality Associated with Ambient Pollution and Cigarette Smoke: Shape of the Exposure-Response Relationships. *Environ. Health Perspect.* **2011**, *119*, 1616–1621, DOI: 10.1289/ehp.1103639.
- [25] Clark, M. L.; Peel, J. L.; Balakrishnan, K.; Breyse, P. N.; Chillrud, S. N.; Naeher, L. P.; Rodes, C. E.; Vette, A. F.; Balbus, J. M. Health and Household Air Pollution from Solid Fuel Use: The Need for Improved Exposure Assessment. *Environ. Health Perspect.* **2013**, *121*, 1120–1128, DOI: 10.1289/ehp.1206429.
- [26] ISO International Workshop on Clean and Efficient Cookstoves. 2012; <http://www.pciaonline.org/files/ISO-IWA-Cookstoves.pdf> (accessed Feb 25, 2014).
- [27] U.S. Environmental Protection Agency (EPA), Nonroad Compression-Ignition Engines – Exhaust Emission Standards. <http://www3.epa.gov/otaq/standards/nonroad/nonroadci.htm> (accessed Mar 8, 2016).
- [28] Control of Emissions from New and In-Use Nonroad Compression-Ignition Engines. *Code of Federal Regulations*, Part 89, Title 40, 1994.
- [29] Control of Emissions from New and In-Use Nonroad Compression-Ignition Engines. *Code of Federal Regulations*, Part 1039, Title 40, 2004.
- [30] The Water Boiling Test: Version 4.2.3. 2014; <http://cleancookstoves.org/binary-data/DOCUMENT/file/000/000/399-1.pdf> (accessed Jan 4, 2016).
- [31] World Health Organization, *Air Quality Guidelines: Global Update 2005*; WHO Regional Office for Europe: Copenhagen, Denmark, 2005; [http://www.euro.who.int/\\_data/assets/pdf\\_file/0005/78638/E90038.pdf](http://www.euro.who.int/_data/assets/pdf_file/0005/78638/E90038.pdf) (accessed Mar 9, 2016).
- [32] World Health Organization, *WHO Guidelines for Indoor Air Quality: Selected Pollutants*; WHO Regional Office for Europe: Copenhagen, Denmark, 2010; [http://www.euro.who.int/\\_data/assets/pdf\\_file/0009/128169/e94535.pdf](http://www.euro.who.int/_data/assets/pdf_file/0009/128169/e94535.pdf) (accessed Mar 9, 2016).

- [33] Oberdörster, G. Pulmonary effects of inhaled ultrafine particles. *Int. Arch. Occup. Environ. Health* **2001**, *74*, 1–8, DOI: 10.1007/s004200000185.
- [34] Health Effects Institute, *Understanding the Health Effects of Ambient Ultrafine Particles*; HEI Perspectives 3; Health Effects Institute: Boston, MA, 2013; <http://pubs.healtheffects.org/getfile.php?u=893> (accessed Mar 10, 2016).
- [35] Health Effects Institute, *Traffic-Related Air Pollution: A Critical Review of the Literature on Emissions, Exposure, and Health Effects*; Special Report 17; Health Effects Institute: Boston, MA, 2010; Chapter 3, pp 3–1–3–84, <http://pubs.healtheffects.org/getfile.php?u=553> (accessed Mar 10, 2016).
- [36] Just, B.; Rogak, S.; Kandlikar, M. Characterization of Ultrafine Particulate Matter from Traditional and Improved Biomass Cookstoves. *Environ. Sci. Technol.* **2013**, *47*, 3506–3512, DOI: 10.1021/es304351p.
- [37] Mills, N. L.; Miller, M. R.; Lucking, A. J.; Beveridge, J.; Flint, L.; Boere, A. J. F.; Fokkens, P. H.; Boon, N. A.; Sandstrom, T.; Blomberg, A. et al. Combustion-derived nanoparticulate induces the adverse vascular effects of diesel exhaust inhalation. *Eur. Heart J.* **2011**, *31*, 2660–2671, DOI: 10.1093/eurheartj/ehr195.
- [38] Smith, K. R. In praise of petroleum? *Science* **2002**, *298*, 1847.
- [39] Goldemberg, J.; Johansson, T. B.; Reddy, A. K. N.; Williams, R. H. A global clean cooking fuel initiative. *Energy Sustainable Dev.* **2004**, *8*, 5–12, DOI: 10.1016/S0973-0826(08)60462-7.
- [40] Sagar, A. D. Alleviating energy poverty for the world’s poor. *Energy Policy* **2005**, *33*, 1367–1372, DOI: 10.1016/j.enpol.2004.01.001.
- [41] Clean break. *Nature* **2014**, *509*, 533–534, DOI: 10.1038/509533b.
- [42] Lewis, J. J.; Pattanayak, S. K. Who Adopts Improved Fuels and Cookstoves? A Systematic Review. *Environ. Health Perspect.* **2012**, *120*, 637–645, DOI: 10.1289/ehp.1104194.
- [43] Puzzolo, E.; Rehfuess, E.; Stanistreet, D.; Pope, D.; Bruce, N. *WHO Indoor Air Quality Guidelines: Household Fuel Combustion – Review 7: Factors influencing the adoption and sustained use of improved cookstoves and clean household energy*; World Health Organization: Geneva, Switzerland, 2014; [http://www.who.int/indoorair/guidelines/hhfc/Review\\_7.pdf](http://www.who.int/indoorair/guidelines/hhfc/Review_7.pdf) (accessed Mar 19, 2016).
- [44] Rehfuess, E. A.; Puzzolo, E.; Stanistreet, D.; Pope, D.; Bruce, N. G. Enablers and Barriers to Large-Scale Uptake of Improved Solid Fuel Stoves: A Systematic Review. *Environ. Health Perspect.* **2014**, *122*, 120–130, DOI: 10.1289/ehp.1306639.
- [45] Rehfuess, E.; Mehta, S.; Prüss-Üstün, A. Assessing household solid fuel use: Multiple implications for the millenium development goals. *Environ. Health Perspect.* **2006**, *114*, 373–378.

- [46] Global Alliance for Clean Cookstoves, *Igniting Change: A Strategy for Universal Adoption of Clean Cookstoves and Fuels*; Global Alliance for Clean Cookstoves: Washington DC, 2011; <http://cleancookstoves.org/resources/272.html> (accessed Mar 20, 2016).
- [47] Masera, O. R.; Saatkamp, B. D.; Kammen, D. M. From Linear Fuel Switching to Multiple Cooking Strategies: A Critique and Alternative to the Energy Ladder Model. *World Dev.* **2000**, *28*, 2083–2103, DOI: 10.1016/S0305-750X(00)00076-0.
- [48] Ruiz-Mercado, I.; Masera, O.; Zamora, H.; Smith, K. R. Adoption and sustained use of improved cookstoves. *Energy Policy* **2011**, *39*, 7557–7566, DOI: 10.1016/j.enpol.2011.03.028.
- [49] Ruiz-Mercado, I.; Canuz, E.; Walker, J. L.; Smith, K. R. Quantitative metrics of stove adoption using Stove Use Monitors (SUMs). *Biomass Bioenergy* **2013**, *57*, 136–148, DOI: 10.1016/j.biombioe.2013.07.002.
- [50] Ruiz-Mercado, I.; Masera, O. Patterns of Stove Use in the Context of Fuel-Device Stacking: Rationale and Implications. *EcoHealth* **2015**, *12*, 42–56, DOI: 10.1007/s10393-015-1009-4.
- [51] Subramanian, M. Deadly dinners. *Nature* **2014**, *509*, 548–551, DOI: 10.1038/509548a.
- [52] Johnson, M. A.; Chiang, A., Ranyee Quantitative Guidance for Stove Usage and Performance to Achieve Health and Environmental Targets. *Environ. Health Perspect.* **2015**, *123*, 820–826, DOI: 10.1289/ehp.1408681.
- [53] U.S. Department of Energy, *Biomass Cookstoves Technical Meeting: Summary Report*; U.S. Department of Energy: Alexandria, VA, 2011; [http://energy.gov/sites/prod/files/2014/04/f14/cookstove\\_meeting\\_summary.pdf](http://energy.gov/sites/prod/files/2014/04/f14/cookstove_meeting_summary.pdf) (accessed Apr 10, 2016).
- [54] Smith, K. R.; Balakrishnan, K. Mitigating climate, meeting MDGs, and moderating chronic disease: The health co-benefits landscape. In *Commonwealth Health Ministers' Update 2009*; Commonwealth Secretariat: London, 2009; Chapter 4, pp 59–65.
- [55] Smith, K. R.; Dutta, K. “Cooking with Gas”. *Energy Sustainable Dev.* **2011**, *15*, 115–116, DOI: 10.1016/j.esd.2011.05.001.
- [56] Simon, G. L.; Bailis, R.; Baumgartner, J.; Hyman, J.; Laurent, A. Current debates and future research needs in the clean cookstove sector. *Energy Sustainable Dev.* **2014**, *20*, 49–57, DOI: 10.1016/j.esd.2014.02.006.
- [57] Reed, T. B.; Larson, R. A wood-gas stove for developing countries. *Energy Sustainable Dev.* **1996**, *3*, 34–37, DOI: 10.1016/S0973-0826(08)60589-X.
- [58] Reed, T. B.; Das, A. *Handbook of Biomass Downdraft Gasifier Engine Systems*; SERI/SP-271-3022; Solar Energy Research Institute, U.S. Government Printing Office: Washington DC, 1988; pp 21–47.

- [59] Anderson, P. S.; Reed, T. B.; Wever, P. W. Micro-Gasification: What it is and why it works. *Boiling Point* **2007**, *53*, 35–37.
- [60] Thurber, M. C.; Phadke, H.; Nagavarapu, S.; Shrimali, G.; Zerriffi, H. ‘Oorja’ in India: Assessing a large-scale commercial distribution of advanced biomass stoves to households. *Energy Sustainable Dev.* **2014**, *19*, 138–150, DOI: 10.1016/j.esd.2014.01.002.
- [61] Panwar, N. L.; Rathore, N. S. Design and performance evaluation of a 5 kW producer gas stove. *Biomass Bioenergy* **2008**, *32*, 1349–1352, DOI: 10.1016/j.biombioe.2008.04.007.
- [62] Mukunda, H. S.; Dasappa, S.; Paul, P. J.; Rajan, N. K. S.; Yagnaraman, M.; Kumar, D. R.; Deogaonkar, M. Gasifier stoves — science, technology and field outreach. *Curr. Sci.* **2010**, *98*, 627–638.
- [63] Johnson, M. A.; Pilco, V.; Torres, R.; Joshi, S.; Shrestha, R. M.; Yagnaraman, M.; Lam, N. L.; Doroski, B.; Mitchell, J.; Canuz, E. et al. Impacts on household fuel consumption from biomass stove programs in India, Nepal, and Peru. *Energy Sustainable Dev.* **2013**, *17*, 403–411, DOI: 10.1016/j.esd.2013.04.004.
- [64] Kar, A.; Rehman, I. H.; Burney, J.; Puppala, S. P.; Suresh, R.; Singh, L.; Singh, V. K.; Ahmed, T.; Ramanathan, N.; Ramanathan, V. Real-Time Assessment of Black Carbon Pollution in Indian Households Due to Traditional and Improved Biomass Cookstoves. *Environ. Sci. Technol.* **2012**, *46*, 2993–3000, DOI: 10.1021/es203388g.
- [65] Singh, S.; Gupta, G. P.; Kumar, B.; Kulshrestha, U. C. Comparative study of indoor air pollution using traditional and improved cooking stoves in rural households of Northern India. *Energy Sustainable Dev.* **2014**, *19*, 1–6, DOI: 10.1016/j.esd.2014.01.007.
- [66] Sambandam, S.; Balakrishnan, K.; Ghosh, S.; Sadasivam, A.; Madhav, S.; Ramasamy, R.; Samanta, M.; Mukhopadhyay, K.; Rehman, H.; Ramanathan, V. Can Currently Available Advanced Combustion Biomass Cook-Stoves Provide Health Relevant Exposure Reductions? Results from Initial Assessment of Select Commercial Models in India. *EcoHealth* **2015**, *12*, 25–41, DOI: 10.1007/s10393-014-0976-1.
- [67] Carter, E. M.; Shan, M.; Yang, X.; Li, J.; Baumgartner, J. Pollutant Emissions and Energy Efficiency of Chinese Gasifier Cooking Stoves and Implications for Future Intervention Studies. *Environ. Sci. Technol.* **2014**, *48*, 6461–6467, DOI: 10.1021/es405723w.
- [68] Huangfu, Y.; Li, H.; Chen, X.; Xue, C.; Chen, C.; Liu, G. Effects of moisture content in fuel on thermal performance and emission of biomass semi-gasified cookstove. *Energy Sustainable Dev.* **2014**, *21*, 60–65, DOI: 10.1016/j.esd.2014.05.007.
- [69] Belonio, A. T. *Rice Husk Gas Stove Handbook*; Appropriate Technology Center, Department of Agricultural Engineering and Environmental Management, College of Agriculture, Central Philippine University: Iloilo City, Philippines, 2005; [http://www.bioenergylists.org/stovesdoc/Belonio/Belonio\\_gasifier.pdf](http://www.bioenergylists.org/stovesdoc/Belonio/Belonio_gasifier.pdf) (accessed Mar 30, 2016).

- [70] Roth, C. *Micro-gasification: cooking with gas from dry biomass*, 2nd ed.; Deutsche Gesellschaft für Internationale Zusammenarbeit (GIZ) GmbH: Eschborn, Germany, 2014; <https://www.giz.de/fachexpertise/downloads/giz2014-en-micro-gasification-manual-hera.pdf> (accessed Mar 30, 2016).
- [71] Lobscheid, A. B.; Lodoysamba, S.; Maddalena, R. L.; Dale, L. L. A pilot study of traditional and energy-efficient stove use in Ulaanbaatar, Mongolia. *Boiling Point* **2015**, *66*, 40–43.
- [72] Reed, T. B.; Anselmo, E.; Kircher, K. Testing & Modeling the Wood-Gas Turbo Stove. In *Progress in Thermochemical Biomass Conversion*; Bridgwater, A., Ed.; Blackwell Science Ltd: Oxford, U.K., 2008; pp 693–704.
- [73] Jetter, J. J.; Kariher, P. Solid-fuel household cook stoves: Characterization of performance and emissions. *Biomass Bioenergy* **2009**, *33*, 294–305, DOI: 10.1016/j.biombioe.2008.05.014.
- [74] MacCarty, N.; Still, D.; Ogle, D. Fuel use and emissions performance of fifty cooking stoves in the laboratory and related benchmarks of performance. *Energy Sustainable Dev.* **2010**, *14*, 161–171, DOI: 10.1016/j.esd.2010.06.002.
- [75] Jetter, J.; Zhao, Y.; Smith, K. R.; Khan, B.; Yelverton, T.; DeCarlo, P.; Hays, M. D. Pollutant Emissions and Energy Efficiency under Controlled Conditions for Household Biomass Cookstoves and Implications for Metrics Useful in Setting International Test Standards. *Environ. Sci. Technol.* **2012**, *46*, 10827–10834, DOI: 10.1021/es301693f.
- [76] Bain, R.; Graboski, M. Properties of Biomass Relevant to Gasification. In *Biomass Gasification: Principles and Technology*; Reed, T. B., Ed.; Energy Technology Review; Noyes Data Corporation: Park Ridge, NJ, 1981; Vol. 67; Chapter 3, pp 41–71.
- [77] Tillman, D. A. *The Combustion of Solid Fuels and Wastes*; Academic Press, Inc.: San Diego, CA, 1991.
- [78] Tanger, P.; Field, J. L.; Jahn, C. E.; DeFoort, M. W.; Leach, J. E. Biomass for thermochemical conversion: targets and challenges. *Frontiers in Plant Science* **2013**, *4*, 1–20, DOI: 10.3389/fpls.2013.00218.
- [79] Klemm, D.; Schmauder, H.-P.; Heinze, T. Cellulose. In *Polysaccharides II, Polysaccharides from Eukaryotes*; De Baets, S., Vandamme, E. J., Steinbüchel, A., Eds.; Biopolymers; Wiley-VCH Verlag GmbH: Weinheim, Germany, 2002; Vol. 6; Chapter 10, pp 275–319.
- [80] Taiz, L.; Zeiger, E. *Plant Physiology*, 4th ed.; Sinauer Associates, Inc.: Sunderland, MA, 2006.
- [81] Mehrtens, B. MCB 150 Frequently Asked Questions. 2007; <https://www.life.illinois.edu/mcb/150/private/faq/index.php?action=artikel&cat=3&id=10&artlang=en> (accessed Apr 2, 2016).

- [82] Faik, A. “Plant Cell Wall Structure-Pretreatment” the Critical Relationship in Biomass Conversion to Fermentable Sugars. In *Green Biomass Pretreatment for Biofuels Production*; Gu, T., Ed.; Springer: Dordrecht, Netherlands, 2013; Chapter 1, pp 1–30, DOI: 10.1007/978-94-007-6052-3\_1.
- [83] Fry, S. C. Cell Walls and Fibers. In *Encyclopedia of Applied Plant Sciences*; Thomas, B., Murphy, D. J., Murray, B. G., Eds.; Elsevier Ltd.: San Diego, CA, 2003; Vol. 1; pp 75–105.
- [84] Tillman, D. A.; Rossi, A. J.; Kitto, W. D. *Wood Combustion: Principles, Processes, and Economics*; Academic Press: New York, 1981.
- [85] Bajpai, P. *Pretreatment of Lignocellulosic Biomass for Biofuel Production*; Springer: Singapore, 2016; Chapter 2, pp 7–12, DOI: 10.1007/978-981-10-0687-6\_2.
- [86] Lai, Y.-Z. Wood and Wood Products. In *Handbook of Industrial Chemistry and Biotechnology*, twelfth ed.; Kent, J. A., Ed.; Springer: New York, 2012; Vol. 2; Chapter 28, pp 1057–1115, DOI: 10.1007/978-1-4614-4259-2\_28.
- [87] Thompson, N. S. Hemicellulose. In *Kirk-Othmer Encyclopedia of Chemical Technology*; John Wiley & Sons, Inc.: New York, 2000; DOI: 10.1002/0471238961.0805130920081513.a01.
- [88] ASTM International, *Standard Test Method for Volatile Matter in the Analysis of Particulate Wood Fuels*; E872 – 82; ASTM International: West Conshohocken, PA, DOI: 10.1520/E0872-82R13.
- [89] ASTM International, *Standard Test Method for Determination of Ash Content of Particulate Wood Fuels*; D1534 – 93; ASTM International: West Conshohocken, PA, DOI: 10.1520/E1534-93R13.
- [90] ASTM International, *Standard Test Methods for Analysis of Wood Fuels*; E870 – 82; ASTM International: West Conshohocken, PA, DOI: 10.1520/E0870-82R06.
- [91] Ragland, K. W.; Bryden, K. M. *Combustion Engineering*, 2nd ed.; CRC Press: Boca Raton, FL, 2011.
- [92] Turns, S. R. *An Introduction to Combustion: Concepts and Applications*, 3rd ed.; McGraw-Hill: New York, 2012; Chapter 2, pp 12–78.
- [93] ASTM International, *Standard Test Method for Gross Calorific Value of Coal and Coke*; D5865 – 13; ASTM International: West Conshohocken, PA, DOI: 10.1520/D5865-13.
- [94] Siau, J. F. *Transport Processes in Wood*; Springer-Verlag: New York, 1984; Chapter 3, pp 73–104.
- [95] Tillman, D. A.; Harding, N. S. *Fuels of Opportunity: Characteristics and uses in Combustion Systems*; Elsevier: San Diego, CA, 2004.

- [96] Pettersen, R. C. The Chemical Composition of Wood. In *The Chemistry of Solid Wood*; Rowell, R., Ed.; Adv. Chem. Ser.; American Chemical Society: Washington, DC, 1984; Vol. 207; Chapter 2, pp 57–126.
- [97] Demirbaş, A. Calculation of higher heating values of biomass fuels. *Fuel* **1997**, *76*, 431–434.
- [98] Shafizadeh, F. The Chemistry of Pyrolysis and Combustion. In *The Chemistry of Solid Wood*; Rowell, R., Ed.; Adv. Chem. Ser.; American Chemical Society: Washington, DC, 1984; Vol. 207; Chapter 13, pp 489–529.
- [99] Bryden, K. M.; Ragland, K. W.; Rutland, C. J. Modeling thermally thick pyrolysis of wood. *Biomass Bioenergy* **2002**, *22*, 41–53, DOI: 10.1016/S0961-9534(01)00060-5.
- [100] Edwards, J. B. *Combustion: The Formation and Emission of Trace Species*; Ann Arbor Science Publishers Inc.: Ann Arbor, MI, 1974.
- [101] Faravelli, T.; Frassoldati, A.; Barker Hemings, E.; Ranzi, E. Multistep Kinetic Model of Biomass Pyrolysis. In *Cleaner Combustion: Developing Detailed Chemical Kinetic Models*; Battin-Leclerc, F., Simmie, J. M., Blurock, E., Eds.; Green Energy and Technology; Springer-Verlag: London, 2013; Chapter 6, pp 111–139, DOI: 10.1007/978-1-4471-5307-8\_5.
- [102] Simell, P.; Ståhlberg, P.; Kurkela, E.; Albrecht, J.; Deutsch, S.; Sjöström, Provisional protocol for the sampling and analysis of tar and particulates in the gas from large-scale biomass gasifiers. Version 1998. *Biomass Bioenergy* **2000**, *18*, 19–38, DOI: 10.1016/S0961-9534(99)00064-1.
- [103] Evans, R. J.; Milne, T. A. Molecular Characterization of the Pyrolysis of Biomass. 1. Fundamentals. *Energy Fuels* **1987**, *1*, 123–137.
- [104] Evans, R. J.; Milne, T. A. Chemistry of Tar Formation and Maturation in the Thermochemical Conversion of Biomass. In *Developments in Thermochemical Biomass Conversion*; Bridgwater, A. V., Boocock, D. G. B., Eds.; Springer Science+Business Media: Dordrecht, Netherlands, 1997; Vol. 2; pp 803–816.
- [105] Milne, T. A.; Evans, R. J.; Abatzoglou, N. *Biomass Gasifier “Tars”: Their Nature, Formation, and Conversion*; NREL/TP-570-25357; National Renewable Energy Laboratory, National Technical Information Service (NTIS): Springfield, VA, 1998.
- [106] Yang, H.; Yan, R.; Chen, H.; Lee, D. H.; Zheng, C. Characteristics of hemicellulose, cellulose and lignin pyrolysis. *Fuel* **2007**, *86*, 1781–1788, DOI: 10.1016/j.fuel.2006.12.013.
- [107] Liu, Q.; Zhong, Z.; Wang, S.; Luo, Z. Interactions of biomass components during pyrolysis: A TG-FTIR study. *J. Anal. Appl. Pyrolysis* **2011**, *90*, 213–218, DOI: 10.1016/j.jaap.2010.12.009.
- [108] Worasuwannarak, N.; Sonobe, T.; Tanthapanichakoon, W. Pyrolysis behaviors of rice straw, rice husk, and corncob by TG-MS technique. *J. Anal. Appl. Pyrolysis* **2007**, *78*, 265–271, DOI: 10.1016/j.jaap.2006.08.002.

- [109] Hosoya, T.; Kawamoto, H.; Saka, S. Pyrolysis behaviors of wood and its constituent polymers at gasification temperature. *J. Anal. Appl. Pyrolysis* **2007**, *78*, 328–336, DOI: 10.1016/j.jaap.2006.08.008.
- [110] Jensen, A.; Dam-Johansen, K. TG-FTIR Study of the Influence of Potassium Chloride on Wheat Straw Pyrolysis. *Energy Fuels* **1998**, *12*, 929–938, DOI: 10.1021/ef980008i.
- [111] Ranzi, E.; Cuoci, A.; Faravelli, T.; Frassoldati, A.; Migliavacca, G.; Pierucci, S.; Sommariva, S. Chemical Kinetics of Biomass Pyrolysis. *Energy Fuels* **2008**, *22*, 4292–4300, DOI: 10.1021/ef800551t.
- [112] Hosoya, T.; Kawamoto, H.; Saka, S. Cellulose-hemicellulose and cellulose-lignin interactions in wood pyrolysis at gasification temperature. *J. Anal. Appl. Pyrolysis* **2007**, *80*, 118–125, DOI: 10.1016/j.jaap.2007.01.006.
- [113] Di Blasi, C. Influences of physical properties on biomass devolatilization characteristics. *Fuel* **1997**, *76*, 957–964, DOI: 10.1016/S0016-2361(97)00096-3.
- [114] Neves, D.; Thunman, H.; Matos, A.; Tarelho, L.; Gómez-Barea, A. Characterization and prediction of biomass pyrolysis products. *Prog. Energy Combust. Sci.* **2011**, *37*, 611–630, DOI: 10.1016/j.peccs.2011.01.001.
- [115] Glassman, I.; Yetter, R. A.; Glumac, N. G. *Combustion*, 5th ed.; Academic Press: Waltham, MA, 2015; Chapter 3, pp 71–146.
- [116] Geier, M.; Shaddix, C. R.; Holzleithner, F. A mechanistic char oxidation model consistent with observed CO<sub>2</sub>/CO production ratios. *Proc. Combust. Inst.* **2013**, *34*, 2411–2418, DOI: 10.1016/j.proci.2012.07.009.
- [117] Tilghman, M. B.; Mitchell, R. E. Coal and biomass char reactivities in gasification and combustion environments. *Combust. Flame* **2015**, *162*, 3220–3235, DOI: 10.1016/j.combustflame.2015.05.009.
- [118] Law, C. K. *Combustion Physics*; Cambridge University Press: New York, 2006.
- [119] Radovic, L. R. Carbons and Graphites, Reactivity of. In *Encyclopedia of Materials: Science and Technology*; Jürgen Buschow, K. H., Cahn, R. W., Flemings, M. C., Ilshner, B., Kramer, E. J., Mahajan, S., Eds.; Elsevier Science Ltd: Oxford, UK, 2001; Vol. 2; pp 975–985.
- [120] Jenkins, R. G. Thermal Gasification of Biomass – A Primer. In *Bioenergy: Biomass to Biofuels*; Dahiya, A., Ed.; Academic Press: London, 2015; Chapter 16, pp 261–286.
- [121] Reed, T. B.; Jantzen, D. Introductions. In *Biomass Gasification: Principles and Technology*; Reed, T. B., Ed.; Energy Technology Review; Noyes Data Corporation: Park Ridge, NJ, 1981; Vol. 67; Chapter 1, pp 28–34.

- [122] Graham, R. G.; Huffman, D. R. Gasification of Wood in a Commercial-Scale Downdraft Gasifier. In *Energy from biomass and wastes V: symposium papers presented January 26-30, 1981, Lake Buena Vista, Florida*; Klass, D. L., Weatherly III, J. W., Eds.; Institute of Gas Technology: Chicago, IL, 1981; pp 633–647.
- [123] Demirbas, A. *Methane Gas Hydrate*; Springer: London, 2010; Chapter 2, p 60.
- [124] Desrosiers, R. Thermodynamics of Gas-Char Reactions. In *Biomass Gasification: Principles and Technology*; Reed, T. B., Ed.; Energy Technology Review; Noyes Data Corporation: Park Ridge, NJ, 1981; Vol. 67; Chapter 6, pp 119–153.
- [125] Klass, D. L. *Biomass for Renewable Energy, Fuels, and Chemicals*, 2nd ed.; Academic Press: San Diego, CA, 1998; Chapter 9, pp 271–331.
- [126] Basu, P. *Biomass Gasification, Pyrolysis, and Torrefaction: Practical Design and Theory*, 2nd ed.; Academic Press: London, 2013; Chapter 7, pp 199–248.
- [127] Kersten, S. R. A.; de Jong, W. Thermochemical Conversion: (Co)gasification and Hydrothermal Gasification. In *Biomass as a Sustainable Energy Source for the Future: Fundamentals of Conversion Processes*; de Jong, W., van Ommen, J. R., Eds.; John Wiley & Sons, Inc.: Hoboken, NJ, 2015; Chapter 10, pp 298–358.
- [128] Kim, T. J.; Yetter, R. A.; Dryer, F. L. New results on moist CO oxidation: high pressure, high temperature experiments and comprehensive kinetic modeling. *Symp. (Int.) Combust.* **1994**, *25*, 759–766, DOI: 10.1016/S0082-0784(06)80708-3.
- [129] Lighty, J. S.; Veranth, J. M.; Sarofim, A. F. Combustion Aerosols: Factors Governing Their Size and Composition and Implications to Human Health. *J. Air Waste Manage. Assoc.* **2000**, *50*, 1565–1618, DOI: 10.1080/10473289.2000.10464197.
- [130] Khalek, I. A.; Kittelson, D. B.; Brear, F. *Nanoparticle Growth During Dilution and Cooling of Diesel Exhaust: Experimental Investigation and Theoretical Assessment*; 2000-01-0515; SAE International: Warrendale, PA, 2000.
- [131] Kuo, K. K. *Principles of Combustion*, 2nd ed.; John Wiley & Sons, Inc.: Hoboken, NJ, 2005.
- [132] Gelencsér, A. *Carbonaceous Aerosol*; Atmospheric and Oceanographic Sciences Library; Springer: Dordrecht, Netherlands, 2004; Vol. 30; Chapter 3, pp 45–68.
- [133] Haynes, B. S.; Wagner, H. G. Soot Formation. *Prog. Energy Combust. Sci.* **1981**, *7*, 229–273.
- [134] Vander Wal, R. L.; Tomasek, A. J. Soot nanostructure: dependence upon synthesis conditions. *Combust. Flame* **2004**, *136*, 129–140, DOI: 10.1016/j.combustflame.2003.09.008.
- [135] Wang, H. Formation of nascent soot and other condensed-phase materials in flames. *Proc. Combust. Inst.* **2011**, *33*, 41–67, DOI: 10.1016/j.proci.2010.09.009.

- [136] Frenklach, M. Reaction mechanism of soot formation in flames. *Phys. Chem. Chem. Phys.* **2002**, *4*, 2028–2037, DOI: 10.1039/B110045A.
- [137] Fitzpatrick, E. M.; Jones, J. M.; Pourkashanian, M.; Ross, A. B.; Williams, A.; Bartle, K. D. Mechanistic Aspects of Soot Formation from the Combustion of Pine Wood. *Energy Fuels* **2008**, *22*, 3771–3778.
- [138] Li, J.; Pósfai, M.; Hobbs, P. V.; Buseck, P. R. Individual particles from biomass burning in southern Africa: 2. Compositions and aging of inorganic particles. *J. Geophys. Res.: Atmos.* **2003**, *108*, DOI: 10.1029/2002JD002310, 8484.
- [139] Pósfai, M.; Simonics, R.; Li, J.; Hobbs, P. V.; Buseck, P. R. Individual particles from biomass burning in southern Africa: 1. Compositions and size distributions of carbonaceous particles. *J. Geophys. Res.: Atmos.* **2003**, *108*, DOI: 10.1029/2002JD002291, 8483.
- [140] Pósfai, M.; Gelencsér, A.; Simonics, R.; Arató, K.; Li, J.; Hobbs, P. V.; Buseck, P. R. Atmospheric tar balls: Particles from biomass and biofuel burning. *J. Geophys. Res.: Atmos.* **2004**, *109*, DOI: 10.1029/2003JD004169, D06213.
- [141] Torvela, T.; Tissari, J.; Sippula, O.; Kaivosoja, T.; Leskinen, J.; Virén, A.; Lähde, A.; Jokiniemi, J. Effect of wood combustion conditions on the morphology of freshly emitted fine particles. *Atmos. Environ.* **2014**, *87*, 65–76, DOI: 10.1016/j.atmosenv.2014.01.028.
- [142] Xu, F.; El-Leathy, A. M.; Kim, C. H.; Faeth, G. M. Soot surface oxidation in hydrocarbon/air diffusion flames at atmospheric pressure. *Combust. Flame* **2003**, *132*, 43–57, DOI: 10.1016/S0010-2180(02)00459-5.
- [143] Guo, H.; Anderson, P. M.; Sunderland, P. B. Optimized rate expressions for soot oxidation by OH and O<sub>2</sub>. *Fuel* **2016**, *172*, 248–252, DOI: 10.1016/j.fuel.2016.01.030.
- [144] Kaplan, C. R.; Kailasanath, K. Flow-field Effects on Soot Formation in Normal and Inverse Methane-Air Diffusion Flames. *Combust. Flame* **2001**, *124*, 275–294, DOI: 10.1016/S0010-2180(00)00196-6.
- [145] Shaddix, C. R.; Williams, T. C.; Blevins, L. G.; Schefer, R. W. Flame structure of steady and pulsed sooting inverse jet diffusion flames. *Proc. Combust. Inst.* **2005**, *30*, 1501–1508, DOI: 10.1016/j.proci.2004.08.244.
- [146] Kang, K. T.; Hwang, J. Y.; Chung, S. H.; Lee, W. Soot Zone Structure and Sooting Limit in Diffusion Flames: Comparison of Counterflow and Co-Flow Flames. *Combust. Flame* **1997**, *109*, 266–281, DOI: 10.1016/S0010-2180(96)00163-0.
- [147] Wendelbo, P. The Peko Pe biomass household energy program. 2012; <http://wendelborecho.wordpress.com/2012/05/10/downloads> (accessed Feb 25, 2014).

- [148] DeFoort, M.; L'Orange, C.; Kreutzer, C.; Lorenz, N.; Kamping, W.; Alders, J. *Stove Manufacturers Emissions and Performance Test Protocol (EPTP)*; Engines and Energy Conversion Laboratory, Colorado State University: Fort Collins, CO, 2010; <http://cleancookstoves.org/binary-data/DOCUMENT/file/000/000/73-1.pdf> (accessed Jan 4, 2016).
- [149] Chiang, R.; Farr, K. Stove testing update - Release of Water Boiling Test protocol 4.2.3. 2014; <http://www.cleancookstoves.org/blog/release-wbt-protocol-4-2-3.html> (accessed Jun 23, 2014).
- [150] L'Orange, C.; DeFoort, M.; Willson, B. Influence of testing parameters on biomass stove performance and development of an improved testing protocol. *Energy Sustainable Dev.* **2012**, *16*, 3–12, DOI: 10.1016/j.esd.2011.10.008.
- [151] Incropera, F. P.; DeWitt, D. P.; Bergman, T. L.; Lavine, A. S. *Fundamentals of Heat and Mass Transfer*, sixth ed.; John Wiley and Sons: Hoboken, NJ, 2007.
- [152] Churchill, S. W.; Chu, H. H. S. Correlating equations for laminar and turbulent free convection from a vertical plate. *Int. J. Heat Mass Transfer* **1975**, *18*, 1323–1329, DOI: 10.1016/0017-9310(75)90243-4.
- [153] Nagendra, H. R.; Tirunarayanan, M. A.; Ramachandran, A. Free convection heat transfer in vertical annuli. *Chem. Eng. Sci.* **1970**, *25*, 605–610, DOI: 10.1016/0009-2509(70)85092-8.
- [154] Naeher, L. P.; Smith, K. R.; Leaderer, B. P.; Mage, D.; Grajeda, R. Indoor and outdoor PM<sub>2.5</sub> and CO in high- and low-density Guatemalan villages. *J. Exposure Anal. Environ. Epidemiol.* **2000**, *10*, 544–551, DOI: 10.1038/sj.jea.7500113.
- [155] Tian, L.; Lan, Q.; Yang, D.; He, X.; Yu, I. T. S.; Hammond, S. K. Effect of chimneys on indoor air concentrations of PM<sub>10</sub> and benzo[a]pyrene in Xuan Wei, China. *Atmos. Environ.* **2009**, *43*, 3352–3355, DOI: 10.1016/j.atmosenv.2009.04.004.
- [156] Northcross, A.; Chowdhury, Z.; McCracken, J.; Canuz, E.; Smith, K. R. Estimating personal PM<sub>2.5</sub> exposures using CO measurements in Guatemalan households cooking with wood fuel. *J. Environ. Monit.* **2010**, *12*, 873–878, DOI: 10.1039/B916068J.
- [157] Tryner, J.; Willson, B. D.; Marchese, A. J. The effects of fuel type and stove design on emissions and efficiency of natural-draft semi-gasifier biomass cookstoves. *Energy Sustainable Dev.* **2014**, *23*, 99–109, DOI: 10.1016/j.esd.2014.07.009.
- [158] Varunkumar, S.; Rajan, N. K. S.; Mukunda, H. S. Experimental and computational studies on a gasifier based stove. *Energy Convers. Manage.* **2011**, *53*, 135–141, DOI: 10.1016/j.enconman.2011.08.022.
- [159] Varunkumar, S.; Rajan, N. K. S.; Mukunda, H. S. Single Particle and Packed Bed Combustion in Modern Gasifier Stoves — Density Effects. *Combust. Sci. Technol.* **2011**, *183*, 1147–1163, DOI: 10.1080/00102202.2011.576658.

- [160] Kirch, T.; Birzer, C. H.; Medwell, P. R.; Holden, L. The role of primary and secondary air on wood combustion in cookstoves. *Int. J. Sustainable Energy* **2016**, 1–10, DOI: 10.1080/14786451.2016.1166110.
- [161] Kirch, T.; Medwell, P. R.; Birzer, C. H. Natural draft and forced primary air combustion properties of a top-lit up-draft research furnace. *Biomass Bioenergy* **2016**, *91*, 108–115, DOI: 10.1016/j.biombioe.2016.05.003.
- [162] Maddalena, R. L.; Lunden, M. M.; Wilson, D. L.; Ceballos, C.; Kirchstetter, T. W.; Slack, J. L.; Dale, L. L. Quantifying Space Heating Stove Emissions Related to Different Use Pattern in Mongolia. *Energy and Environ. Res.* **2014**, *4*, 147–157, DOI: 10.5539/eer.v4n3p147.
- [163] James R., A. M.; Yuan, W.; Boyette, M. D. The Effect of Biomass Physical Properties on Top-Lit Updraft Gasification of Woodchips. *Energies* **2016**, *9*, DOI: 10.3390/en9040283, 283.
- [164] Saravanakumar, A.; Haridasan, T. M.; Reed, T. B.; Bai, R. K. Experimental investigation and modeling study of long stick wood gasification in a top lit updraft fixed bed gasifier. *Fuel* **2007**, *86*, 2846–2856, DOI: 10.1016/j.fuel.2007.03.028.
- [165] Birzer, C.; Medwell, P.; Wilkey, J.; West, T.; Higgins, M.; MacFarlane, G.; Read, M. An analysis of combustion from a top-lit up-draft (TLUD) cookstove. *J. Humanitarian Eng.* **2013**, *2*, 1–8.
- [166] Report on tests on reverse downdraft stoves (REDS) for stove applications - 2003 to 2008. 2014; <http://cgpl.iisc.ernet.in/site/Portals/0/Publications/Report2004-2008.pdf> (accessed Apr 16, 2016).
- [167] Kshirsagar, M. P.; Kalamkar, V. R. A comprehensive review on biomass cookstoves and a systematic approach for modern cookstove design. *Renewable Sustainable Energy Rev.* **2014**, *30*, 580–603, DOI: 10.1016/j.rser.2013.10.039.
- [168] Anderson, P. S. Construction Plans for the “Champion-2008” TLUD Gasifier Cookstove. 2009; <http://www.drtdlud.com/?resource=ppt09320> (accessed Jun 21, 2015).
- [169] Clean Cooking Catalog. <http://catalog.cleancookstoves.org/stoves> (accessed Jul 2, 2016).
- [170] BioLite CampStove. <http://www.bioliteenergy.com/products/biolite-campstove> (accessed Jul 2, 2016).
- [171] Wang, Y.; Sohn, M. D.; Wang, Y.; Lask, K. M.; Kirchstetter, T. W.; Gadgil, A. J. How many replicate tests are needed to test cookstove performance and emissions?—Three is not always adequate. *Energy Sustainable Dev.* **2014**, *20*, 21–29, DOI: 10.1016/j.esd.2014.02.002.
- [172] Gustafsson, E.; Lin, L.; Strand, M. Characterization of particulate matter in the hot product gas from atmospheric fluidized bed biomass gasifiers. *Biomass Bioenergy* **2011**, *35*, S71–S78, DOI: 10.1016/j.biombioe.2011.02.053.

- [173] Morgalla, M.; Lin, L.; Seemann, M.; Strand, M. Characterization of particulate matter formed during wood pellet gasification in an indirect bubbling fluidized bed gasifier using aerosol measurement techniques. *Fuel Process. Technol.* **2015**, *138*, 578–587, DOI: 10.1016/j.fuproc.2015.06.041.
- [174] Böhm, B.; Heeger, C.; Gordon, R. L.; Dreizler, A. New Perspectives on Turbulent Combustion: Multi-Parameter High-Speed Planar Laser Diagnostics. *Flow, Turbul. Combust.* **2011**, *86*, 313–341, DOI: 10.1007/s10494-010-9291-2.
- [175] Boxx, I.; Stöhr, M.; Carter, C.; Meier, W. Sustained multi-kHz flamefront and 3-component velocity field measurements for the study of turbulent flames. *Appl. Phys. B: Lasers Opt.* **2009**, *95*, 23–29, DOI: 10.1007/s00340-009-3420-4.
- [176] Steinberg, A. M.; Boxx, I.; Stöhr, M.; Carter, C. D.; Meier, W. Flow-flame interactions causing acoustically coupled heat release fluctuations in a thermo-acoustically unstable gas turbine model combustor. *Combust. Flame* **2010**, *157*, 2250–2266, DOI: 10.1016/j.combustflame.2010.07.011.
- [177] Steinberg, A. M.; Boxx, I.; Arndt, C. M.; Frank, J. H.; Meier, W. Experimental study of flame-hole reignition mechanisms in a turbulent non-premixed jet flame using sustained multi-kHz PIV and crossed-lane OH PLIF. *Proc. Combust. Inst.* **2011**, *33*, 1663–1672, DOI: 10.1016/j.proci.2010.06.134.
- [178] Juddoo, M.; Masri, A. R. High-speed OH-PLIF imaging of extinction and re-ignition in non-premixed flames with various levels of oxidation. *Combust. Flame* **2011**, *158*, 902–914, DOI: 10.1016/j.combustflame.2011.02.003.
- [179] Steinberg, A. M.; Coriton, B.; Frank, J. H. Influence of combustion on principal strain-rate transport in turbulent premixed flames. *Proc. Combust. Inst.* **2015**, *35*, 1287–1294, DOI: 10.1016/j.proci.2014.06.089.
- [180] Stöhr, M.; Arndt, C. M.; Meier, W. Transient effects of fuel–air mixing in a partially-premixed turbulent swirl flame. *Proc. Combust. Inst.* **2015**, *35*, 3327–3335, DOI: 10.1016/j.proci.2014.06.095.
- [181] Franzelli, B.; Scoufflaire, P.; Candel, S. Time-resolved spatial patterns and interactions of soot, PAH and OH in a turbulent diffusion flame. *Proc. Combust. Inst.* **2015**, *35*, 1921–1929, DOI: 10.1016/j.proci.2014.06.123.
- [182] Hardalupas, Y.; Orain, M. Local measurements of the time-dependent heat release rate and equivalence ratio using chemiluminescent emission from a flame. *Combust. Flame* **2004**, *139*, 188–207, DOI: 10.1016/j.combustflame.2004.08.003.
- [183] Marchese, A. J.; Dryer, F. L.; Nayagam, V.; Colantonio, R. O. Hydroxyl Radical Chemiluminescence Imaging and the Structure of Microgravity Droplet Flames. *Symp. (Int.) Combust.* **1996**, *26*, 1219–1226, DOI: 10.1016/S0082-0784(96)80338-9.
- [184] Gaydon, A. G. *The Spectroscopy of Flames*; John Wiley & Sons Inc.: New York, 1957; Chapter 10, pp 195–197.

- [185] Dandy, D. S.; Vosen, S. R. Numerical and Experimental Studies of Hydroxyl Radical Chemiluminescence in Methane-Air Flames. *Combust. Sci. Technol.* **1992**, *82*, 131–150, DOI: 10.1080/00102209208951816.
- [186] Sadanandan, R.; Stöhr, M.; Meier, W. Simultaneous OH-PLIF and PIV measurements in a gas turbine model combustor. *Appl. Phys. B: Lasers Opt.* **2008**, *90*, 609–618, DOI: 10.1007/s00340-007-2928-8.
- [187] Lozano, A.; Yip, B.; Hanson, R. K. Acetone: a tracer for concentration measurements in gaseous flows by planar laser-induced fluorescence. *Exp. Fluids* **1992**, *13*, 369–376, DOI: 10.1007/BF00223244.
- [188] Denshchikov, V. A.; Kondrat'ev, V. N.; Romashov, A. N. Interaction Between Two Opposed Jets. *Fluid Dyn.* **1978**, *13*, 924–926.
- [189] Denshchikov, V. A.; Kondrat'ev, V. N.; Romashov, A. N.; Chubarov, V. M. Auto-Oscillations of Planar Colliding Jets. *Fluid Dyn.* **1983**, *18*, 460–462.
- [190] Besbes, S.; Mhiri, H.; Le Palec, G.; Bournot, P. Numerical and experimental study of two turbulent opposed plane jets. *Heat Mass Transfer* **2003**, *39*, 675–686, DOI: 10.1007/s00231-002-0336-5.
- [191] Li, W.-F.; Yao, T.-L.; Liu, H.-F.; Wang, F.-C. Experimental Investigation of Flow Regimes of Axisymmetric and Planar Opposed Jets. *AIChE J.* **2011**, *57*, 1434–1445, DOI: 10.1002/aic.12369.
- [192] Tu, G.; Li, W.; Du, K.; Huang, G.; Wang, F. Onset and influencing factors of deflecting oscillation in planar opposed jets. *Chem. Eng. J. (Amsterdam, Neth.)* **2014**, *247*, 125–133, DOI: 10.1016/j.cej.2014.02.097.
- [193] Pawlowski, R. P.; Salinger, A. G.; Shadid, J. N.; Mountziaris, T. J. Bifurcation and stability analysis of laminar isothermal counterflowing jets. *J. Fluid Mech.* **2006**, *551*, 117–139, DOI: 10.1017/S0022112005008396.
- [194] Mouqallid, M.; Borghi, R.; Lecordier, J. C.; Paranthoen, P. Velocity and Temperature Measurements in Counterflowing Jets. In *Turbulence Heat and Mass Transfer 1*; Pereira, J. C. F., Hanjalić, K., Eds.; Begell House, 1995; pp 76–82.
- [195] Ciani, A.; Kreutner, W.; Frouzakis, C. E.; Lust, K.; Coppola, G.; Boulouchos, K. An experimental and numerical study of the structure and stability of laminar opposed-jet flows. *Comput. Fluids* **2010**, *39*, 114–124, DOI: 10.1016/j.compfluid.2009.07.006.
- [196] Li, W.-F.; Yao, T.-L.; ; Wang, F.-C. Study on Factors Influencing Stagnation Point Offset of Turbulent Opposed Jets. *AIChE J.* **2010**, *56*, 2513–2522, DOI: 10.1002/aic.12188.
- [197] Sultan, M. A.; Fonte, C. P.; Dias, M. M.; Lopes, J. C. B.; Santos, R. J. Experimental study of flow regime and mixing in T-jets mixers. *Chem. Eng. Sci.* **2012**, *73*, 388–399, DOI: 10.1016/j.ces.2012.02.010.

- [198] Wood, P.; Hrymak, A.; Yeo, R.; Johnson, D.; Tyagi, A. Experimental and computational studies of the fluid mechanics in an opposed jet mixing head. *Phys. Fluids A* **1991**, *3*, 1362–1368, DOI: 10.1063/1.858205.
- [199] Unger, D. R.; Muzzio, F. J. Laser-Induced Fluorescence Technique for the Quantification of Mixing in Impinging Jets. *AIChE J.* **1999**, *45*, 2477–2486, DOI: 10.1002/aic.690451203.
- [200] Johnson, D. A.; Wood, P. E. Self-sustained Oscillations in Opposed Impinging Jets in an Enclosure. *Can. J. Chem. Eng.* **2000**, *78*, 867–875, DOI: 10.1002/cjce.5450780503.
- [201] Li, W.-F.; Du, K.-J.; Yu, G.-S.; Liu, H.-F.; ; Wang, F.-C. Experimental Study of Flow Regimes in Three-Dimensional Confined Impinging Jets Reactor. *AIChE J.* **2014**, *60*, 3033–3045, DOI: 10.1002/aic.14459.
- [202] Fonte, C. P.; Sultan, M. A.; Santos, R. J.; Dias, M. M.; Lopes, J. C. B. Flow imbalance and Reynolds number impact on mixing in Confined Impinging Jets. *Chem. Eng. J. (Amsterdam, Neth.)* **2015**, *260*, 316–330, DOI: 10.1016/j.cej.2014.08.090.
- [203] Tillotson, J. W. M.Sc. thesis, Colorado State University, Fort Collins, CO, 2016.
- [204] Johnson, M.; Edwards, R.; Frenk, C. A.; Masera, O. In-field greenhousegas emissions from cookstoves in rural Mexican households. *Atmos. Environ.* **2008**, *42*, 1206–1222, DOI: 10.1016/j.atmosenv.2007.10.034.
- [205] Roden, C. A.; Bond, T. C.; Conway, S.; Osorto Pinel, A. B.; MacCarty, N.; Still, D. Laboratory and field investigations of particulate and carbon monoxide emissions from traditional and improved cookstoves. *Atmos. Environ.* **2009**, *46*, 1170–1181, DOI: 10.1016/j.atmosenv.2008.05.041.
- [206] Berkeley Air Monitoring Group, *Stove Performance Inventory Report*; Global Alliance for Clean Cookstoves: Washington DC, 2012; [http://cleancookstoves.org/resources\\_files/stove-performance-inventory-pdf.pdf](http://cleancookstoves.org/resources_files/stove-performance-inventory-pdf.pdf) (accessed Jun 1, 2016).
- [207] Johnson, M.; Edwards, R.; Berrueta, V.; Masera, O. New Approaches to Performance Testing of Improved Cookstoves. *Environ. Sci. Technol.* **2010**, *44*, 368–374, DOI: 10.1021/es9013294.
- [208] Chen, Y.; Roden, C. A.; Bond, T. C. Characterizing Biofuel Combustion with Patterns of Real-Time Emission Data (PaRTED). *Environ. Sci. Technol.* **2012**, *46*, 6110–6117, DOI: 10.1021/es3003348.
- [209] Rubiano, C. Characterization of Tar from a Fluidized Bed Steam Reformer of Black Liquor. M.Sc. thesis, University of Utah, Salt Lake City, UT, 2006.
- [210] Hawley, B.; Volckens, J. Proinflammatory effects of cookstove emissions on human bronchial epithelial cells. *Indoor Air* **2013**, *23*, 4–13, DOI: 10.1111/j.1600-0668.2012.00790.x.

## APPENDIX A

### Additional Information on the Methods for the Experiments Described in Chapter 3<sup>4</sup>

**Table A.1: Data collected and instrumentation used in the experiments with natural draft gasifier cookstoves described in Chapter 3.**

Variable	Description	Units	Sample rate	Instrument
$m_{fuel}$	Mass of fuel consumed	g	-	Acculab SVI-10A balance
$m_{char}$	Mass of char produced	g	-	Acculab SVI-10A balance
$m_{water}$	Mass of water boiled	g	-	Acculab SVI-10A balance
CO	CO emissions	mole fraction	1 Hz	Testo 335 / Testo 350 / Siemens Ultramat 6
PM <sub>10</sub>	Mass of particulate matter emitted	μg	N/A	URG Corp 10 μm cyclone, 47-mm-dia PTFE filters
$T_{water}$	Water temperature	°C	.6875 Hz	Type K thermocouple, 1.6-mm-dia probe
$T_{pa,1..n}$	Primary air temperatures	°C	1 Hz	Type K thermocouple, 24 AWG
$T_{sa,1..n}$	Secondary air temperatures	°C	1 Hz	Type K thermocouple, 24 AWG
$T_{ex,1..n}$	Exhaust air temperatures	°C	1 Hz	Type K thermocouple, 24 AWG
$T_{top,1..n}$	Fuel chamber temperatures	°C	1 Hz	Type K thermocouple, 3-mm-dia probe
$T_{middle,1..n}$	Fuel chamber temperatures	°C	1 Hz	Type K thermocouple, 3-mm-dia probe
$T_{bottom,1..n}$	Fuel chamber temperatures	°C	1 Hz	Type K thermocouple, 3-mm-dia probe
$T_{stove,1..n}$	Stove body temperatures	°C	1 Hz	Type K thermocouple, 20 AWG bolt-on
$T_{inner,1..n}$	Under pot temperatures (stoves 1, 2, and 3 only)	°C	1 Hz	Type K thermocouple, 3-mm-dia probe

---

<sup>4</sup>This appendix contains material that was originally published in the Supplemental Information accompanying an article in *Energy for Sustainable Development: Tryner, J; Willson, B. D.; Marchese, A. J. The effects of fuel type and stove design on emissions and efficiency of natural-draft semi-gasifier biomass cookstoves. Energy Sustainable Dev. 2014, 23, 99-109, DOI: 10.1016/j.esd.2014.07.009.* My contributions to this publication included performing the experiments, analyzing the data, creating the figures, and writing the manuscript. Much of the material that was originally contained in the Supplemental Information has been integrated into Chapter 3. Table A.1 has been reformatted to match the format of this dissertation.

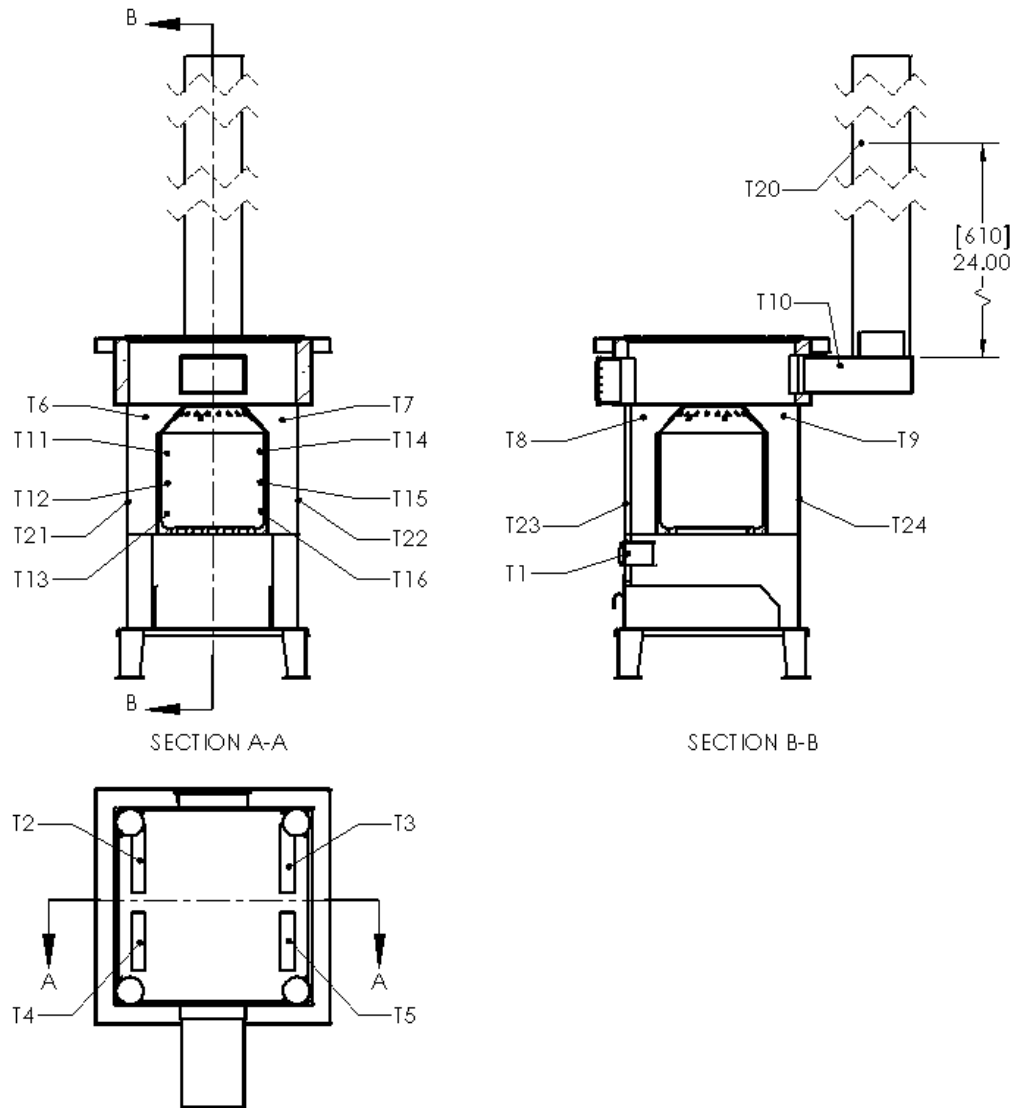


Figure A.1: Placement of the thermocouples installed on Stoves 1, 2, and 3.

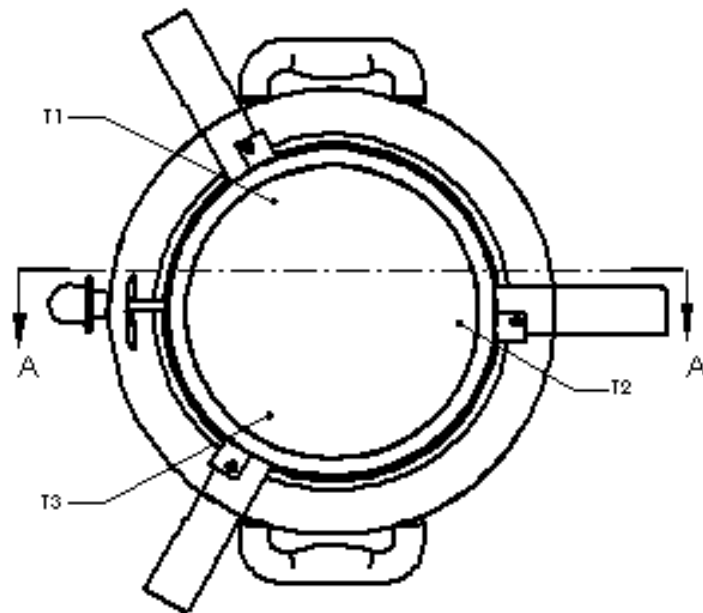
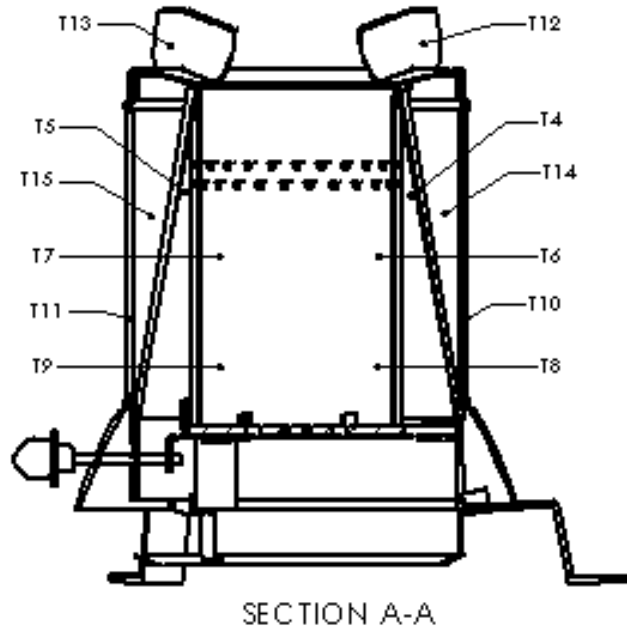


Figure A.2: Placement of the thermocouples installed on Stove 4.

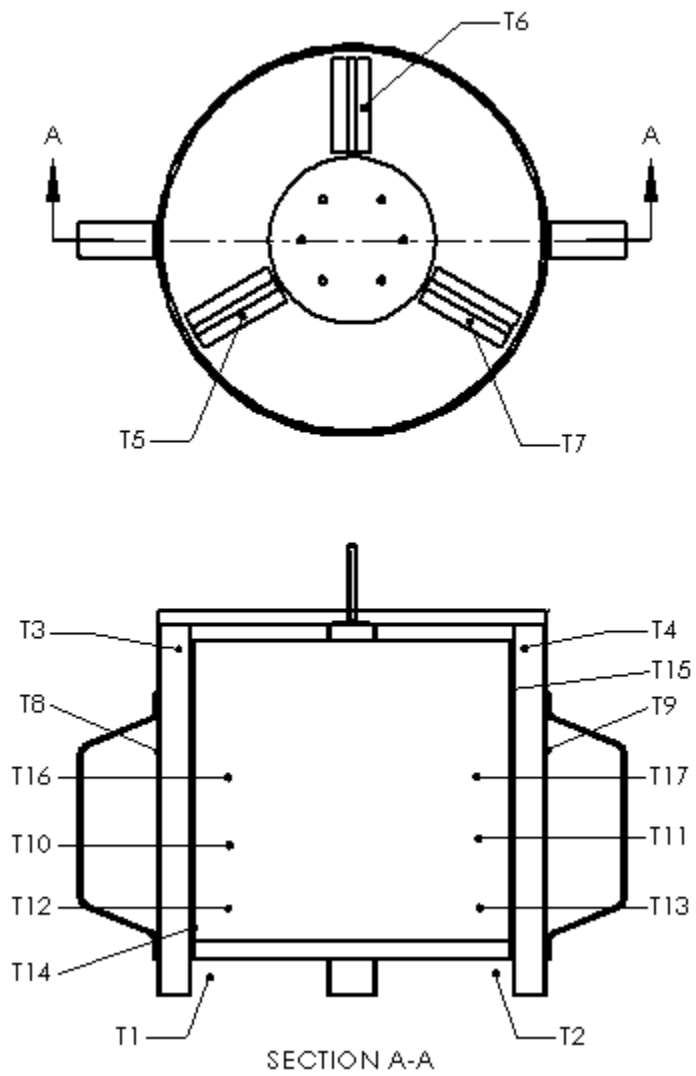


Figure A.3: Placement of the thermocouples installed on Stove 5.

## APPENDIX B

### Additional Information on the Methods and Complete Set of Results for the Experiments Described in Chapter 4<sup>5</sup>

#### B.1 Experimental

The locations of the thermocouples installed on the test bed are shown in Figure B.1. Information on the significance of each temperature measurement and the types of thermocouples used is provided in Table B.1. All of the tests that were completed, and the values that each parameter was set to during each test, are listed in Tables B.2 and B.3. The default case is listed separately at the top of each table and the variable in each test case is shown in **bold**. The number of replicates for each data point is shown in Table B.4.

---

<sup>5</sup>This appendix contains material that has been submitted as part of the Supporting Information accompanying a journal article: Tryner, J; Tillotson, J. W.; Baumgardner, M. E.; Mohr, J. T.; DeFoort, M. W.; Marchese, A. J. The effects of air flow rates, secondary air inlet geometry, type, and operating mode on the performance of semi-gasifier cookstoves. My contributions to this publication included performing the experiments (in conjunction with James Tillotson), analyzing the data (also in conjunction with James Tillotson), creating the figures, and writing the manuscript. Much of the material that was originally contained in the Supporting Information document has been integrated into Chapter 4. The tables and figures have been reformatted to match the format of this dissertation.

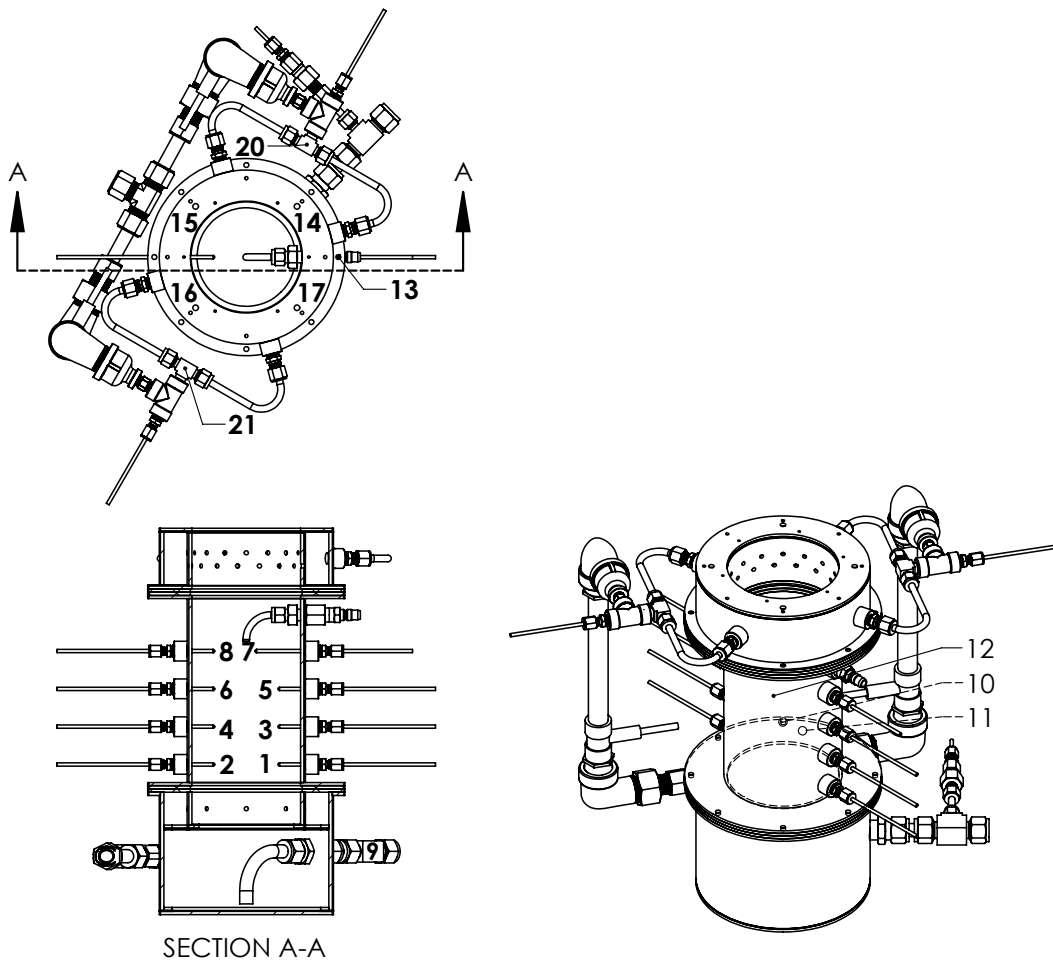


Figure B.1: A drawing of the test bed with the locations of the thermocouples listed in Table B.1 shown.

**Table B.1: Thermocouples used to collect temperature data.**

No.	Measurement description	Omega part no.	Thermocouple description
1	Fuel chamber bottom - 1	KMTSS-125U-6	Type K, 1/8" dia. probe, ungrounded
2	Fuel chamber bottom - 2	KMTSS-125U-6	Type K, 1/8" dia. probe, ungrounded
3	Fuel chamber middle - 1	KMTSS-125U-6	Type K, 1/8" dia. probe, ungrounded
4	Fuel chamber middle - 2	KMTSS-125U-6	Type K, 1/8" dia. probe, ungrounded
5	Fuel chamber top - 1	KMTSS-125U-6	Type K, 1/8" dia. probe, ungrounded
6	Fuel chamber top - 2	KMTSS-125U-6	Type K, 1/8" dia. probe, ungrounded
7	Gas - 1	KMTSS-125U-6	Type K, 1/8" dia. probe, ungrounded
8	Gas - 2	KMTSS-125U-6	Type K, 1/8" dia. probe, ungrounded
9	Primary air	TC-K-1/8NPT-E	Type K, exposed junction, 1/8" NPT
10	Stove body - 1	WTK-8-24	Type K, bolt-on
11	Stove body - 2	WTK-8-24	Type K, bolt-on
12	Stove body - 3	WTK-8-24	Type K, bolt-on
13	Stove body - 4	WTK-8-24	Type K, bolt-on
14	Exhaust - 1	HH-K-24-SLE	Type K, 24 AWG, exposed junction
15	Exhaust - 2	HH-K-24-SLE	Type K, 24 AWG, exposed junction
16	Exhaust - 3	HH-K-24-SLE	Type K, 24 AWG, exposed junction
17	Exhaust - 4	HH-K-24-SLE	Type K, 24 AWG, exposed junction
18	Balance surface	SA2F-K-72	Type K, stick-on
19	Water	KMTSS-125G-6	Type K, 1/8" dia. probe, grounded
20	Secondary air - 1	KMTSS-125G-6	Type K, 1/8" dia. probe, grounded
21	Secondary air - 2	KMTSS-125G-6	Type K, 1/8" dia. probe, grounded

**Table B.2: Test matrix 1 — Secondary air delivery parameters.**

Test no.	Fuel Type	Fuel		Primary air flow rate (g·min <sup>-1</sup> )	Secondary to primary air flow ratio	Secondary air			Pot gap (mm)	Flow constriction	Other features	
		Moisture content (%)	Bulk density (kg·m <sup>-3</sup> )			Temp. (°C)	Hole diameter (mm)	Swirl angle				Downward angle
1	Douglas fir chips	7	156	25	3	200	4	0°	0°	15	None	None
2	Douglas fir chips	7	156	25	<b>2</b>	200	4	0°	0°	15	None	None
3	Douglas fir chips	7	156	25	<b>4</b>	200	4	0°	0°	15	None	None
4	Douglas fir chips	7	156	25	<b>5</b>	200	4	0°	0°	15	None	None
5	Douglas fir chips	7	156	25	3	<b>100</b>	4	0°	0°	15	None	None
6	Douglas fir chips	7	156	25	3	<b>150</b>	4	0°	0°	15	None	None
7	Douglas fir chips	7	156	25	3	<b>250</b>	4	0°	0°	15	None	None
8	Douglas fir chips	7	156	25	3	<b>300</b>	4	0°	0°	15	None	None
9	Douglas fir chips	7	156	25	3	200	<b>6</b>	0°	0°	15	None	None
10	Douglas fir chips	7	156	25	3	200	<b>8</b>	0°	0°	15	None	None
11	Douglas fir chips	7	156	25	3	200	<b>10</b>	0°	0°	15	None	None
12	Douglas fir chips	7	156	25	3	200	4	<b>15°</b>	0°	15	None	None
13	Douglas fir chips	7	156	25	3	200	4	<b>30°</b>	0°	15	None	None
14	Douglas fir chips	7	156	25	3	200	4	<b>45°</b>	0°	15	None	None
15	Douglas fir chips	7	156	25	3	200	4	0°	<b>10°</b>	15	None	None
16	Douglas fir chips	7	156	25	3	200	4	0°	<b>20°</b>	15	None	None
17	Douglas fir chips	7	156	25	3	200	4	0°	<b>30°</b>	15	None	None
18	Douglas fir chips	7	156	25	3	200	4	0°	0°	<b>30</b>	None	None
19	Douglas fir chips	7	156	25	3	200	4	0°	0°	<b>45</b>	None	None
20	Douglas fir chips	7	156	25	3	200	4	0°	0°	15	<b>Before secondary air inlet, 2.50:4.25 ratio</b>	None
21	Douglas fir chips	7	156	25	3	200	4	0°	0°	15	<b>After secondary air inlet, 2.50:4.25 ratio</b>	None

**Table B.3: Test matrix 2 —Primary air flow rates, fuel properties, and secondary air delivery parameters.**

Test no.	Fuel Type	Fuel		Primary air flow rate (g·min <sup>-1</sup> )	Secondary to primary air flow ratio	Secondary air			Pot gap (mm)	Flow constriction	Other features	
		Moisture content (%)	Bulk density (kg·m <sup>-3</sup> )			Temp. (°C)	Hole diameter (mm)	Swirl angle				Downward angle
22	Douglas fir chips	7	160	25	3	200	4	0°	0°	15	None	None
23	Douglas fir chips	7	160	<b>15</b>	3	200	4	0°	0°	15	None	None
24	Douglas fir chips	7	160	<b>20</b>	3	200	4	0°	0°	15	None	None
25	Douglas fir chips	7	160	<b>30</b>	3	200	4	0°	0°	15	None	None
26	Douglas fir chips	<b>0</b>	160	25	3	200	4	0°	0°	15	None	None
27	Douglas fir chips	<b>15</b>	160	25	3	200	4	0°	0°	15	None	None
28	Douglas fir chips	<b>25</b>	160	25	3	200	4	0°	0°	15	None	None
29	<b>Corn cobs chips</b>	6	174	25	3	200	4	0°	0°	15	None	None
30	<b>Eucalyptus chips</b>	7	230	25	3	200	4	0°	0°	15	None	None
31	<b>Lodgepole pine pellets</b>	7	636	25	3	200	4	0°	0°	15	None	None
32	Corn cobs	6	<b>137</b>	25	3	200	4	0°	0°	15	None	None
33	Corn cobs	6	<b>126</b>	25	3	200	4	0°	0°	15	None	None
34	Douglas fir chips	7	160	25	3	200	<b>2</b>	0°	0°	15	None	None
35	Douglas fir chips	7	160	25	3	200	4	0°	0°	15	None	<b>Insulated chimney</b>
36	Douglas fir chips	7	160	25	3	200	4	0°	0°	15	None	<b>Early secondary air injection</b>

**Table B.4: Number of replicates of each data point.**

Test no.	Description	Phase 1					Phase 2					Phase 3		Gas samples	
		CO	PM <sub>2.5</sub>	Power output	Fuel consumption	Mass loss rate	CO	PM <sub>2.5</sub>	Power output	Fuel consumption	Mass loss rate	CO	PM <sub>2.5</sub>		Mass loss rate
1	Baseline 1	3	0	3	3	3	3	0	3	3	3	3	0	1	0
2	2:1	3	0	3	3	3	3	0	3	3	3	3	0	2	0
3	4:1	5	0	5	5	5	4	0	4	4	4	4	0	3	0
4	5:1	4	0	4	4	3	4	0	4	4	3	4	0	3	0
5	100 °C	2	0	2	2	2	2	0	2	2	2	2	0	2	0
6	150 °C	2	0	2	2	2	2	0	2	2	2	2	0	2	0
7	250 °C	3	0	3	3	2	3	0	3	3	2	3	0	2	0
8	300 °C	2	0	2	2	2	2	0	2	2	2	2	0	2	0
9	6-mm-dia. holes	2	0	2	2	2	2	0	2	2	2	2	0	2	0
10	8-mm-dia. holes	2	0	3	3	3	2	0	3	3	3	2	0	2	0
11	10-mm-dia. holes	2	0	2	2	2	2	0	2	2	2	2	0	2	0
12	15° swirl	2	0	2	2	1	2	0	2	2	2	2	0	2	0
13	30° swirl	4	0	4	3	3	3	0	3	3	3	3	0	2	0
14	45° swirl	2	0	2	2	1	2	0	2	2	2	2	0	1	0
15	10° down	3	0	3	3	3	3	0	3	3	3	3	0	3	0
16	20° down	3	0	3	3	2	3	0	3	3	2	3	0	2	0
17	30° down	3	0	3	3	3	3	0	3	3	3	3	0	3	0
18	30 mm pot gap	3	0	3	3	3	3	0	3	3	3	3	0	3	0
19	45 mm pot gap	3	0	3	3	3	3	0	3	3	3	2	0	3	0
20	Constriction before	3	0	3	3	2	3	0	3	3	2	3	0	1	0
21	Constriction after	3	0	3	3	3	3	0	3	3	2	3	0	3	0
22	Baseline 2	8	4	8	8	8	7	4	8	8	7	8	4	7	6
23	15 g·min <sup>-1</sup> primary air	5	4	5	5	5	5	4	5	5	5	5	4	5	4
24	20 g·min <sup>-1</sup> primary air	5	4	5	5	5	5	4	5	5	5	5	4	5	4
25	30 g·min <sup>-1</sup> primary air	4	3	4	4	4	4	3	4	4	4	4	3	4	4
26	0% moisture	3	3	3	3	3	3	3	3	3	3	3	3	2	3
27	15% moisture	4	4	4	4	4	4	4	4	4	4	4	4	4	3
28	25% moisture	3	3	3	3	3	3	3	3	3	3	3	3	1	3
29	Corn cob chips	4	3	4	4	4	4	4	4	4	4	4	4	3	4
30	Eucalyptus chips	4	4	4	4	4	4	4	4	4	4	4	4	4	4
31	Lodgepole pine pellets	3	3	3	3	3	3	3	3	3	3	3	3	3	3
32	Corn cobs, 137 kg·m <sup>-3</sup>	4	4	4	4	4	4	4	4	4	4	4	4	4	4
33	Corn cobs, 126 kg·m <sup>-3</sup>	3	3	3	3	3	3	3	3	3	2	3	3	3	3
34	2-mm-dia. holes	9	3	12	12	12	9	3	12	11	12	9	3	10	6
35	Insulated chimney	6	3	7	7	7	6	3	7	7	7	6	3	7	4
36	Early secondary air	8	3	8	7	8	7	3	7	7	7	7	3	7	0

**Table B.5: Instrumentation used for data collection.**

Variable	Unit	Logging rate (Hz)	Instrumentation	Data logging software
Mass of pot and water	g	N/A	Adam Equipment GBK 35a balance	N/A
Mass of fuel	g	N/A	Adam Equipment GBK 35a balance	N/A
Mass of test bed	g	1	Mettler Toledo MS32001L balance	LabXDirect Balance
CO emissions	ppm	1	Siemens ULTRAMAT 6 NDIR sensor	Program written in LabVIEW™
PM emissions	$\mu\text{g}$	N/A	URG Corp. URG-2000-30EHS 2.5 $\mu\text{m}$ , 16.7 LPM cyclone URG Corp. stainless steel filter holder Whatman 7592-104 47-mm PTFE filters	N/A
Active flow control for gravimetric PM sampling	N/A	1	Alicat scientific MCPH-50SLPM-D-30PSIA mass flow controller Omegadyne PX219-015A5V pressure transducer Type K thermocouple	Program written in LabVIEW™
Temperatures	$^{\circ}\text{C}$	1	Pico Technology TC-08 thermocouple loggers	PicoLog

## B.2 Results

### B.2.1 Test Matrix 1 – Secondary Air Delivery Parameters

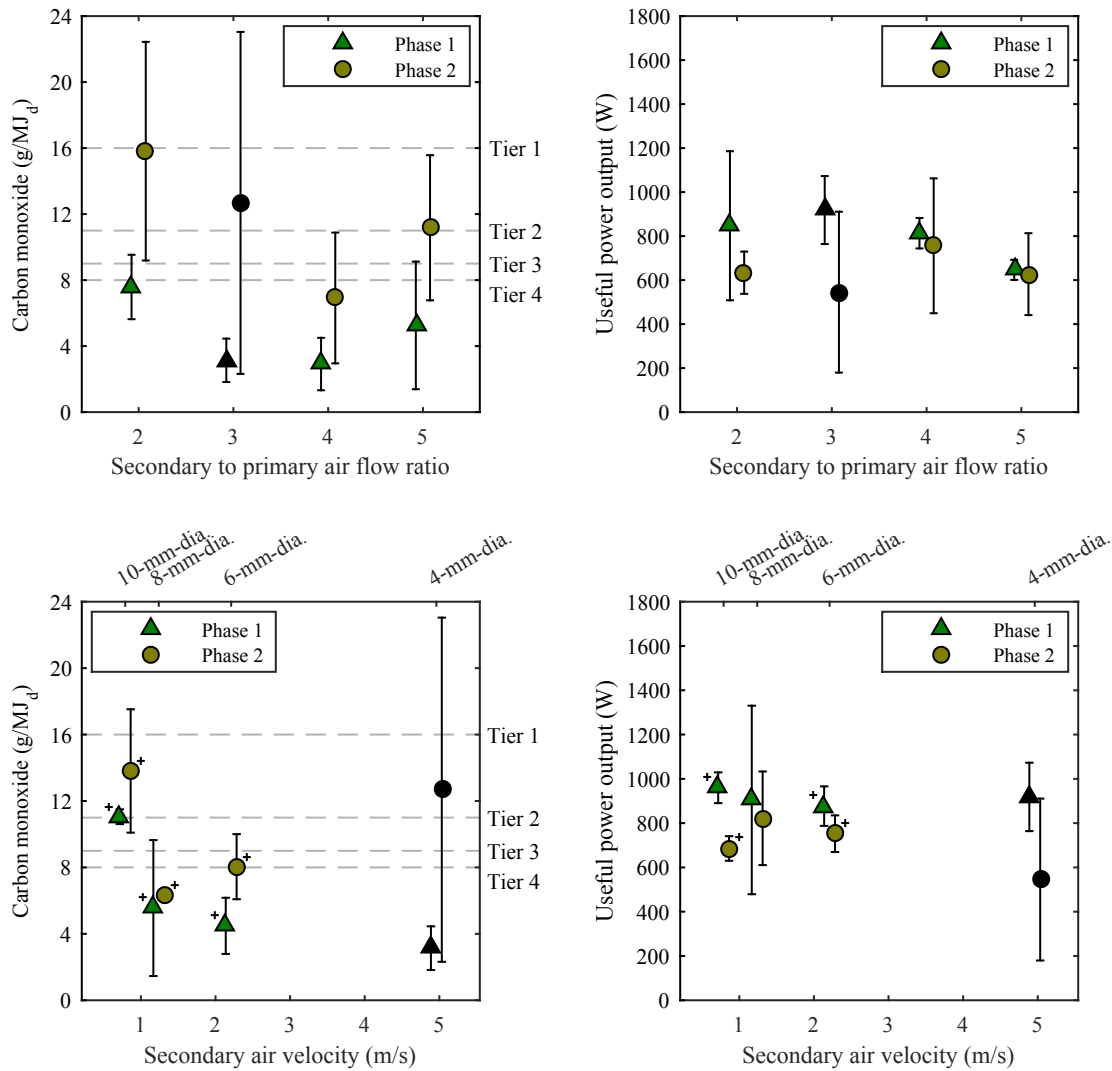


**Figure B.2:** Effects of varying secondary to primary air flow ratio and secondary air opening size (secondary air velocity) on average high-power CO emissions and useful power output during normal operation (Phase 1, green triangles) and post-refueling (Phase 2, gold circles). Black symbols refer to the baseline configuration (Douglas fir chip fuel, 7% moisture content, 25 g·min<sup>-1</sup> primary air, 75 g·min<sup>-1</sup> secondary air, 200 °C secondary air temperature, 4-mm-dia. secondary air holes, no swirl, no downward angle, 15 mm pot gap, no flow constriction, no other features). Average values that were calculated from only two replicates are marked with a '+'. Error bars represent 90% confidence intervals for markers with no '+' and the total range of the measurements for markers with a '+'. Data points have been offset slightly on either side of the values listed in Table 4.1 to improve the readability of the plot.

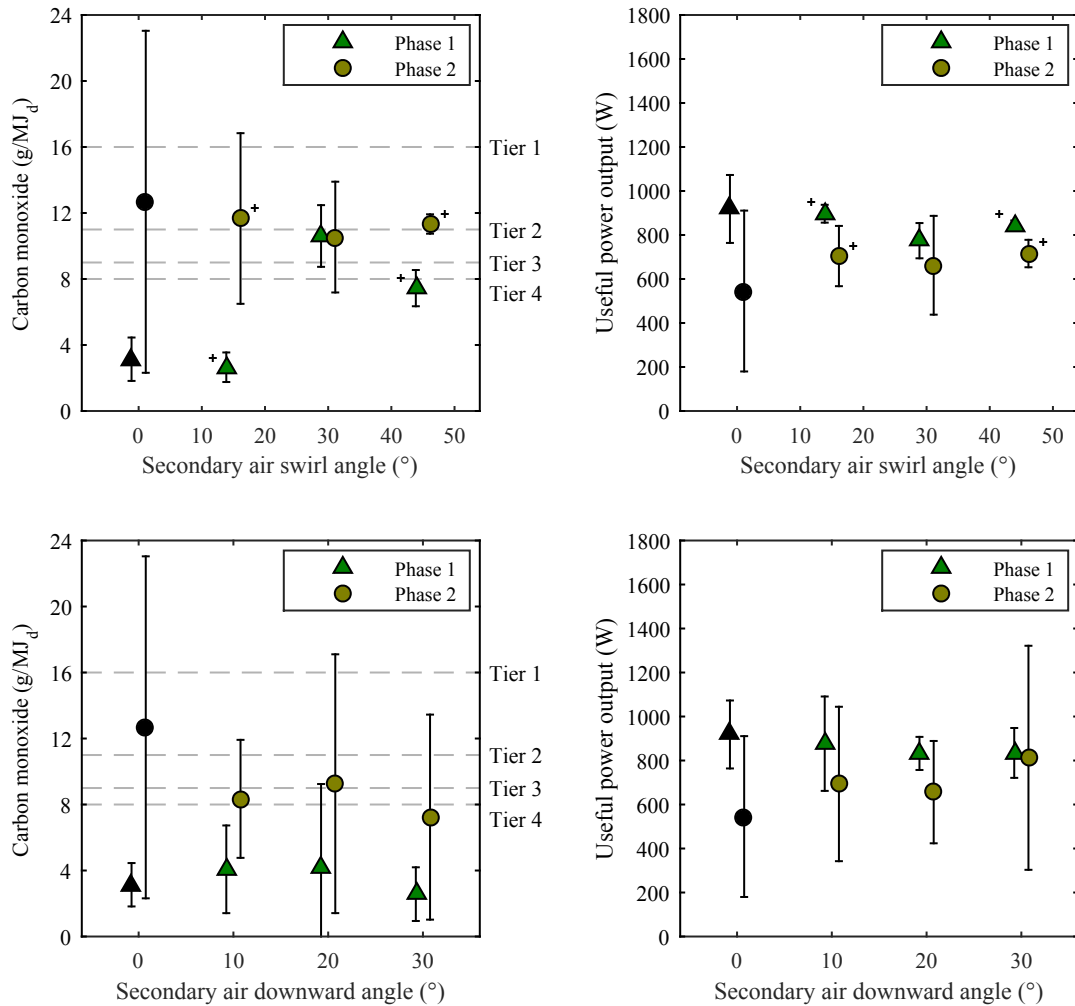


**Figure B.3:** Effects of varying secondary air swirl angle and downward angle on average high-power CO emissions and useful power output during normal operation (Phase 1, green triangles) and post-refueling (Phase 2, gold circles). Black symbols refer to the baseline configuration (Douglas fir chip fuel, 7% moisture content, 25 g·min<sup>-1</sup> primary air, 75 g·min<sup>-1</sup> secondary air, 200 °C secondary air temperature, 4-mm-dia. secondary air holes, no swirl, no downward angle, 15 mm pot gap, no flow constriction, no other features). Average values that were calculated from only two replicates are marked with a '+'. Error bars represent 90% confidence intervals for markers with no '+' and the total range of the measurements for markers with a '+'. Data points have been offset slightly on either side of the values listed in Table 4.1 to improve the readability of the plot.

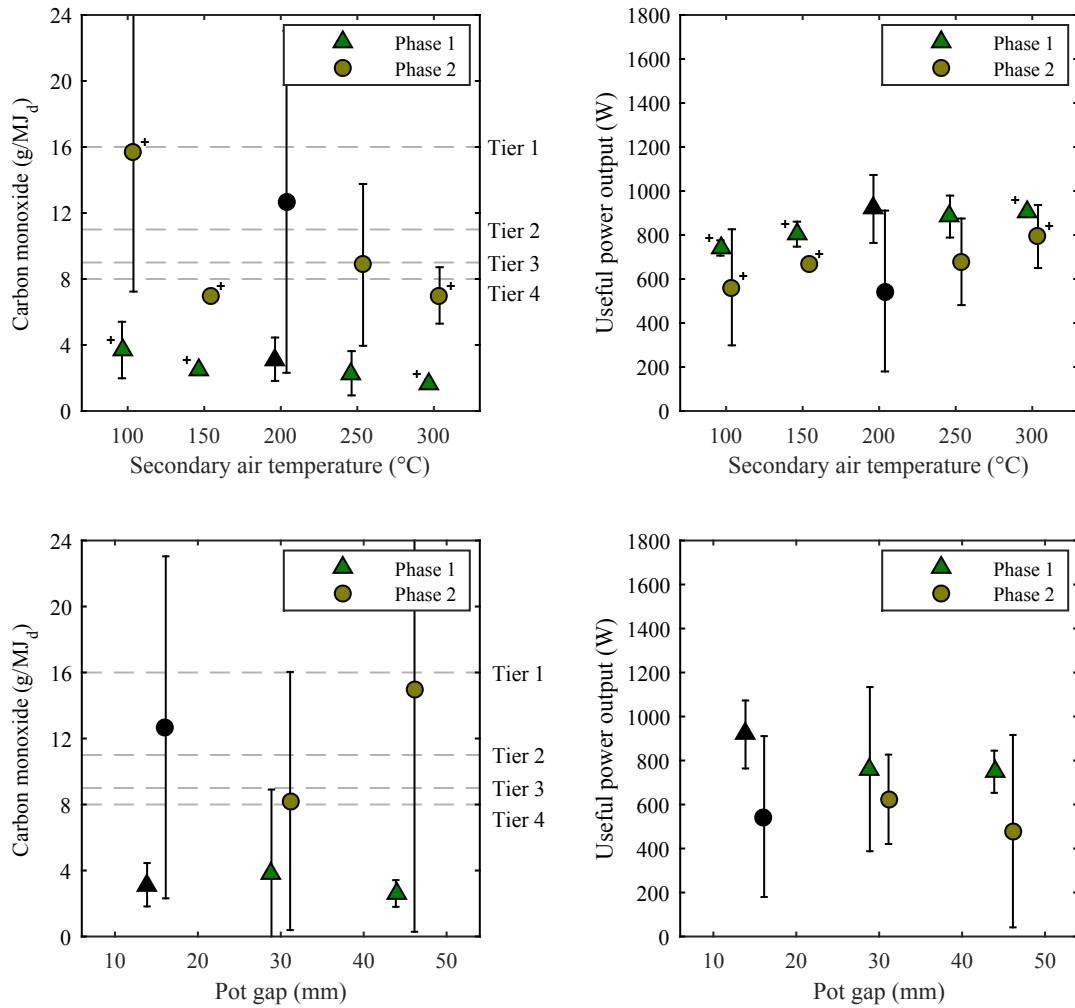


**Figure B.4: Effects of varying secondary air temperature and the pot gap on average high-power CO emissions and useful power output during normal operation (Phase 1, green triangles) and post-refueling (Phase 2, gold circles). Black symbols refer to the baseline configuration (Douglas fir chip fuel, 7% moisture content, 25 g·min<sup>-1</sup> primary air, 75 g·min<sup>-1</sup> secondary air, 200 °C secondary air temperature, 4-mm-dia. secondary air holes, no swirl, no downward angle, 15 mm pot gap, no flow constriction, no other features). Average values that were calculated from only two replicates are marked with a '+'. Error bars represent 90% confidence intervals for markers with no '+' and the total range of the measurements for markers with a '+'. Data points have been offset slightly on either side of the values listed in Table 4.1 to improve the readability of the plot.**

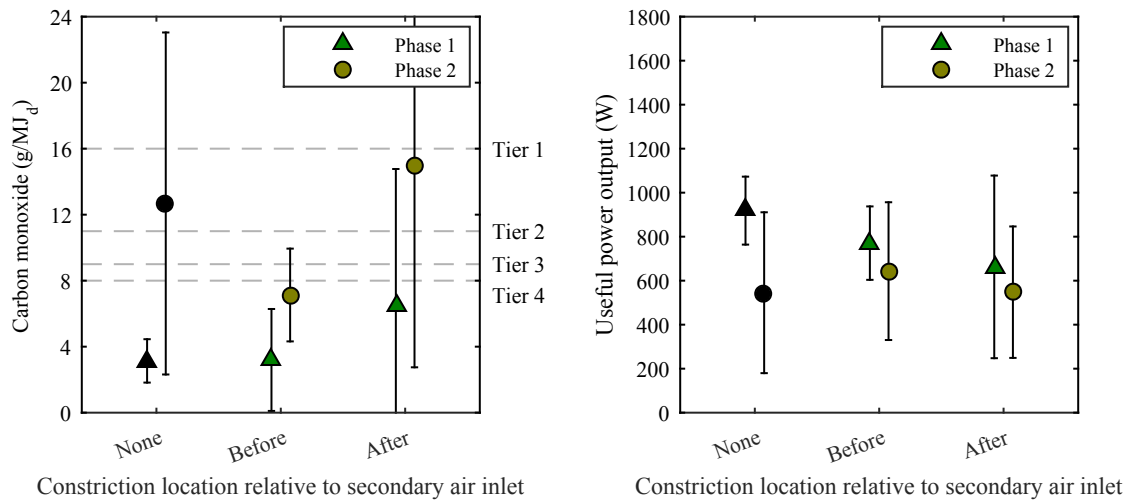


**Figure B.5:** Effects of varying the constriction location on average high-power CO emissions and useful power output during normal operation (Phase 1, green triangles) and post-refueling (Phase 2, gold circles). Black symbols refer to the baseline configuration (Douglas fir chip fuel, 7% moisture content,  $25 \text{ g}\cdot\text{min}^{-1}$  primary air,  $75 \text{ g}\cdot\text{min}^{-1}$  secondary air,  $200 \text{ }^\circ\text{C}$  secondary air temperature, 4-mm-dia. secondary air holes, no swirl, no downward angle, 15 mm pot gap, no flow constriction, no other features). Error bars represent 90% confidence intervals. Data points have been offset slightly on either side of the values listed in Table 4.1 to improve the readability of the plot.

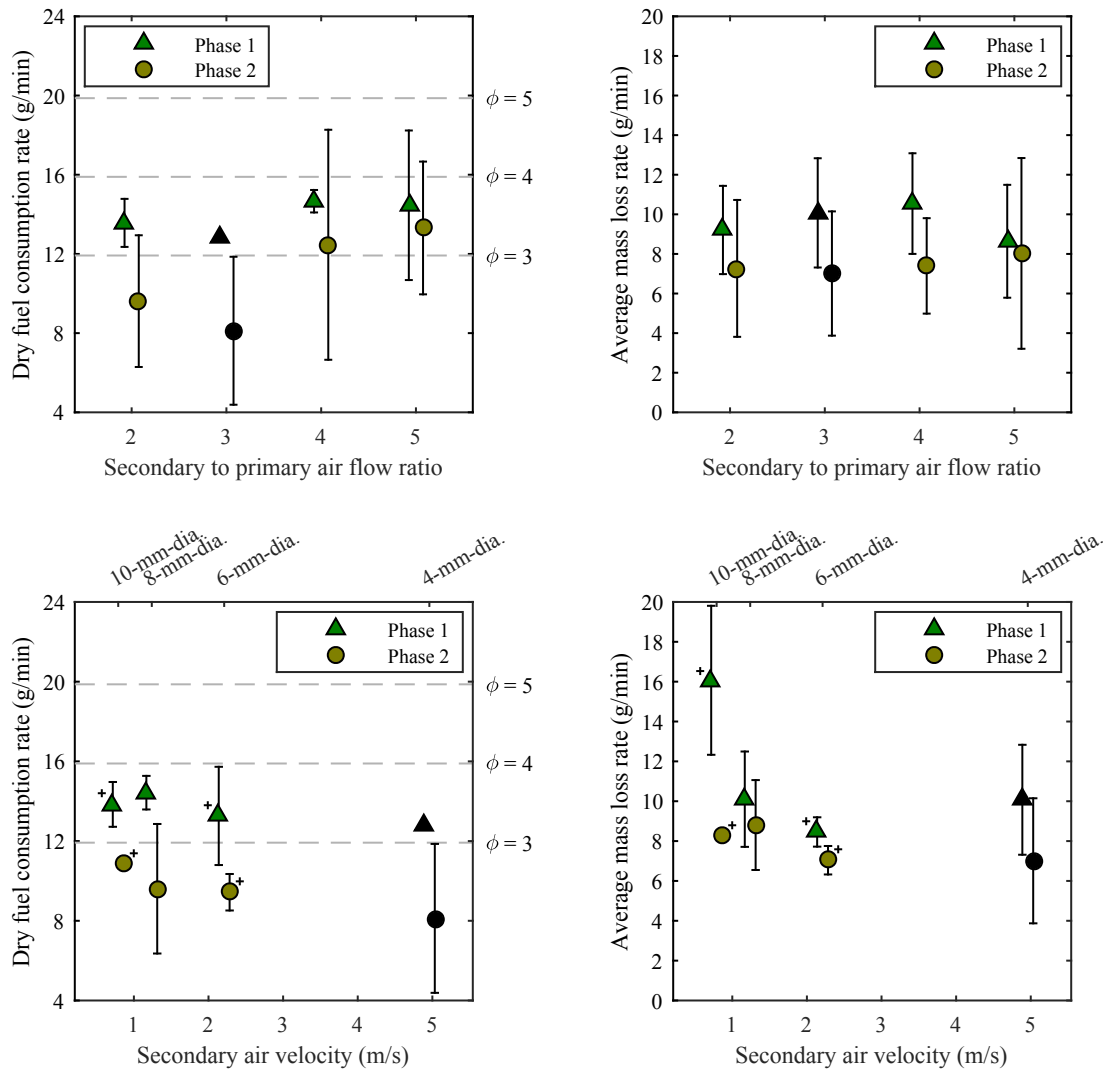
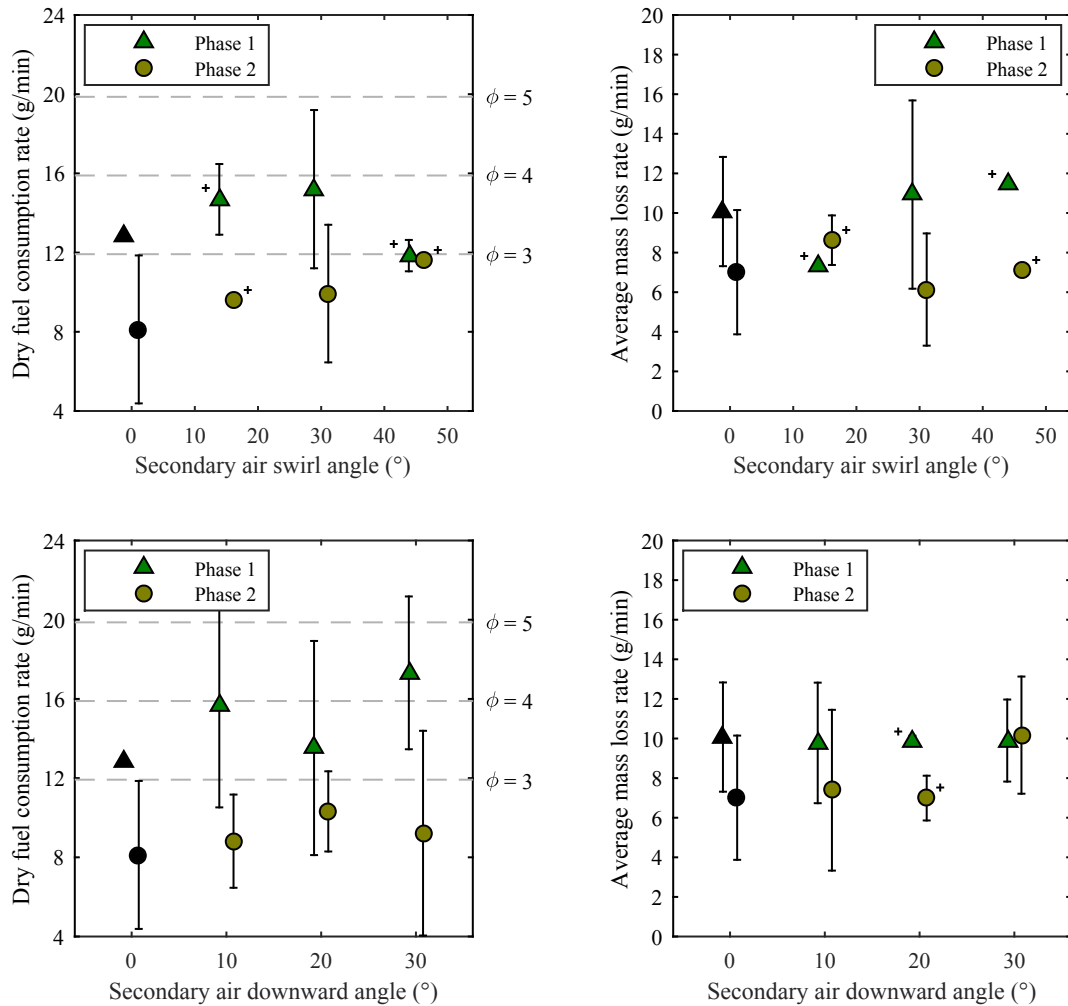


Figure B.6: Effects of varying secondary to primary air flow ratio and secondary air opening size (secondary air velocity) average high-power dry fuel consumption rate and mass loss rate during normal operation (Phase 1, green triangles) and post-refueling (Phase 2, gold circles). Black symbols refer to the baseline configuration (Douglas fir chip fuel, 7% moisture content, 25 g·min<sup>-1</sup> primary air, 75 g·min<sup>-1</sup> secondary air, 200 °C secondary air temperature, 4-mm-dia. secondary air holes, no swirl, no downward angle, 15 mm pot gap, no flow constriction, no other features). Average values that were calculated from only two replicates are marked with a '+'. Error bars represent 90% confidence intervals for markers with no '+' and the total range of the measurements for markers with a '+'. Data points have been offset slightly on either side of the values listed in Table 4.1 to improve the readability of the plot.



**Figure B.7:** Effects of varying secondary air swirl angle and downward angle on average high-power dry fuel consumption rate and mass loss rate during normal operation (Phase 1, green triangles) and post-refueling (Phase 2, gold circles). Black symbols refer to the baseline configuration (Douglas fir chip fuel, 7% moisture content, 25 g·min<sup>-1</sup> primary air, 75 g·min<sup>-1</sup> secondary air, 200 °C secondary air temperature, 4-mm-dia. secondary air holes, no swirl, no downward angle, 15 mm pot gap, no flow constriction, no other features). Average values that were calculated from only two replicates are marked with a '+'. Error bars represent 90% confidence intervals for markers with no '+' and the total range of the measurements for markers with a '+'. Data points have been offset slightly on either side of the values listed in Table 4.1 to improve the readability of the plot.

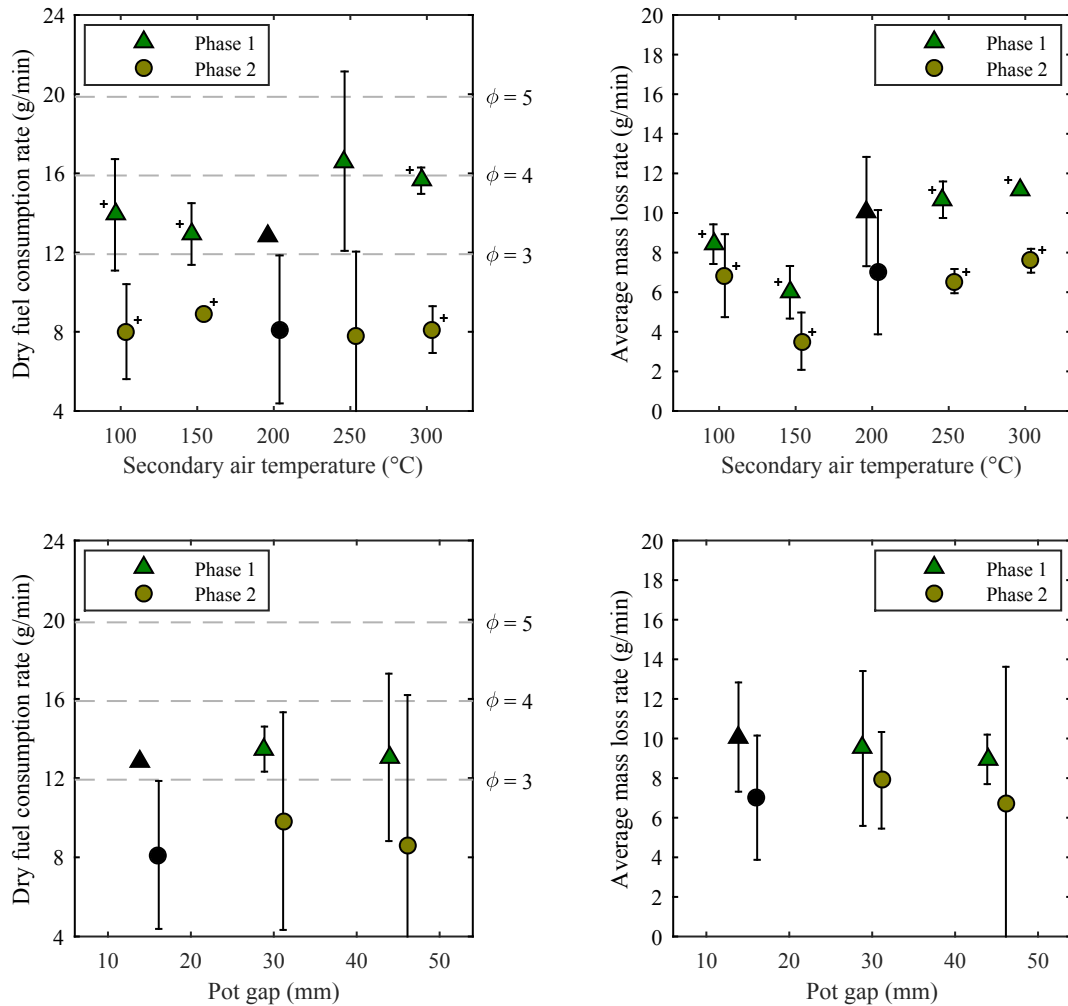
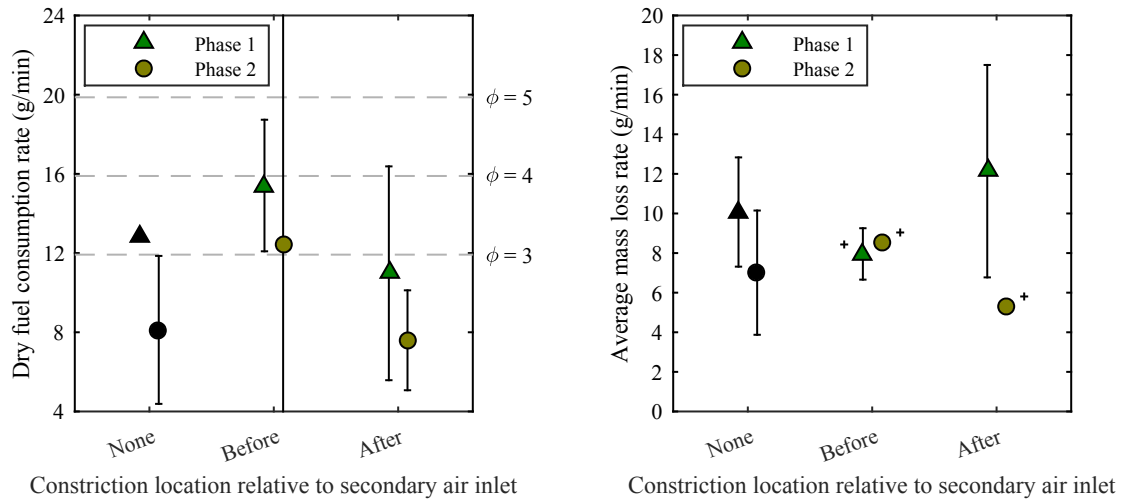
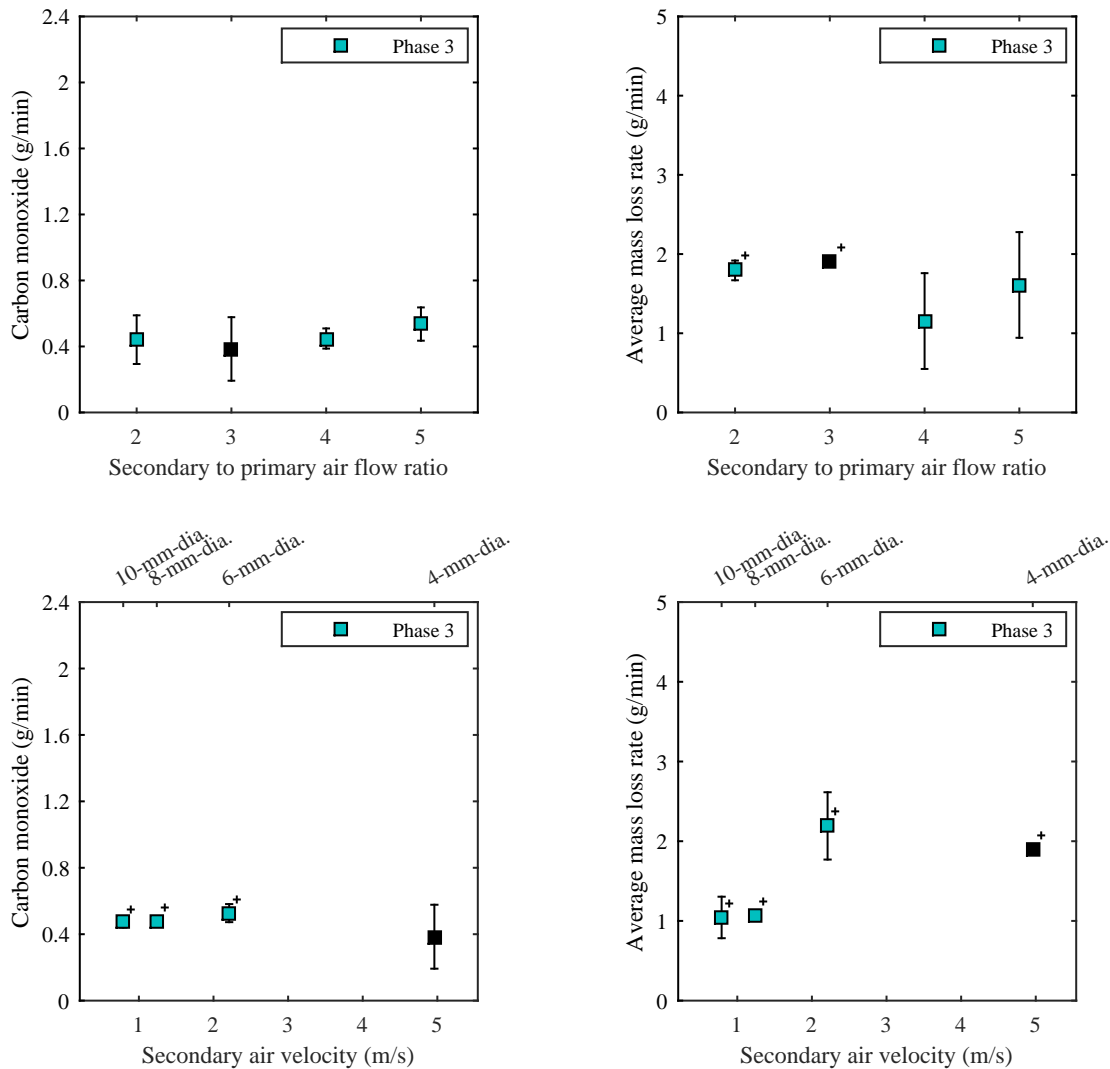


Figure B.8: Effects of varying secondary air temperature and the pot gap on average high-power dry fuel consumption rate and mass loss rate during normal operation (Phase 1, green triangles) and post-refueling (Phase 2, gold circles). Black symbols refer to the baseline configuration (Douglas fir chip fuel, 7% moisture content, 25 g·min<sup>-1</sup> primary air, 75 g·min<sup>-1</sup> secondary air, 200 °C secondary air temperature, 4-mm-dia. secondary air holes, no swirl, no downward angle, 15 mm pot gap, no flow constriction, no other features). Average values that were calculated from only two replicates are marked with a '+'. Error bars represent 90% confidence intervals for markers with no '+' and the total range of the measurements for markers with a '+'. Data points have been offset slightly on either side of the values listed in Table 4.1 to improve the readability of the plot.



**Figure B.9: Effects of varying the constriction location on average high-power dry fuel consumption rate and mass loss rate during normal operation (Phase 1, green triangles) and post-refueling (Phase 2, gold circles). Black symbols refer to the baseline configuration (Douglas fir chip fuel, 7% moisture content, 25 g·min<sup>-1</sup> primary air, 75 g·min<sup>-1</sup> secondary air, 200 °C secondary air temperature, 4-mm-dia. secondary air holes, no swirl, no downward angle, 15 mm pot gap, no flow constriction, no other features). Average values that were calculated from only two replicates are marked with a '+'. Error bars represent 90% confidence intervals for markers with no '+' and the total range of the measurements for markers with a '+'. Data points have been offset slightly on either side of the values listed in Table 4.1 to improve the readability of the plot.**



**Figure B.10: Effects of varying secondary to primary air flow ratio and secondary air opening size (secondary air velocity) on average CO emissions and mass loss rate during char burnout. Black symbols refer to the baseline configuration (Douglas fir chip fuel, 7% moisture content,  $25 \text{ g}\cdot\text{min}^{-1}$  primary air,  $75 \text{ g}\cdot\text{min}^{-1}$  secondary air,  $200 \text{ }^\circ\text{C}$  secondary air temperature, 4-mm-dia. secondary air holes, no swirl, no downward angle, 15 mm pot gap, no flow constriction, no other features). Average values that were calculated from only two replicates are marked with a '+'. Error bars represent 90% confidence intervals for markers with no '+' and the total range of the measurements for markers with a '+'.**

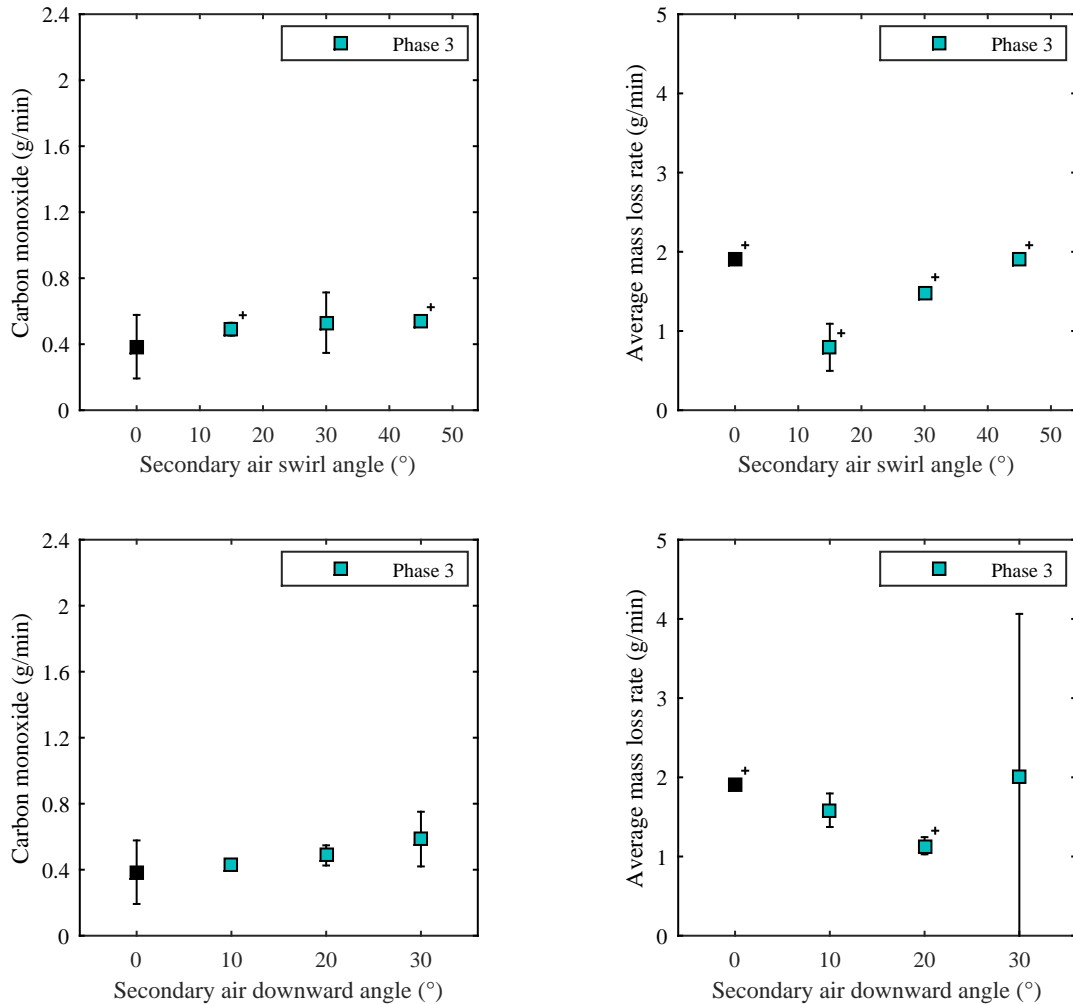


Figure B.11: Effects of varying secondary air swirl angle and downward angle on average CO emissions and mass loss rate during char burnout. Black symbols refer to the baseline configuration (Douglas fir chip fuel, 7% moisture content,  $25 \text{ g}\cdot\text{min}^{-1}$  primary air,  $75 \text{ g}\cdot\text{min}^{-1}$  secondary air,  $200 \text{ }^\circ\text{C}$  secondary air temperature, 4-mm-dia. secondary air holes, no swirl, no downward angle, 15 mm pot gap, no flow constriction, no other features). Average values that were calculated from only two replicates are marked with a '+'. Error bars represent 90% confidence intervals for markers with no '+' and the total range of the measurements for markers with a '+'.

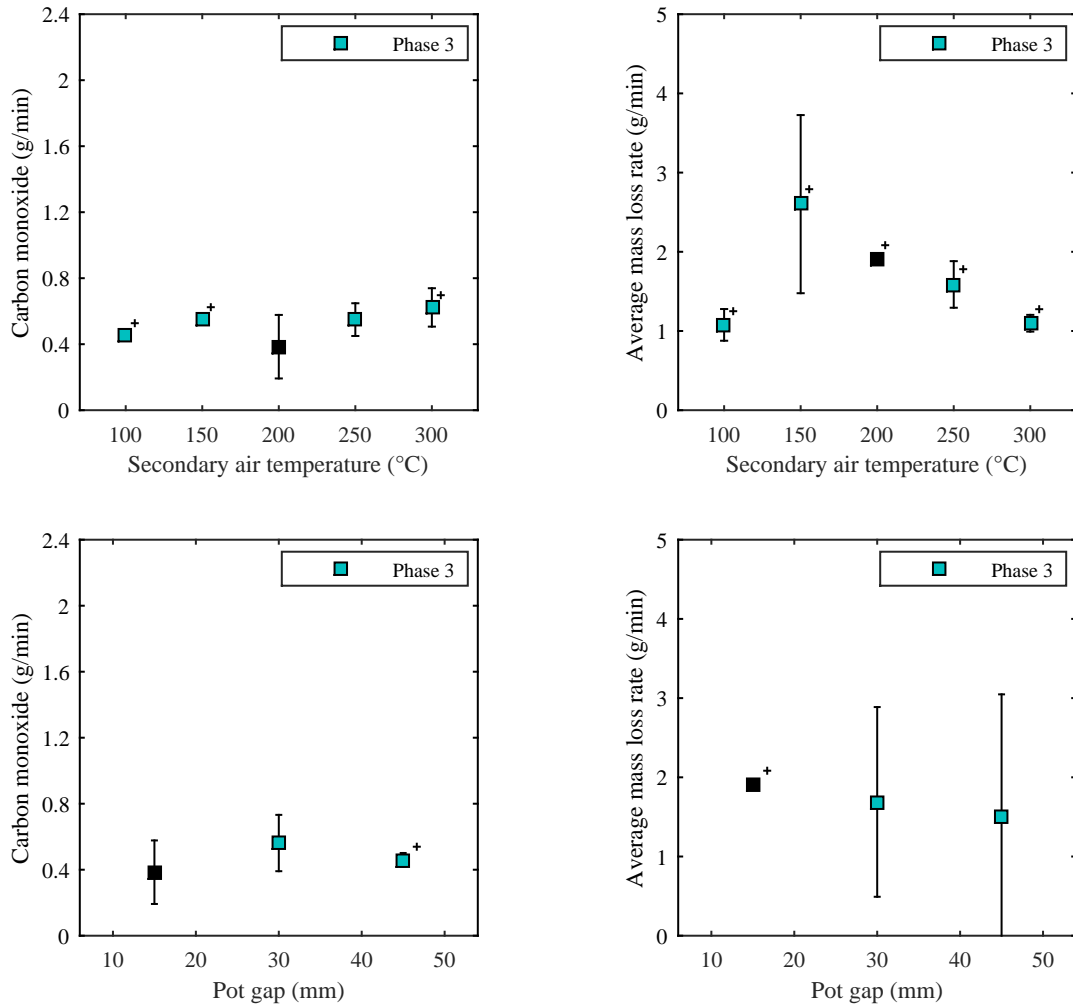
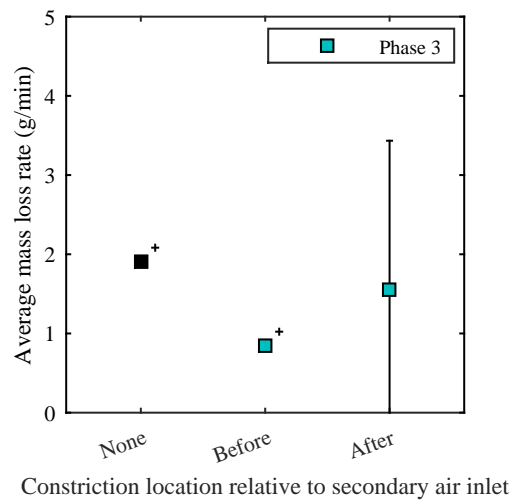
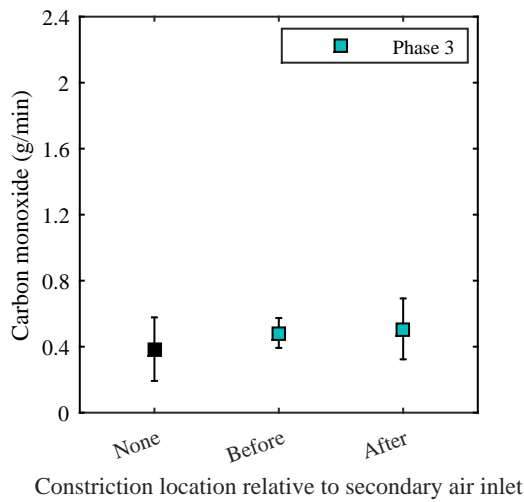
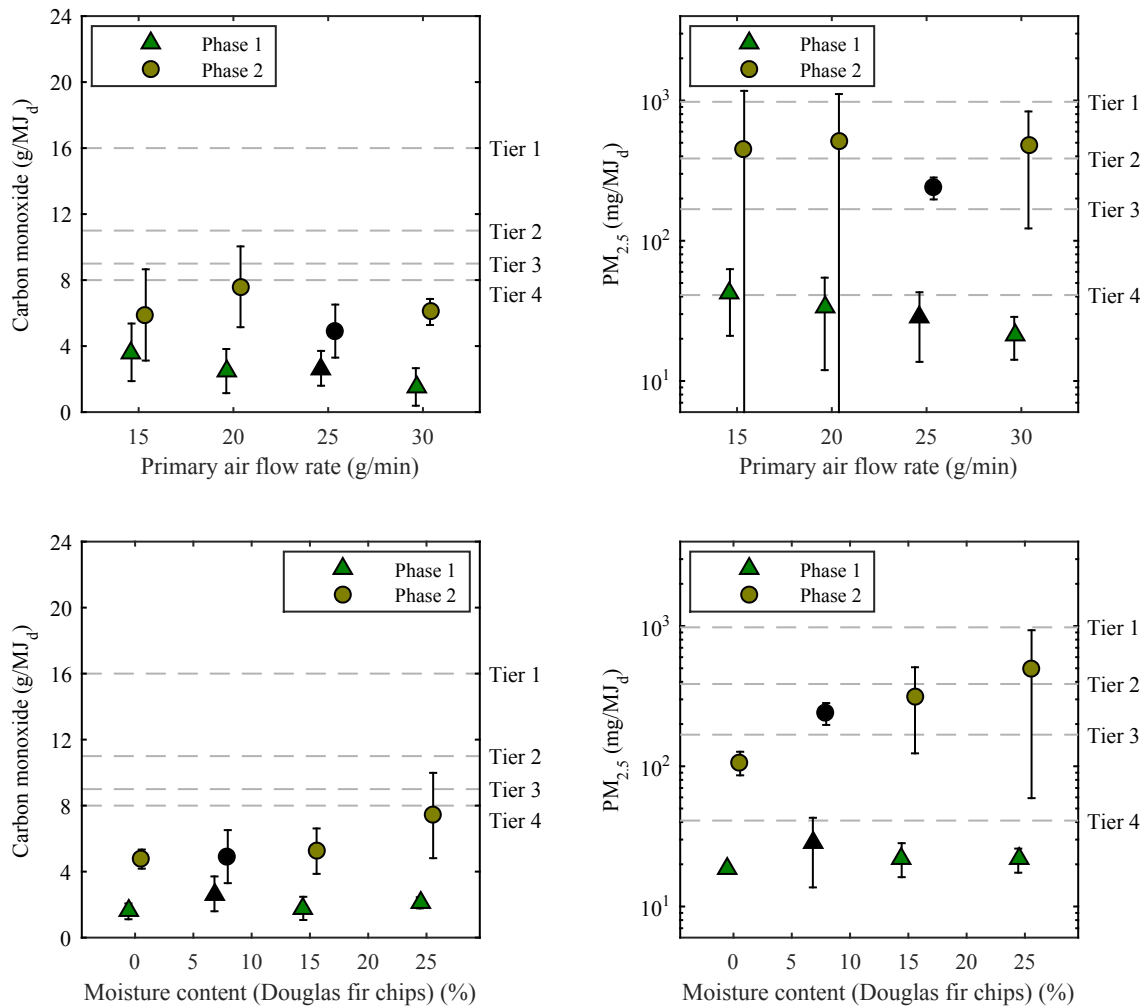


Figure B.12: Effects of varying secondary air temperature and the pot gap on average CO emissions and mass loss rate during char burnout. Black symbols refer to the baseline configuration (Douglas fir chip fuel, 7% moisture content,  $25 \text{ g}\cdot\text{min}^{-1}$  primary air,  $75 \text{ g}\cdot\text{min}^{-1}$  secondary air,  $200 \text{ }^\circ\text{C}$  secondary air temperature, 4-mm-dia. secondary air holes, no swirl, no downward angle, 15 mm pot gap, no flow constriction, no other features). Average values that were calculated from only two replicates are marked with a '+'. Error bars represent 90% confidence intervals for markers with no '+' and the total range of the measurements for markers with a '+'.



**Figure B.13: Effects of varying the constriction location on average CO emissions and mass loss rate during char burnout.** Black symbols refer to the baseline configuration (Douglas fir chip fuel, 7% moisture content,  $25 \text{ g}\cdot\text{min}^{-1}$  primary air,  $75 \text{ g}\cdot\text{min}^{-1}$  secondary air,  $200 \text{ }^\circ\text{C}$  secondary air temperature, 4-mm-dia. secondary air holes, no swirl, no downward angle, 15 mm pot gap, no flow constriction, no other features). Average values that were calculated from only two replicates are marked with a '+'. Error bars represent 90% confidence intervals for markers with no '+' and the total range of the measurements for markers with a '+'.

## B.2.2 Test Matrix 2 – Primary Air Flow Rates, Fuel Properties, and Secondary Air Delivery Parameters



**Figure B.14: Effects of varying primary air flow rate and fuel moisture content on average high-power CO and PM<sub>2.5</sub> emissions during normal operation (Phase 1, green triangles) and post-refueling (Phase 2, gold circles). Black symbols refer to the baseline configuration (Douglas fir chip fuel, 7% moisture content, 25 g·min<sup>-1</sup> primary air, 75 g·min<sup>-1</sup> secondary air, 200 °C secondary air temperature, 4-mm-dia. secondary air holes, no swirl, no downward angle, 15 mm pot gap, no flow constriction, no other features). Error bars represent 90% confidence intervals. Data points have been offset slightly on either side of the values listed in Table 4.1 to improve the readability of the plot.**

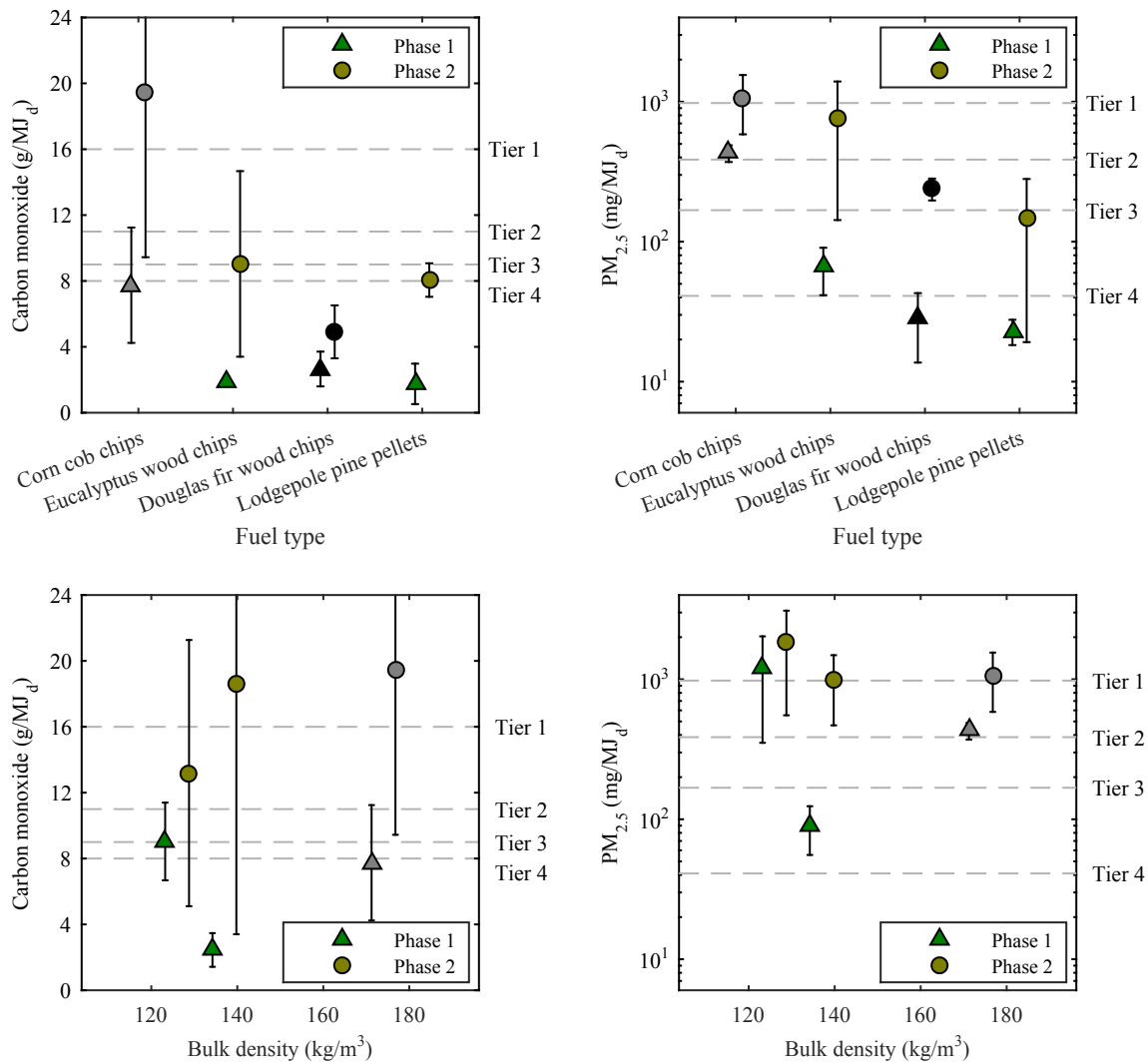


Figure B.15: Effects of varying fuel type and fuel bulk density on average high-power CO and PM<sub>2.5</sub> emissions during normal operation (Phase 1, green triangles) and post-refueling (Phase 2, gold circles). Black symbols refer to the baseline configuration (Douglas fir chip fuel, 7% moisture content, 25 g·min<sup>-1</sup> primary air, 75 g·min<sup>-1</sup> secondary air, 200 °C secondary air temperature, 4-mm-dia. secondary air holes, no swirl, no downward angle, 15 mm pot gap, no flow constriction, no other features). Gray symbols correspond to the test case with the highest bulk density corn cobs (174 kg·m<sup>-3</sup>). Error bars represent 90% confidence intervals. Data points have been offset slightly on either side of the values listed in Table 4.1 to improve the readability of the plot.

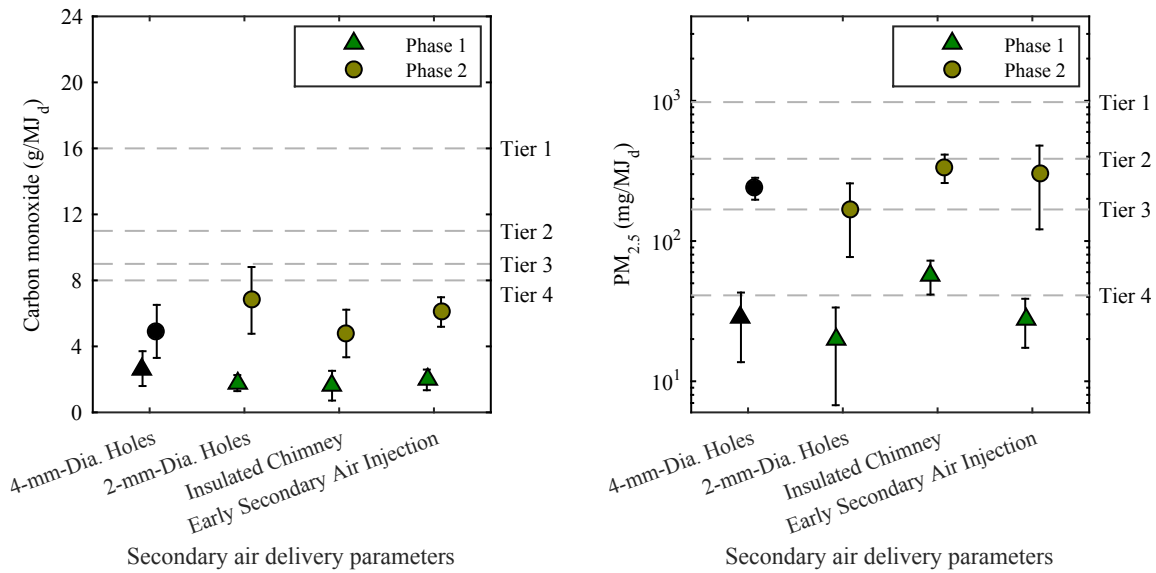
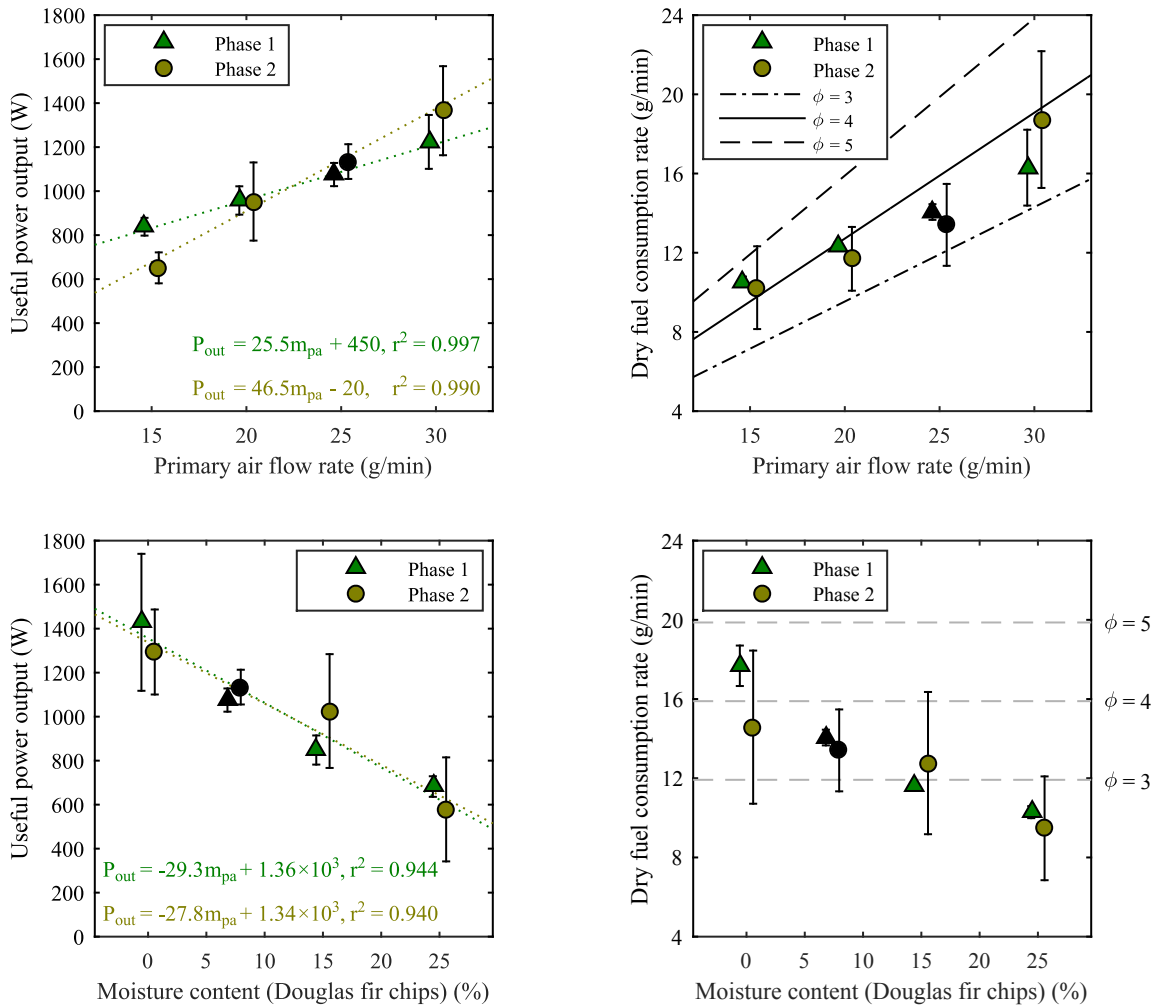


Figure B.16: Effects of varying secondary air delivery parameters on average high-power CO and PM<sub>2.5</sub> emissions during normal operation (Phase 1, green triangles) and post-refueling (Phase 2, gold circles). Black symbols refer to the baseline configuration (Douglas fir chip fuel, 7% moisture content, 25 g·min<sup>-1</sup> primary air, 75 g·min<sup>-1</sup> secondary air, 200 °C secondary air temperature, 4-mm-dia. secondary air holes, no swirl, no downward angle, 15 mm pot gap, no flow constriction, no other features). Error bars represent 90% confidence intervals. Data points have been offset slightly to improve the readability of the plot.



**Figure B.17: Effects of varying primary air flow rate and fuel moisture content on average high-power useful power output and fuel consumption rate during normal operation (Phase 1, green triangles) and post-refueling (Phase 2, gold circles). Black symbols refer to the baseline configuration (Douglas fir chip fuel, 7% moisture content,  $25 \text{ g} \cdot \text{min}^{-1}$  primary air,  $75 \text{ g} \cdot \text{min}^{-1}$  secondary air,  $200 \text{ }^\circ\text{C}$  secondary air temperature, 4-mm-dia. secondary air holes, no swirl, no downward angle, 15 mm pot gap, no flow constriction, no other features). Error bars represent 90% confidence intervals. Data points have been offset slightly on either side of the values listed in Table 4.1 to improve the readability of the plot.**

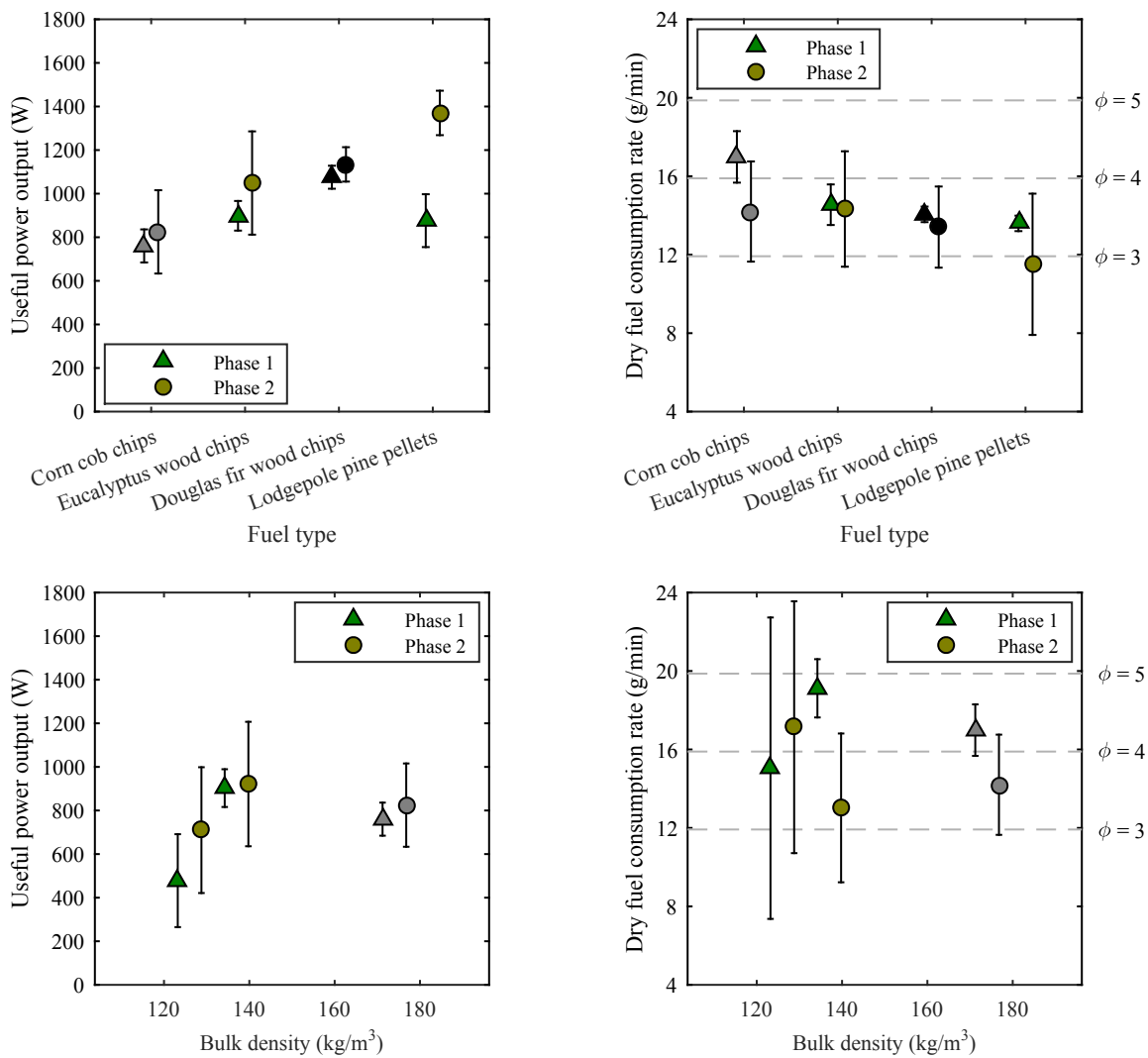
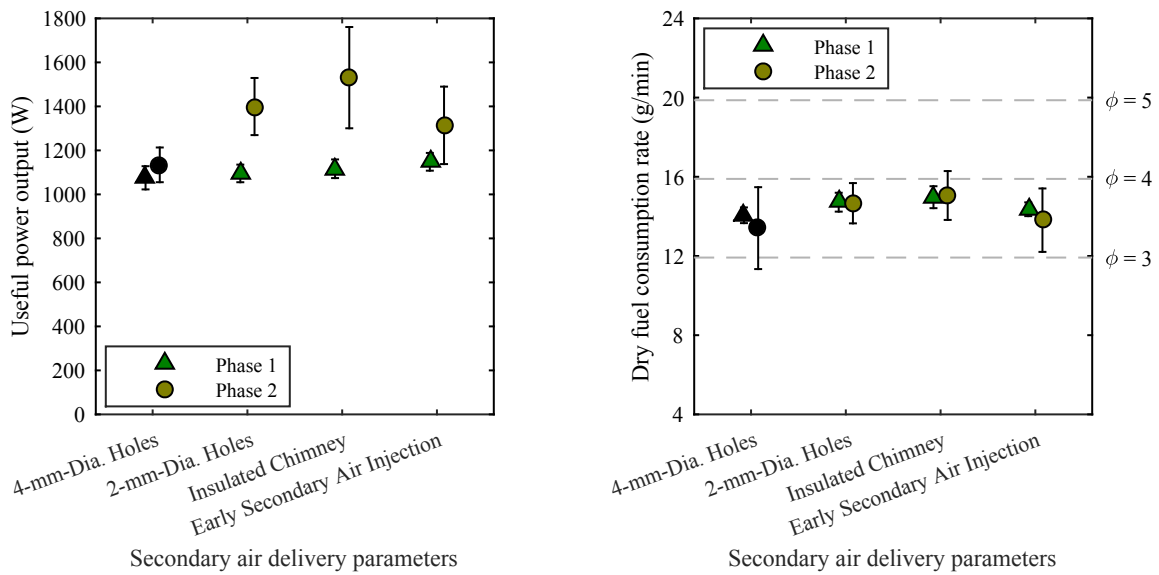
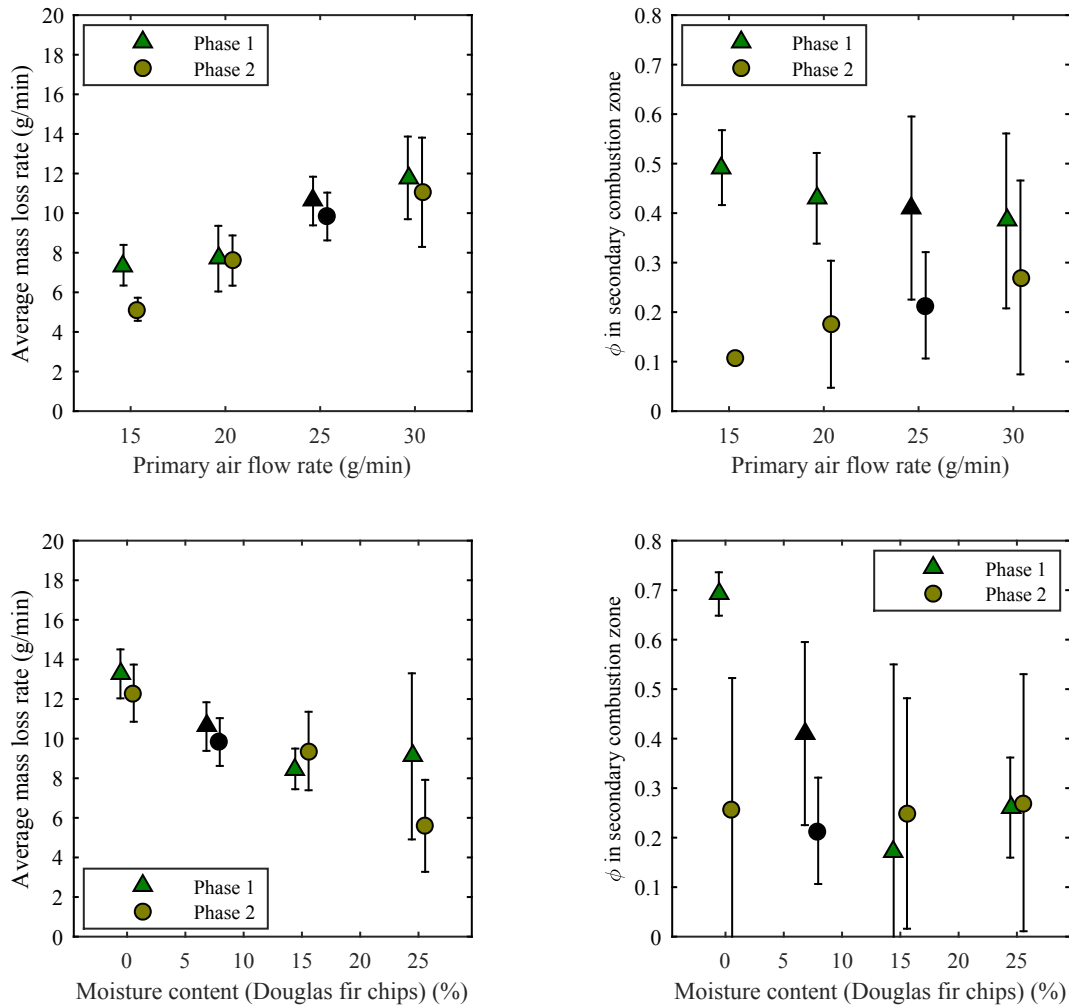


Figure B.18: Effects of varying fuel type and fuel bulk density on average high-power useful power output and fuel consumption rate during normal operation (Phase 1, green triangles) and post-refueling (Phase 2, gold circles). Black symbols refer to the baseline configuration (Douglas fir chip fuel, 7% moisture content, 25 g·min<sup>-1</sup> primary air, 75 g·min<sup>-1</sup> secondary air, 200 °C secondary air temperature, 4-mm-dia. secondary air holes, no swirl, no downward angle, 15 mm pot gap, no flow constriction, no other features). Gray symbols correspond to the test case with the highest bulk density corn cobs (174 kg·m<sup>-3</sup>). Error bars represent 90% confidence intervals. Data points have been offset slightly on either side of the values listed in Table 4.1 to improve the readability of the plot.



**Figure B.19: Effects of varying secondary air delivery parameters on average useful power output and fuel consumption rate during normal operation (Phase 1, green triangles) and post-refueling (Phase 2, gold circles). Black symbols refer to the baseline configuration (Douglas fir chip fuel, 7% moisture content, 25 g·min<sup>-1</sup> primary air, 75 g·min<sup>-1</sup> secondary air, 200 °C secondary air temperature, 4-mm-dia. secondary air holes, no swirl, no downward angle, 15 mm pot gap, no flow constriction, no other features). Error bars represent 90% confidence intervals. Data points have been offset slightly to improve the readability of the plot.**



**Figure B.20: Effects of varying primary air flow rate and fuel moisture content on average high-power mass loss rate and global equivalence ratio in the secondary combustion zone during normal operation (Phase 1, green triangles) and post-refueling (Phase 2, gold circles). Black symbols refer to the baseline configuration (Douglas fir chip fuel, 7% moisture content,  $25 \text{ g}\cdot\text{min}^{-1}$  primary air,  $75 \text{ g}\cdot\text{min}^{-1}$  secondary air,  $200 \text{ }^\circ\text{C}$  secondary air temperature, 4-mm-dia. secondary air holes, no swirl, no downward angle, 15 mm pot gap, no flow constriction, no other features). Error bars represent 90% confidence intervals. Data points have been offset slightly on either side of the values listed in Table 4.1 to improve the readability of the plot.**

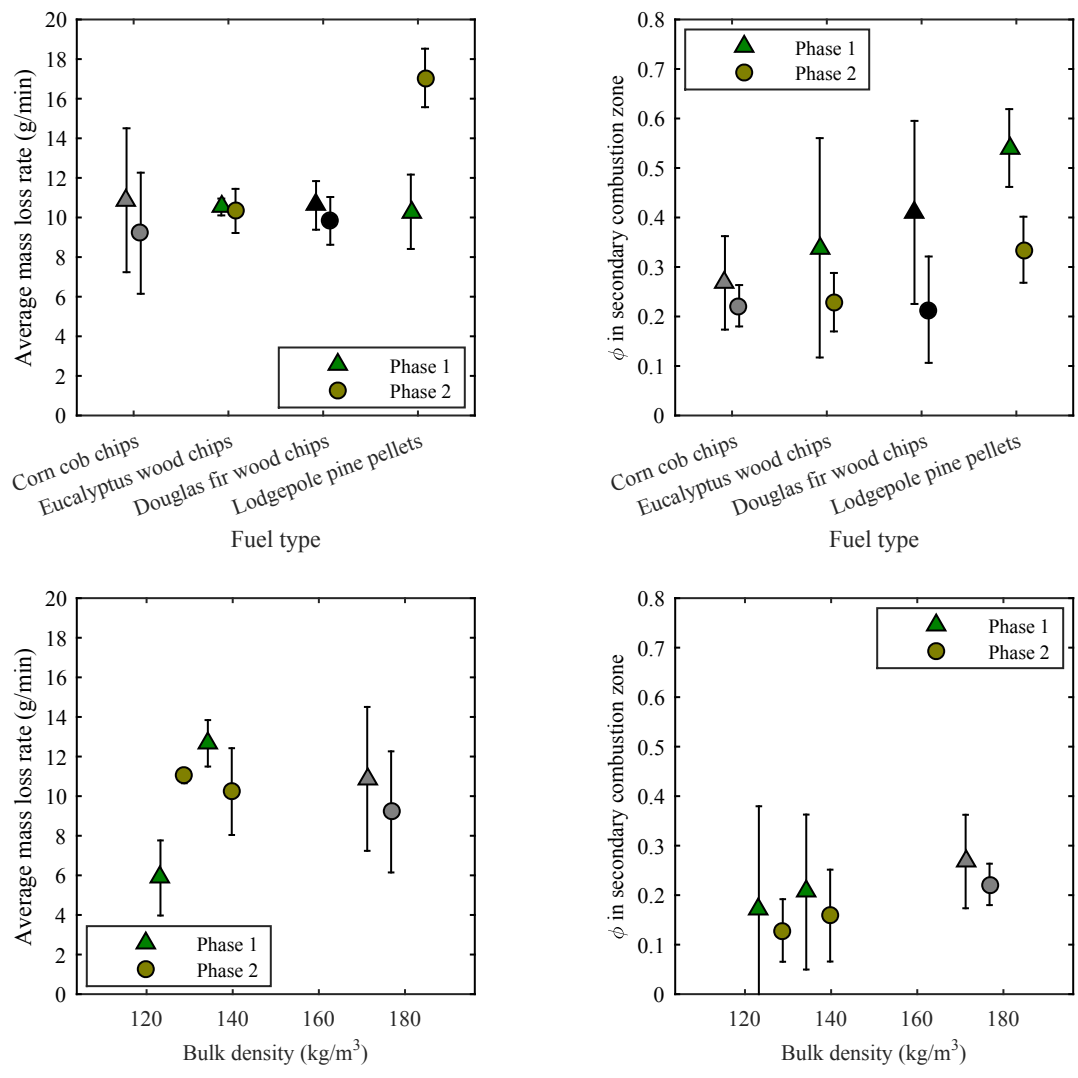
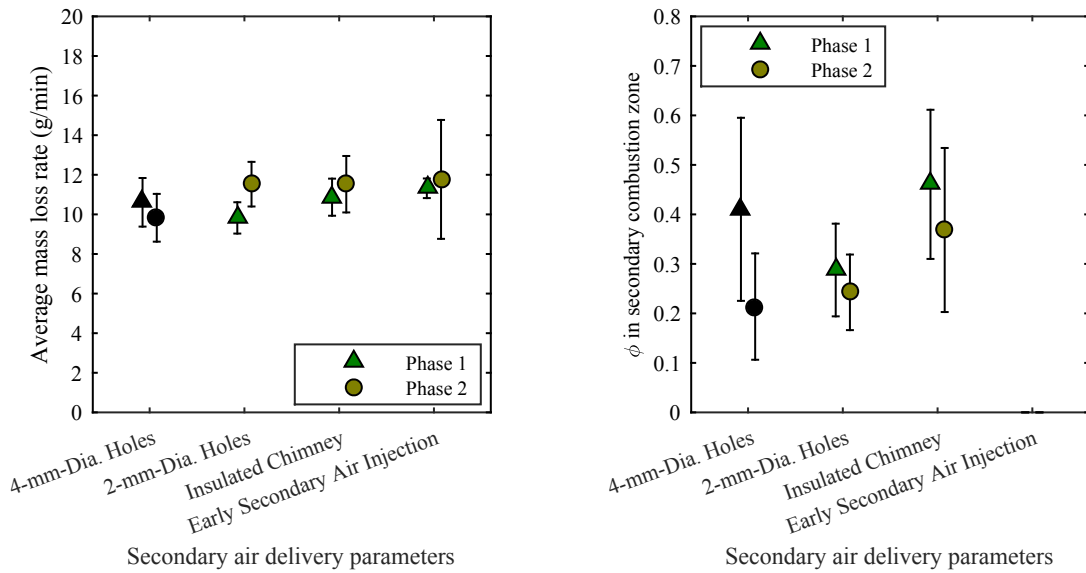
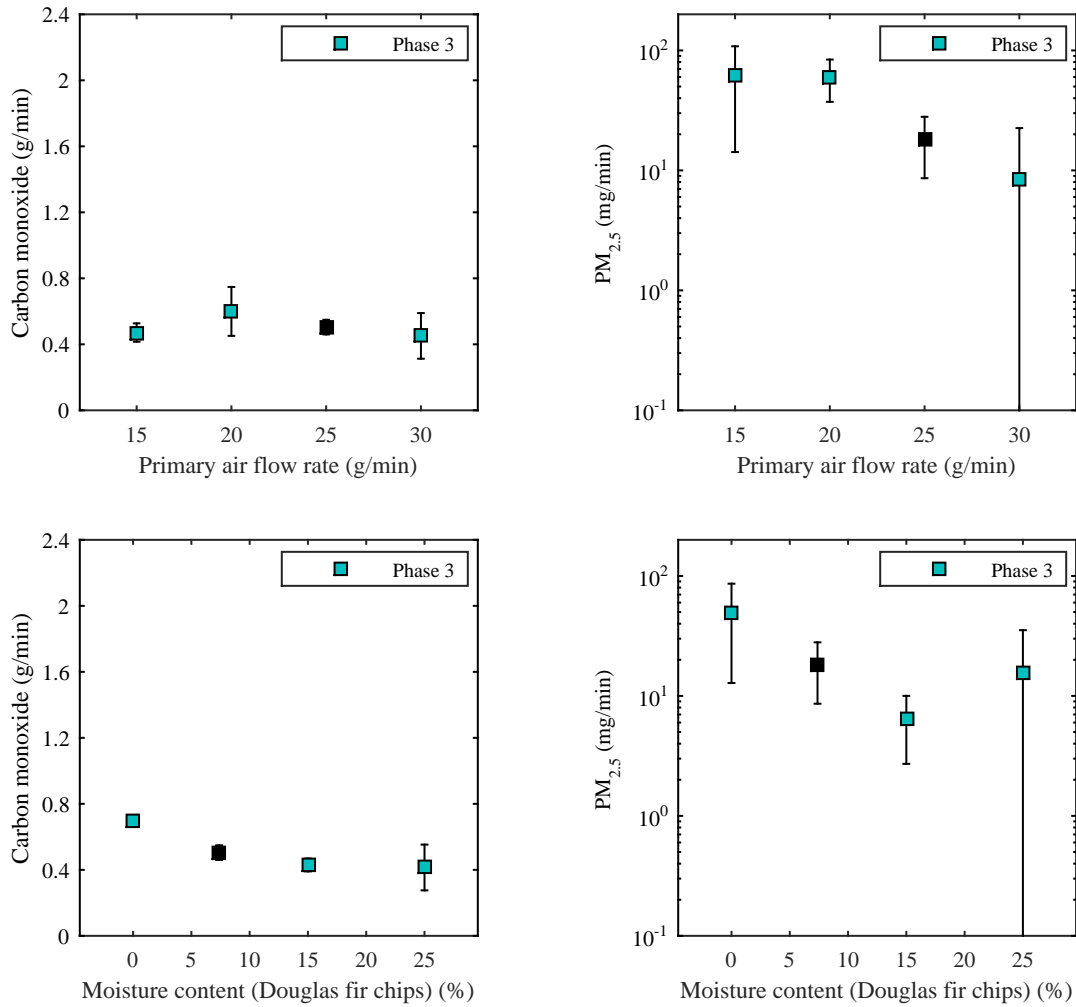


Figure B.21: Effects of varying fuel type and fuel bulk density on average high-power mass loss rate and global equivalence ratio in the secondary combustion zone during normal operation (Phase 1, green triangles) and post-refueling (Phase 2, gold circles). Black symbols refer to the baseline configuration (Douglas fir chip fuel, 7% moisture content, 25 g·min<sup>-1</sup> primary air, 75 g·min<sup>-1</sup> secondary air, 200 °C secondary air temperature, 4-mm-dia. secondary air holes, no swirl, no downward angle, 15 mm pot gap, no flow constriction, no other features). Gray symbols correspond to the test case with the highest bulk density corn cobs (174 kg·m<sup>-3</sup>). Error bars represent 90% confidence intervals. Data points have been offset slightly on either side of the values listed in Table 4.1 to improve the readability of the plot.



**Figure B.22:** Effects of varying secondary air delivery parameters on average high-power mass loss rate and global equivalence ratio in the secondary combustion zone during normal operation (Phase 1, green triangles) and post-refueling (Phase 2, gold circles). Black symbols refer to the baseline configuration (Douglas fir chip fuel, 7% moisture content,  $25 \text{ g}\cdot\text{min}^{-1}$  primary air,  $75 \text{ g}\cdot\text{min}^{-1}$  secondary air,  $200 \text{ }^\circ\text{C}$  secondary air temperature, 4-mm-dia. secondary air holes, no swirl, no downward angle, 15 mm pot gap, no flow constriction, no other features). Error bars represent 90% confidence intervals. Data points have been offset slightly to improve the readability of the plot.



**Figure B.23:** Effects of varying primary air flow rate and fuel moisture content on average CO and PM<sub>2.5</sub> emissions during char burnout. Black symbols refer to the baseline configuration (Douglas fir chip fuel, 7% moisture content, 25 g·min<sup>-1</sup> primary air, 75 g·min<sup>-1</sup> secondary air, 200 °C secondary air temperature, 4-mm-dia. secondary air holes, no swirl, no downward angle, 15 mm pot gap, no flow constriction, no other features). Error bars represent 90% confidence intervals.

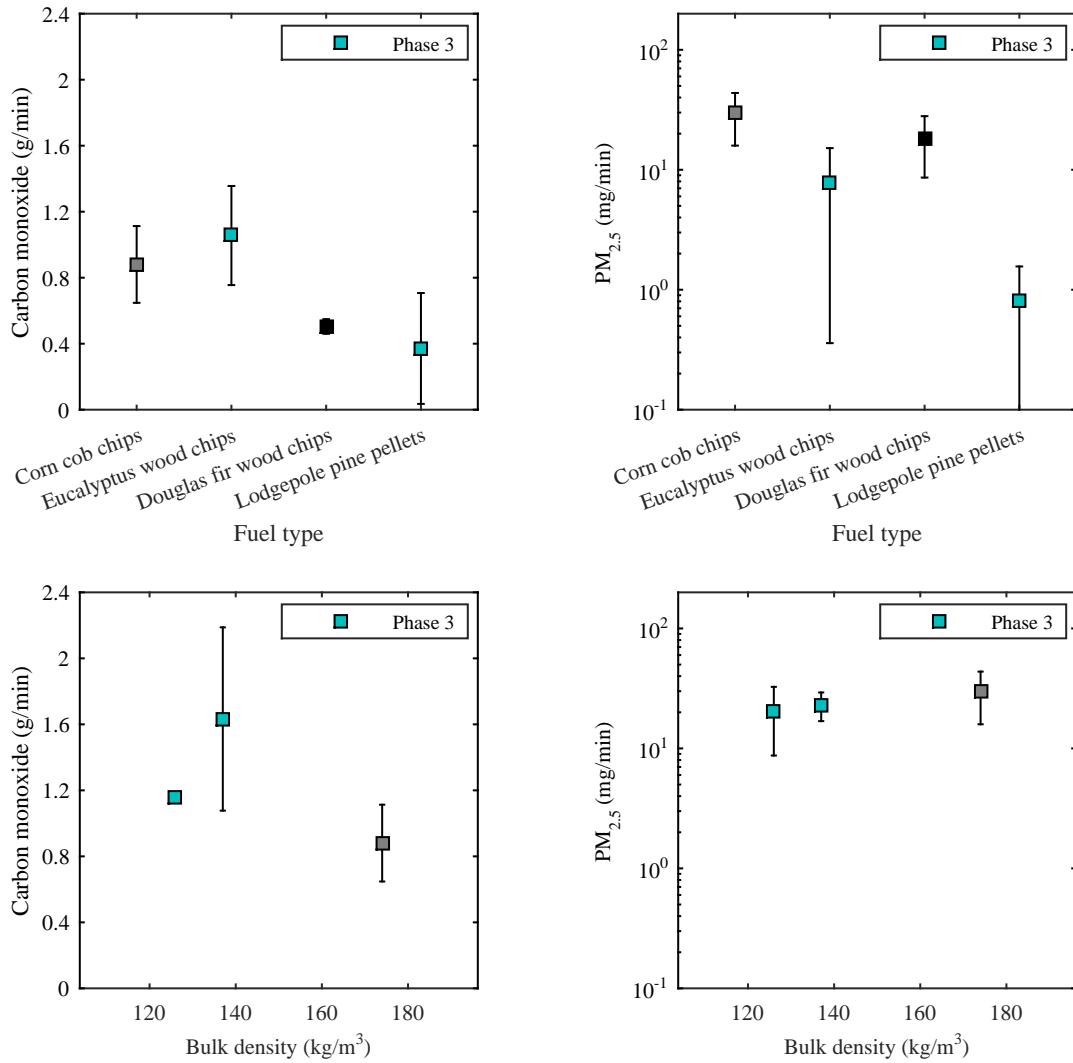


**Figure B.24: Effects of varying fuel type and fuel bulk density on average CO and PM<sub>2.5</sub> emissions during char burnout.** Black symbols refer to the baseline configuration (Douglas fir chip fuel, 7% moisture content, 25 g·min<sup>-1</sup> primary air, 75 g·min<sup>-1</sup> secondary air, 200 °C secondary air temperature, 4-mm-dia. secondary air holes, no swirl, no downward angle, 15 mm pot gap, no flow constriction, no other features). Gray symbols correspond to the test case with the highest bulk density corn cobs (174 kg·m<sup>-3</sup>). Error bars represent 90% confidence intervals.

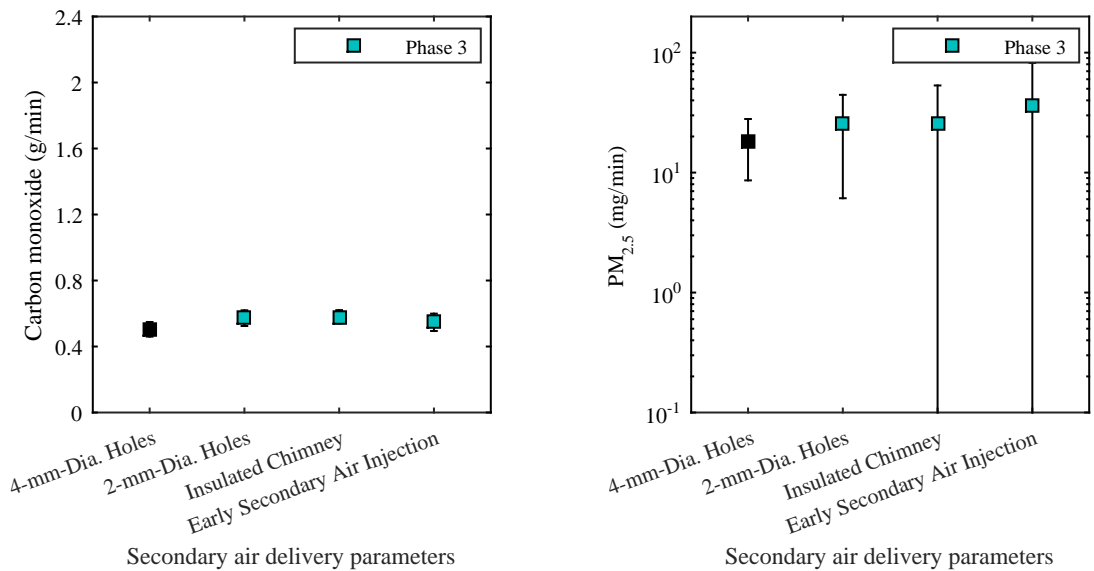


**Figure B.25: Effects of varying secondary air delivery parameters on average CO and PM<sub>2.5</sub> emissions during char burnout. Black symbols refer to the baseline configuration (Douglas fir chip fuel, 7% moisture content, 25 g·min<sup>-1</sup> primary air, 75 g·min<sup>-1</sup> secondary air, 200 °C secondary air temperature, 4-mm-dia. secondary air holes, no swirl, no downward angle, 15 mm pot gap, no flow constriction, no other features). Error bars represent 90% confidence intervals.**

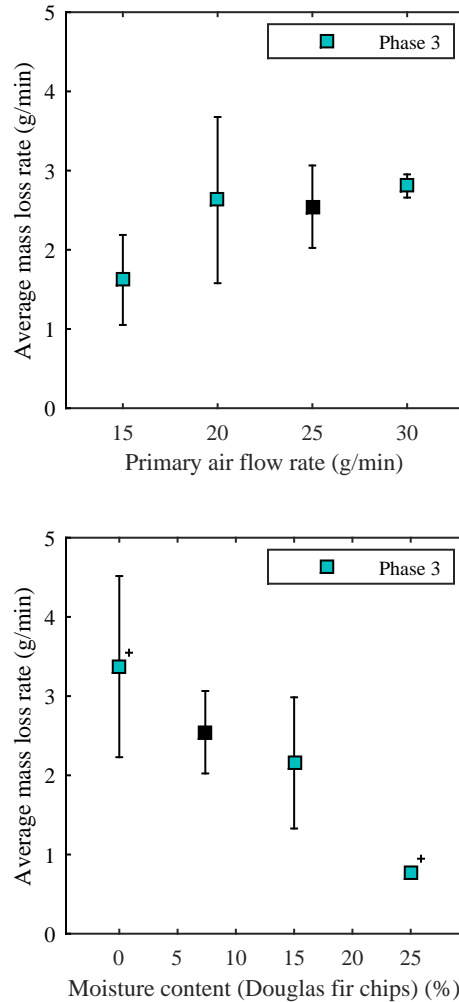
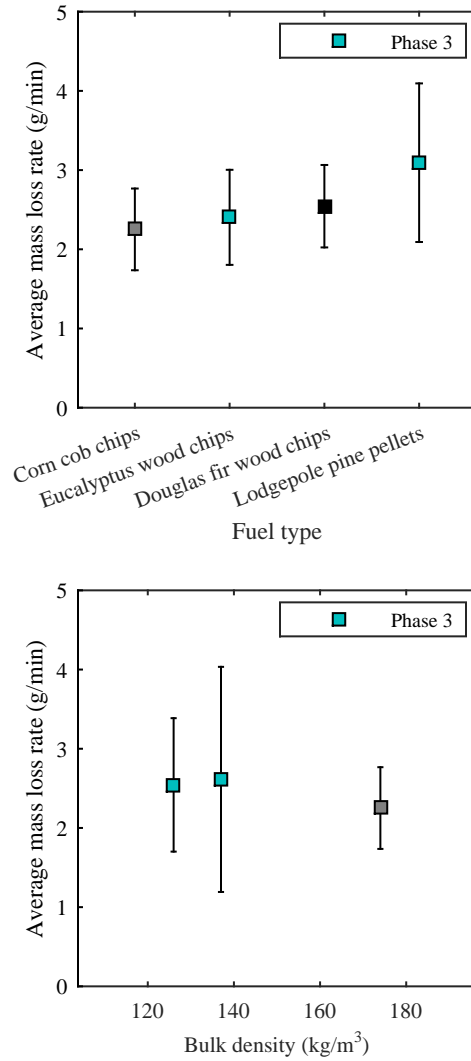
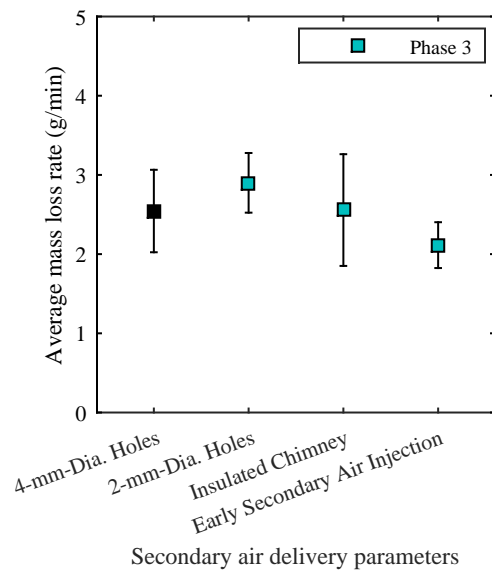


Figure B.26: Effects of varying primary air flow rate and fuel moisture content on the average mass loss rate during char burnout. Black symbols refer to the baseline configuration (Douglas fir chip fuel, 7% moisture content,  $25 \text{ g}\cdot\text{min}^{-1}$  primary air,  $75 \text{ g}\cdot\text{min}^{-1}$  secondary air,  $200 \text{ }^\circ\text{C}$  secondary air temperature, 4-mm-dia. secondary air holes, no swirl, no downward angle, 15 mm pot gap, no flow constriction, no other features). Average values that were calculated from less than three replicates are marked with a '+'. Error bars represent 90% confidence intervals for markers with no '+' and the total range of the measurements for markers with a '+'.



**Figure B.27:** Effects of varying fuel type and fuel bulk density on the average mass loss rate during char burnout. Black symbols refer to the baseline configuration (Douglas fir chip fuel, 7% moisture content, 25 g·min<sup>-1</sup> primary air, 75 g·min<sup>-1</sup> secondary air, 200 °C secondary air temperature, 4-mm-dia. secondary air holes, no swirl, no downward angle, 15 mm pot gap, no flow constriction, no other features). Gray symbols correspond to the test case with the highest bulk density corn cobs (174 kg·m<sup>-3</sup>). Error bars represent 90% confidence intervals.



**Figure B.28:** Effects of varying secondary air delivery parameters on the average mass loss rate during char burnout. Black symbols refer to the baseline configuration (Douglas fir chip fuel, 7% moisture content,  $25 \text{ g}\cdot\text{min}^{-1}$  primary air,  $75 \text{ g}\cdot\text{min}^{-1}$  secondary air,  $200 \text{ }^\circ\text{C}$  secondary air temperature, 4-mm-dia. secondary air holes, no swirl, no downward angle, 15 mm pot gap, no flow constriction, no other features). Error bars represent 90% confidence intervals.

### B.2.3 Gas Composition Results and Fuel Bed Temperatures

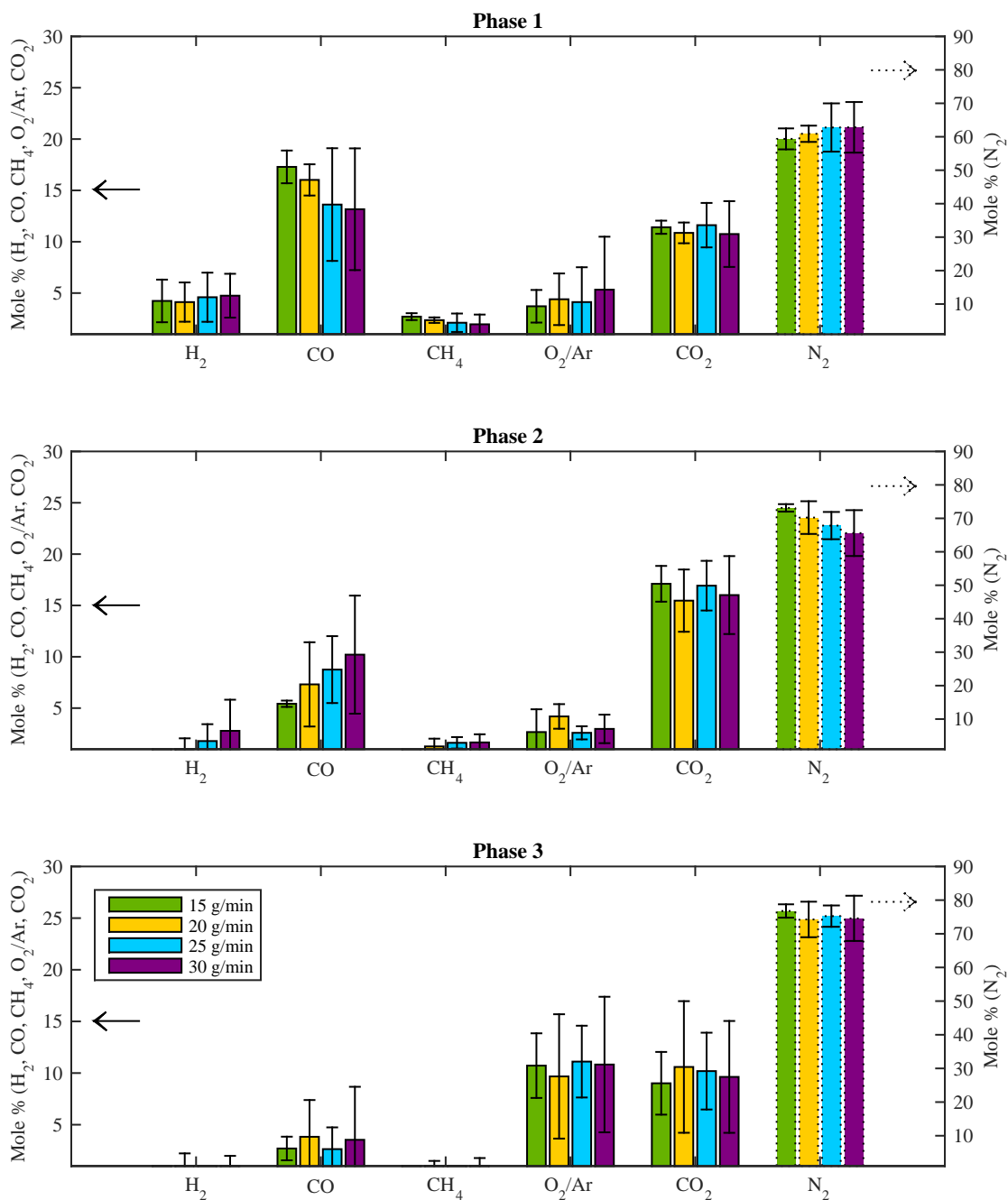
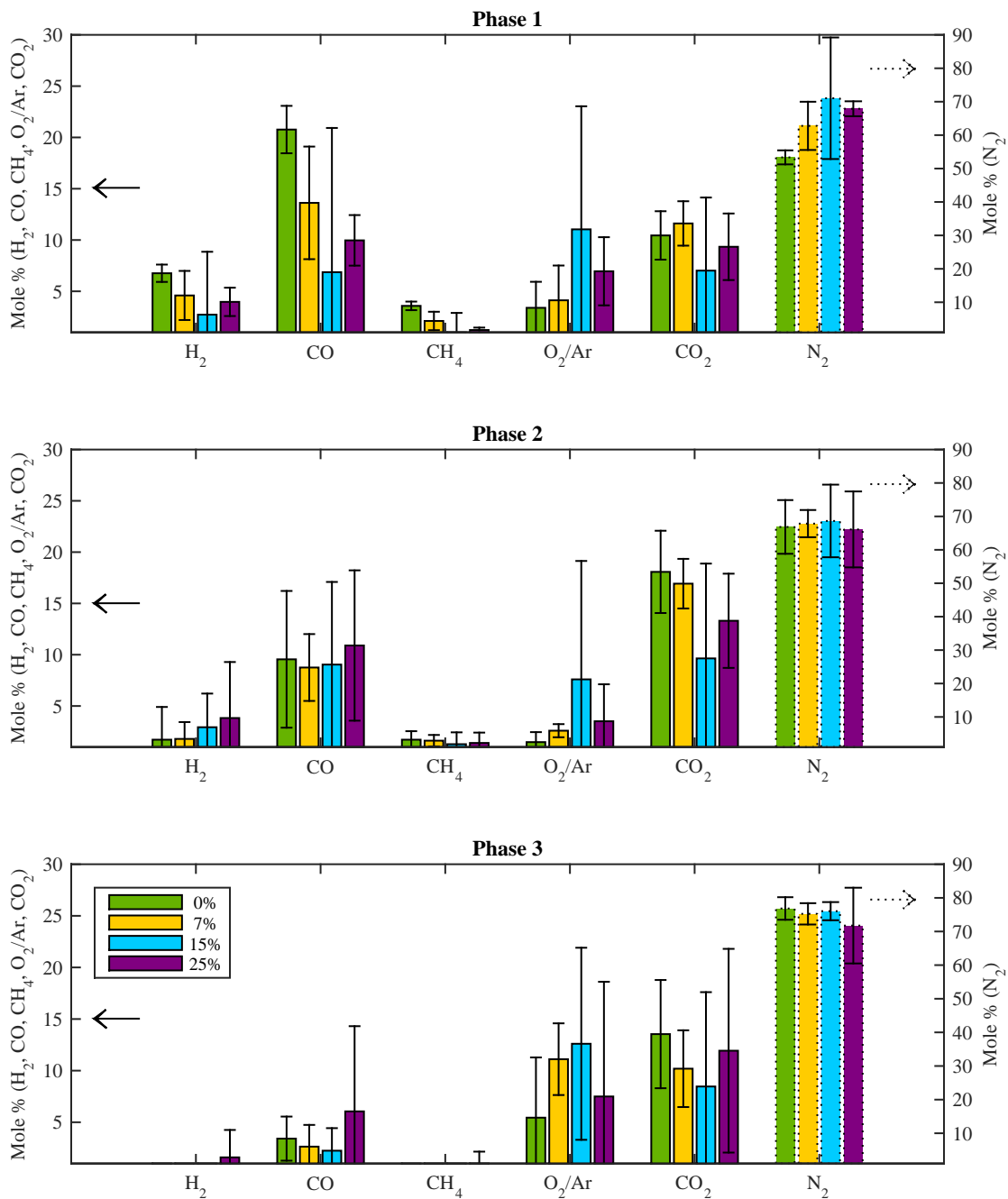


Figure B.29: Effects of primary air flow rate on the average concentrations of H<sub>2</sub>, CO, CH<sub>4</sub>, O<sub>2</sub>/Ar, CO<sub>2</sub> and N<sub>2</sub> in the producer gas entering the secondary combustion zone during normal operation (Phase 1), post-refueling (Phase 2) and during char burnout (Phase 3). Error bars represent 90% confidence intervals.



**Figure B.30:** Effects of fuel moisture content (for Douglas fir chips) on the average concentrations of H<sub>2</sub>, CO, CH<sub>4</sub>, O<sub>2</sub>/Ar, CO<sub>2</sub> and N<sub>2</sub> in the producer gas entering the secondary combustion zone during normal operation (Phase 1), post-refueling (Phase 2) and during char burnout (Phase 3). Error bars represent 90% confidence intervals.

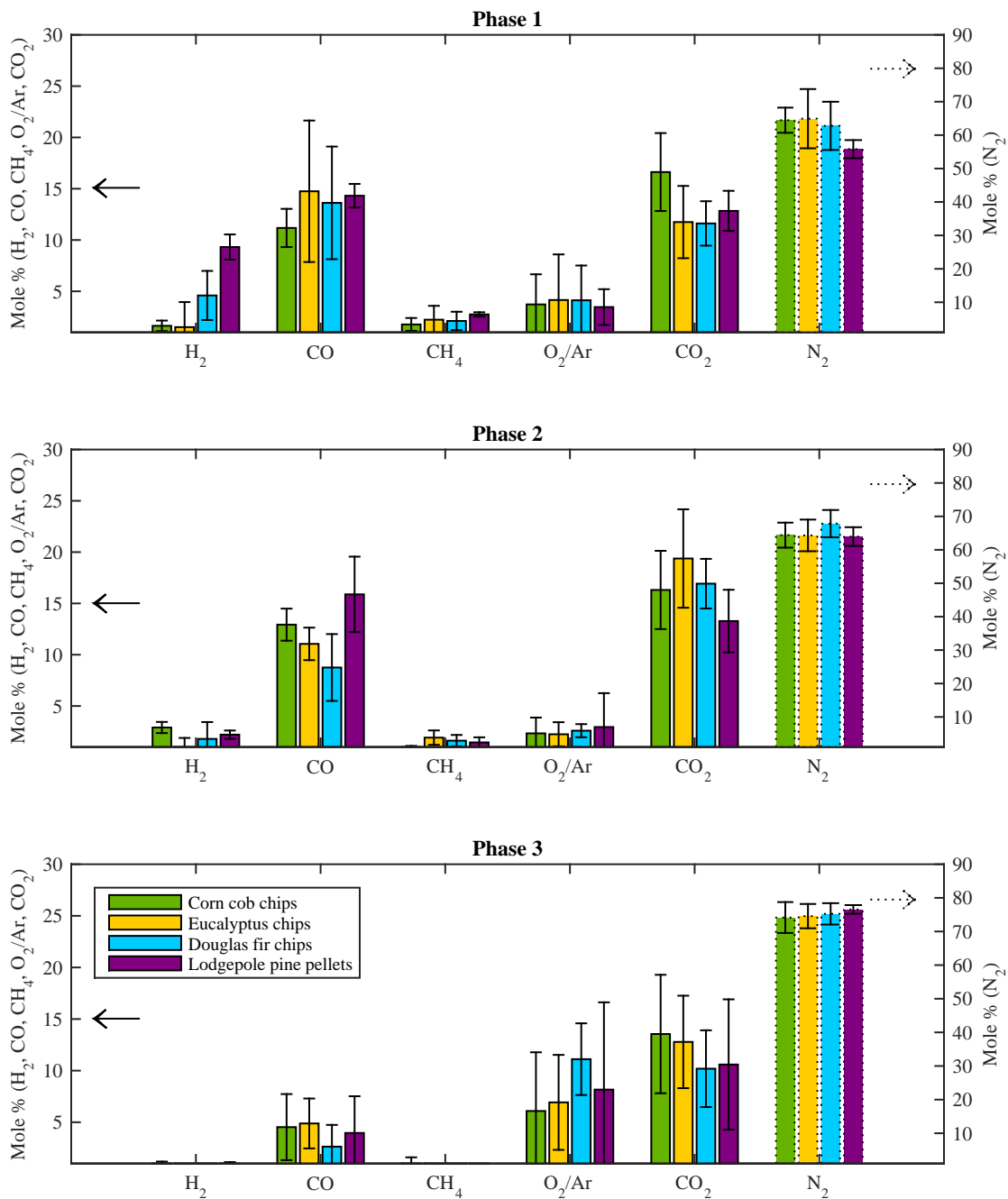
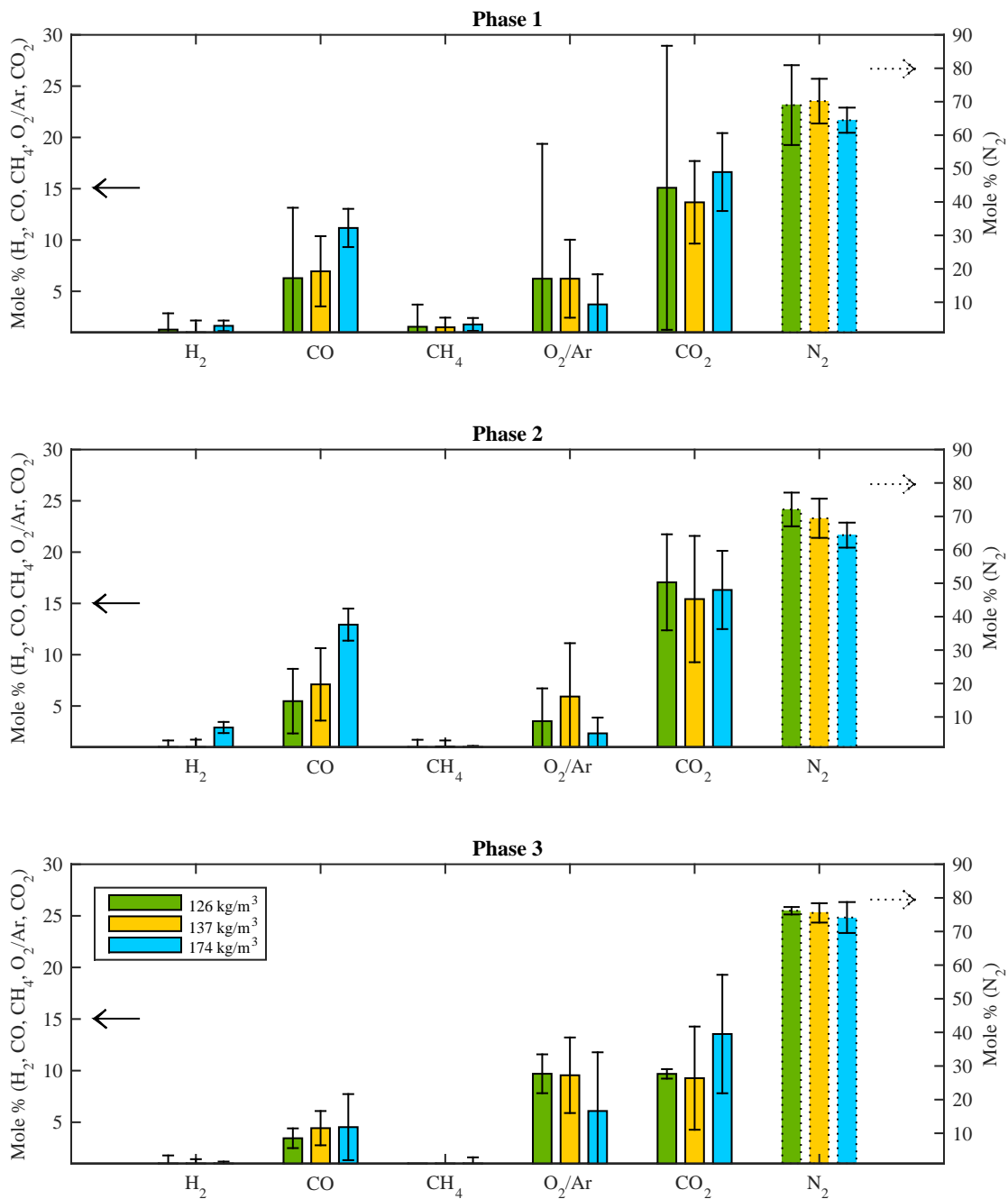
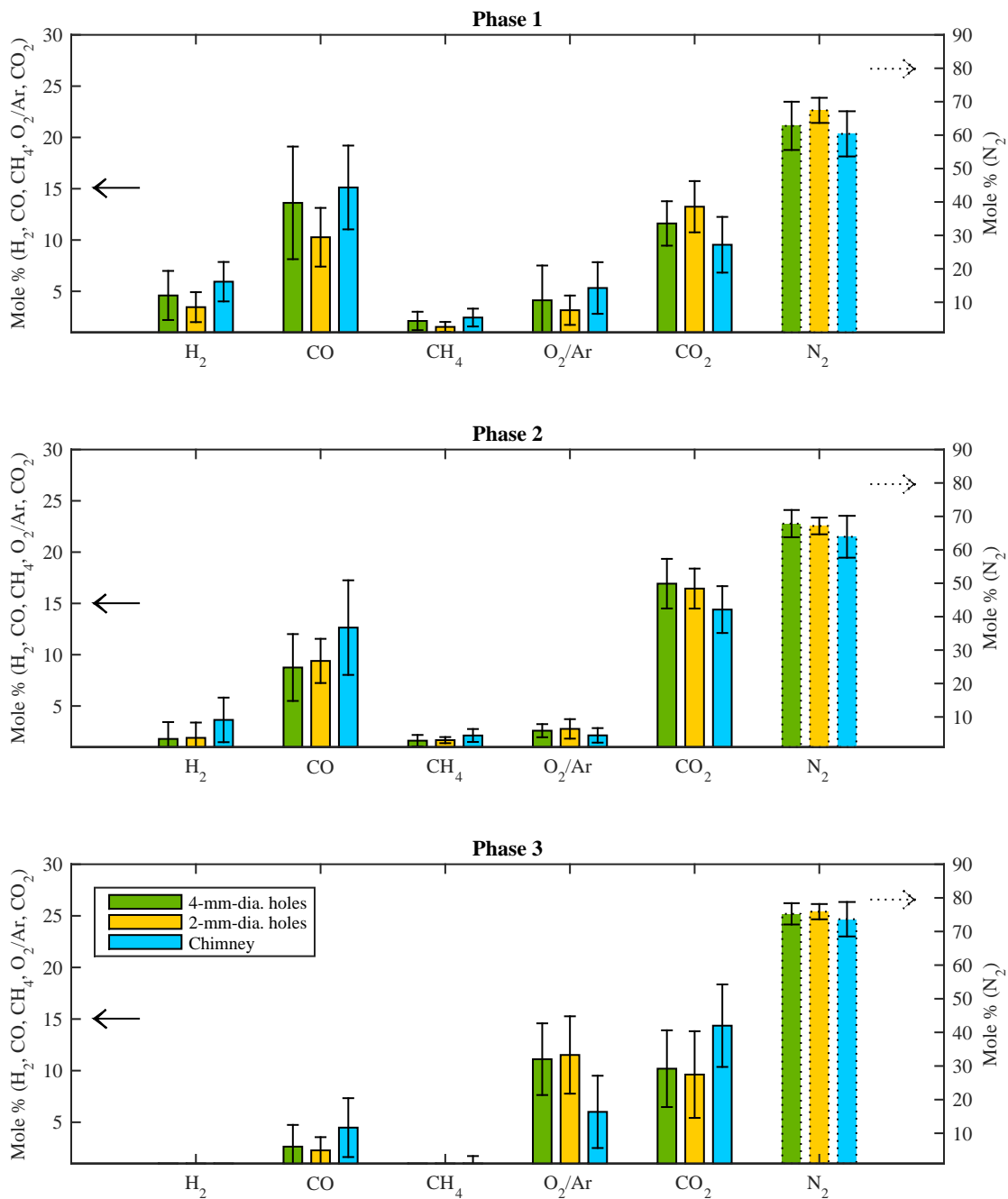


Figure B.31: Effects of fuel type on the average concentrations of H<sub>2</sub>, CO, CH<sub>4</sub>, O<sub>2</sub>/Ar, CO<sub>2</sub> and N<sub>2</sub> in the producer gas entering the secondary combustion zone during normal operation (Phase 1), post-refueling (Phase 2) and during char burnout (Phase 3). Error bars represent 90% confidence intervals.



**Figure B.32:** Effects of fuel bulk density (for corn cobs) on the average concentrations of H<sub>2</sub>, CO, CH<sub>4</sub>, O<sub>2</sub>/Ar, CO<sub>2</sub> and N<sub>2</sub> in the producer gas entering the secondary combustion zone during normal operation (Phase 1), post-refueling (Phase 2) and during char burnout (Phase 3). Error bars represent 90% confidence intervals.



**Figure B.33:** Effects of secondary air delivery parameters on the average concentrations of H<sub>2</sub>, CO, CH<sub>4</sub>, O<sub>2</sub>/Ar, CO<sub>2</sub> and N<sub>2</sub> in the producer gas entering the secondary combustion zone during normal operation (Phase 1), post-refueling (Phase 2) and during char burnout (Phase 3). Error bars represent 90% confidence intervals.

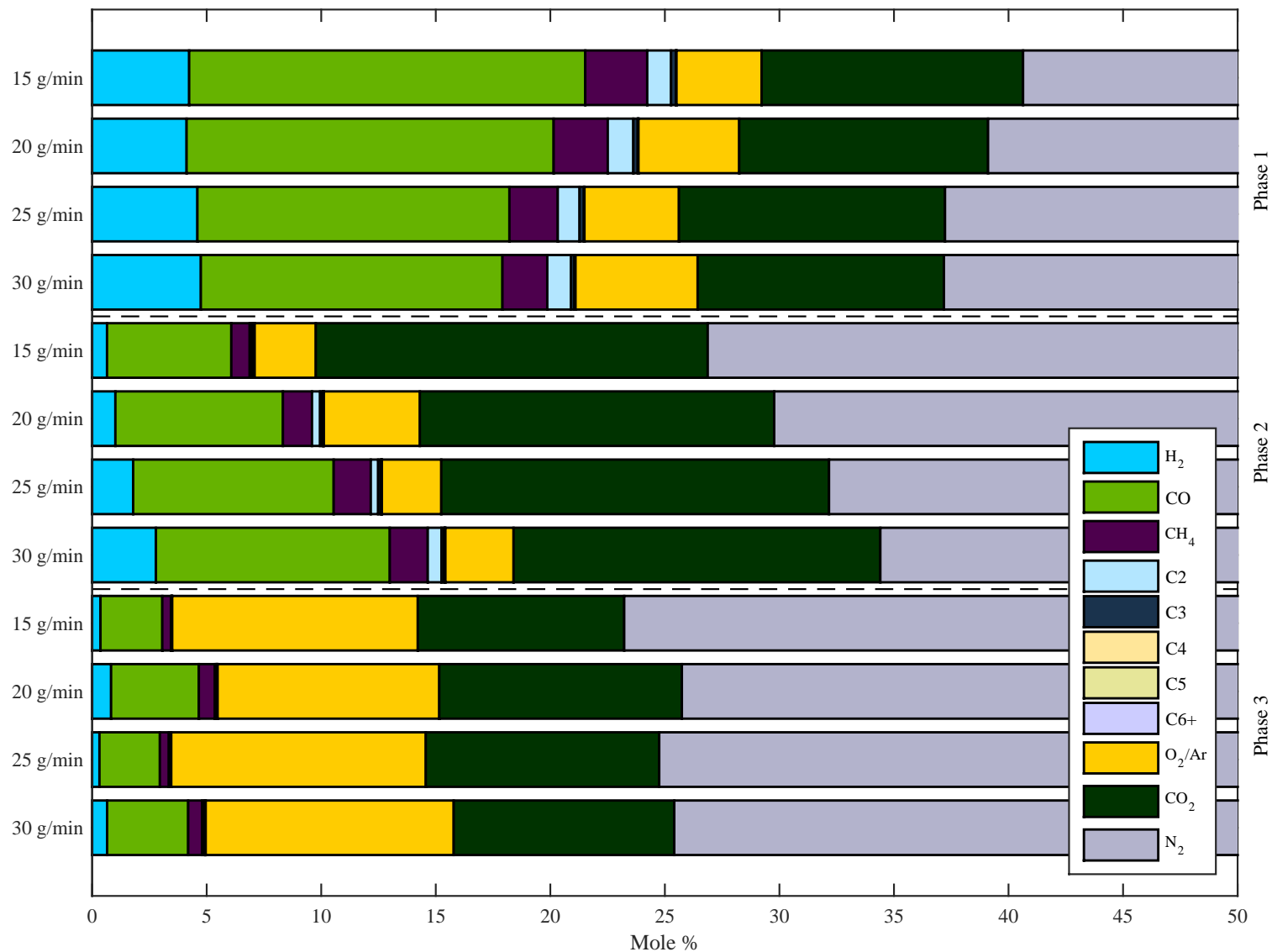


Figure B.34: Effects of primary air flow rate on the average composition of the producer gas entering the secondary combustion zone during normal operation (Phase 1), post-refueling (Phase 2) and during char burnout (Phase 3).

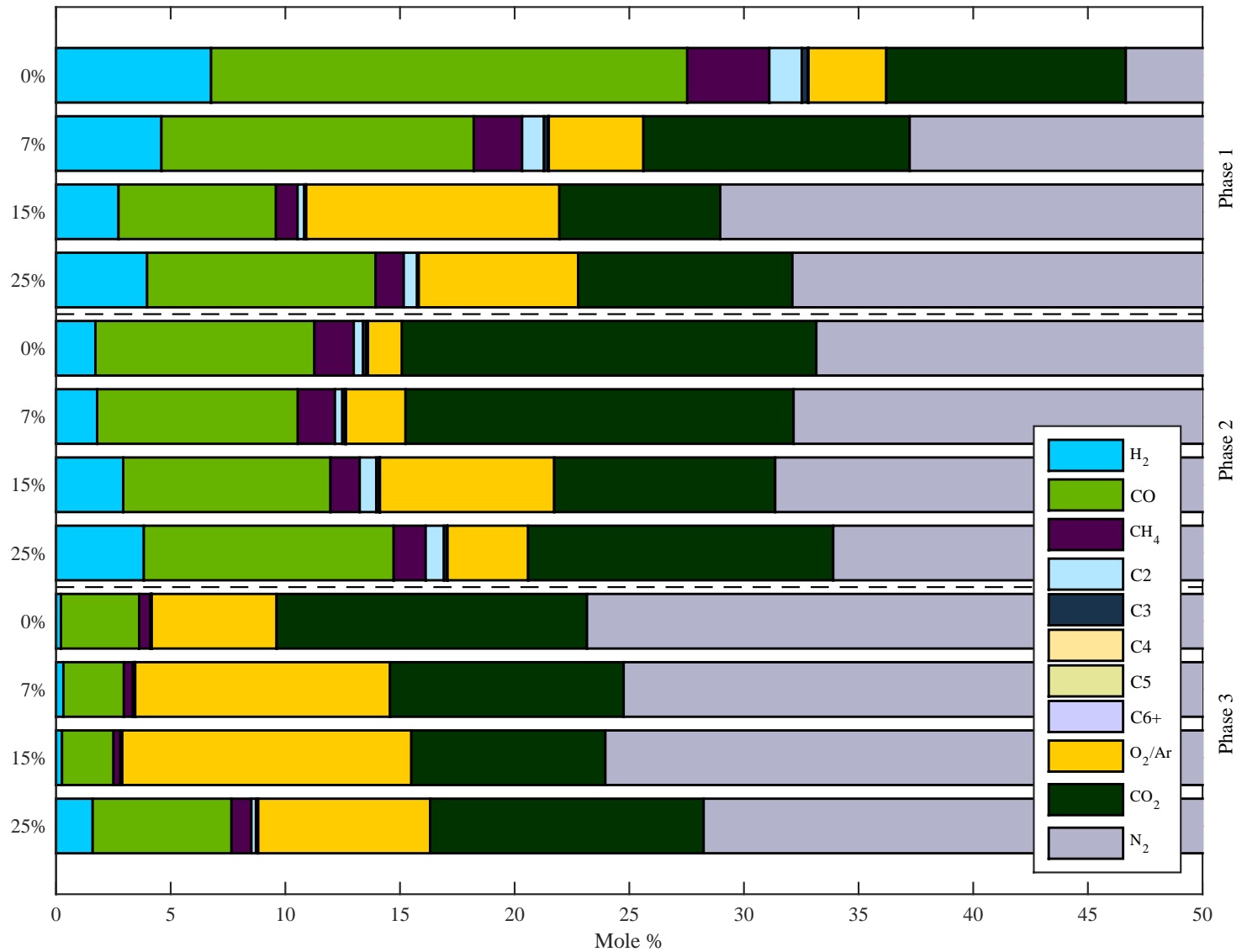


Figure B.35: Effects of fuel moisture content (for Douglas fir chips) on the average composition of the producer gas entering the secondary combustion zone during normal operation (Phase 1), post-refueling (Phase 2) and during char burnout (Phase 3).

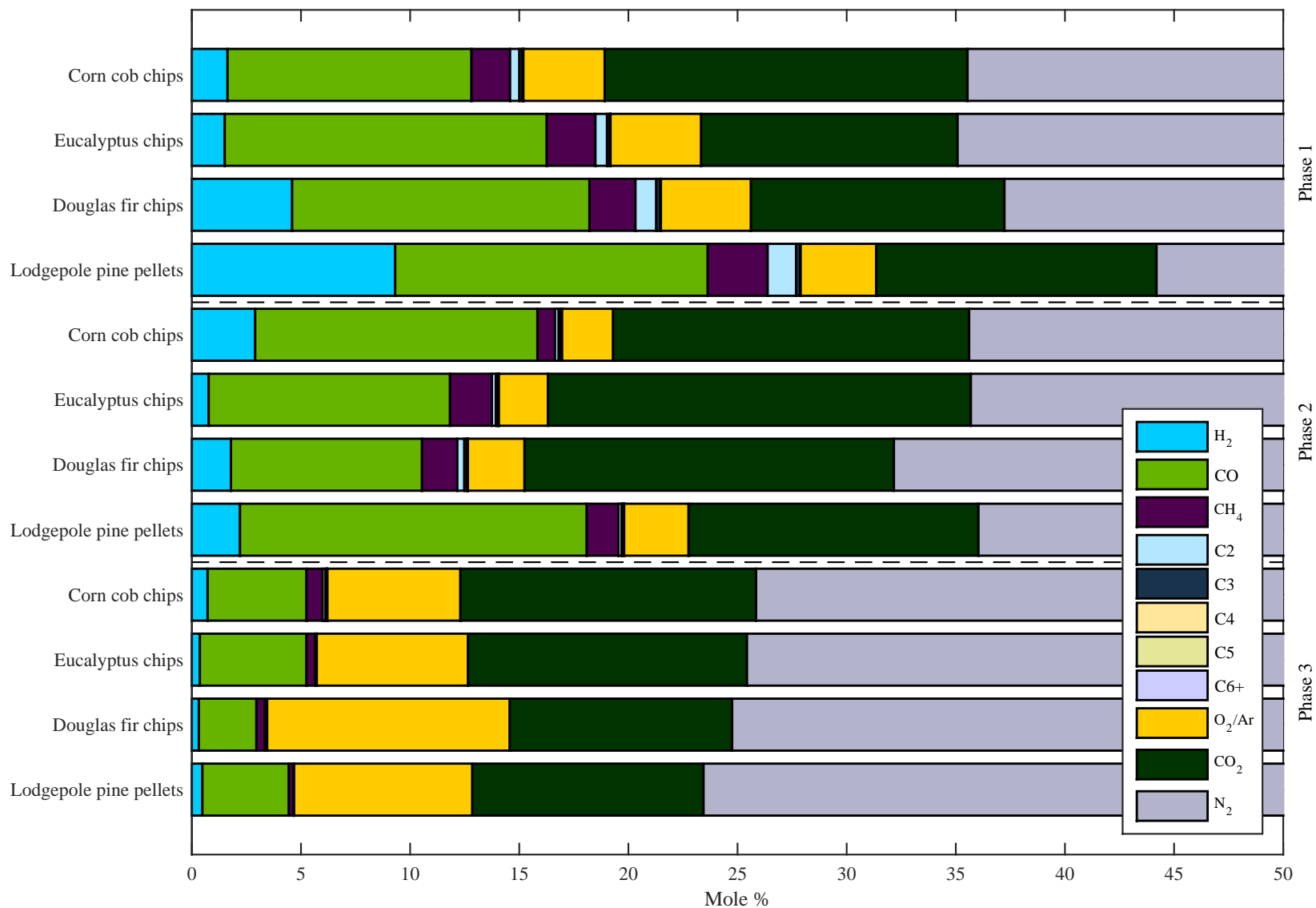


Figure B.36: Effects of fuel type on the average composition of the producer gas entering the secondary combustion zone during normal operation (Phase 1), post-refueling (Phase 2) and during char burnout (Phase 3).

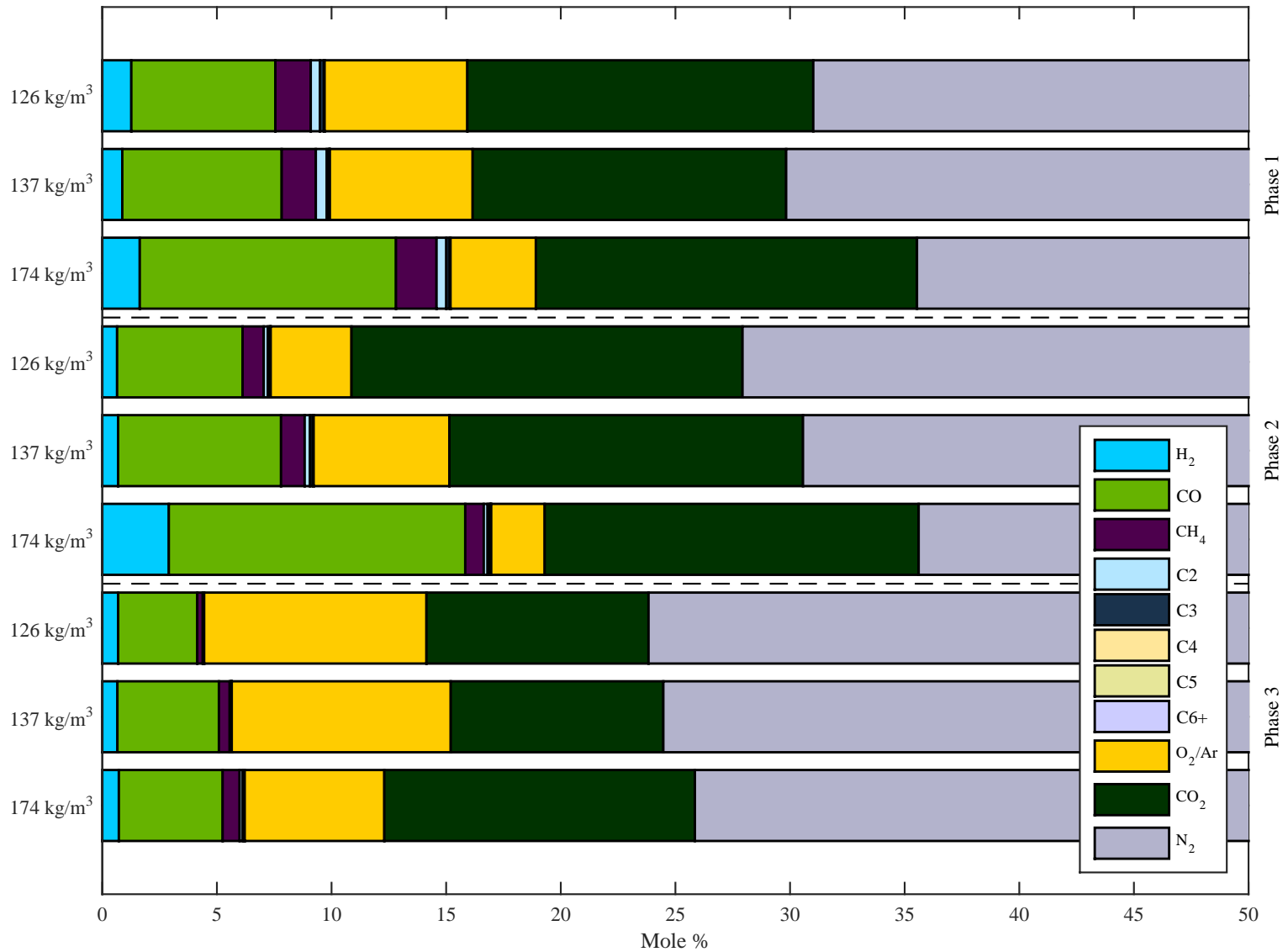


Figure B.37: Effects of fuel bulk density (for corn cobs) on the average composition of the producer gas entering the secondary combustion zone during normal operation (Phase 1), post-refueling (Phase 2) and during char burnout (Phase 3).

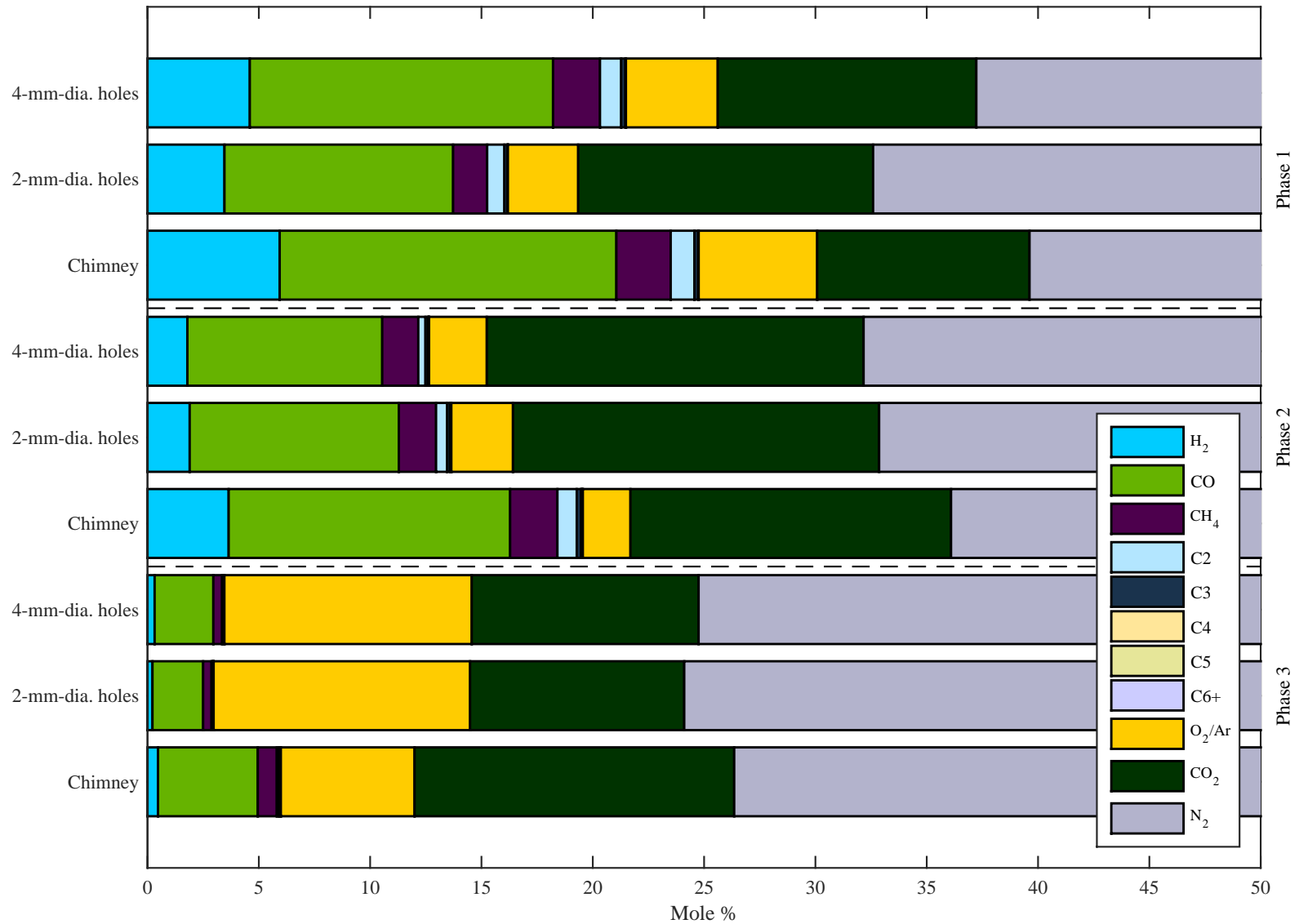


Figure B.38: Effects of secondary air delivery parameters on the average composition of the producer gas entering the secondary combustion zone during normal operation (Phase 1), post-refueling (Phase 2) and during char burnout (Phase 3).

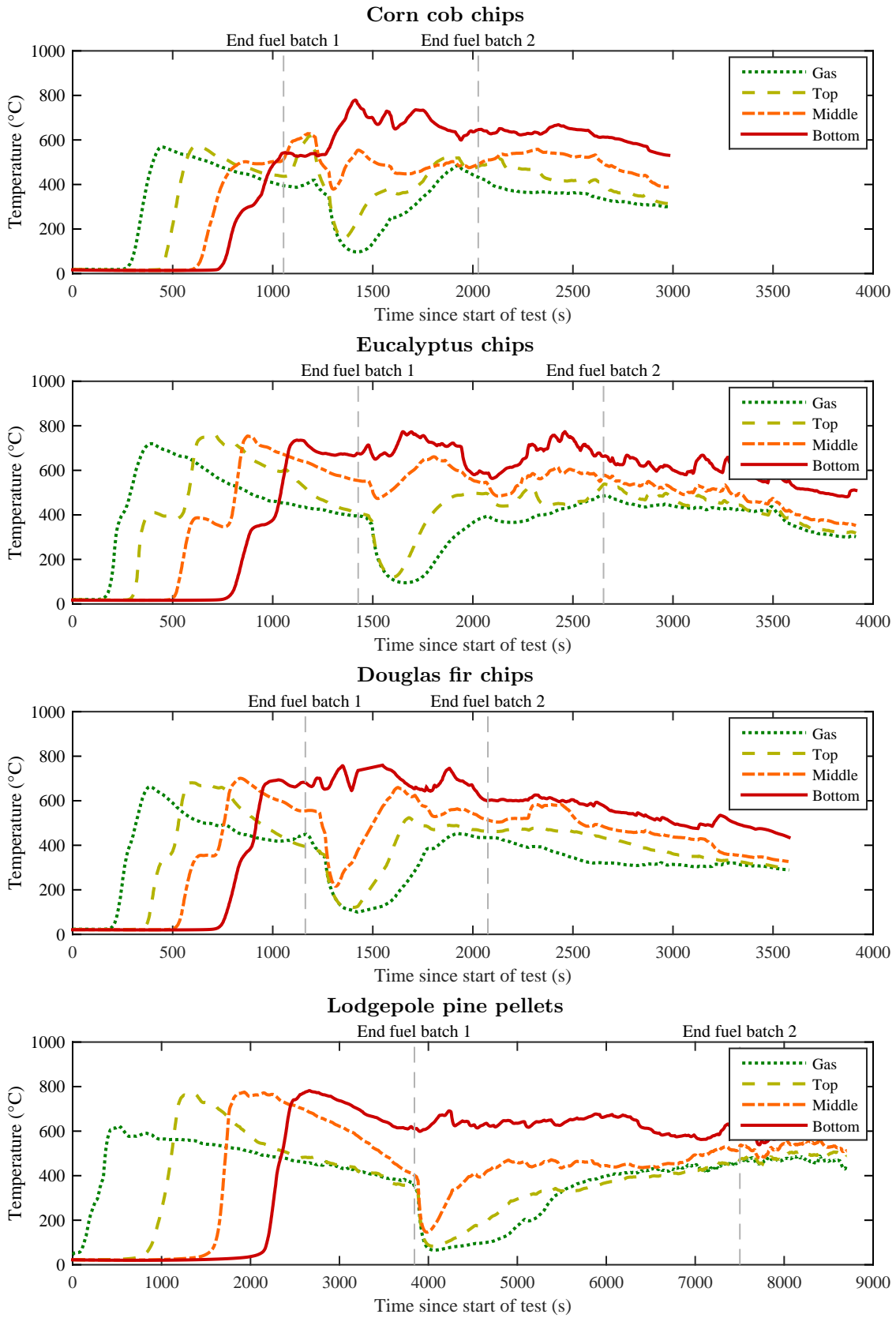


Figure B.39: Fuel bed temperatures measured with different fuel types.

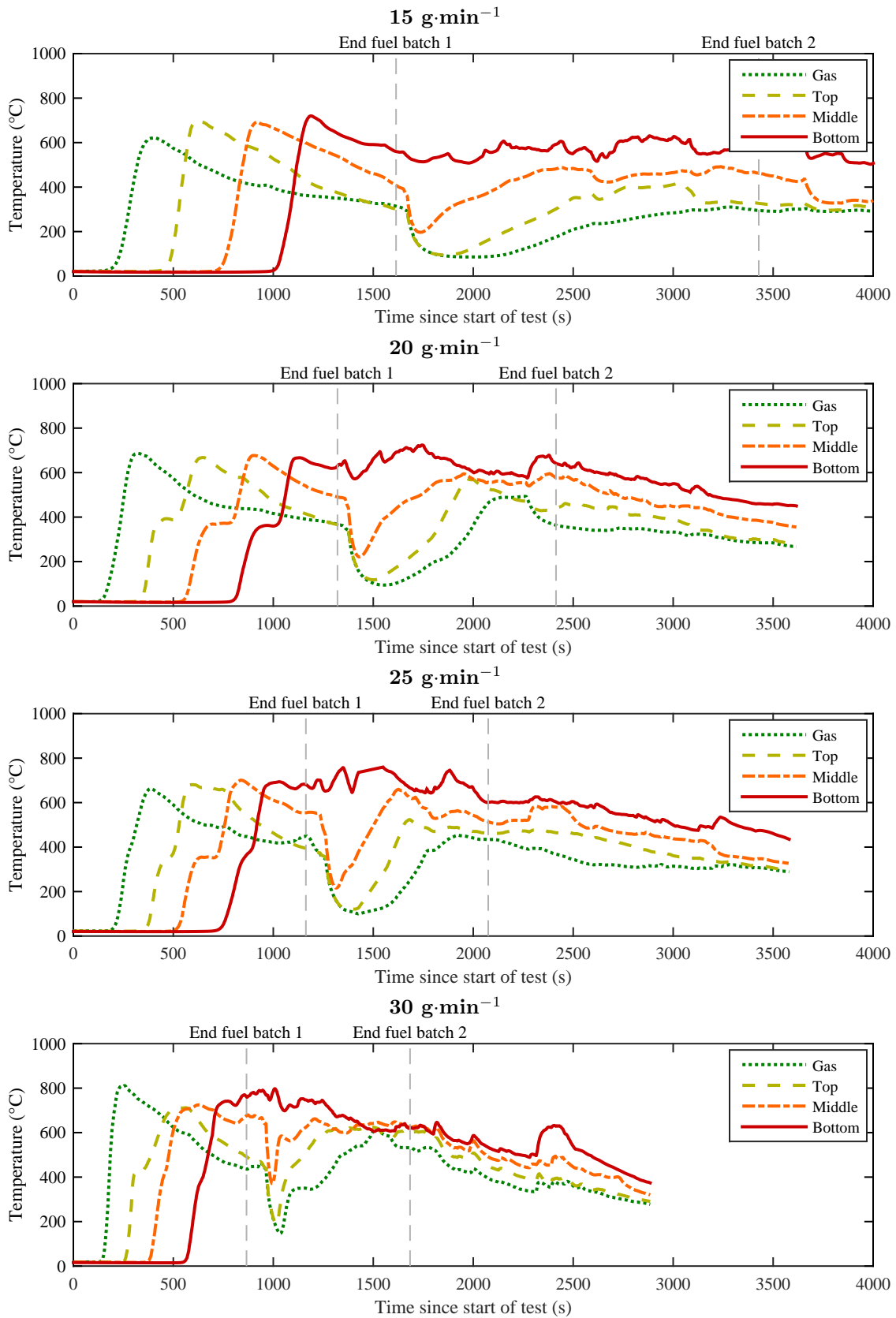


Figure B.40: Fuel bed temperatures measured with different primary air flow rates.

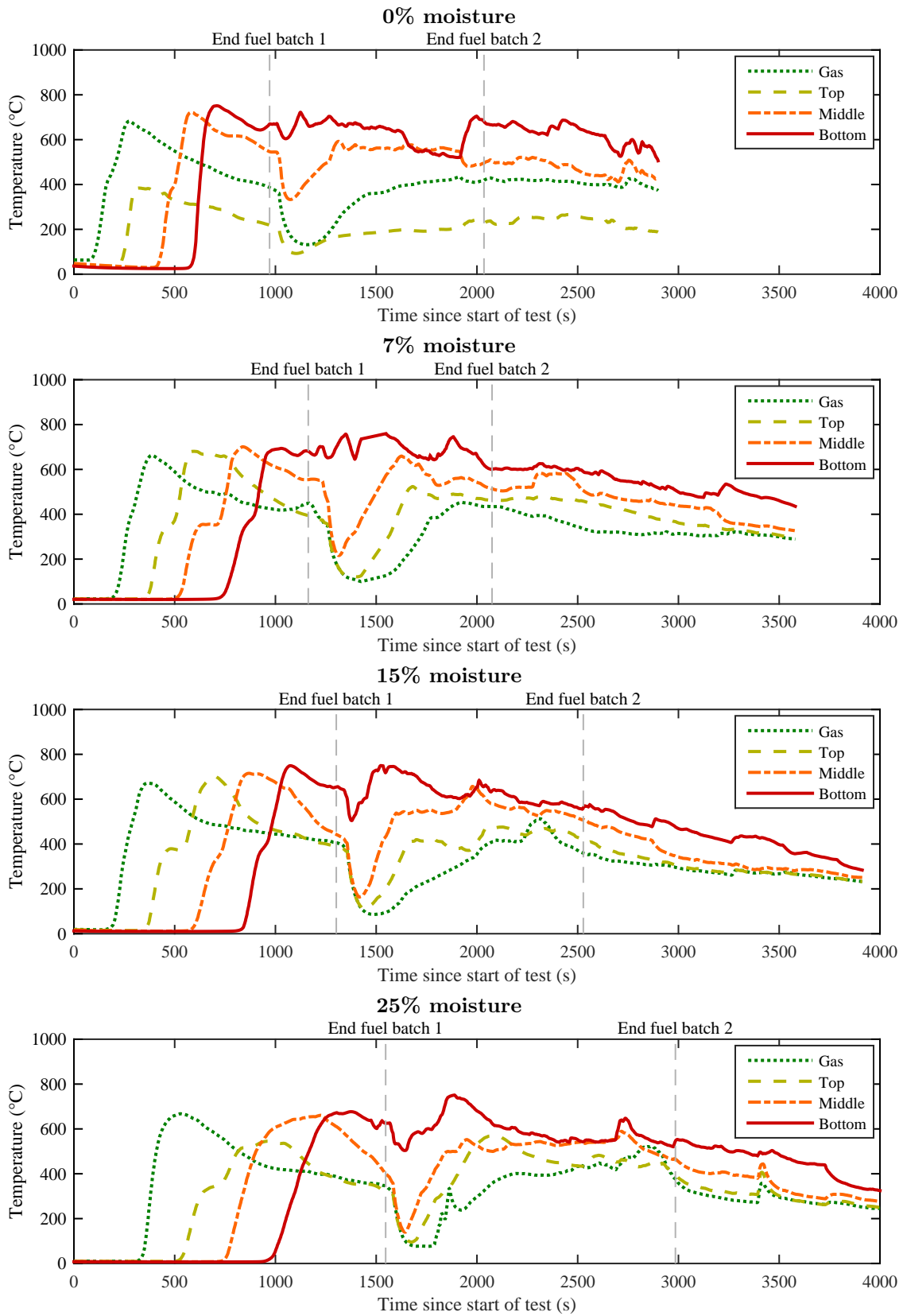


Figure B.41: Fuel bed temperatures measured with different moisture contents.